ABSTRACT

Title of Dissertation: A MODERN AEROMECHANICAL ANALYSIS OF HINGELESS HUB TILTROTORS WITH MODEL- AND FULL-SCALE WIND TUNNEL VALIDATION

Seyhan Gul
Doctor of Philosophy, 2022

Dissertation Directed by: Professor Anubhav Datta
Department of Aerospace Engineering

A new aeromechanics solver was developed, verified, and validated systematically to explore how whirl flutter might be eliminated to achieve significantly higher cruise speeds with future tiltrotor aircraft. The hub explored is hingeless, more advanced than the gimballed hub of current generation tiltrotors. The major finding is that whirl flutter is not the barrier at all for hingeless hubs, instead air resonance, which is another fascinating instability particular to soft in-plane rotors. A possible design change to achieve high cruise speeds with thin, low-profile wings is blade tip sweep. The key mechanism is the aerodynamic center shift. The trade-off is the increase in blade and control system loads.

A fundamental understanding of the physics for soft in-plane hingeless hub stability was provided. The induced flow model showed no effect on high-speed stability, as the wake is quickly washed away and insignificant for airplane mode flight. Predictions in powered mode are necessary. At least the first rotor flap, lag, and torsion modes need to be included. Rotor aerodynamics should use airfoil tables; wing aerodynamics is not essential for air resonance. Periodic solution before stability analysis is necessary for powered mode flight.

Details of the mathematical model were reported. The solver was built to study high-speed stability of hingeless hub tiltrotors; hence the verification and validation cases were chosen accordingly. The stability predictions were verified with U.S. Army's CAMRAD II and RCAS results that were obtained for hypothetical wing/pylon and rotor models. Soft in-plane, stiff in-plane, hyper-stiff in-plane, and rigid rotors were studied with a simple and a generic wing/pylon model. A total of nine cases were investigated. A satisfactory agreement was achieved.

Validation was carried out with Boeing Model 222 test data from 1972. This rotor utilized a soft in-plane hingeless hub. Good agreement was observed for performance predictions. Trends for the oscillatory blade loads were captured, but differences in the magnitudes are present. The agreement between the stability predictions and test data was good for low speeds, but some offset in the damping levels was observed for high speeds. U.S. Army also published stability predictions for this rotor, which agreed well with the present predictions.

A further parametric validation study was carried out using the University of Maryland's Maryland Tiltrotor Rig test data. This is a brand new rig that was first tested for stability in October – November 2021. Eight different configurations were tested. Baseline data is gimbal-free, freewheeling mode, wing fairings on with straight and swept-tip blades. Gimbal-locked, powered mode, and wing fairings off data was also collected, all with straight and swept-tip blades. Wing beam mode damping showed good agreement with the test data. Wing chord mode damping was generally under-predicted. The trends for this mode for the gimbal-locked, straight blade configurations (freewheeling and powered) were not captured by the analysis. Swept-tip blades showed an increase in wing chord mode damping for gimbal-locked, freewheeling configuration. Locking the gimbal increased wing chord damping, which was picked up by the analysis. Powered mode also increased the wing chord damping compared to freewheeling mode, but the analysis did not predict this behavior. Wing beam mode damping test data showed an increase at high speeds due to wing aerodynamics, and the analysis agreed.

A MODERN AEROMECHANICAL ANALYSIS OF HINGELESS HUB TILTROTORS WITH MODEL- AND FULL-SCALE WIND TUNNEL VALIDATION

by

Seyhan Gul

Dissertation submitted to the Faculty of the Graduate School of the
University of Maryland, College Park in partial fulfillment
of the requirements for the degree of
Doctor of Philosophy
2022

Advisory Committee:
Professor Anubhav Datta, Chair/Advisor
Professor Inderjit Chopra
Professor James Baeder
Professor Amr Baz
Professor Maria Cameron

Dedicated to all those whom I've learned so much from,

and who have been with me through happiness and sorrow.

Acknowledgments

This work was possible with Army/Navy/NASA Vertical Lift Research Center of Excellence (VLRCOE) funding. Guidance from Dr. Hyeonsoo Yeo and Dr. Wayne Johnson is greatly appreciated. I would also like to thank Jeff Bosworth from Bell for sharing the Army hypothetical generic wing/pylon model, which was very useful for verifying the solver.

Dr. Anubhav Datta made a big impact on my life. He was not only my advisor; he was also my mentor and will always be a role model for me. I have never known any advisor who is as interested as he has been in their student's life and well-being. I am grateful for everything he taught me and his never-ending support.

My mother Ayşe and my father Bülent deserve a long paragraph here, but I will try to keep it short. They were ready to give up every comfort in their life for our education. They gave us the vision to pursue a Ph.D. but never pushed us in our decisions. It is not easy for parents to encourage both of their children to travel overseas, even for a good cause like this. They were selfless in every aspect of my life, and I will never be able to thank them enough.

My brother Sercan deserves a special acknowledgment. He received his Ph.D. from the University of Texas at Austin in Petroleum Engineering in 2021. We have always had a healthy competition throughout our education but never stopped helping each other out. We shared this journey together, which made everything so much easier.

My partner Masha listened to my enthusiastic talks about my research patiently, even when I was not doing a good job explaining it to her. She was accommodating and was always there for me whenever I needed. I found myself working harder and more disciplined after our time and trips together, which only helped me have a more balanced life and added to my success.

My friends Başar, Gizem, Kaan, Selay, Sina, Buse, Batu, Volkan, Ezgi, Anıl, and Erce also have a special place in my heart. My phone calls with them during the most stressful times brightened my day. Every time I went back to Turkey to visit them and my family, they showed immense hospitality and interest in my life.

I would also like to acknowledge my colleagues Fred, James, Emily, Ravi, Mrinal, Shashank, Abhishek, Lex, Wanyi, Akinola, Nathan, Xavier, Matt, and Eric from the Alfred Gessow Rotorcraft Center. Their ideas inspired me, and I have learned so much from them. Fred and James, with the help of Akinola, Nathan, and Xavier, provided the Maryland Tiltrotor Rig test data, which was a big effort and resulted in important parametric validation data.

Table of Contents

Dedication ii

Acknowledgements iii

Table of Contents v

List of Tables viii

List of Figures ix

Chapter 1: Introduction 1
- 1.1 Motivation 1
- 1.2 High-Speed Stability of Tiltrotors 3
- 1.3 Aeromechanics Analysis of Tiltrotors 6
- 1.4 Wind Tunnel Testing of Tiltrotors 9
  - 1.4.1 Gimballed/Articulated Hub Tests 10
  - 1.4.2 Hingeless Hub Tests 17
- 1.5 Objective of Present Research 21
- 1.6 Contribution of Present Research 22
- 1.7 Organization of the Dissertation 23

Chapter 2: Theory 24
- 2.1 Description of the Solver 24
  - 2.1.1 Structural Model 25
  - 2.1.2 Aerodynamic Model 26
  - 2.1.3 Trim and Transient Solution 27
  - 2.1.4 Stability 28
- 2.2 Geometry and Frames 28
- 2.3 Hamilton's Principle 32
- 2.4 Strain Energy 33
- 2.5 Hub Motions 47
- 2.6 Blade Inertial Loads 49
  - 2.6.1 Forces 49
  - 2.6.2 Moments 52
- 2.7 Blade Aerodynamic Loads 53
  - 2.7.1 Section Angle of Attack and Sideslip Angle 54
  - 2.7.2 Unsteady Thin Airfoil Theory 56

2.7.3 Radial Flow Corrections 59
2.7.4 Reverse Flow 59
2.7.5 Freewake Model 60
2.7.6 Nearwake Model 61
2.8 Sectional Loads 63
2.8.1 Loads by Force Summation 63
2.8.2 Loads by Deformation 64
2.9 Hub Loads 67
2.10 Advanced Geometry Blades 67
2.11 Finite Element Discretization 69
2.12 Numerical Extraction of Matrices 71
2.13 Fixed–Rotating Interface 73
2.14 Joints 76
2.15 System Matrices 78
2.15.1 Strain Energy 78
2.15.2 Aerodynamic/Inertial Loads 82
2.16 Multiblade Coordinate Transformation (MCT) 87
2.17 Solution Methods 91
2.17.1 Finite Element in Time 92
2.17.2 Time Marching 97
2.18 Aeroelastic Stability 98
2.18.1 Eigenanalysis 99
2.18.2 Transient Response 100

Chapter 3: Verification with U.S. Army Hypothetical Case 102
3.1 Rigid Pylon Results 105
3.2 Generic Wing/Pylon Results 111
3.3 Summary and Conclusions 111

Chapter 4: Validation with Full-Scale Boeing M222 Test and Fundamental Understanding 116
4.1 Boeing M222 Rotor 116
4.2 Performance 125
4.2.1 Hover 125
4.2.2 Transition 127
4.2.3 Cruise 127
4.2.4 Freewheeling 128
4.3 Blade Loads 129
4.3.1 Hover 130
4.3.2 Transition 130
4.3.3 Cruise 130
4.4 Aeroelastic Stability 134
4.5 Fundamental Understanding 146
4.6 Summary and Conclusions 160

Chapter 5: Validation with Maryland Tiltrotor Rig and Parametric Study 162
5.1 Maryland Tiltrotor Rig (MTR) 162
5.2 Testing Procedure 175
5.3 Freewheeling 175
5.4 Aeroelastic Stability 178
5.5 Comparison of Test Configurations 184
5.6 Summary and Conclusions 190

Chapter 6: Advanced Geometry Blades 191
6.1 Stability 191
6.2 Loads 201
6.3 Summary and Conclusions 205

Chapter 7: Summary and Conclusions 206
7.1 Key Conclusions 206
7.2 Future Work 209
7.2.1 Analysis 209
7.2.2 Testing 210

Bibliography 212

List of Tables

2.1 Nondimensionalization Parameters 37

3.1 U.S. Army rigid pylon properties (Ref. [19]) 102
3.2 U.S. Army hypothetical generic NASTRAN wing/pylon frequencies and mass-normalized mode shapes at the rotor hub (Ref. [19]) 103
3.3 U.S. Army hypothetical hingeless rotor properties (Ref. [19]) 103
3.4 U.S. Army hypothetical hingeless rotor frequencies (Ref. [19]) 103

4.1 Boeing M222 rotor properties 117
4.2 Full-stiffness NASA dynamic wing test stand properties 117
4.3 Boeing M222 test points 118
4.4 Boeing M222 wing beam mode mass-normalized mode shape (Ref. [71]) 123
4.5 Boeing M222 wing chord mode mass-normalized mode shape (Ref. [71]) 124
4.6 Boeing M222 wing torsion mode mass-normalized mode shape (Ref. [71]) 124

5.1 MTR rotor properties 165
5.2 MTR wing/pylon properties 165
5.3 MTR wing beam mode mass-normalized mode shape 172
5.4 MTR wing chord mode mass-normalized mode shape 173
5.5 MTR wing torsion mode mass-normalized mode shape 173
5.6 Flutter test conditions 176

List of Figures

1.1 Rotor/pylon/wing modes . . . 3
1.2 XV-3 in the NASA Ames 40-ft × 80-ft wind tunnel (Ref. [48]) . . . 10
1.3 Bell Model 300 in the NASA Ames 40-ft × 80-ft wind tunnel (Ref. [50]) . . . 11
1.4 Full-scale XV-15 in the NASA Ames 40-ft × 80-ft wind tunnel (Ref. [48]) . . . 12
1.5 WRATS in the NASA Langley Transonic Dynamics Tunnel (Ref. [20]) . . . 13
1.6 VDTR in the United Technologies Research Center wind tunnel (Ref. [59]) . . . 14
1.7 TRAM wind tunnel tests . . . 15
1.8 NASA TTR in the NASA Ames 40-ft × 80-ft wind tunnel (Ref. [65]) . . . 15
1.9 Maryland Tiltrotor Rig (MTR) in the Navy Carderock wind tunnel (Ref. [67]) . . . 17
1.10 TRAST in the NASA Langley Transonic Dynamics Tunnel (Ref. [70]) . . . 17
1.11 Full-scale Boeing M222 in the NASA Ames 40-ft × 80-ft wind tunnel (Ref. [71]) 18
1.12 $1/9.244$ Froude-scaled Boeing M222 in the MIT Wright Brothers wind tunnel (Ref. [72]) . . . 19
1.13 $1/4.622$ Froude-scaled Boeing M222 in the Boeing V/STOL wind tunnel (Ref. [74]) 20

2.1 Schematic of rotor/pylon/wing system . . . 30
2.2 Undeformed and deformed frames . . . 30
2.3 Induced velocity of vortex filament A-B at point O . . . 62
2.4 Nearwake geometry . . . 62
2.5 Finite element degrees of freedom . . . 70
2.6 Joint schematic . . . 76
2.7 Finite element in time . . . 92
2.8 Transient response method . . . 101

3.1 U.S. Army hypothetical rigid pylon model (Ref. [19]) . . . 104
3.2 U.S. Army hypothetical generic NASTRAN wing/pylon model (Ref. [19]) . . . 104
3.3 Aeroelastic stability verification for rigid pylon and rigid rotor (solid: U.S. Army predictions with CAMRAD II and RCAS (Ref. [19]), dash: UMD predictions with UMARC-II) . . . 106
3.4 Aeroelastic stability verification for rigid pylon and soft in-plane rotor (solid: U.S. Army predictions with CAMRAD II and RCAS (Ref. [19]), dash: UMD predictions with UMARC-II) . . . 107
3.5 Aeroelastic stability verification for rigid pylon and stiff in-plane 1 rotor (solid: U.S. Army predictions with CAMRAD II and RCAS (Ref. [19]), dash: UMD predictions with UMARC-II) . . . 108

3.6 Aeroelastic stability verification for rigid pylon and stiff in-plane 2 rotor (solid: U.S. Army predictions with CAMRAD II and RCAS (Ref. [19]), dash: UMD predictions with UMARC-II) . . . 109
3.7 Aeroelastic stability verification for rigid pylon and slowed rotor (solid: U.S. Army predictions with CAMRAD II and RCAS (Ref. [19]), dash: UMD predictions with UMARC-II) . . . 110
3.8 Aeroelastic stability verification for generic wing/pylon and soft in-plane rotor (solid: U.S. Army predictions with CAMRAD II and RCAS (Ref. [19]), dash: UMD predictions with UMARC-II) . . . 112
3.9 Aeroelastic stability verification for generic wing/pylon and stiff in-plane 1 rotor (solid: U.S. Army predictions with CAMRAD II and RCAS (Ref. [19]), dash: UMD predictions with UMARC-II) . . . 113
3.10 Aeroelastic stability verification for generic wing/pylon and stiff in-plane 2 rotor (solid: U.S. Army predictions with CAMRAD II and RCAS (Ref. [19]), dash: UMD predictions with UMARC-II) . . . 114
3.11 Aeroelastic stability verification for generic wing/pylon and slowed rotor (solid: U.S. Army predictions with CAMRAD II and RCAS (Ref. [19]), dash: UMD predictions with UMARC-II) . . . 115

4.1 UMARC-II model of the Boeing M222 tiltrotor (rotor, pylon, and wing are beams, panels show aerodynamic segments) . . . 119
4.2 Boeing M222 rotor properties . . . 122
4.3 Boeing M222 mode shape points . . . 123
4.4 Boeing M222 fanplot (solid: predictions for $8.8°$ collective, dash: predictions for $40°$ collective, symbols: test data) . . . 125
4.5 Comparison of hover thrust and power coefficient predictions with Boeing M222 test data (lines: predictions, symbols: test data) . . . 126
4.6 Comparison of 105-knots transition power versus thrust coefficient predictions with Boeing M222 test data ($\mu = 0.11$, $\lambda_c = 0.21$, $i_N = 27°$ from the flow) (lines: predictions, symbols: test data) . . . 127
4.7 Comparison of 140-knots cruise power versus thrust coefficient predictions with Boeing M222 test data ($\mu = 0.08$, $\lambda_c = 0.44$, $i_N = 10°$ from the flow) (lines: predictions, symbols: test data) . . . 128
4.8 Comparison of freewheeling collective predictions with Boeing M222 test data (lines: predictions, symbols: test data) . . . 129
4.9 Comparison of hover alternating bending moment predictions with Boeing M222 test data (solid: predictions with control angles, dot: predictions with hub load trim, symbols: test data) . . . 131
4.10 Comparison of hover hub moment predictions with Boeing M222 test data (solid: predictions with control angles, dot: predictions with hub load trim, symbols: test data) . . . 132
4.11 Comparison of 105-knots transition alternating bending moment predictions with Boeing M222 test data ($\mu = 0.11$, $\lambda_c = 0.21$, $i_N = 27°$ from the flow) (solid: predictions with control angles, dot: predictions with hub load trim, symbols: test data) . . . 133

4.12 Comparison of 105-knots transition hub moment predictions with Boeing M222 test data ($\mu = 0.11$, $\lambda_c = 0.21$, $i_N = 27°$ from the flow) (solid: predictions with control angles, dot: predictions with hub load trim, symbols: test data) 134
4.13 Comparison of 140-knots cruise alternating bending moment predictions with Boeing M222 test data ($\mu = 0.08$, $\lambda_c = 0.44$, $i_N = 10°$ from the flow) (solid: predictions with control angles, dot: predictions with hub load trim, symbols: test data) 135
4.14 Comparison of 140-knots cruise hub moment predictions with Boeing M222 test data ($\mu = 0.08$, $\lambda_c = 0.44$, $i_N = 10°$ from the flow) (solid: predictions with control angles, dot: predictions with hub load trim, symbols: test data) 136
4.15 Stability roots of isolated rotor modes at the design rotor speed (386 rpm) 138
4.16 Stability roots of isolated wing modes 139
4.17 Stability roots of coupled modes at the design rotor speed (386 rpm) 140
4.18 Eigenvectors for the wing torsion mode 141
4.19 Stability roots of coupled modes at 100-knots (lines: UMD (UMARC-II) and U.S. Army (RCAS, Ref. [33]) predictions, symbols: test data) 143
4.20 Wing beam mode damping (lines: UMD (UMARC-II) and U.S. Army (RCAS, Ref. [33]) predictions, symbols: test data) 145
4.21 Effect of induced flow (solid: uniform inflow – baseline, dash: no induced flow, dot: Maryland Freewake) 149
4.22 Effect of rotor speed perturbation and powered mode operation (solid: freewheeling with rotor speed perturbation – baseline, dash: freewheeling with constant rotor speed (ideal engine), dot: powered with constant rotor speed (ideal engine)) . . . 150
4.23 Effect of rotor modes (solid: first 10 modes – baseline, dash: first flap, lag, and torsion modes, dot: first flap and lag modes) 151
4.24 Effect of rotor modes (solid: first flap and lag modes, dash: first flap mode only) . 152
4.25 Effect of rotor modes (solid: first flap and lag modes, dash: first lag mode only) . 153
4.26 Effect of blade airloads model (solid: C81 airfoil decks with unsteady terms – baseline, dash: C81 airfoil decks without unsteady terms, dot: linear aerodynamics with Glauert correction) 154
4.27 Effect of blade airloads model (solid: linear aerodynamics with Glauert correction, dash: incompressible linear aerodynamics) 155
4.28 Effect of wing aerodynamic model (solid: C81 airfoil deck – baseline, dash: C81 airfoil decks without unsteady terms, dot: incompressible linear aerodynamics) . 156
4.29 Effect of wing aerodynamic model (solid: incompressible linear aerodynamics, dash: no aerodynamics) 157
4.30 Effect of periodic solution for freewheeling (solid: baseline, dash: no periodic solution) 158
4.31 Effect of periodic solution for powered mode (solid: powered mode, dash: powered mode with no periodic solution) 159

5.1 UMARC-II model of the MTR (rotor, pylon, and wing are beams, panels show aerodynamic segments) 164
5.2 MTR blades 165
5.3 MTR rotor properties 168

5.4 MTR wing/pylon properties . . . 171
5.5 MTR mode shape points . . . 172
5.6 MTR fanplot (solid: predictions, symbols: test data) . . . 174
5.7 Comparison of freewheeling collective predictions with MTR test data at 1050 rpm (lines: predictions, symbols: test data) . . . 177
5.8 Comparison of frequency predictions with wind tunnel test data for gimbal-free, freewheeling, wing fairings on configuration (lines: predictions, symbols: test data) 179
5.9 Comparison of damping predictions with wind tunnel test data for gimbal-free, freewheeling, wing fairings on configuration (lines: predictions, symbols: test data) 180
5.10 Comparison of damping predictions with wind tunnel test data for gimbal-free, freewheeling, wing fairings off configuration (lines: predictions, symbols: test data) 181
5.11 Comparison of damping predictions with wind tunnel test data for gimbal-locked, freewheeling, wing fairings off configuration (lines: predictions, symbols: test data) 182
5.12 Comparison of damping predictions with wind tunnel test data for gimbal-locked, powered, wing fairings off configuration (lines: predictions, symbols: test data) . 183
5.13 Comparison of straight and swept-tip blade damping test data for gimbal-free, freewheeling, wing fairings on configuration (lines: predictions, symbols: test data) 185
5.14 Comparison of straight and swept-tip blade damping test data for gimbal-locked, freewheeling, wing fairings off configuration (lines: predictions, symbols: test data) 186
5.15 Comparison of gimbal-free and gimbal-locked damping test data for freewheeling, wing fairings off, straight blades configuration (lines: predictions, symbols: test data) . . . 187
5.16 Comparison of freewheeling and powered mode damping test data for gimbal-locked, wing fairings off, straight blades configuration (lines: predictions, symbols: test data) . . . 188
5.17 Comparison of wing fairings on and off damping test data for gimbal-free, freewheeling, straight blades configuration (lines: predictions, symbols: test data) . . . 189

6.1 UMARC-II model of the Boeing M222 tiltrotor with swept-tip blades (rotor, pylon, and wing are beams, panels show aerodynamic segments) . . . 192
6.2 Effect of tip sweep (solid: straight blades – baseline, dash: 10° sweep, dot: 20° sweep) . . . 193
6.3 Effect of c.g. sweep (solid: 20° sweep, dash: 20° sweep – c.g. unswept) . . . 194
6.4 Effect of sweep with no tip aerodynamics (solid: straight blades – baseline, dash: 20° sweep) . . . 196
6.5 Stabiliizing effect of blade tip sweep . . . 197
6.6 Effect of spar in the swept region (solid: 20° sweep, dash: 20° sweep without spar – case 1) . . . 198
6.7 Effect of spar in the swept region (solid: 20° sweep, dash: 20° sweep without spar – case 2) . . . 199
6.8 Effect of double-sweep (solid: straight blades – baseline, dash: 20° sweep, dot: 20° double-sweep) . . . 200
6.9 Flapwise bending moment (solid: straight blades – baseline, dash: 20° sweep without spar) . . . 202

6.10 Chordwise bending moment (solid: straight blades – baseline, dash: 20° sweep without spar) 203
6.11 Torsional moment (positive pitch up) (solid: straight blades – baseline, dash: 20° sweep without spar) 204

7.1 CAD Model of the Maryland Tiltrotor Rig hingeless hub 211

Chapter 1: Introduction

This chapter introduces the topic of this dissertation. It covers motivation, a description of the problem, and a survey of past and present analysis and test data to bring the reader up to the state of the art.

1.1 Motivation

The modern tiltrotor is a versatile rotary-wing aircraft tailored for cruise at high speeds up to $270 – 280$ knots (V-22 and V-280). One of the major barriers to achieving even higher speeds is whirl flutter or drag penalty due to the thick wings required to prevent it. Flutter of tiltrotors is a unique instability that arises with large rotors and blade flapping which are essential for good hover and helicopter mode flight. Whether the blades, hubs, or wings can be refined or altered for higher cruise speeds still remains an interesting area of research.

The current technology is gimballed hubs with positive pitch-flap coupling (negative δ_3). Hingeless hubs may have better flutter characteristics and lighter weight than their gimballed counterparts despite the increase in flap bending moments in helicopter mode. For both gimballed and hingeless hubs, three kinds of in-plane frequencies are possible: soft in-plane (lag frequency less than $1/\mathrm{rev}$), stiff in-plane (lag frequency greater than $1/\mathrm{rev}$), and hyper-stiff in-plane (lag frequency greater than $3/\mathrm{rev}$). Here $1/\mathrm{rev}$ equals the rotor rotational frequency. Stiff in-plane is the current tiltrotor technology. Hyper-stiff hingeless hub envisions advanced, ultralight blade materials to push the frequencies up. Soft in-plane is a conservative helicopter-like approach where blade materials can remain as today. The hub is softer, so in-plane bending loads can also be alleviated. The exploration in this dissertation is focused on soft in-plane as it is the only data available for validation.

A tiltrotor aircraft with a hingeless hub was identified by NASA Heavy Lift Rotorcraft Systems Investigation as having the best potential to meet the technology goals for large civil transport (stiff in-plane, Ref. [1]). Karem Aircraft's design for the Joint Multi-Role demonstration also utilized a hingeless hub tiltrotor (hyper-stiff in-plane, Refs. [2, 3]). However, none of these aircraft were built or tested in model scale; hence, there is no data set to prove or refute the assertions. In general, a thorough understanding of high-speed instability characteristics of hingeless hubs is acutely missing. The purpose of this research is to bridge this gap, starting with analysis.

In order to study the stability mechanisms from the first principles, a new aeromechanics solver was developed in this work. The solver was named UMARC-II. The predictions were first verified with a hypothetical problem created by the U.S. Army. Next, available test data and properties were consolidated from a Boeing full-scale test for comprehensive modeling and validation. This was followed by a parametric validation using the recently acquired Maryland Tiltrotor Rig test results. The solver was then used to understand the fundamental nature of hingeless hub instabilities and the mechanisms that drive and influence it. Based on this understanding, the impact of swept-tip blades on stability and loads was explored. The effects of aerodynamic and inertial couplings were isolated, and insight was offered on how flutter speed can be significantly increased.

1.2 High-Speed Stability of Tiltrotors

Tiltrotor aircraft encounter whirl flutter at high cruise speeds in airplane mode. This dissertation reports that soft in-plane hingeless hubs may also experience a phenomenon called proprotor air resonance. Both whirl flutter and proprotor air resonance are results of dynamic coupling of rotating and fixed structures, but the instability mechanisms are very different.

Figure 1.1 introduces the primary rotor and wing modes of motion and some general notations. Throughout this dissertation, the degrees of freedom are labeled as follows: q_1 is wing beam bending, q_2 is wing chord bending, p is wing torsion, β is rotor flap, and ζ is rotor lag. Fixed frame rotor modes are labeled as follows: collective flap and lag modes are β and ζ, respectively, low-frequency modes are $\beta - 1$ and $\zeta - 1$, and high-frequency modes are $\beta + 1$ and $\zeta + 1$. The rotor rotation speed is Ω. The details are given later.

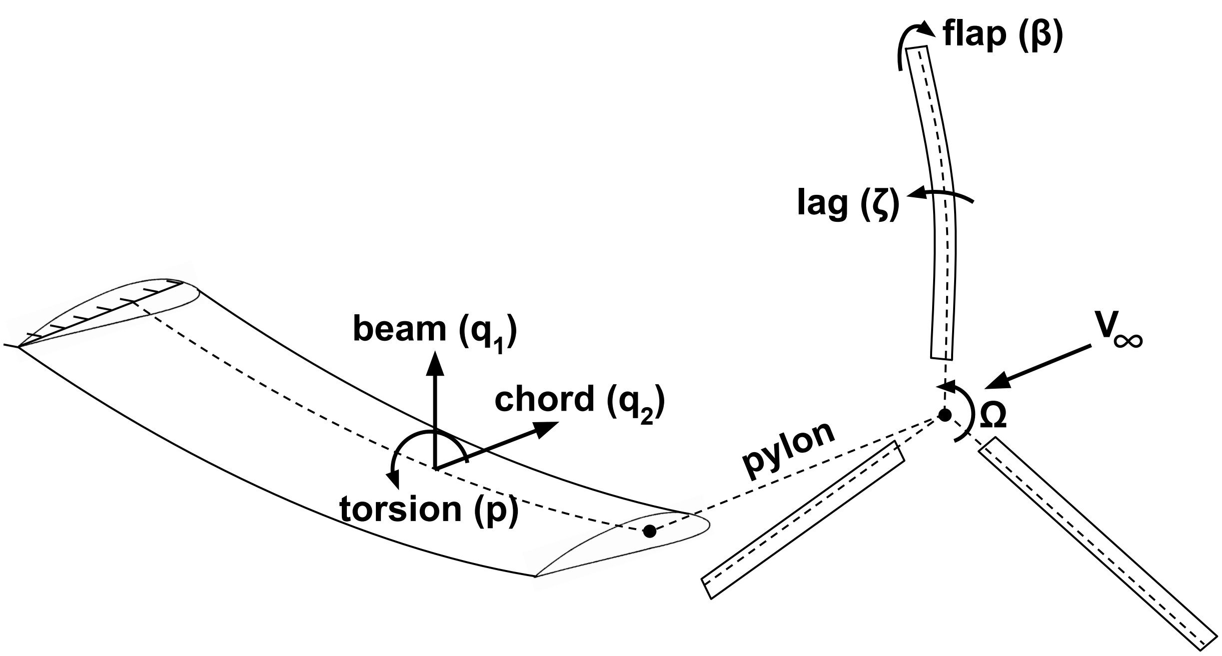

Figure 1.1: Rotor/pylon/wing modes

Whirl flutter is an aeroelastic instability phenomenon specific to wing-mounted propellers (classical whirl flutter) and proprotors (tiltrotor whirl flutter) in axial flight. The word "proprotor" is a combination of "propeller" and "rotor". Proprotors have a high twist angle like propellers for axial flight, and they also flap like helicopter rotors to alleviate bending moments in edgewise flight (helicopter mode). Although the mechanisms between classical and tiltrotor whirl flutter are drastically different, the work on proprotor whirl flutter has its roots in classical whirl flutter (Ref. [4]), which was first recognized by Taylor and Browne (Ref. [5]). This dissertation addresses tiltrotor whirl flutter, which is broader in scope and carries classical whirl flutter as a subset.

Whirl flutter occurs due to the aeroelastic coupling between the rotor flap (β) and the wing motions. The rotor lag (ζ) participates but is not a key driver. Typically, the wing beam (q_1) or chord (q_2) mode coalesces with the rotor modes and goes unstable. The instability occurs near the corresponding wing frequency. Wing chordwise and torsion motions cause pylon yaw and pitch, respectively, which are both required for instability. Coriolis forces couple the pylon modes; a perturbation in the pylon yaw results in a motion in the pitch direction.

Consider a perturbation of the pylon in the pitch direction. The hub will follow the pylon, but because the blades are not rigidly fixed to the hub, the rotor will lag this motion until the effective longitudinal flap angle is high enough to generate the moment for it to precess and follow. Due to the changing flapping velocity on the blade as it rotates around the shaft, the aerodynamic forces will increase on one side and decrease on the other. These forces have out-of-plane and in-plane components. The out-of-plane component will generate the necessary moment for precession. The in-plane component will destabilize the wing/pylon. The destabilizing action appears only at high inflow, which is why large angles are essential for tiltrotor analysis. This action is subdued by stabilizing forces/moments up to a certain speed.

There are two primary stabilizing mechanisms. The first one is the moment generated by the thrust with respect to the wing when a perturbation occurs. The thrust is perpendicular to the tip-path plane, so it will have a component perpendicular to the pylon, which will create a stabilizing moment. The second is the flapping moment due to the blade retention at the hub. This would reduce the effective blade flapping due to a perturbation and alleviate the in-plane aerodynamic loads due to high inflow aerodynamics. This moment is zero for a gimballed hub but can be substantial for a hingeless hub, which is the promise of the hingeless hub.

Proprotor air resonance, on the other hand, is driven by the coupling of the low-frequency lag ($\zeta - 1$) and wing beam (q_1) or torsion (p) motion. The rotor flap (β) participates but is not a key driver. An in-plane motion is generated at the rotor hub due to the wing beam (q_1) or torsion (p), and this excites the rotor lag (ζ) motion. The instability occurs at the frequency of the low-frequency lag ($\zeta - 1$) mode. This instability can be the limiting phenomenon for soft in-plane ($\nu_\zeta < 1$) hingeless hubs.

Proprotor air resonance shares some similarities with helicopter air resonance. Helicopter air resonance is also a critical instability for soft in-plane hingeless hubs where frequencies of coupled rotor flap and body angular modes coalesce with the rotor lag motion. However, in helicopter air resonance, flap is the key driver. Thus, the mechanism is similar but not the same. The word air resonance is used because the perturbation of wing beam (q_1) and torsion (p) motion to the proprotor is the same as fuselage roll and pitch motion to the helicopter rotor. The response to these perturbations is different due to the high inflow in proprotors. So, the modeling requirements for aerodynamics are also vastly different.

1.3 Aeromechanics Analysis of Tiltrotors

Comprehensive analysis of rotorcraft date back to the 1960s, when digital computers first became available to engineers. Many codes have been developed by the academia, government, and industry (Ref. [6]). Some of the notable ones are C81/COPTER family, CAMRAD family, RCAS, UMARC family, MBDyn, and DYMORE. A survey of these solvers and work conducted pertinent to tiltrotors are given below.

In a 1962 paper (Ref. [7]), Blankenship and Harvey discuss a digital computer program designed for IBM 7070 that can calculate helicopter performance and rotor blade bending moments. This was the predecessor of the first rotorcraft comprehensive analysis code C81. C81 was developed by Bell Helicopter with support from the U.S. Army. The first complete documentation is given in Ref. [8]. The last official version was released in 1981 (Ref. [9]). Features typical of all rotorcraft analysis – finite element beams, unsteady aerodynamics/dynamic stall, and freewake were available. It is not clear whether large inflow and large aerodynamic angles were allowed. A multiblade coordinate transformation for the fixed–rotating interface that is useful for flutter analysis of rotorcraft was not included. Stability analysis could be performed with transient analysis. Frequency and damping could be extracted with Moving-Block or Prony methods. The first elastic airframe/pylon model was included in the early 1970s (Refs. [10, 11]). The pylon model was in the shape of frequency and mode shape inputs from an external solver such as NASTRAN. The configuration was not generic; only two rotors and two pylons could be modeled.

In 1979, Bell started the development of COPTER (Comprehensive Program for Theoretical Evaluation of Rotorcraft, Ref. [12]). The development history is given in Ref. [10]. Unsteady aerodynamics/dynamic stall and freewake were included. Multiblade coordinate transformation was available. Stability analysis could be performed with linearized eigenanalysis, outputs of which were eigenvalues and eigenvectors. An elastic airframe could be modeled with modal inputs from NASTRAN. Initially, only two rotors were allowed. Later, COPTER 2000 removed this limitation. Reference [10] studied interactional aerodynamics, performance, loads, vibrations, and gust response for Quad Tiltrotor (QTR) and V-22 with COPTER 2000. Reference [12] reports validation for isolated and ground resonance stability of a hingeless rotor and air resonance stability of a bearingless rotor in forward flight with an earlier version of this code. Reference [13] reports validation for performance, loads, and vibration predictions for seven hingeless and bearingless rotors.

CAMRAD (Comprehensive Analytical Model of Rotorcraft Aerodynamics and Dynamics, Refs. [14, 15]) was developed at Ames research center for NASA and U.S. Army by Wayne Johnson. Applications of CAMRAD on rotorcraft problems led to separate extensions and modifications. CAMRAD/JA (Ref. [16]) was developed by Johnson Aeronautics in 1986 – 1988 as a revised software implementation of CAMRAD with new capabilities for the aerodynamic and wake models. The structural model did not change. CAMRAD/JA still had limitations, such as a single load path for the blade, small dynamic motion, and a single solution method. CAMRAD II (Refs. [17, 18]) was developed to eliminate these limitations. Finite element beams, unsteady aerodynamics/dynamic stall, and freewake are available. High inflow axial flight aerodynamics and large aerodynamic angles are allowed (Ref. [6]). Multiblade coordinate transformation is included. Stability analysis can be carried out with linearized eigenanalysis or transient response. An elastic airframe can be modeled with either modal inputs from an external solver or as a simple mass, spring, and damper system. Building-block approach is used to achieve flexibility in modeling; any geometry is possible. Important tiltrotor work with CAMRAD is reported chronologically in Refs. [19–26].

RCAS (Rotorcraft Comprehensive Analysis System) was developed for the U.S. Army by Advanced Rotorcraft Technology, Inc. (ART) as an advancement over the earlier 2GCHAS. The first release was in June 2003 (Refs. [27–30]). Its capabilities are comparable to CAMRAD II. Unsteady aerodynamics/dynamic stall, freewake, and Viscous Vortex Particle Method (VVPM) models are available. Large inflow and large aerodynamic angles are allowed. Multiblade coordinate transformation is included. Stability analysis is carried out with linearized eigenanalysis or transient response. The solver can either model the airframe with simple masses, springs, and dampers, or external modal inputs can be admitted. The solver is robust and flexible; any geometry can be modeled. Overview and validation results can be found in Refs. [31,32]. Notable work for tiltrotor analysis is given in Refs. [19–21, 33, 34].

UMARC (University of Maryland Advanced Rotorcraft Code, Ref. [35]) was developed at the University of Maryland (UMD) starting in the late 1980s. Unsteady aerodynamics/dynamic stall and freewake models are included. Inflow and aerodynamic angles are small due to the analytical nature of derivatives. Multiblade coordinates can be used. Similar to CAMRAD and RCAS, stability analysis can be performed with linearized eigenanalysis or transient solution. Multibody dynamics capability was developed (Ref. [36]), but never integrated into the original solver. A version of UMARC could model the rotor and the wing together. The configuration is not generic; it is fixed to one rotor located at the wing tip. Notable work on tiltrotors with UMARC is given in Refs. [37–39]. Most of the tiltrotor-related capability was lost over time due to lack of research.

Modern multibody dynamics codes have also been applied on tiltrotor whirl flutter as the wake is unimportant and simple aerodynamics is often sufficient. The notable ones are MBDyn (Refs. [40–43]) and DYMORE (Ref. [44]), which have been used to model and study U.S. and European tiltrotor models/concepts. Other important analytical work is given in Refs. [4, 45–47].

The present solver was developed to allow focus on the principal mechanisms and flexibility for changes in the modeling parameters. It includes features typical of all rotorcraft analysis except dynamic stall. The aerodynamic and inertial matrices are generated by numerical differentiation. Large inflow and aerodynamic angles are allowed due to the numerical nature of derivatives. Either multiblade or individual blade coordinates can be used. Stability solution can be obtained with linearized eigenanalysis or transient solution. The wing and the pylon can be modeled directly as beams or external modal inputs can be admitted. The rotor and the wing/pylon configurations are generic and can be built up as multibody systems, but only a single rotor on a single wing/pylon is currently allowed as it is the only configuration for which test data is available and the most relevant for current aircraft. Some of these features are also available in commercial solvers, but the pursuit of fundamental understanding of the problem at hand and dissection of its principal mechanisms favored the development of a new solver. Henceforth the code and its expansions will be referred to as versions of UMARC-II with multibody dynamics and large angle exact aerodynamics distinguishing it from the earlier generation. More detailed information is given in Chapter 2.

1.4 Wind Tunnel Testing of Tiltrotors

Many full-scale and model-scale tiltrotor wind tunnel tests have been conducted since the 1950s. Most of them utilized gimballed hub proprotors. Only a few tests were conducted on hingeless hubs. The most important tests are chronologically described below.

1.4.1 Gimballed/Articulated Hub Tests

The XV-3 (Bell Model 200) tiltrotor was the Bell proposal in response to the Convertible Aircraft Program Request for Proposal (RFP) by the U.S. Army and Air Force for the design of a “convertiplane” in 1951. The contract was awarded for two full-scale aircraft in October 1953 (Ref. [48]). On October 25, 1956, one aircraft crashed due to a rotor/pylon/wing instability. As a result, the original three-bladed, articulated rotor was replaced by a two-bladed stiff-in-plane rotor to alleviate any instability. In September – October 1957 and October 1958, the aircraft with its new rotors underwent two wind tunnel entries in the NASA Ames $40\text{-ft} \times 80\text{-ft}$ wind tunnel (Fig. 1.2). These were the first tiltrotor whirl flutter tests. During this period, additional design changes were made to improve stability. The rotor diameter was reduced from $25\ \text{ft}$ to $23\ \text{ft}$, external struts were added to stiffen the wing, and the stiffness of rotor controls was increased.

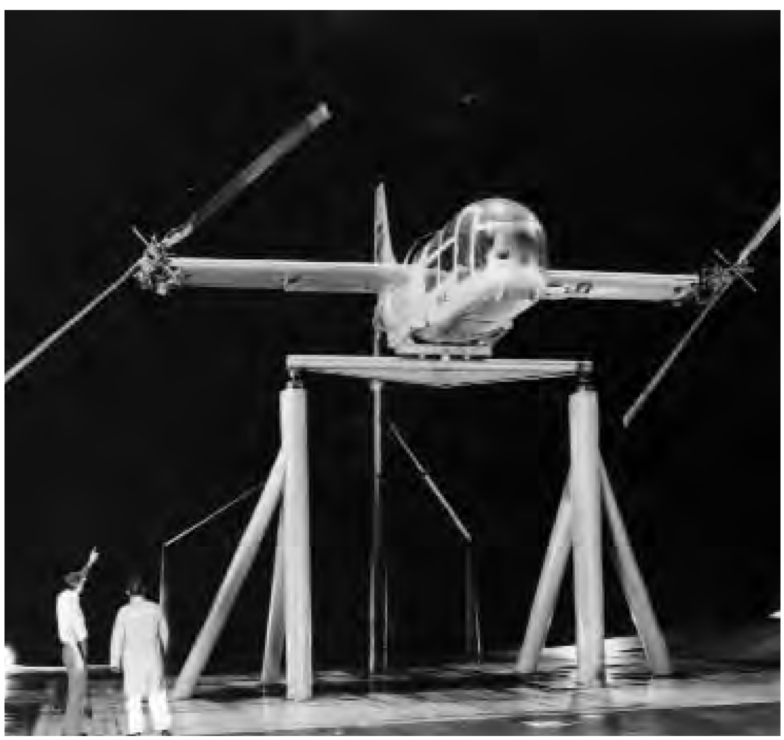

Figure 1.2: XV-3 in the NASA Ames $40\text{-ft} \times 80\text{-ft}$ wind tunnel (Ref. [48])

After a gap of almost ten years, the Bell Model 300 was tested in the NASA Ames $40\text{-ft} \times 80\text{-ft}$ wind tunnel in July – November 1970 (Fig. 1.3). The design summary of the aircraft is given in Ref. [49]. The Model 300 had a 25-ft diameter rotor with a gimballed hub and a negative δ_3, which was the same rotor as the later XV-15 tiltrotor aircraft. Wind tunnel test results are reported in Ref. [50]. Rotor/pylon/wing stability and performance were investigated. The rotor was tested up to $202\ \text{knots}$. This was a limitation of the wind tunnel; additional tests were conducted on a quarter-stiffness wing with reduced rotor speed to simulate higher equivalent cruise speeds (twice the speed of the full-stiffness wing).

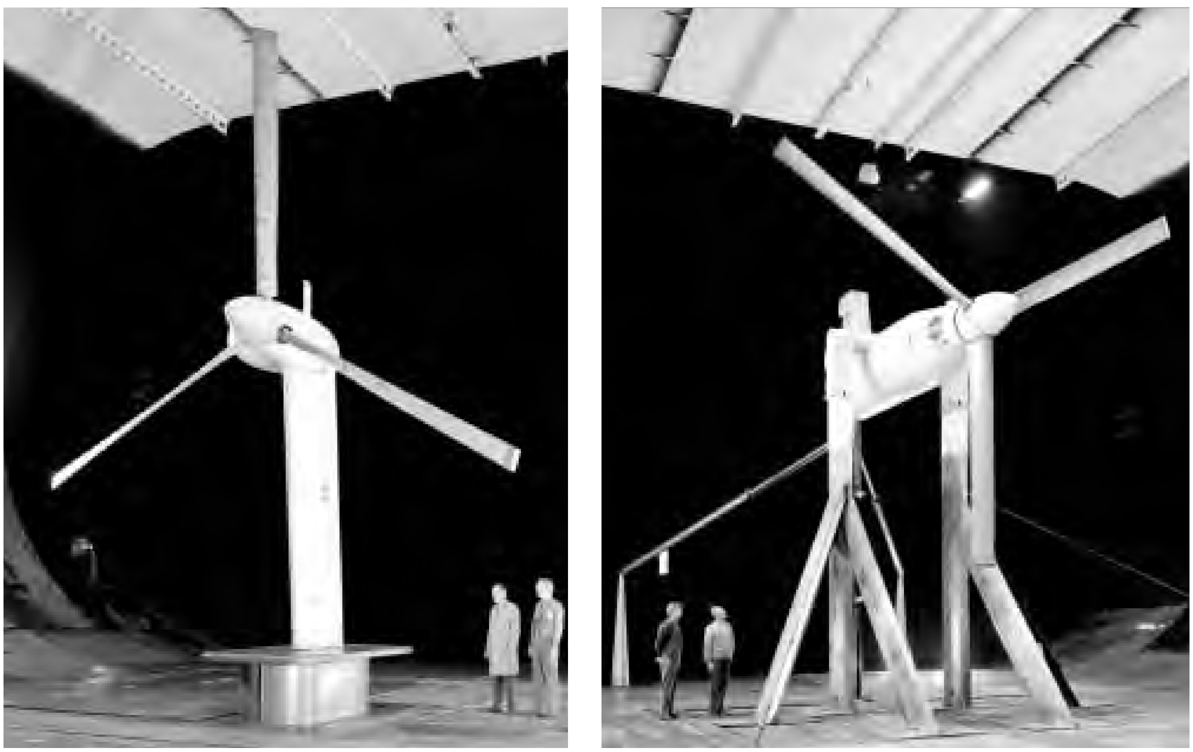

(a) Mounted on NASA dynamic wing test stand (b) Mounted on NASA powered propeller test rig

Figure 1.3: Bell Model 300 in the NASA Ames $40\text{-ft} \times 80\text{-ft}$ wind tunnel (Ref. [50])

Wind tunnel test of full-scale XV-15 tiltrotor aircraft was completed in the NASA Ames $40\text{-ft} \times 80\text{-ft}$ wind tunnel on June 23, 1978 (Fig. 1.4). The objective of the test was to collect data for an assessment of aerodynamic and aeroelastic characteristics, and structural loads within the flight envelope. Rotor/pylon/wing stability was not tested. XV-15 is an experimental tiltrotor aircraft based on the Bell Model 301 design. A detailed description of the aircraft is given in Ref. [51]. Reference [52] reports the test results.

Figure 1.4: Full-scale XV-15 in the NASA Ames $40\text{-ft} \times 80\text{-ft}$ wind tunnel (Ref. [48])

During the 1980s, a $1/5$ Froude-scaled semi-span aeroelastic model of the JVX tiltrotor aircraft (which would eventually become V-22) was tested by Bell-Boeing. A history of the tests is given in Ref. [53]. These systematic tests led to the V-22 Osprey. The first two tests (February – April and June – July 1984) were in the NASA Langley Transonic Dynamics Tunnel (TDT, $16\text{-ft} \times 16\text{-ft}$ test section). The objectives were to provide experimental data to guide the design and validation data for analysis. The impact of compressibility, wing stiffness, control system stiffness, pitch-flap coupling, and rotor blade stiffness on the rotor/pylon/wing stability was studied. Loads and vibration data was also collected. The test data and comparison with predictions are documented in Ref. [25]. This model later became a tiltrotor research testbed at Langley and was named Wing and Rotor Aeroelastic Test System (WRATS).

Numerous tests have been carried out with WRATS in the NASA Langley Transonic Dynamics Tunnel (Fig. 1.5). The first test was in August 1995. Properties and parametric stability test results for the WRATS model with hydraulically-actuated swashplate are given in Ref. [54]. References [55,56] give the design, analysis, and testing of a composite-tailored wing to improve the stability boundary. Reference [57] reports test of a four-bladed, semi-articulated, soft in-plane rotor system on WRATS. The effect of active control on stability was explored in Ref. [58].

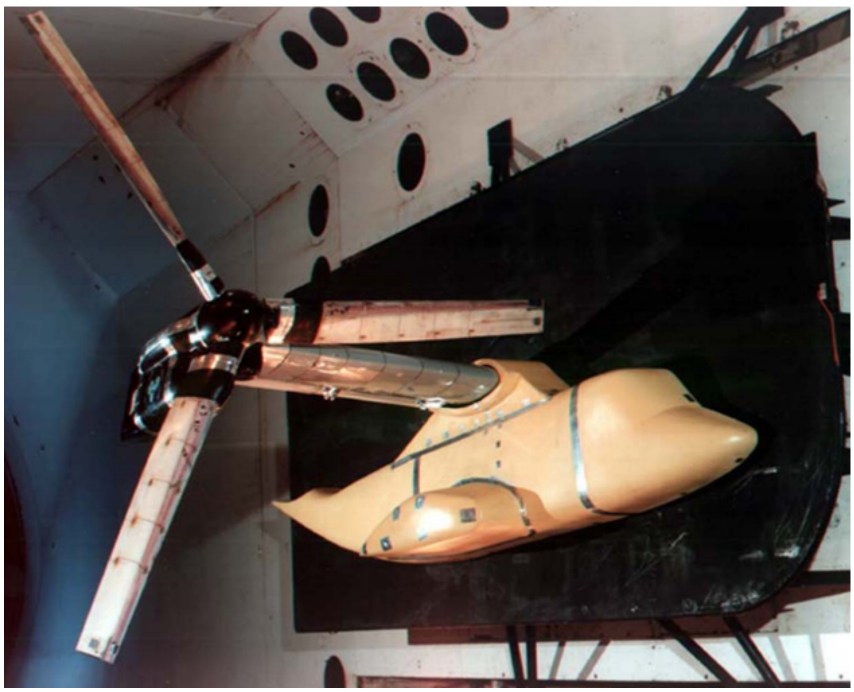

Figure 1.5: WRATS in the NASA Langley Transonic Dynamics Tunnel (Ref. [20])

A 1/6-scale model of the Variable-Diameter Tiltrotor (VDTR) was tested by Sikorsky Aircraft in the United Technologies Research Center wind tunnel (UTRC, 18-ft test section) in the early 1990s (Fig. 1.6). The model was a semi-span tiltrotor rig and had a three-bladed gimballed rotor. The maximum rotor diameter was 8.2 ft, which could be reduced to 5.4 ft (a reduction of 34%). Performance and loads data was collected. Aeroelastic stability was not investigated. The model properties and test results are reported in Refs. [59,60].

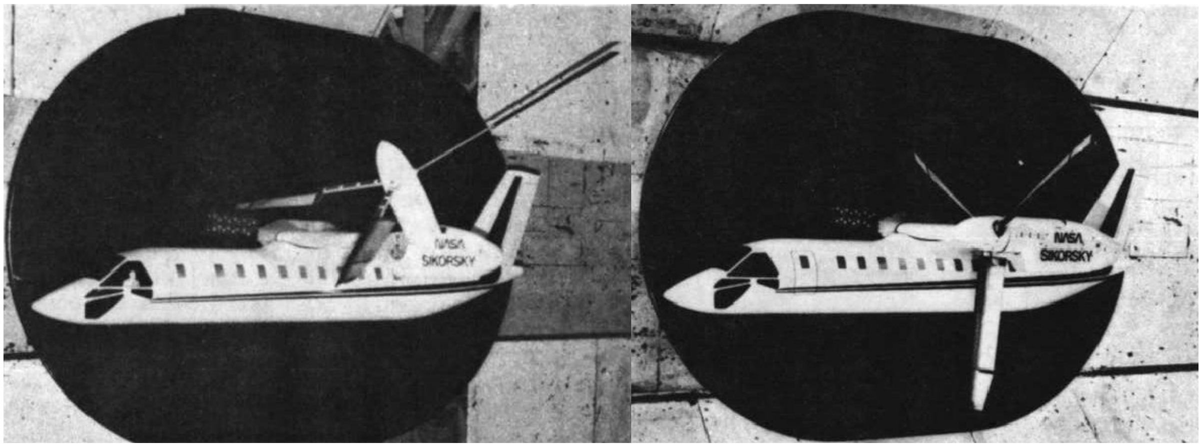

(a) Transition (rotor fully extended) (b) Cruise (rotor fully retracted)

Figure 1.6: VDTR in the United Technologies Research Center wind tunnel (Ref. [59])

Tilt Rotor Aeroacoustic Model (TRAM) isolated rotor was tested in the German-Dutch wind tunnel (DNW, $6\text{-m} \times 8\text{-m}$ test section was used) in April – May 1998 (Fig. 1.7a). Data for performance, airloads, and blade structural loads was collected. The objective was to provide validation data for tiltrotor performance and aeroacoustic prediction methodologies. TRAM is a 1/4-scale representation of the V-22 aircraft. It utilizes a 9.5-ft diameter gimballed rotor. An overview of the model is given in Ref. [61]. Rotor properties, test data from the isolated rotor test, and comparison with predictions are given in Ref. [62]. The full-span model (including the fuselage and the wing) was tested in the NASA Ames $40\text{-ft} \times 80\text{-ft}$ wind tunnel in late 2000 (Fig. 1.7b). Data for hover power and thrust, mean flap bending and pitch link loads, and wing pressure was collected. Forward flight data repeated fuselage drag polar. This test did not investigate rotor/pylon/wing aeroelastic stability as the wing was rigid to maximize dynamic stability. The full-span test is reported in Ref. [63].

The first test of NASA Tiltrotor Test Rig (TTR) was completed in NASA Ames $40\text{-ft} \times 80\text{-ft}$ wind tunnel in November 2018 (Fig. 1.8). The 26-ft diameter stiff in-plane, gimballed rotor was derived from the right-hand rotor of the Leonardo AW609 tiltrotor aircraft. The objective

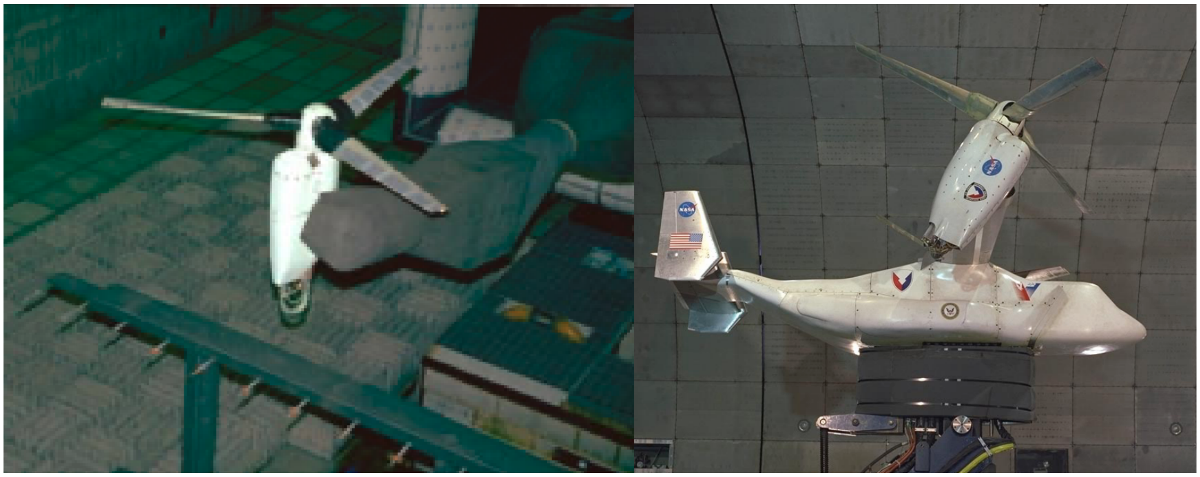

(a) Isolated rotor model in the German-Dutch wind tunnel (Ref. [62])

(b) Full-span model in the NASA Ames $40\text{-ft} \times 80\text{-ft}$ wind tunnel (Ref. [63])

Figure 1.7: TRAM wind tunnel tests

was to collect rotor performance and loads data. Rotor/pylon/wing stability was not part of the program. Description of the TTR and the initial testing is given in Ref. [64]. The test data and correlation with analysis are reported in Ref. [65].

Figure 1.8: NASA TTR in the NASA Ames $40\text{-ft} \times 80\text{-ft}$ wind tunnel (Ref. [65])

University of Maryland's Maryland Tiltrotor Rig (MTR) was inaugurated in the Glenn L. Martin wind tunnel ($7.75\text{-ft} \times 11\text{-ft}$ test section with 200-knots maximum speed) on November 4 – 8, 2019, before the COVID-19 shutdown. It was finally tested for stability in the Naval Surface Warfare Center Carderock Division subsonic wind tunnel (NSWCCD, $8\text{-ft} \times 10\text{-ft}$ test section) on October 26 – November 2, 2021 (Fig. 1.9). Eight different configurations were tested, including straight and swept-tip blades. MTR is a semi-span, optionally powered, interchangeable hub rig meant for testing proprotors up to 4.75-ft diameter in the Glenn L. Martin wind tunnel. The design is loosely based on the XV-15 aircraft ($1/5.26$ Froude-scaled). Both gimballed and hingeless hubs can be tested. The objective of this facility is to provide a testbed for basic parametric research on aeromechanics of high-speed tiltrotors. The design of the MTR is reported in Ref. [66]. An overview of the test is given in Ref. [67]. The details of the swept-tip blades are reported in Ref. [68]. A comparison of the test data with the predictions of the present solver is reported in Chapter 5.

TiltRotor Aeroelastic Stability Testbed (TRAST) was tested in the NASA Langley Transonic Dynamics Tunnel in 2021 (Fig. 1.10). TRAST was developed by the U.S. Army and NASA. It is contemporary to the MTR. It is a semi-span rig with a 8-ft diameter, three-bladed rotor. The design is also loosely based on the XV-15 aircraft; it is 0.32 Mach-scaled for heavy gas testing in TDT. Both gimballed and hingeless hubs can be accommodated. The δ_3 angle can be modified between $0°$ and $-30°$ in $5°$ increments. Two tuning springs are included between the pylon and the wing, which can control the mounting stiffness in pitch, yaw, and roll directions. These properties give this rig a lot of flexibility for wind tunnel testing and parametric study. An overview of TRAST is given in Ref. [69]. Pretest predictions are given in Ref. [70].

Figure 1.9: Maryland Tiltrotor Rig (MTR) in the Navy Carderock wind tunnel (Ref. [67])

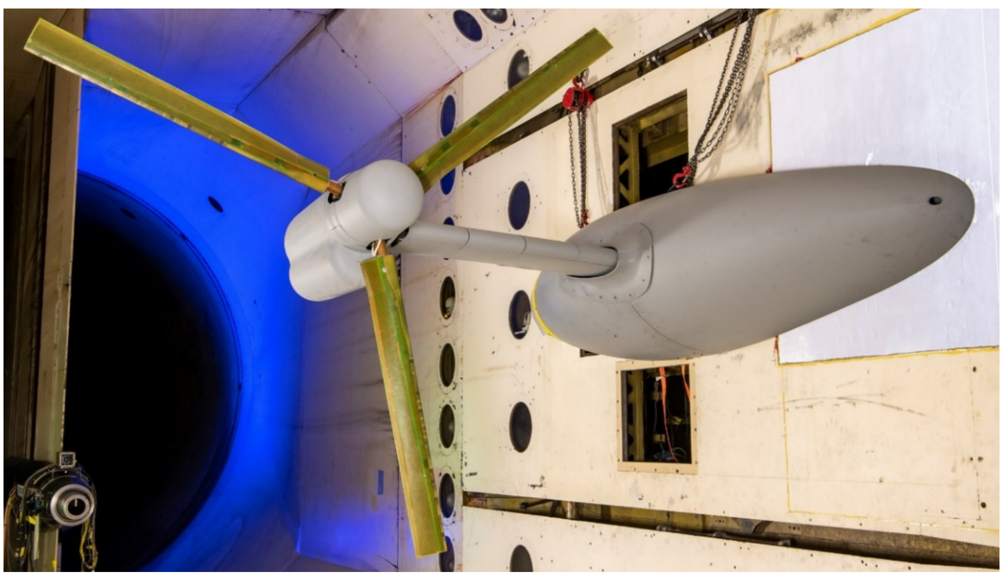

Figure 1.10: TRAST in the NASA Langley Transonic Dynamics Tunnel (Ref. [70])

1.4.2 Hingeless Hub Tests

The only data sets available for hingeless hub proprotors are from three models of the Boeing Model 222: a full-scale, a $1/9.244$ Froude-scaled, and a $1/4.622$ Froude-scaled model tested in the 1970s. These rotors had soft in-plane hubs.

The most useful data on a hingeless hub proprotor was acquired by the full-scale Boeing M222 tiltrotor tests in the NASA Ames $40\text{-ft} \times 80\text{-ft}$ wind tunnel in 1972. The objectives were to investigate the rotor/pylon/wing aeroelastic behavior and to measure performance, blade and control loads, and stability derivatives. Two types of tests were conducted: unpowered (freewheeling) rotor on two vertically mounted semi-span wings (full- and quarter-stiffness NASA dynamic wing test stands, Fig. 1.11a) and powered rotor on an isolated propeller test rig (Fig. 1.11b). These were the same dynamic wing test stands that were used for the Bell Model 300 tests described before. The tests were limited to one set of blades (straight, twisted). The tunnel speed was low for any instability at the design rotor speed. Reference [71] reports the test results. References [4, 33, 71] give the rotor and wing properties and comparison of experimental data with predictions. Chapter 4 compares the predictions of the present solver with the test data.

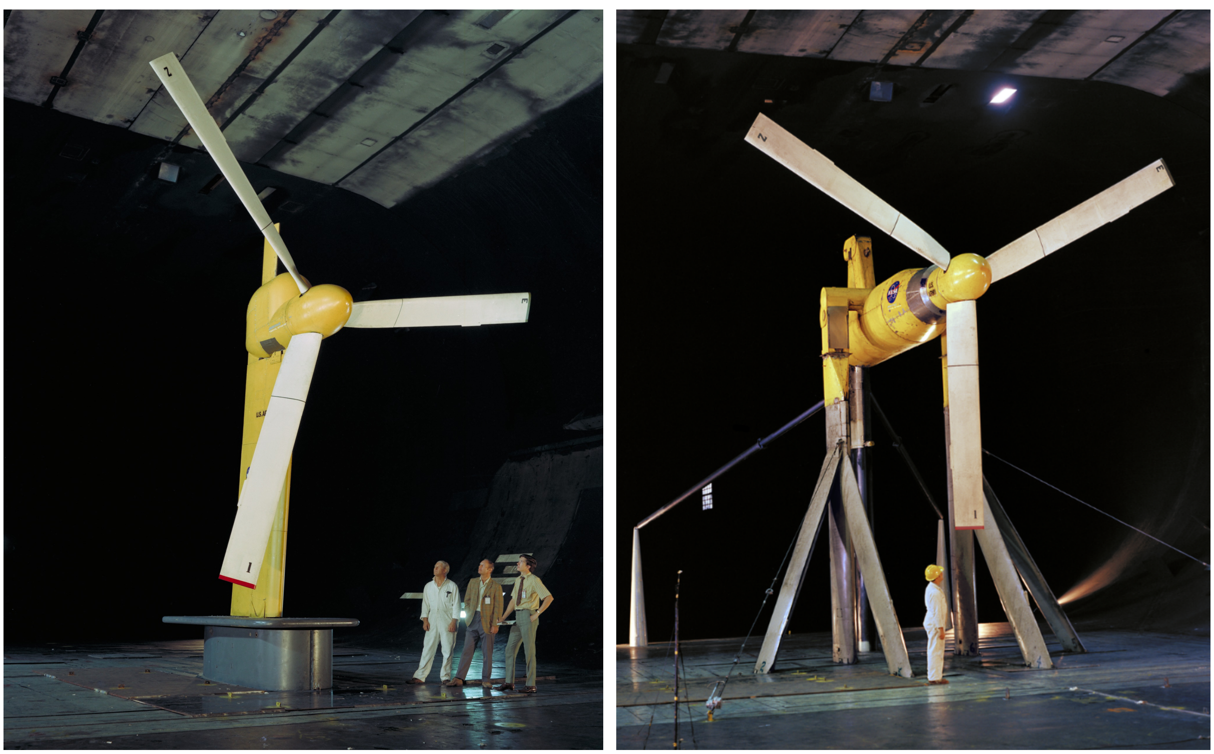

(a) Mounted on NASA dynamic wing test stand (b) Mounted on NASA powered propeller test rig

Figure 1.11: Full-scale Boeing M222 in the NASA Ames $40\text{-ft} \times 80\text{-ft}$ wind tunnel (Ref. [71])

A $1/9.244$ Froude-scaled model of the Boeing M222 rotor was tested in the MIT Wright Brothers tunnel (10-ft $\times$ 7-ft test section) in the 1970s (Fig. 1.12). A $1/8.888$ Froude-scaled model of the Bell Model 300 rotor was also tested on the same wing. Both rotors were 2.8 ft in diameter. This test is historic, as it was an interchangeable hub test. The primary objective was to determine the response to vertical and longitudinal gusts. Different gust frequencies were tested at a single tunnel and rotor speed. Neither whirl flutter nor loads was investigated. Reference [72] reports the test results and comparison with the theory. Reference [73] gives the properties for the wing and the rotor.

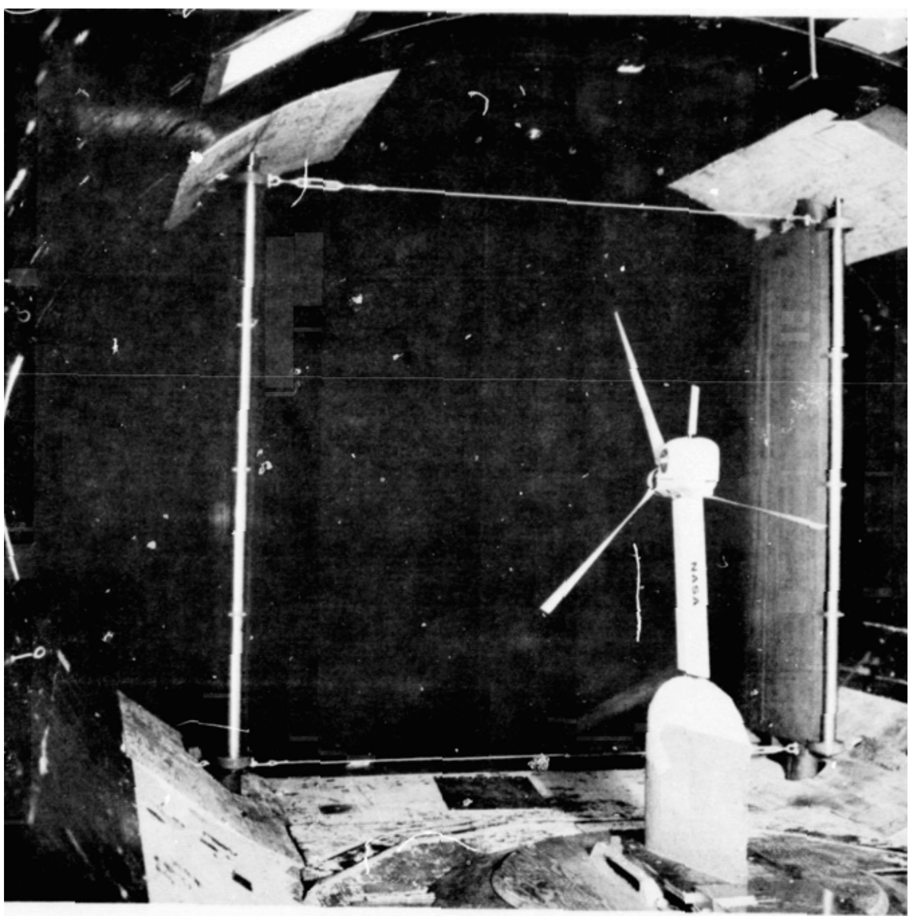

Figure 1.12: $1/9.244$ Froude-scaled Boeing M222 in the MIT Wright Brothers wind tunnel (Ref. [72])

A $1/4.622$ Froude-scaled full-span model of the Boeing M222 rotor was built and tested in Boeing V/STOL wind tunnel (20-ft $\times$ 20-ft test section) in 1976 (Fig. 1.13). Parametric blade, pitch link, hub, and airframe loads for different tunnel speeds, nacelle tilt angles, collective and cyclic pitch controls, wing flap angles, and aircraft attitudes were collected. The primary objective was to provide an understanding of the rotor and airframe behavior of this aircraft. A secondary objective was to examine the feasibility of a control system to minimize the rotor loads by changing the blade control angles and providing control using aircraft control surfaces in cruise. Whirl flutter stability was not investigated. Reference [74] reports the test results.

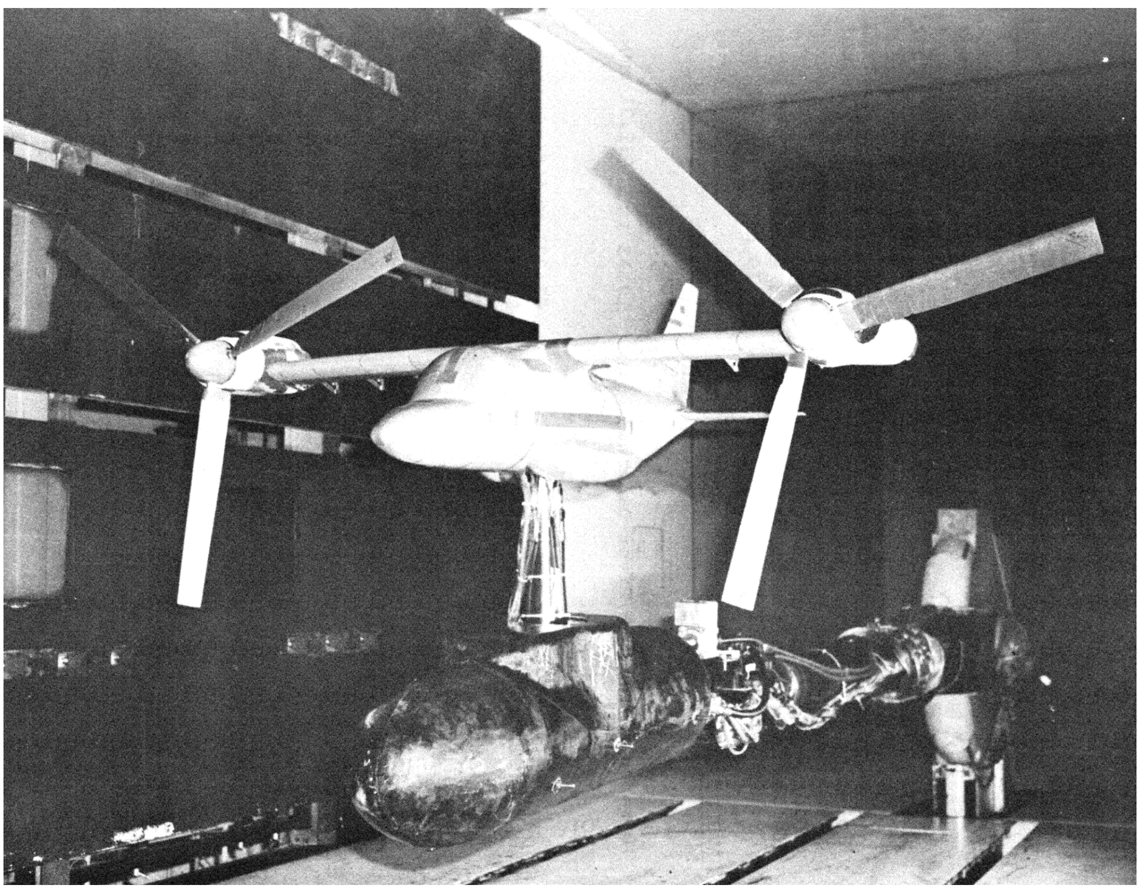

Figure 1.13: $1/4.622$ Froude-scaled Boeing M222 in the
Boeing V/STOL wind tunnel (Ref. [74])

1.5 Objective of Present Research

Following the wind tunnel tests, the industry focus shifted to stiff in-plane gimballed hubs. No further tests were conducted thereafter on the hingeless hubs. Today, with materials, controls, and simulation capabilities improved dramatically, a reevaluation of the hingeless hub proprotors is appropriate. A thorough understanding of whirl flutter and air resonance characteristics of hingeless hubs is acutely missing. The objective of this research is to bridge this gap, starting with analysis.

The research was carried out in two steps. The first step was developing and validating a new comprehensive analysis for performance, loads, and stability predictions of any rotorcraft, but in particular tiltrotors. It was especially aimed to eliminate assumptions that have traditionally been used for modeling a conventional helicopter. A tiltrotor analysis must model the wing, pylon, hub motions, their coupling with the rotor motions, and high inflow and high pitch angle aerodynamics of the rotor blades as accurately as possible. The second step was to utilize the developed analysis to explore the nature of instabilities for hingeless hub proprotors and to provide a fundamental understanding of their behavior. Half-span tiltrotor models were built and the impact of different parameters on the stability predictions was studied to guide future testing and analysis. A systematic validation was carried out to interpret existing test data and to identify gaps in understanding and technical barriers. Blade tip sweep in various configurations was explored to delay instability in future tiltrotor aircraft. The stabilizing mechanism was explained. Detailed documentation of the theory, validation, and exploration were provided for future researchers.

1.6 Contribution of Present Research

This research presents the first consolidated and comprehensive analysis and validation of hingeless hub tiltrotor aeroelastic stability and loads. The key contributions are listed as follows:

1. Consolidation of all existing research data – from the 1970s to 2021, full-scale to model-scale, industry/government to academia.
2. Exposition of air resonance as the primary instability mechanism.
3. Explanation of how, when, and why air resonance appears.
4. Exploration of tip sweep as a potential remedy. Isolating aerodynamic and inertial effects in analysis to dissect the impact on stability.
5. Revelation of some key barriers for the future, such as the impact of electric drive on stability.
6. Clear exposition of theory needed for accurate modeling of tiltrotors and where it departs from edgewise helicopter rotors.
7. Comprehensive validation with all existing research data and verification with U.S. Army hypothetical cases.
8. Design of the MTR hingeless hub for future researchers.

1.7 Organization of the Dissertation

The dissertation is organized into seven chapters. Following this chapter, Chapter 2 reports the theory for the developed solver. The key equations are given in a detailed manner. Chapter 3 reports a verification study for a hypothetical rotor/pylon/wing model made up recently by the U.S. Army. Stability predictions of the developed solver are verified for different wing/pylon models combined with four different hingeless rotors that exhibit different frequencies. Chapter 4 reports a validation study for performance, loads, and stability predictions using the Boeing M222 test data, explains the physics behind the data, and provides a fundamental understanding of the stability of hingeless hub tiltrotors. The instability mechanism and the impact of modeling/testing parameters on stability are studied. Chapter 5 extends the validation study to the recently acquired Maryland Tiltrotor Rig test results. Freewheeling and stability predictions are validated. Eight different configurations are studied for stability: straight and swept-tip blades, gimbal-free and gimbal-locked, freewheeling and powered modes, and wing fairings on and off configurations. A parametric comparison is reported. Chapter 6 explores the effect of blade tip sweep on the stability boundary. Sweep provides aerodynamic benefits at high speed but is also a dominant mechanism to introduce pitch-flap and pitch-lag couplings. A thorough study is carried out with different blade sweep configurations to provide a detailed understanding and to explain the stabilizing mechanism. Finally, Chapter 7 lists the key conclusions.

Chapter 2: Theory

This chapter describes the theory of a new solver developed at the University of Maryland. It covers structural model, aerodynamic model, hub motions, loads, advanced geometry blades, fixed–rotating interface, joints, finite element discretization, numerical extraction of system matrices, numerical multiblade coordinate transformation, solution methods for the equations of motion, and aeroelastic stability solution.

2.1 Description of the Solver

Special features are required to predict the blade and hub vibratory loads, and stability roots of a tiltrotor aircraft. This means accurate structural and aerodynamic models with no small angle or small inflow assumptions as well as incorporation of hub motions through flexible wing and pylon that couple with the rotor. The developed solver meets these requirements with finite element blades, wing, pylon, multibody joints, unsteady aerodynamics, freewake, a fixed–rotating interface, and solution procedures for trim, transient and stability in both frequency and time domains. The coverage of various disciplines is comprehensive and the fidelity of modeling is uniform in texture; hence it qualifies as a comprehensive analysis – a term unique to multidisciplinary rotorcraft analysis (Ref. [6]).

2.1.1 Structural Model

The structural model uses beams and multibody joints. The beams have flap, lag, axial, and torsion deformations, and all nonlinear inertial couplings that arise from rotation. The joints connect to the beams and they can be actuated or commanded. Joint stiffness and damping can be specified. The assumption is that they are holonomic, which is adequate for rotors. Contact or friction are out of scope.

The Euler-Bernoulli assumption is made for the beams. Hodges and Dowell's formulation is used for the strain-displacement relations (Ref. [75]) even though the small strain assumption, inherent to all beam models, is retained. The axial degree of freedom can be treated as a quasi-coordinate or as total deformation that makes modeling of multiple load paths easier (Ref. [76]). Deformations can be moderate as the model includes nonlinearities at least up to second order. Some higher than second-order structural terms that are important particularly for hingeless proprotors are also retained. These are products of flap and lag curvature and elastic twist terms that govern coupling of flap and lag motions. Advanced geometry blades are modeled by sweeping and drooping the elastic axis, which is taken into account with inter-element compatibility equations and elastic axis positions. A fixed–rotating interface can be implemented. The wing and the pylon can be modeled directly as beams and coupled with the rotor. Alternatively, frequency and mode shapes from NASTRAN-like higher-order models can be admitted for the fixed structure.

The Hamilton's Principle with Finite Element discretization is used to obtain the governing ordinary differential equations. Joints have six degrees of freedom: three displacements and three rotations. Each finite element is straight, and has 15 degrees of freedom, 12 of which are at the boundaries. The boundary degrees of freedom can be eliminated when connected to joints or other beam elements. Axial and torsion deformations use third- and second-order Lagrange polynomials respectively as shape functions (for continuity of displacement) while flap and lag deformations use third-order Hermite polynomials (for continuity of displacement and slope). The inputs are cross-sectional stiffness EI and GJ; mass, moment of inertia; center of gravity, tension center, quarter-chord offsets; pretwist, sweep, anhedral angles; and joint actuation and connection to the elements. These are specified as a function of span and can vary along an element. A six-point Gaussian quadrature integration is used for each element.

Inertial terms are obtained exactly by numerical perturbation, with no small-term assumption. A Taylor Series expansion is used to linearize the inertial loads about deflection, slope, and corresponding linear and angular velocities and accelerations.

2.1.2 Aerodynamic Model

The aerodynamic model uses 2D airfoil tables and lifting-line theory with freewake for inflow. Both the rotor and the wing can use the same aerodynamic model.

Sectional angles of attack are calculated exactly from flexible blade deformations, hub motions, and inflow. C81 airfoil decks with tabulated lift, drag, and moment coefficients versus angle of attack and Mach number are used. These are input from test data or 2D CFD calculations. Radial flow corrections on the angle of attack and airfoil properties are then applied (Ref. [77]).

The Maryland Freewake with a full-span nearwake model calculates the rotor induced flow. Simpler prescribed wake or uniform inflow options can also be used. Freewake is essential in helicopter mode. In airplane mode, the rotor is in axial flow; hence, freewake is inconsequential and in fact the least important piece of the model. The wake is washed away, so the induced flow becomes very small. More important is to exactly account for the high cruise inflow in the section angle of attack calculation.

The virtual work from aerodynamic forcing is linearized by numerical perturbation to extract the aerodynamic stiffness and damping matrices. Similar to the inertial loads, a Taylor Series expansion is used.

2.1.3 Trim and Transient Solution

First, the system is trimmed. The solution procedure finds the rotor control angles needed for equilibrium. The equilibrium can be specified in various ways such as aircraft equilibrium, or rotor mean forces and moments needed for that equilibrium, or perhaps just a subset such as thrust and torque, including zero torque which is a special test condition for tiltrotors. Finite Element in Time (FET) or time marching methods can be used for the trim solution. FET is a fast and efficient method to extract the periodic solution directly, whereas time marching requires computation until the solution settles down to periodic response with the assumption that it does. FET can find unstable orbits where initial conditions will not die out. Hence, FET is always desired even for stability to find points at and beyond the boundary. After trim, a transient analysis can be performed for time-varying controls with a time marching solution. The rotor equations are solved in the rotating frame and the wing/pylon equations are solved in the fixed frame in a fully coupled manner.

2.1.4 Stability

After the trim solution, the stability solution can be obtained in two ways. Option 1 is to perturb the degrees of freedom and extract the mass, damping, and stiffness matrices. Eigenvalues are calculated from these matrices. The real and imaginary parts of the eigenvalues give the damping and frequency. Option 2 is to simply perturb the control angles and march over time. Frequency and damping are then extracted from the transient response using the Moving-Block method (Ref. [78]). This is how testing is performed. Here, just as in testing, the model must include all blades either individually in the rotating frame or using multiblade coordinate transformation in the fixed frame. Multiblade coordinates are superior when a constant coefficient approximation may be possible. Hence, multiblade coordinates are used for option 1, and rotating coordinates are used for option 2.

2.2 Geometry and Frames

Geometry and frames are the starting point of any comprehensive analysis. Figure 2.1 shows a schematic of rotor/pylon/wing system and the frames used. The following frames are defined: inertial frame I, wing deformed frame W, nonrotating hub frame H, rotating frame R, blade undeformed frame U, and blade deformed frame D. The inertial frame I is fixed. Wing deformed frame W follows the wing deformation with origin on wing elastic axis. Nonrotating hub frame H is fixed to the hub. Rotating hub frame R has the same origin as the nonrotating hub frame H but it rotates with the blades. It is shown separately in Figure 2.1 for clarity. Blade undeformed frame U accounts for the precone angle with the origin on blade elastic axis. It translates with the blade deformation but does not rotate. Blade deformed frame D shares the same origin with blade deformed frame U but also rotates with blade deformation. The rotations are in Z–Y–X order, which are given in Eq. 2.1. The direction cosine matrices C^{WI}, C^{RH}, C^{UR}, and C^{DU} are given in Eqs. 2.2 to 2.5. C^{AB} rotates the axes from B to A, so the unit vector in A is located by premultiplying the unit vector in B by the matrix C^{AB}. The direction cosine matrix C^{HW} is from the topology of the system and is an input to the analysis. The pylon is considered part of the wing. Figure 2.2 shows the undeformed and deformed frames along with deformations. The unit vectors for the deformed frame are ξ along x, η along y, and ζ along z. Linear deformations are in the undeformed frame and they are denoted by u, v, and w. Angular deformations are denoted by ζ, β, and θ. The angular deformations of the wing/pylon are denoted by ζ_w, β_w, and θ_w. The angle θ includes the control angle (for the rotor), pretwist, and elastic twist as shown in Eq. 2.6. Here θ_{75} is collective, θ_{1c} is lateral cyclic, θ_{1s} is longitudinal cyclic, ψ is azimuth, Λ_1 is pretwist, Λ_1' is twist rate, and $\hat{\phi}$ is elastic twist. Twist defines the principal axis for the structural model and the chord line for the aerodynamic model. The term β_p is the precone angle.

$$X = \begin{bmatrix} 1 & 0 & 0 \\ 0 & \cos & \sin \\ 0 & -\sin & \cos \end{bmatrix} \qquad Y = \begin{bmatrix} \cos & 0 & -\sin \\ 0 & 1 & 0 \\ \sin & 0 & \cos \end{bmatrix} \qquad Z = \begin{bmatrix} \cos & \sin & 0 \\ -\sin & \cos & 0 \\ 0 & 0 & 1 \end{bmatrix} \tag{2.1}$$

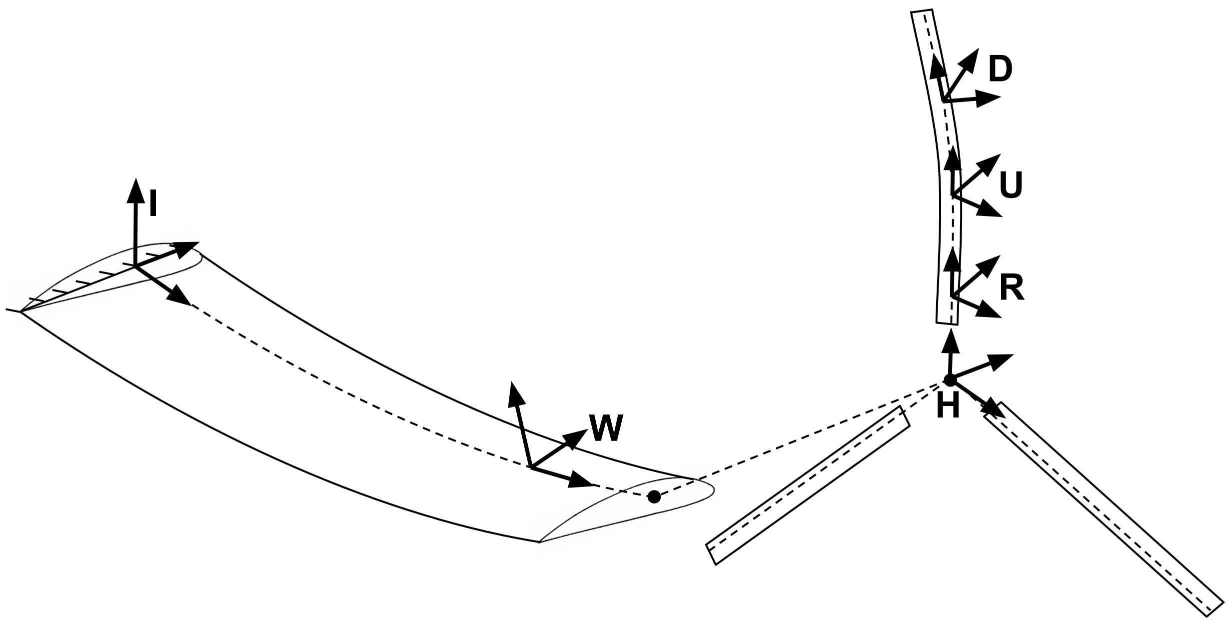

Figure 2.1: Schematic of rotor/pylon/wing system

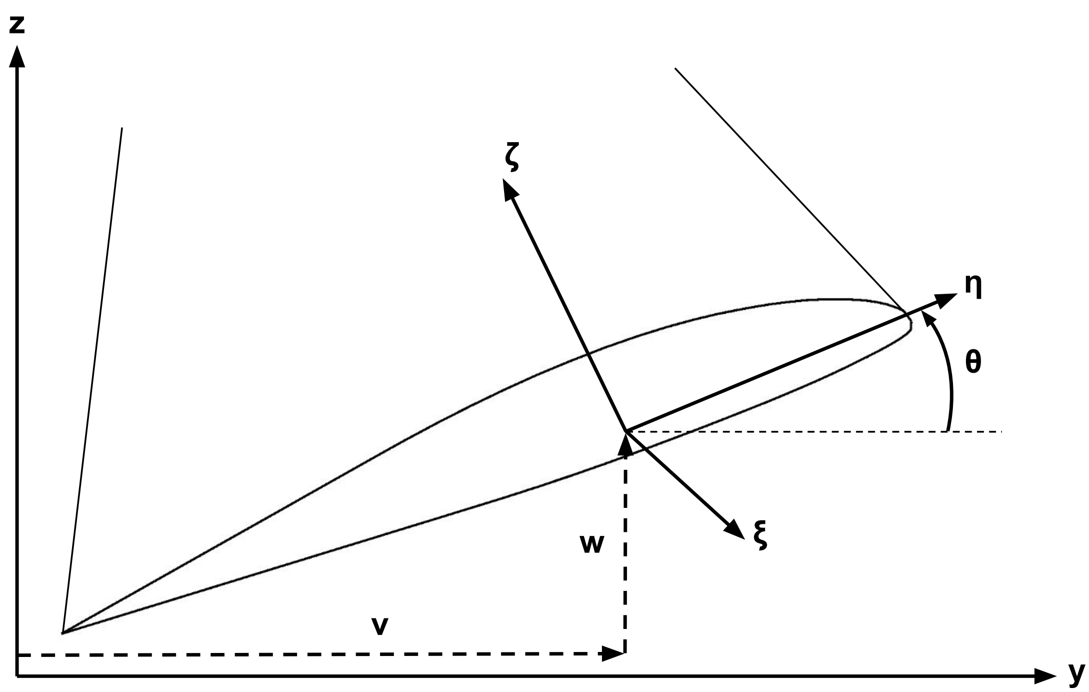

Figure 2.2: Undeformed and deformed frames

$$
\begin{aligned}
C^{WI} =& X_{\theta_w} Y_{\beta_w} Z_{\zeta_w} \\
=& \begin{bmatrix} 1 & 0 & 0 \\ 0 & \cos\theta_w & \sin\theta_w \\ 0 & -\sin\theta_w & \cos\theta_w \end{bmatrix} \begin{bmatrix} \cos\beta_w & 0 & -\sin\beta_w \\ 0 & 1 & 0 \\ \sin\beta_w & 0 & \cos\beta_w \end{bmatrix} \begin{bmatrix} \cos\zeta_w & \sin\zeta_w & 0 \\ -\sin\zeta_w & \cos\zeta_w & 0 \\ 0 & 0 & 1 \end{bmatrix}
\end{aligned} \tag{2.2}
$$

$$
C^{RH} = Z_{\psi} = \begin{bmatrix} \cos\psi & \sin\psi & 0 \\ -\sin\psi & \cos\psi & 0 \\ 0 & 0 & 1 \end{bmatrix} \tag{2.3}
$$

$$
C^{UR} = Y_{-\beta_p} = \begin{bmatrix} \cos\beta_p & 0 & \sin\beta_p \\ 0 & 1 & 0 \\ -\sin\beta_p & 0 & \cos\beta_p \end{bmatrix} \tag{2.4}
$$

$$
\begin{aligned}
C^{DU} =& X_{\theta} Y_{\beta} Z_{\zeta} \\
=& \begin{bmatrix} 1 & 0 & 0 \\ 0 & \cos\theta & \sin\theta \\ 0 & -\sin\theta & \cos\theta \end{bmatrix} \begin{bmatrix} \cos\beta & 0 & -\sin\beta \\ 0 & 1 & 0 \\ \sin\beta & 0 & \cos\beta \end{bmatrix} \begin{bmatrix} \cos\zeta & \sin\zeta & 0 \\ -\sin\zeta & \cos\zeta & 0 \\ 0 & 0 & 1 \end{bmatrix}
\end{aligned} \tag{2.5}
$$

So, β is positive down although β_p is positive up per normal convention.

$$\begin{aligned}\theta &= \theta_0 + \hat{\phi} \\ &= \theta_c + \Lambda_1 + \hat{\phi} \\ &= \theta_{75} + \theta_{1c}\cos\psi + \theta_{1s}\sin\psi + \Lambda_1 + \hat{\phi} \qquad (2.6)\\ \theta' &= \theta_0' + \hat{\phi}' \\ &= \Lambda_1' + \hat{\phi}' \qquad (2.7)\end{aligned}$$

2.3 Hamilton's Principle

The governing equations of motion are derived using Hamilton's variational principle. For a conservative system, Hamilton's principle states that the true motion of a system between times t_1 and t_2 is the one that the time integral of the difference between the potential and kinetic energies is a minimum (Ref. [79]). For a rotor blade, nonconservative forces apply. The generalized Hamilton's principle is expressed as follows:

$$\delta\Pi = \int_{t_1}^{t_2} (\delta U - \delta T - \delta W)dt = 0 \qquad (2.8)$$

Where δU and δT and variations in strain and kinetic energies, and δW is the virtual work. These terms have contributions from the rotor blades and the wing.

$$
\begin{aligned}
\delta U &= \delta U_r + \delta U_w = \sum_{m=1}^{N_b} \delta U_b + \delta U_w \\
\delta T &= \delta T_r + \delta T_w = \sum_{m=1}^{N_b} \delta T_b + \delta T_w \\
\delta W &= \delta W_r + \delta W_w = \sum_{m=1}^{N_b} \delta W_b + \delta W_w
\end{aligned}
\tag{2.9}
$$

Where N_b is the number of blades and subscripts r, b, w are used for the rotor, blades, and wing, respectively. The variation in the kinetic energy is calculated as virtual work by the inertial loads, so the virtual work contains both aerodynamic and inertial loads.

2.4 Strain Energy

Long and slender beam assumption is made so the strains are small compared to unity. Uniaxial stress assumption ($\sigma_{\eta\eta} = \sigma_{\eta\zeta} = \sigma_{\zeta\zeta} = 0$) holds. For an isotropic material,

$$
\begin{aligned}
\sigma_{\xi\xi} &= E\epsilon_{\xi\xi} \\
\sigma_{\xi\eta} &= G\epsilon_{\xi\eta} \\
\sigma_{\xi\zeta} &= G\epsilon_{\xi\zeta}
\end{aligned}
\tag{2.10}
$$

where $\sigma_{\xi\xi}$ is axial strain, $\sigma_{\xi\eta}$ and $\sigma_{\xi\zeta}$ are engineering shear strains, E is elastic modulus, and G is shear modulus. The expression for the strain energy is therefore as follows:

$$
\begin{aligned}
U &= \frac{1}{2}\int_0^R \iint_A (\sigma_{\xi\xi}\epsilon_{\xi\xi} + \sigma_{\xi\eta}\epsilon_{\xi\eta} + \sigma_{\xi\zeta}\epsilon_{\xi\zeta}) d\eta d\zeta dr \\
&= \frac{1}{2}\int_0^R \iint_A (E\epsilon_{\xi\xi}^2 + G\epsilon_{\xi\eta}^2 + G\epsilon_{\xi\zeta}^2) d\eta d\zeta dr
\end{aligned}
\tag{2.11}
$$

Taking the variation,

$$\delta U = \int_0^R \iint_A (E\epsilon_{\xi\xi}\delta\epsilon_{\xi\xi} + G\epsilon_{\xi\eta}\delta\epsilon_{\xi\eta} + G\epsilon_{\xi\zeta}\delta\epsilon_{\xi\zeta})d\eta d\zeta dr \tag{2.12}$$

Nonlinear beam strain-displacement relations up to second order are reported in Ref. [75] as follows:

$$\begin{aligned}
\epsilon_{\xi\xi} =& u_e' - \lambda_T\phi'' + (\eta^2+\zeta^2)\Big(\theta_0'\phi' + \frac{\phi'^2}{2}\Big) \\
& - v''(\eta\cos\theta - \zeta\sin\theta) - w''(\eta\sin\theta + \zeta\cos\theta) \\
\epsilon_{\xi\eta} =& -\Big(\zeta + \frac{\partial\lambda_T}{\partial\eta}\Big)\phi' = -\hat{\zeta}\phi' \\
\epsilon_{\xi\zeta} =& \Big(\eta - \frac{\partial\lambda_T}{\partial\zeta}\Big)\phi' = \hat{\eta}\phi'
\end{aligned} \tag{2.13}$$

The terms u_e and ϕ are elastic deformations (also called quasi-coordinates) in axial and twist directions. The total deformations include elastic deformations and kinematic effects due to flap and lag deflections (Ref. [76]):

$$u = u_e - \frac{1}{2}\int_0^r (v'^2 + w'^2)d\rho + O(\epsilon^4) \tag{2.14}$$

$$\hat{\phi} = \phi - \int_0^r w'v''d\rho + O(\epsilon^3) \tag{2.15}$$

Where the integrals are from root to the spanwise position of interest. Using the quasi-coordinate u_e enables the derivation of the centrifugal stiffening terms explicitly, which improves convergence. Using the deformation variable u makes modeling of multiple load paths easier. For the elastic twist, the total deformation is of interest. The equations in this chapter are derived in terms of u_e and $\hat{\phi}$. Using Eq. 2.15,

$$
\begin{aligned}
&\phi = \hat{\phi} + \int_0^r w'v''d\rho \\
&\phi' = \hat{\phi}' + w'v'' \\
&\phi'' = \hat{\phi}'' + w'v''' + w''v''
\end{aligned}
\tag{2.16}
$$

Substituting Eq. 2.16 into Eq. 2.13:

$$
\begin{aligned}
\epsilon_{\xi\xi} =& u_e' - \lambda_T(\hat{\phi}'' + w'v''' + w''v'') \\
&+ (\eta^2 + \zeta^2)\Big(\theta_0'\hat{\phi}' + \theta_0' w'v'' + \frac{\hat{\phi}'^2}{2} + \frac{w'^2 v''^2}{2} + \hat{\phi}' w'v''\Big) \\
&- v''(\eta\cos\theta - \zeta\sin\theta) - w''(\eta\sin\theta + \zeta\cos\theta) \\
\epsilon_{\xi\eta} =& -\hat{\zeta}(\hat{\phi}' + w'v'') \\
\epsilon_{\xi\zeta} =& \hat{\eta}(\hat{\phi}' + w'v'')
\end{aligned}
\tag{2.17}
$$

Taking the variation,

$$
\begin{aligned}
\delta\epsilon_{\xi\xi} =& \delta u_e' - \lambda_T(\delta\hat{\phi}'' + v'''\delta w' + v''\delta w'' + w'\delta v''' + w''\delta v'') \\
&+ (\eta^2 + \zeta^2)\Big(\theta_0'\delta\hat{\phi}' + \theta_0' v''\delta w' + \theta_0' w'\delta v'' + (\hat{\phi}' + w'v'')(\delta\hat{\phi}' + v''\delta w' + w'\delta v'')\Big) \\
&- (\delta v'' + w''\delta\hat{\phi})(\eta\cos\theta - \zeta\sin\theta) - (\delta w'' - v''\delta\hat{\phi})(\eta\sin\theta + \zeta\cos\theta) \\
\delta\epsilon_{\xi\eta} =& -\hat{\zeta}(\delta\hat{\phi}' + v''\delta w' + w'\delta v'') \\
\delta\epsilon_{\xi\zeta} =& \hat{\eta}(\delta\hat{\phi}' + v''\delta w' + w'\delta v'')
\end{aligned}
$$

Variation of the strain energy can be written in terms of the deformation variables:

$$
\delta U = \int_0^R (U_{u_e'}\delta u_e' + U_{w'}\delta w' + U_{v''}\delta v'' + U_{w''}\delta w'' + U_{v'''}\delta v''' + U_{\hat{\phi}}\delta\hat{\phi} + U_{\hat{\phi}'}\delta\hat{\phi}' + U_{\hat{\phi}''}\delta\hat{\phi}'')dr \tag{2.18}
$$

The following section properties are required:

$$\begin{aligned}
&\iint_A E d\eta d\zeta = EA && \iint_A E(\eta^2+\zeta^2)^2 d\eta d\zeta = EB_1 && \iint_A E\zeta d\eta d\zeta = 0 \\
&\iint_A E\eta d\eta d\zeta = EAe_A && \iint_A E\eta(\eta^2+\zeta^2) d\eta d\zeta = EB_2 && \iint_A E\eta\zeta d\eta d\zeta = 0 \\
&\iint_A E\zeta^2 d\eta d\zeta = EI_n && \iint_A E\lambda_T^2 d\eta d\zeta = EC_1 && \iint_A E\zeta(\eta^2+\zeta^2) d\eta d\zeta = 0 \\
&\iint_A E\eta^2 d\eta d\zeta = EI_c && \iint_A E\zeta\lambda_T d\eta d\zeta = EC_2 && \iint_A \lambda_T d\eta d\zeta = 0 \qquad (2.19) \\
&\iint_A G(\hat{\eta}^2+\hat{\zeta}^2) d\eta d\zeta = GJ && && \iint_A E\eta\lambda_T d\eta d\zeta = 0 \\
&\iint_A E(\eta^2+\zeta^2) d\eta d\zeta = EAK_A^2 && && \iint_A E(\eta^2+\zeta^2)\lambda_T = 0
\end{aligned}$$

Where E is the elastic modulus, EA is the axial stiffness, e_A is the position of the tension center with respect to the elastic axis (positive toward leading edge), EI_c, EI_n, and GJ are lag, flap, and torsion stiffness (GJ includes the effect of cross-sectional warping), K_A is the modulus weighted polar radius of gyration, EC_1 is the warping rigidity, EC_2 is another property related to the warping of the cross-section, and λ_T is an antisymmetric ($\lambda_T \propto \eta\zeta$) warping function. The warping function specifies the distribution of the axial warping displacement within the cross-section.

The order of magnitude analysis is carried out in the nondimensional form. Table 2.1 shows the nondimensionalization parameters. Any physical quantity can be nondimensionalized by the combination of these parameters. The term m_0 is the mass per length of a uniform blade with the same flap moment of inertia, R is the radius, and Ω is the rotation speed. The ordering is based on the parameter ϵ. The order of magnitudes of nondimensional physical quantities are given in Eq. 2.20. Here x is the nondimensional spanwise coordinate (r/R).

Table 2.1: Nondimensionalization Parameters

Physical quantity	**Nondimensionalization**
Mass/length	m_0
Length	R
Time	Ω

$$
\begin{aligned}
&\frac{u}{R} = O(\epsilon^2) && \frac{v}{R}, \frac{w}{R}, \frac{\phi}{R} = O(\epsilon) \\
&\theta_0, \theta, \Lambda_1 = O(1) && \frac{\eta}{R}, \frac{\zeta}{R} = O(\epsilon) \\
&\lambda_T = O(\epsilon^2) && \frac{\partial}{\partial x} = O(1) \\
&\frac{EA}{m_0\Omega^2R^2} = O(\epsilon^{-2}) && \frac{EI_c}{m_0\Omega^2R^4}, \frac{EI_n}{m_0\Omega^2R^4}, \frac{GJ}{m_0\Omega^2R^4} = O(1) \\
&\frac{EB_1}{m_0\Omega^2R^6}, \frac{EC_1}{m_0\Omega^2R^6} = O(\epsilon^2) && \frac{EB_2}{m_0\Omega^2R^5}, \frac{EC_2}{m_0\Omega^2R^5} = O(\epsilon) \\
&\frac{K_A}{R} = O(\epsilon) && \frac{e_A}{R} = O(\epsilon^{3/2})
\end{aligned}
\tag{2.20}
$$

Some trigonometric identities are required. For small $\hat{\phi}$ ($\sin\hat{\phi} \simeq \hat{\phi}$ and $\cos\hat{\phi} \simeq 1$):

$$
\begin{aligned}
\sin\theta &= \sin(\theta_0 + \hat{\phi}) = \sin\theta_0\cos\hat{\phi} + \cos\theta_0\sin\hat{\phi} \simeq \sin\theta_0 + \hat{\phi}\cos\theta_0 \\
\cos\theta &= \cos(\theta_0 + \hat{\phi}) = \cos\theta_0\cos\hat{\phi} - \sin\theta_0\sin\hat{\phi} \simeq \cos\theta_0 - \hat{\phi}\sin\theta_0
\end{aligned}
\tag{2.21}
$$

For terms containing EI_c and EI_n, higher-order terms are retained for accuracy:

$$
\begin{aligned}
\sin\theta &\simeq \left(1 - \frac{\hat{\phi}^2}{2}\right)\sin\theta_0 + \hat{\phi}\cos\theta_0 \\
\cos\theta &\simeq \left(1 - \frac{\hat{\phi}^2}{2}\right)\cos\theta_0 - \hat{\phi}\sin\theta_0
\end{aligned}
\tag{2.22}
$$

The coefficients of Eq. 2.18 are derived as follows:

$$
\begin{aligned}
U_{u'_e} =& \iint_A E\Big[u'_e - \cancelto{0}{\lambda_T}(\hat{\phi}'' + w'v''' + w''v'') \\
&\qquad + (\eta^2+\zeta^2)\Big(\theta'_0\hat{\phi}' + \theta'_0 w'v'' + \frac{\hat{\phi}'^2}{2} + \cancelto{\epsilon^4}{\frac{w'^2v''^2}{2}} + \cancelto{\epsilon^3}{\hat{\phi}'w'v''}\Big) \\
&\qquad - v''(\eta\cos\theta - \cancelto{0}{\zeta}\sin\theta) - w''(\eta\sin\theta + \cancelto{0}{\zeta}\cos\theta)\Big]d\eta d\zeta \\
=& EAu'_e + EAK_A^2\Big(\theta'_0\hat{\phi}' + \theta'_0 w'v'' + \frac{\hat{\phi}'^2}{2}\Big) - EAe_A\Big[v''\cos\theta + w''\sin\theta\Big] \\
=& EAu'_e + EAK_A^2\Big(\theta'_0\hat{\phi}' + \theta'_0 w'v'' + \frac{\hat{\phi}'^2}{2}\Big) \\
& - EAe_A\Big[v''(\cos\theta_0 - \hat{\phi}\sin\theta_0) + w''(\sin\theta_0 + \hat{\phi}\cos\theta_0)\Big]
\end{aligned}
\tag{2.23}
$$

$$
\begin{aligned}
U_{w'} = \iint_A \Big(& - E\lambda_T v'''\Big[\cancelto{0}{u'_e} - \cancelto{\epsilon^3}{\lambda_T}(\hat{\phi}'' + w'v''' + w''v'') \\
&\qquad + \cancelto{0}{(\eta^2+\zeta^2)}\Big(\theta'_0\hat{\phi}' + \theta'_0 w'v'' + \frac{\hat{\phi}'^2}{2} + \frac{w'^2v''^2}{2} + \hat{\phi}'w'v''\Big) \\
&\qquad - v''(\cancelto{0}{\eta}\cos\theta - \cancelto{\epsilon^3}{\zeta}\sin\theta) - w''(\cancelto{0}{\eta}\sin\theta + \cancelto{\epsilon^3}{\zeta}\cos\theta)\Big] \\
& + E(\eta^2+\zeta^2)\theta'_0 v''\Big[u'_e - \cancelto{0}{\lambda_T}(\hat{\phi}'' + w'v''' + w''v'') \\
&\qquad + (\eta^2+\zeta^2)\Big(\theta'_0\hat{\phi}' + \cancelto{\epsilon^5}{\theta'_0 w'v''} + \cancelto{\epsilon^5}{\frac{\hat{\phi}'^2}{2}} + \cancelto{\epsilon^7}{\frac{w'^2v''^2}{2}} + \cancelto{\epsilon^6}{\hat{\phi}'w'v''}\Big) \\
&\qquad - v''(\cancelto{\epsilon^3}{\eta}\cos\theta - \cancelto{0}{\zeta}\sin\theta) - w''(\cancelto{\epsilon^3}{\eta}\sin\theta + \cancelto{0}{\zeta}\cos\theta)\Big] \\
& + E(\eta^2+\zeta^2)\hat{\phi}' v''\Big[\cancelto{\epsilon^4}{u'_e} - \cancelto{0}{\lambda_T}(\hat{\phi}'' + w'v''' + w''v'') \\
&\qquad + \cancelto{\epsilon^4}{(\eta^2+\zeta^2)}\Big(\theta'_0\hat{\phi}' + \theta'_0 w'v'' + \frac{\hat{\phi}'^2}{2} + \frac{w'^2v''^2}{2} + \hat{\phi}'w'v''\Big) \\
&\qquad - v''(\cancelto{\epsilon^4}{\eta}\cos\theta - \cancelto{0}{\zeta}\sin\theta) - w''(\cancelto{\epsilon^4}{\eta}\sin\theta + \cancelto{0}{\zeta}\cos\theta)\Big] \\
& + \cancelto{\epsilon^3}{E(\eta^2+\zeta^2)w'v''^2}\Big[u'_e - \lambda_T(\hat{\phi}'' + w'v''' + w''v'')
\end{aligned}
$$

$$
\begin{aligned}
&+(\eta^2+\zeta^2)\Big(\theta_0'\hat{\phi}'+\theta_0'w'v''+\frac{\hat{\phi}'^2}{2}+\frac{w'^2v''^2}{2}+\hat{\phi}'w'v''\Big)\\
&-v''(\eta\cos\theta-\zeta\sin\theta)-w''(\eta\sin\theta+\zeta\cos\theta)\Big]\\
&-G\hat{\zeta}v''\Big[-\hat{\zeta}(\hat{\phi}'+\cancelto{\epsilon^3}{w'v''})\Big]+G\hat{\eta}v''\Big[\hat{\eta}(\hat{\phi}'+\cancelto{\epsilon^3}{w'v''})\Big]\Big)d\eta d\zeta\\
=&EAK_A^2\theta_0'v''u_e'+(GJ+EB_1\theta_0'^2)v''\hat{\phi}' \qquad (2.24)
\end{aligned}
$$

$$
\begin{aligned}
U_{v''}=\iint_A\Big(&-E\lambda_T w''\Big[\cancelto{0}{u_e'}-\cancelto{\epsilon^3}{\lambda_T}(\hat{\phi}''+w'v'''+w''v'')\\
&+\cancelto{0}{(\eta^2+\zeta^2)}\Big(\theta_0'\hat{\phi}'+\theta_0'w'v''+\frac{\hat{\phi}'^2}{2}+\frac{w'^2v''^2}{2}+\hat{\phi}'w'v''\Big)\\
&-v''(\cancelto{0}{\eta}\cos\theta-\cancelto{\epsilon^3}{\zeta}\sin\theta)-w''(\cancelto{0}{\eta}\sin\theta+\cancelto{\epsilon^3}{\zeta}\cos\theta)\Big]\\
&+E(\eta^2+\zeta^2)\theta_0'w'\Big[u_e'-\cancelto{0}{\lambda_T}(\hat{\phi}''+w'v'''+w''v'')\\
&+(\eta^2+\zeta^2)\Big(\theta_0'\hat{\phi}'+\cancelto{\epsilon^5}{\theta_0'w'v''}+\cancelto{\epsilon^5}{\frac{\hat{\phi}'^2}{2}}+\cancelto{\epsilon^7}{\frac{w'^2v''^2}{2}}+\cancelto{\epsilon^6}{\hat{\phi}'w'v''}\Big)\\
&-v''(\cancelto{\epsilon^3}{\eta}\cos\theta-\cancelto{0}{\zeta}\sin\theta)-w''(\cancelto{\epsilon^3}{\eta}\sin\theta+\cancelto{0}{\zeta}\cos\theta)\Big]\\
&+E(\eta^2+\zeta^2)\hat{\phi}'w'\Big[\cancelto{\epsilon^4}{u_e'}-\cancelto{0}{\lambda_T}(\hat{\phi}''+w'v'''+w''v'')\\
&+\cancelto{\epsilon^4}{(\eta^2+\zeta^2)}\Big(\theta_0'\hat{\phi}'+\theta_0'w'v''+\frac{\hat{\phi}'^2}{2}+\frac{w'^2v''^2}{2}+\hat{\phi}'w'v''\Big)\\
&-v''(\cancelto{\epsilon^4}{\eta}\cos\theta-\cancelto{0}{\zeta}\sin\theta)-w''(\cancelto{\epsilon^4}{\eta}\sin\theta+\cancelto{0}{\zeta}\cos\theta)\Big]\\
&+\cancelto{\epsilon^3}{E(\eta^2+\zeta^2)v''w'^2}\Big[u_e'-\lambda_T(\hat{\phi}''+w'v'''+w''v'')\\
&+(\eta^2+\zeta^2)\Big(\theta_0'\hat{\phi}'+\theta_0'w'v''+\frac{\hat{\phi}'^2}{2}+\frac{w'^2v''^2}{2}+\hat{\phi}'w'v''\Big)\\
&-v''(\eta\cos\theta-\zeta\sin\theta)-w''(\eta\sin\theta+\zeta\cos\theta)\Big]\\
&-E(\eta\cos\theta-\zeta\sin\theta)\Big[u_e'-\lambda_T(\hat{\phi}''+\cancelto{\epsilon^3}{w'v'''}+\cancelto{\epsilon^3}{w''v''})
\end{aligned}
$$

$$
\begin{aligned}
&+ (\eta^2+\zeta^2)\Big(\theta_0'\hat{\phi}' + \cancelto{\epsilon^3}{\theta_0' w' v''} + \frac{\cancelto{\epsilon^3}{\hat{\phi}'^2}}{\cancel{2}} + \cancelto{\epsilon^5}{\frac{w'^2 v''^2}{2}} + \cancelto{\epsilon^4}{\hat{\phi}' w' v''}\Big) \\
&- v''(\eta\cos\theta - \zeta\sin\theta) - w''(\eta\sin\theta + \zeta\cos\theta)\Big] \\
&-G\hat{\zeta}w'\Big[-\hat{\zeta}(\hat{\phi}' + \cancelto{\epsilon^3}{w'v''})\Big] + G\hat{\eta}w'\Big[\hat{\eta}(\hat{\phi}' + \cancelto{\epsilon^3}{w'v''})\Big]\Big)d\eta d\zeta
\end{aligned}
$$

$$
\begin{aligned}
=&\iint_A \Big(- E\eta\cos\theta\Big[u_e' - \cancelto{0}{\lambda_T}\hat{\phi}'' + (\eta^2+\zeta^2)\theta_0'\hat{\phi}' \\
&- v''(\eta\cos\theta - \cancelto{0}{\zeta}\sin\theta) - w''(\eta\sin\theta + \cancelto{0}{\zeta}\cos\theta)\Big] \\
&+E\zeta\sin\theta\Big[\cancelto{0}{u_e'} - \lambda_T\hat{\phi}'' + \cancelto{0}{(\eta^2+\zeta^2)}\theta_0'\hat{\phi}' \\
&- v''(\cancelto{0}{\eta}\cos\theta - \zeta\sin\theta) - w''(\cancelto{0}{\eta}\sin\theta + \zeta\cos\theta)\Big]\Big)d\eta d\zeta
\end{aligned}
$$

$$
\begin{aligned}
&+EAK_A^2\theta_0'w'u_e' + EB_1\theta_0'^2 w'\hat{\phi}' + GJw'\hat{\phi}' \\
=&-EAe_A u_e'\cos\theta - EB_2\theta_0'\hat{\phi}'\cos\theta - EC_2\hat{\phi}''\sin\theta \\
&+v''(EI_c\cos^2\theta + EI_n\sin^2\theta) + w''\big((EI_c - EI_n)\sin\theta\cos\theta\big) \\
&+EAK_A^2\theta_0'w'u_e' + (GJ + EB_1\theta_0'^2)w'\hat{\phi}' \\
=&-EAe_A u_e'(\cos\theta_0 - \hat{\phi}\sin\theta_0) \\
&-EB_2\theta_0'\hat{\phi}'(\cos\theta_0 - \cancelto{\epsilon^3}{\hat{\phi}}\sin\theta_0) - EC_2\hat{\phi}''(\sin\theta_0 + \cancelto{\epsilon^3}{\hat{\phi}}\cos\theta_0) \\
&+v''\Big(EI_c\Big[\Big(1-\frac{\hat{\phi}^2}{2}\Big)\cos\theta_0 - \hat{\phi}\sin\theta_0\Big]^2 + EI_n\Big[\Big(1-\frac{\hat{\phi}^2}{2}\Big)\sin\theta_0 + \hat{\phi}\cos\theta_0\Big]^2\Big) \\
&+w''\Big((EI_c - EI_n)\Big[\Big(1-\frac{\hat{\phi}^2}{2}\Big)\sin\theta_0 + \hat{\phi}\cos\theta_0\Big]\Big[\Big(1-\frac{\hat{\phi}^2}{2}\Big)\cos\theta_0 - \hat{\phi}\sin\theta_0\Big]\Big) \\
&+EAK_A^2\theta_0'w'u_e' + (GJ + EB_1\theta_0'^2)w'\hat{\phi}' \\
=&-EAe_A u_e'(\cos\theta_0 - \hat{\phi}\sin\theta_0) - EB_2\theta_0'\hat{\phi}'\cos\theta_0 - EC_2\hat{\phi}''\sin\theta_0 \\
&+v''\Big(EI_c\Big[\Big(1 + \frac{\cancelto{\epsilon^5}{\hat{\phi}^4}}{\cancel{4}} - \hat{\phi}^2\Big)\cos^2\theta_0 + \hat{\phi}^2\sin^2\theta_0 - 2\Big(1 - \frac{\cancelto{\epsilon^4}{\hat{\phi}^2}}{\cancel{2}}\Big)\hat{\phi}\sin\theta_0\cos\theta_0\Big]
\end{aligned}
$$

$$
\begin{aligned}
&+EI_n\Big[\Big(1+\cancelto{\epsilon^5}{\frac{\hat{\phi}^4}{4}}-\hat{\phi}^2\Big)\sin^2\theta_0+\hat{\phi}^2\cos^2\theta_0+2\Big(1-\cancelto{\epsilon^4}{\frac{\hat{\phi}^2}{2}}\Big)\hat{\phi}\sin\theta_0\cos\theta_0\Big]\Big)\\
&+w''\Big((EI_c-EI_n)\Big[\Big(1+\cancelto{\epsilon^5}{\frac{\hat{\phi}^4}{4}}-\hat{\phi}^2\Big)\sin\theta_0\cos\theta_0-\hat{\phi}^2\sin\theta_0\cos\theta_0\\
&\qquad\qquad+\Big(1-\cancelto{\epsilon^4}{\frac{\hat{\phi}^2}{2}}\Big)\hat{\phi}(\cos^2\theta_0-\sin^2\theta_0)\Big]\Big)\\
&+EAK_A^2\theta_0'w'u_e'+(GJ+EB_1\theta_0'^2)w'\hat{\phi}'\\
=&-EAe_Au_e'(\cos\theta_0-\hat{\phi}\sin\theta_0)-EB_2\theta_0'\hat{\phi}'\cos\theta_0-EC_2\hat{\phi}''\sin\theta_0\\
&+(EI_c\cos^2\theta_0+EI_n\sin^2\theta_0)v''-(EI_c-EI_n)v''\hat{\phi}^2\cos 2\theta_0\\
&-(EI_c-EI_n)v''\hat{\phi}\sin 2\theta_0+(EI_c-EI_n)w''\sin\theta_0\cos\theta_0\\
&-(EI_c-EI_n)w''\hat{\phi}^2\sin 2\theta_0+(EI_c-EI_n)w''\hat{\phi}\cos 2\theta_0\\
&+EAK_A^2\theta_0'w'u_e'+(GJ+EB_1\theta_0'^2)w'\hat{\phi}'
\end{aligned}
\tag{2.25}
$$

$$
\begin{aligned}
U_{w''}=&\iint_A\Big(-E\lambda_T v''\Big[\cancelto{0}{u_e'}-\cancelto{\epsilon^3}{\lambda_T}(\hat{\phi}''+w'v'''+w''v'')\\
&\qquad+\cancelto{0}{(\eta^2+\zeta^2)}\Big(\theta_0'\hat{\phi}'+\theta_0'w'v''+\frac{\hat{\phi}'^2}{2}+\frac{w'^2v''^2}{2}+\hat{\phi}'w'v''\Big)\\
&\qquad-v''(\cancelto{0}{\eta}\cos\theta-\cancelto{\epsilon^3}{\zeta}\sin\theta)-w''(\cancelto{0}{\eta}\sin\theta+\cancelto{\epsilon^3}{\zeta}\cos\theta)\Big]\\
&-E(\eta\sin\theta+\zeta\cos\theta)\Big[u_e'-\lambda_T(\hat{\phi}''+\cancelto{\epsilon^3}{w'v'''}+\cancelto{\epsilon^3}{w''v''})\\
&\qquad+(\eta^2+\zeta^2)\Big(\theta_0'\hat{\phi}'+\cancelto{\epsilon^3}{\theta_0'w'v''}+\cancelto{\epsilon^3}{\frac{\hat{\phi}'^2}{2}}+\cancelto{\epsilon^5}{\frac{w'^2v''^2}{2}}+\cancelto{\epsilon^4}{\hat{\phi}'w'v''}\Big)\\
&\qquad-v''(\eta\cos\theta-\zeta\sin\theta)-w''(\eta\sin\theta+\zeta\cos\theta)\Big]\Big)d\eta d\zeta\\
=&\iint_A\Big(-E\eta\sin\theta\Big[u_e'-\cancelto{0}{\lambda_T}\hat{\phi}''+(\eta^2+\zeta^2)\theta_0'\hat{\phi}'
\end{aligned}
$$

$$- v''(\eta \cos\theta - \cancelto{0}{\zeta} \sin\theta) - w''(\eta \sin\theta + \cancelto{0}{\zeta} \cos\theta)\Big]$$

$$-E\zeta\cos\theta\Big[\cancelto{0}{u'_e} - \lambda_T \hat{\phi}'' + \cancelto{0}{(\eta^2+\zeta^2)}\theta_0'\hat{\phi}'$$

$$- v''(\cancelto{0}{\eta} \cos\theta - \zeta\sin\theta) - w''(\cancelto{0}{\eta} \sin\theta + \zeta\cos\theta)\Big]\Big) d\eta d\zeta$$

$$= -EAe_A u'_e \sin\theta - EB_2\theta_0'\hat{\phi}'\sin\theta + EC_2\hat{\phi}''\cos\theta$$

$$+ w''(EI_c\sin^2\theta + EI_n\cos^2\theta) + v''\big((EI_c - EI_n)\sin\theta\cos\theta\big)$$

$$= -EAe_A u'_e(\sin\theta_0 + \hat{\phi}\cos\theta_0)$$

$$-EB_2\theta_0'\hat{\phi}'(\sin\theta_0 + \cancelto{\epsilon^3}{\hat{\phi}} \cos\theta_0) + EC_2\hat{\phi}''(\cos\theta_0 - \cancelto{\epsilon^3}{\hat{\phi}} \sin\theta_0)$$

$$+ w''\Bigg(EI_c\Big[\Big(1-\frac{\hat{\phi}^2}{2}\Big)\sin\theta_0 + \hat{\phi}\cos\theta_0\Big]^2 + EI_n\Big[\Big(1-\frac{\hat{\phi}^2}{2}\Big)\cos\theta_0 - \hat{\phi}\sin\theta_0\Big]^2\Bigg)$$

$$+ v''\Bigg((EI_c - EI_n)\Big[\Big(1-\frac{\hat{\phi}^2}{2}\Big)\sin\theta_0 + \hat{\phi}\cos\theta_0\Big]\Big[\Big(1-\frac{\hat{\phi}^2}{2}\Big)\cos\theta_0 - \hat{\phi}\sin\theta_0\Big]\Bigg)$$

$$= -EAe_A u'_e(\sin\theta_0 + \hat{\phi}\cos\theta_0) - EB_2\theta_0'\hat{\phi}'\sin\theta_0 + EC_2\hat{\phi}''\cos\theta_0$$

$$+ w''\Bigg(EI_c\Big[\Big(1 + \cancelto{\epsilon^5}{\frac{\hat{\phi}^4}{4}} - \hat{\phi}^2\Big)\sin^2\theta_0 + \hat{\phi}^2\cos^2\theta_0 + 2\Big(1 - \cancelto{\epsilon^4}{\frac{\hat{\phi}^2}{2}}\Big)\hat{\phi}\sin\theta_0\cos\theta_0\Big]$$

$$+ EI_n\Big[\Big(1 + \cancelto{\epsilon^5}{\frac{\hat{\phi}^4}{4}} - \hat{\phi}^2\Big)\cos^2\theta_0 + \hat{\phi}^2\sin^2\theta_0 - 2\Big(1 - \cancelto{\epsilon^4}{\frac{\hat{\phi}^2}{2}}\Big)\hat{\phi}\sin\theta_0\cos\theta_0\Big]\Bigg)$$

$$+ v''\Bigg((EI_c - EI_n)\Big[\Big(1 + \cancelto{\epsilon^5}{\frac{\hat{\phi}^4}{4}} - \hat{\phi}^2\Big)\sin\theta_0\cos\theta_0 - \hat{\phi}^2\sin\theta_0\cos\theta_0$$

$$+ \Big(1 - \cancelto{\epsilon^4}{\frac{\hat{\phi}^2}{2}}\Big)\hat{\phi}(\cos^2\theta_0 - \sin^2\theta_0)\Big]\Bigg)$$

$$= -EAe_A u'_e(\sin\theta_0 + \hat{\phi}\cos\theta_0) - EB_2\theta_0'\hat{\phi}'\sin\theta_0 + EC_2\hat{\phi}''\cos\theta_0$$

$$+ (EI_c\sin^2\theta_0 + EI_n\cos^2\theta_0)w'' + (EI_c - EI_n)w''\hat{\phi}^2\cos 2\theta_0$$

$$+ (EI_c - EI_n)w''\hat{\phi}\sin 2\theta_0 + (EI_c - EI_n)v''\sin\theta_0\cos\theta_0$$

$$-(EI_c - EI_n)v''\hat{\phi}^2\sin 2\theta_0 + (EI_c - EI_n)v''\hat{\phi}\cos 2\theta_0 \tag{2.26}$$

$$
\begin{aligned}
U_{v'''} =& \iint_A \bigg(-E\lambda_T w' \Big[\cancelto{0}{u'_e} - \cancelto{\epsilon^3}{\lambda_T} (\hat{\phi}'' + w'v''' + w''v'') \\
&\qquad + \cancelto{0}{(\eta^2 + \zeta^2)} \Big(\theta'_0 \hat{\phi}' + \theta'_0 w'v'' + \frac{\hat{\phi}'^2}{2} + \frac{w'^2 v''^2}{2} + \hat{\phi}' w' v'' \Big) \\
&\qquad - v''(\cancelto{0}{\eta} \cos\theta - \cancelto{\epsilon^3}{\zeta} \sin\theta) - w''(\cancelto{0}{\eta} \sin\theta + \cancelto{\epsilon^3}{\zeta} \cos\theta) \Big] \bigg) d\eta d\zeta \\
=& 0
\end{aligned}
\tag{2.27}
$$

$$
\begin{aligned}
U_{\hat{\phi}} =& \iint_A \bigg(-Ew''(\eta\cos\theta - \zeta\sin\theta) \Big[u'_e - \lambda_T (\cancelto{\epsilon^3}{\hat{\phi}''} + \cancelto{\epsilon^4}{w'v'''} + \cancelto{\epsilon^4}{w''v''}) \\
&\qquad + (\eta^2 + \zeta^2) \Big(\cancelto{\epsilon^3}{\theta'_0 \hat{\phi}'} + \cancelto{\epsilon^4}{\theta'_0 w'v''} \\
&\qquad\qquad + \cancelto{\epsilon^4}{\frac{\hat{\phi}'^2}{2}} + \cancelto{\epsilon^6}{\frac{w'^2 v''^2}{2}} + \cancelto{\epsilon^5}{\hat{\phi}' w' v''} \Big) \\
&\qquad - v''\big(\eta\cos\theta - \zeta\sin\theta\big) - w''\big(\eta\sin\theta + \zeta\cos\theta\big) \Big] \\
&+ Ev''(\eta\sin\theta + \zeta\cos\theta) \Big[u'_e - \lambda_T (\cancelto{\epsilon^3}{\hat{\phi}''} + \cancelto{\epsilon^4}{w'v'''} + \cancelto{\epsilon^4}{w''v''}) \\
&\qquad + (\eta^2 + \zeta^2) \Big(\cancelto{\epsilon^3}{\theta'_0 \hat{\phi}'} + \cancelto{\epsilon^4}{\theta'_0 w'v''} \\
&\qquad\qquad + \cancelto{\epsilon^4}{\frac{\hat{\phi}'^2}{2}} + \cancelto{\epsilon^6}{\frac{w'^2 v''^2}{2}} + \cancelto{\epsilon^5}{\hat{\phi}' w' v''} \Big) \\
&\qquad - v''\big(\eta\cos\theta - \zeta\sin\theta\big) - w''\big(\eta\sin\theta + \zeta\cos\theta\big) \Big] \bigg) d\eta d\zeta \\
=& \iint_A \bigg(-Ew''\eta\cos\theta \Big[u'_e - v''\big(\eta\cos\theta - \cancelto{0}{\zeta} \sin\theta\big) - w''\big(\eta\sin\theta + \cancelto{0}{\zeta} \cos\theta\big) \Big] \\
&+ Ew''\zeta\sin\theta \Big[\cancelto{0}{u'_e} - v''\big(\cancelto{0}{\eta} \cos\theta - \zeta\sin\theta\big) - w''\big(\cancelto{0}{\eta} \sin\theta + \zeta\cos\theta\big) \Big] \\
&+ Ev''\eta\sin\theta \Big[u'_e - v''\big(\eta\cos\theta - \cancelto{0}{\zeta} \sin\theta\big) - w''\big(\eta\sin\theta + \cancelto{0}{\zeta} \cos\theta\big) \Big] \\
&+ Ev''\zeta\cos\theta \Big[\cancelto{0}{u'_e} - v''\big(\cancelto{0}{\eta} \cos\theta - \zeta\sin\theta\big) - w''\big(\cancelto{0}{\eta} \sin\theta + \zeta\cos\theta\big) \Big] \bigg) d\eta d\zeta
\end{aligned}
$$

$$
\begin{aligned}
=&-EAe_A w'' u_e' \cos\theta + EAe_A v'' u_e' \sin\theta \\
&+w''v''(EI_c\cos^2\theta + EI_n\sin^2\theta) - v''w''(EI_c\sin^2\theta + EI_n\cos^2\theta) \\
&+w''^2(EI_c - EI_n)\sin\theta\cos\theta - v''^2(EI_c - EI_n)\sin\theta\cos\theta \\
=&-EAe_A w'' u_e'(\cos\theta_0 - \cancelto{\epsilon^{3.5}}{\hat{\phi}}\sin\theta_0) + EAe_A v'' u_e'(\sin\theta_0 + \cancelto{\epsilon^{3.5}}{\hat{\phi}}\cos\theta_0) \\
&+(EI_c - EI_n)w''v''(\cos^2\theta - \sin^2\theta) + (EI_c - EI_n)(w''^2 - v''^2)\sin\theta\cos\theta \\
=&-EAe_A w'' u_e' \cos\theta_0 + EAe_A v'' u_e' \sin\theta_0 \\
&+(EI_c - EI_n)w''v''\left(\left[\left(1 - \frac{\hat{\phi}^2}{2}\right)\cos\theta_0 - \hat{\phi}\sin\theta_0\right]^2 - \left[\left(1 - \frac{\hat{\phi}^2}{2}\right)\sin\theta_0 + \hat{\phi}\cos\theta_0\right]^2\right) \\
&+(EI_c - EI_n)(w''^2 - v''^2)\left[\left(1 - \frac{\hat{\phi}^2}{2}\right)\sin\theta_0 + \hat{\phi}\cos\theta_0\right]\left[\left(1 - \frac{\hat{\phi}^2}{2}\right)\cos\theta_0 - \hat{\phi}\sin\theta_0\right] \\
=&EAe_A u_e'(v''\sin\theta_0 - w''\cos\theta_0) \\
&+(EI_c - EI_n)w''v''\left(\left[\left(1 + \cancelto{\epsilon^6}{\frac{\hat{\phi}^4}{4}} - \cancelto{\epsilon^4}{\hat{\phi}^2}\right)\cos^2\theta_0 + \cancelto{\epsilon^4}{\hat{\phi}^2}\sin^2\theta_0 - 2\left(1 - \cancelto{\epsilon^5}{\frac{\hat{\phi}^2}{2}}\right)\hat{\phi}\sin\theta_0\cos\theta_0\right]\right. \\
&\qquad\qquad\left. -\left[\left(1 + \cancelto{\epsilon^6}{\frac{\hat{\phi}^4}{4}} - \cancelto{\epsilon^4}{\hat{\phi}^2}\right)\sin^2\theta_0 + \cancelto{\epsilon^4}{\hat{\phi}^2}\cos^2\theta_0 + 2\left(1 - \cancelto{\epsilon^5}{\frac{\hat{\phi}^2}{2}}\right)\hat{\phi}\sin\theta_0\cos\theta_0\right]\right) \\
&+(EI_c - EI_n)(w''^2 - v''^2)\left[\left(1 + \cancelto{\epsilon^6}{\frac{\hat{\phi}^4}{4}} - \cancelto{\epsilon^4}{\hat{\phi}^2}\right)\sin\theta_0\cos\theta_0 - \cancelto{\epsilon^4}{\hat{\phi}^2}\sin\theta_0\cos\theta_0\right. \\
&\qquad\qquad\left. +\left(1 - \cancelto{\epsilon^5}{\frac{\hat{\phi}^2}{2}}\right)\hat{\phi}(\cos^2\theta_0 - \sin^2\theta_0)\right]\Bigg) \\
=&EAe_A u_e'(v''\sin\theta_0 - w''\cos\theta_0) \\
&+(EI_c - EI_n)w''v''\cos 2\theta - 2(EI_c - EI_n)w''v''\hat{\phi}\sin 2\theta \\
&+(EI_c - EI_n)(w''^2 - v''^2)\sin\theta_0\cos\theta_0 + (EI_c - EI_n)(w''^2 - v''^2)\hat{\phi}\cos 2\theta_0 \qquad (2.28)
\end{aligned}
$$

$$
\begin{aligned}
U_{\hat{\phi}'} =& \iint_A \Bigg(E(\eta^2+\zeta^2)\theta_0'\Big[u_e' - \cancelto{0}{\lambda_T}(\hat{\phi}'' + w'v''' + w''v'') \\
&\qquad + (\eta^2+\zeta^2)\Big(\theta_0'\hat{\phi}' + \theta_0' w'v'' + \cancelto{\epsilon^4}{\frac{\hat{\phi}'^2}{2}} + \cancelto{\epsilon^6}{\frac{w'^2v''^2}{2}} + \cancelto{\epsilon^5}{\hat{\phi}'w'v''}\Big) \\
&\qquad - v''(\eta\cos\theta - \cancelto{0}{\zeta}\sin\theta) - w''(\eta\sin\theta + \cancelto{0}{\zeta}\cos\theta)\Big] \\
&+E(\eta^2+\zeta^2)(\phi' + w'v'')\Big[u_e' - \cancelto{0}{\lambda_T}(\hat{\phi}'' + w'v''' + w''v'') \\
&\qquad + (\eta^2+\zeta^2)\Big(\theta_0'\hat{\phi}' + \theta_0' w'v'' + \frac{\hat{\phi}'^2}{2} + \frac{w'^2v''^2}{2} + \hat{\phi}'w'v''\Big) \\
&\qquad - v''(\eta\cos\theta - \cancelto{0}{\zeta}\sin\theta) - w''(\eta\sin\theta + \cancelto{0}{\zeta}\cos\theta)\Big] \\
&\qquad -G\hat{\zeta}\Big[-\hat{\zeta}(\hat{\phi}' + w'v'')\Big] + G\hat{\eta}\Big[\hat{\eta}(\hat{\phi}' + w'v'')\Big]\Bigg) d\eta d\zeta \\
=& \iint_A \Bigg(E(\eta^2+\zeta^2)\theta_0'\Big[u_e' + (\eta^2+\zeta^2)(\theta_0'\hat{\phi}' + \theta_0' w'v'') - v''\eta\cos\theta - w''\eta\sin\theta\Big] \\
&+E(\eta^2+\zeta^2)\phi'\Big[u_e' + \cancelto{\epsilon^3}{(\eta^2+\zeta^2)}\Big(\theta_0'\hat{\phi}' + \theta_0' w'v'' + \frac{\hat{\phi}'^2}{2} + \frac{w'^2v''^2}{2} + \hat{\phi}'w'v''\Big) \\
&\qquad - v''\cancelto{\epsilon^3}{\eta}\cos\theta - w''\cancelto{\epsilon^3}{\eta}\sin\theta\Big] \\
&+E(\eta^2+\zeta^2)w'v''\Big[\cancelto{\epsilon^4}{u_e'} + \cancelto{\epsilon^4}{(\eta^2+\zeta^2)}\Big(\theta_0'\hat{\phi}' + \theta_0' w'v'' + \frac{\hat{\phi}'^2}{2} + \frac{w'^2v''^2}{2} + \hat{\phi}'w'v''\Big) \\
&\qquad - v''\cancelto{\epsilon^4}{\eta}\cos\theta - w''\cancelto{\epsilon^4}{\eta}\sin\theta\Big] \\
&\qquad -G\hat{\zeta}\Big[-\hat{\zeta}(\hat{\phi}' + w'v'')\Big] + G\hat{\eta}\Big[\hat{\eta}(\hat{\phi}' + w'v'')\Big]\Bigg) d\eta d\zeta \\
=& EAK_A^2\theta_0'u_e' + EB_1\theta_0'^2(\hat{\phi}' + w'v'') - EB_2\theta_0'(v''\cos\theta + w''\sin\theta) \\
&+EAK_A^2\hat{\phi}'u_e' + GJ(\hat{\phi}' + w'v'') \\
=& EAK_A^2(\theta_0' + \hat{\phi}')u_e' + (GJ + EB_1\theta_0'^2)(\hat{\phi}' + w'v'') \\
&-EB_2\theta_0'\big(v''(\cos\theta_0 - \cancelto{\epsilon^3}{\hat{\phi}}\sin\theta_0) + w''(\sin\theta_0 + \cancelto{\epsilon^3}{\hat{\phi}}\cos\theta_0)\big)
\end{aligned}
$$

$$
\begin{aligned}
&= EAK_A^2(\theta_0' + \hat{\phi}')u_e' + (GJ + EB_1\theta_0'^2)(\hat{\phi}' + w'v'') \\
&\quad - EB_2\theta_0'(v''\cos\theta_0 + w''\sin\theta_0)
\end{aligned} \tag{2.29}
$$

$$
\begin{aligned}
U_{\hat{\phi}''} = \iint_A -E\lambda_T \Big[& \cancelto{0}{u_e'} - \lambda_T(\hat{\phi}'' + \cancelto{\epsilon^4}{w'v'''} + \cancelto{\epsilon^4}{w''v''}) \\
& + (\eta^2 + \zeta^2)\Big(\cancelto{\epsilon^3}{\theta_0'\hat{\phi}'} + \cancelto{\epsilon^4}{\theta_0' w'v''} + \cancelto{\epsilon^4}{\frac{\hat{\phi}'^2}{2}} + \cancelto{\epsilon^6}{\frac{w'^2 v''^2}{2}} + \cancelto{\epsilon^5}{\hat{\phi}' w'v''} \Big) \\
& - v''(\cancelto{0}{\eta}\cos\theta - \zeta\sin\theta) - w''(\cancelto{0}{\eta}\sin\theta + \zeta\cos\theta) \Big] d\eta d\zeta \\
= & EC_1\hat{\phi}'' + EC_2(w''\cos\theta - v''\sin\theta) \\
= & EC_1\hat{\phi}'' + EC_2\big(w''(\cos\theta_0 - \cancelto{\epsilon^3}{\hat{\phi}}\sin\theta_0\big) - v''(\sin\theta_0 + \cancelto{\epsilon^3}{\hat{\phi}}\cos\theta_0)\big) \\
= & EC_1\hat{\phi}'' + EC_2(w''\cos\theta_0 - v''\sin\theta_0)
\end{aligned} \tag{2.30}
$$

The final equations are given below once more for readability.

$$
\begin{aligned}
U_{u_e'} = & EAu_e' + EAK_A^2\Big(\theta_0'\hat{\phi}' + \theta_0' w'v'' + \frac{\hat{\phi}'^2}{2}\Big) \\
& - EAe_A\Big[v''(\cos\theta_0 - \hat{\phi}\sin\theta_0) + w''(\sin\theta_0 + \hat{\phi}\cos\theta_0)\Big]
\end{aligned} \tag{2.31}
$$

$$
U_{w'} = EAK_A^2\theta_0' v'' u_e' + (GJ + EB_1\theta_0'^2)v''\hat{\phi}' \tag{2.32}
$$

$$
\begin{aligned}
U_{v''} = & - EAe_A u_e'(\cos\theta_0 - \hat{\phi}\sin\theta_0) - EB_2\theta_0'\hat{\phi}'\cos\theta_0 - EC_2\hat{\phi}''\sin\theta_0 \\
& + (EI_c\cos^2\theta_0 + EI_n\sin^2\theta_0)v'' - (EI_c - EI_n)v''\hat{\phi}^2\cos 2\theta_0 \\
& - (EI_c - EI_n)v''\hat{\phi}\sin 2\theta_0 + (EI_c - EI_n)w''\sin\theta_0\cos\theta_0 \\
& - (EI_c - EI_n)w''\hat{\phi}^2\sin 2\theta_0 + (EI_c - EI_n)w''\hat{\phi}\cos 2\theta_0 \\
& + EAK_A^2\theta_0' w'u_e' + (GJ + EB_1\theta_0'^2)w'\hat{\phi}'
\end{aligned} \tag{2.33}
$$

$$
\begin{aligned}
U_{w''} =& - EAe_A u_e'(\sin\theta_0 + \hat{\phi}\cos\theta_0) - EB_2\theta_0'\hat{\phi}'\sin\theta_0 + EC_2\hat{\phi}''\cos\theta_0 \\
&+ (EI_c\sin^2\theta_0 + EI_n\cos^2\theta_0)w'' + (EI_c - EI_n)w''\hat{\phi}^2\cos 2\theta_0 \\
&+ (EI_c - EI_n)w''\hat{\phi}\sin 2\theta_0 + (EI_c - EI_n)v''\sin\theta_0\cos\theta_0 \\
&- (EI_c - EI_n)v''\hat{\phi}^2\sin 2\theta_0 + (EI_c - EI_n)v''\hat{\phi}\cos 2\theta_0 \qquad (2.34)
\end{aligned}
$$

$$
U_{v'''} = 0 \qquad (2.35)
$$

$$
\begin{aligned}
U_{\hat{\phi}} =& EAe_A u_e'(v''\sin\theta_0 - w''\cos\theta_0) \\
&+ (EI_c - EI_n)w''v''\cos 2\theta - 2(EI_c - EI_n)w''v''\hat{\phi}\sin 2\theta \\
&+ (EI_c - EI_n)(w''^2 - v''^2)\sin\theta_0\cos\theta_0 + (EI_c - EI_n)(w''^2 - v''^2)\hat{\phi}\cos 2\theta_0 \qquad (2.36)
\end{aligned}
$$

$$
\begin{aligned}
U_{\hat{\phi}'} =& EAK_A^2(\theta_0' + \hat{\phi}')u_e' + (GJ + EB_1\theta_0'^2)(\hat{\phi}' + w'v'') \\
&- EB_2\theta_0'(v''\cos\theta_0 + w''\sin\theta_0) \qquad (2.37)
\end{aligned}
$$

$$
U_{\hat{\phi}''} = EC_1\hat{\phi}'' + EC_2(w''\cos\theta_0 - v''\sin\theta_0) \qquad (2.38)
$$

2.5 Hub Motions

The rotor hub is not stationary due to the wing/pylon motions. Hub motions affect the aerodynamic and inertial loads on the blades.

The pylon is modeled as a beam as part of the wing. This allows for an elastic pylon. The motions of the hub H, shown in Fig. 2.1, are therefore obtained from the finite element solution directly. Velocity and acceleration of the hub with respect to the inertial frame I measured along the axes of the inertial frame are as follows:

$$v^{HI/I} = \begin{Bmatrix} \dot{u}_w \\ \dot{v}_w \\ \dot{w}_w \end{Bmatrix} \qquad a^{HI/I} = \dot{v}^{HI/I} = \begin{Bmatrix} \ddot{u}_w \\ \ddot{v}_w \\ \ddot{w}_w \end{Bmatrix} \tag{2.39}$$

Where u_w, v_w, and w_w denote wing/pylon deformations at the hub. The hub motions are rotated to the nonrotating hub frame H as follows:

$$v^{HI/H} = C^{HI} v^{HI/I} \tag{2.40}$$

$$a^{HI/H} = C^{HI} a^{HI/I} \tag{2.41}$$

Angular velocity of the hub with respect to the inertial frame I measured along the axes of the deformed wing frame W and its time derivative are as follows:

$$\omega^{HI/W} = \begin{Bmatrix} \dot{\theta}_w \\ 0 \\ 0 \end{Bmatrix} + X_{\theta_w} \begin{Bmatrix} 0 \\ \dot{\beta}_w \\ 0 \end{Bmatrix} + C^{WI} \begin{Bmatrix} 0 \\ 0 \\ \dot{\zeta}_w \end{Bmatrix} \tag{2.42}$$

$$\dot{\omega}^{HI/W} = \begin{Bmatrix} \ddot{\theta}_w \\ 0 \\ 0 \end{Bmatrix} + X_{\theta_w} \begin{Bmatrix} 0 \\ \ddot{\beta}_w \\ 0 \end{Bmatrix} + C^{WI} \begin{Bmatrix} 0 \\ 0 \\ \ddot{\zeta}_w \end{Bmatrix} + \dot{X}_{\theta_w} \begin{Bmatrix} 0 \\ \dot{\beta}_w \\ 0 \end{Bmatrix} + \dot{C}^{WI} \begin{Bmatrix} 0 \\ 0 \\ \dot{\zeta}_w \end{Bmatrix} \tag{2.43}$$

Where C^{WI} is the direction cosine matrix evaluated using the angular deformations at the rotor hub due to wing/pylon motions. The terms ζ_w, β_w, and θ_w denote the angular deformations of the wing/pylon at the hub. Time derivative of a direction cosine matrix is related to the angular velocity as follows:

$$\dot{C}^{AB} = -\tilde{\omega}^{AB/A}C^{AB} = C^{AB}\tilde{\omega}^{BA/B} \tag{2.44}$$

Where $\tilde{\omega}$ is the skew-symmetric representation of the angular velocity vector. The hub angular velocity and acceleration are then rotated to the nonrotating hub frame H as follows:

$$\omega^{HI/H} = C^{HW}\omega^{HI/W} \tag{2.45}$$

$$\dot{\omega}^{HI/H} = C^{HW}\dot{\omega}^{HI/W} \tag{2.46}$$

2.6 Blade Inertial Loads

2.6.1 Forces

Position of the section center of gravity C with respect to the inertial frame I measured along the axes of the inertial frame I is calculated as follows:

$$r^{CI/I} = C^{IU}(r^{CH/U} + r^{HI/U}) \tag{2.47}$$

Taking the derivative with respect to time,

$$\begin{aligned}\dot{r}^{CI/I} = v^{CI/I} &= C^{IU}\tilde{\omega}^{UI/U}r^{CH/U} + C^{IU}\dot{r}^{CH/U} + C^{IU}\tilde{\omega}^{UI/U}r^{HI/U} + C^{IU}\dot{r}^{HI/U} \\ &= C^{IU}(\tilde{\omega}^{UI/U}r^{CH/U} + \dot{r}^{CH/U} + \tilde{\omega}^{UI/U}r^{HI/U} + \dot{r}^{HI/U})\end{aligned}$$

$$= C^{IU}(\tilde{\omega}^{UI/U} r^{CH/U} + \dot{r}^{CH/U}) + v^{HI/I} \tag{2.48}$$

Taking the derivative with respect to time once more,

$$\begin{aligned}
\ddot{r}^{CI/I} = a^{CI/I} =& C^{IU}\tilde{\omega}^{UI/U}\tilde{\omega}^{UI/U} r^{CH/U} + C^{IU}\dot{\tilde{\omega}}^{UI/U} r^{CH/U} + C^{IU}\tilde{\omega}^{UI/U}\dot{r}^{CH/U} \\
&+ C^{IU}\tilde{\omega}^{UI/U}\dot{r}^{CH/U} + C^{IU}\ddot{r}^{CH/U} + a^{HI/I} \\
=& C^{IU}(\tilde{\omega}^{UI/U}\tilde{\omega}^{UI/U} r^{CH/U} + \dot{\tilde{\omega}}^{UI/U} r^{CH/U} + 2\tilde{\omega}^{UI/U}\dot{r}^{CH/U} + \ddot{r}^{CH/U}) \\
&+ a^{HI/I}
\end{aligned} \tag{2.49}$$

Rotating to the blade undeformed frame U and rearranging,

$$\begin{aligned}
a^{CI/U} =& C^{UI}C^{IU}(\tilde{\omega}^{UI/U}\tilde{\omega}^{UI/U} r^{CH/U} + \dot{\tilde{\omega}}^{UI/U} r^{CH/U} + 2\tilde{\omega}^{UI/U}\dot{r}^{CH/U} + \ddot{r}^{CH/U}) \\
&+ C^{UI}a^{HI/I} \\
=& a^{HI/U} + \ddot{r}^{CH/U} + \tilde{\omega}^{UI/U}\tilde{\omega}^{UI/U} r^{CH/U} + \dot{\tilde{\omega}}^{UI/U} r^{CH/U} + 2\tilde{\omega}^{UI/U}\dot{r}^{CH/U}
\end{aligned} \tag{2.50}$$

Inertial forces at the section center of gravity can then be calculated as follows:

$$f^{C/U} = -m a^{CI/U} \tag{2.51}$$

The terms on the right-hand side of Eq. 2.50 are given below. The first term ($a^{HI/U}$) is obtained by rotating the acceleration of the hub from the nonrotating hub frame H to the blade undeformed frame U as follows:

$$a^{HI/U} = C^{UH} a^{HI/H} \tag{2.52}$$

Position of the section center of gravity C with respect to the nonrotating hub frame H measured along the axes of the blade undeformed frame U and its time derivatives are as follows:

$$r^{CH/U} = r^{DH/U} + C^{UD} r^{CD/D} \tag{2.53}$$

$$= \begin{Bmatrix} x_{ea} + u \\ y_{ea} + v \\ z_{ea} + w \end{Bmatrix} + C^{UD} \begin{Bmatrix} 0 \\ e_{cg} \\ 0 \end{Bmatrix} \tag{2.54}$$

$$\dot{r}^{CH/U} = \begin{Bmatrix} \dot{u} \\ \dot{v} \\ \dot{w} \end{Bmatrix} + \dot{C}^{UD} \begin{Bmatrix} 0 \\ e_{cg} \\ 0 \end{Bmatrix} \tag{2.55}$$

$$\ddot{r}^{CH/U} = \begin{Bmatrix} \ddot{u} \\ \ddot{v} \\ \ddot{w} \end{Bmatrix} + \ddot{C}^{UD} \begin{Bmatrix} 0 \\ e_{cg} \\ 0 \end{Bmatrix} \tag{2.56}$$

Where u, v, and w are deformations in the blade undeformed frame U (u is comprised of axial deformation and foreshortening), e_{cg} is the position of the center of gravity with respect to the elastic axis in the blade deformed frame D (positive toward leading edge), and x_{ea}, y_{ea}, z_{ea} denote the position of the elastic axis with respect to hub in the blade undeformed frame U.

Angular velocity of the blade undeformed frame U with respect to the inertial frame I measured along the axes of the blade undeformed frame U is calculated as follows:

$$
\begin{aligned}
\omega^{UI/U} &= \omega^{UH/U} + C^{UH}\omega^{HI/H} \\
&= C^{UR}\begin{Bmatrix} 0 \\ 0 \\ \Omega \end{Bmatrix} + C^{UH}\omega^{HI/H}
\end{aligned} \tag{2.57}
$$

Taking the derivative with respect to time,

$$
\begin{aligned}
\dot{\omega}^{UI/U} &= \cancelto{0}{\dot{C}^{UR}}\begin{Bmatrix} 0 \\ 0 \\ \Omega \end{Bmatrix} + C^{UR}\begin{Bmatrix} 0 \\ 0 \\ \cancelto{0}{\dot{\Omega}} \end{Bmatrix} + \dot{C}^{UH}\omega^{HI/H} + C^{UH}\dot{\omega}^{HI/H} \\
&= -\tilde{\omega}^{UH/U}C^{UH}\omega^{HI/H} + C^{UH}\dot{\omega}^{HI/H}
\end{aligned} \tag{2.58}
$$

Note that $\dot{\Omega} = 0$ was assumed in Eq. 2.58 because the rotor speed perturbation would be taken into account through the hub roll motion; another perturbation term is unnecessary.

2.6.2 Moments

Inertial moment at the section center of gravity C measured along the axis of the blade deformed frame D is calculated as follows:

$$
m^{C/D} = -(I\dot{\omega}^{DI/D} + \tilde{\omega}^{DI/D}I\omega^{DI/D}) \tag{2.59}
$$

Where I is the moment of inertia tensor with respect to the section center of gravity in the blade deformed frame D.

Angular velocity of the blade deformed frame D with respect to the inertial frame I measured along the axes of the blade deformed frame D is calculated as follows:

$$\omega^{DI/D} = \omega^{DU/D} + C^{DU}\omega^{UI/U} \tag{2.60}$$

Taking the derivative with respect to time,

$$\begin{aligned}\dot{\omega}^{DI/D} =& \dot{\omega}^{DU/D} + \dot{C}^{DU}\omega^{UI/U} + C^{DU}\dot{\omega}^{UI/U} \\ =& \dot{\omega}^{DU/D} - \omega^{DU/D}C^{DU}\omega^{UI/U} + C^{DU}\dot{\omega}^{UI/U}\end{aligned} \tag{2.61}$$

Where

$$\omega^{DU/D} = \begin{Bmatrix}\dot{\theta} \\ 0 \\ 0\end{Bmatrix} + X_\theta \begin{Bmatrix}0 \\ \dot{\beta} \\ 0\end{Bmatrix} + C^{DU} \begin{Bmatrix}0 \\ 0 \\ \dot{\zeta}\end{Bmatrix} \tag{2.62}$$

The inertial moments are then translated from section the center of gravity C to the elastic axis:

$$m^{U/U} = m^{D/U} = C^{UD}(m^{C/D} + \tilde{r}^{CD/D}C^{DU}f^{C/U}) \tag{2.63}$$

2.7 Blade Aerodynamic Loads

Hub motions, blade deformations, high pitch angles, and high inflow are exactly accounted for in the section angle of attack calculation. Unsteady thin airfoil theory with C81 airfoil decks is used. The airfoil decks tabulate lift, drag, and moment coefficients with respect to angle of attack and Mach number. Radial flow corrections for edgewise flight and blade sweep are included. Reverse flow is taken into account. Inflow model can use uniform inflow, linear inflow, prescribed wake, or freewake, combined with a full-span nearwake.

2.7.1 Section Angle of Attack and Sideslip Angle

Position of the section three quarter-chord A with respect to the inertial frame I measured along the axes of the inertial frame I is calculated as follows:

$$r^{AI/I} = C^{IU}(r^{AH/U} + r^{HI/U}) \tag{2.64}$$

Taking the derivative with respect to time,

$$\begin{aligned}\dot{r}^{AI/I} = v^{AI/I} &= C^{IU}\tilde{\omega}^{UI/U}r^{AH/U} + C^{IU}\dot{r}^{AH/U} + C^{IU}\tilde{\omega}^{UI/U}r^{HI/U} + C^{IU}\dot{r}^{HI/U} \\ &= C^{IU}(\tilde{\omega}^{UI/U}r^{AH/U} + \dot{r}^{AH/U} + \tilde{\omega}^{UI/U}r^{HI/U} + \dot{r}^{HI/U}) \\ &= C^{IU}(\tilde{\omega}^{UI/U}r^{AH/U} + \dot{r}^{AH/U}) + v^{HI/I}\end{aligned} \tag{2.65}$$

Adding the wind velocity ($v^{W/U}$), rotating to the blade deformed frame D, and rearranging,

$$\begin{aligned}v^{AI/D} &= C^{DU}C^{UI}\Big(C^{IU}(\tilde{\omega}^{UI/U}r^{AH/U} + \dot{r}^{AH/U}) + v^{HI/I}\Big) - C^{DU}v^{W/U} \\ &= C^{DU}(v^{HI/U} + \dot{r}^{AH/U} + \tilde{\omega}^{UI/U}r^{AH/U} - v^{W/U})\end{aligned} \tag{2.66}$$

The section angle of attack, sideslip angle, and Mach number can then be calculated as follows:

$$v_{2D} = \sqrt{(v_y^{AI/D})^2 + (v_z^{AI/D})^2} \tag{2.67}$$

$$\alpha = \tan^{-1}\left(-\frac{v_z^{AI/D}}{v_y^{AI/D}}\right) \tag{2.68}$$

$$\beta = \tan^{-1}\left(\frac{v_x^{AI/D}}{v_{2D}}\right) \tag{2.69}$$

$$M = \frac{v_{2D}}{a} \tag{2.70}$$

Where a is the speed of sound. The terms on the right-hand side of Eq. 2.66 are given below. The first three terms pertain the blade velocity and the last term ($v^{W/U}$) pertains the wind velocity. The first term ($v^{HI/U}$) is obtained by rotating the velocity of the hub from the nonrotating hub frame H to the blade undeformed frame U as follows:

$$v^{HI/U} = C^{UH} v^{HI/H} \tag{2.71}$$

Position of the section three quarter-chord A with respect to the nonrotating hub frame H measured along the axes of the blade undeformed frame U and its first time derivative are calculated as in Eqs. 2.54 to 2.55, only replacing e_{cg} by e_{tqc}:

$$r^{AH/U} = \begin{Bmatrix} x_{ea} + u \\ y_{ea} + v \\ z_{ea} + w \end{Bmatrix} + C^{UD} \begin{Bmatrix} 0 \\ e_{tqc} \\ 0 \end{Bmatrix} \tag{2.72}$$

$$\dot{r}^{AH/U} = \begin{Bmatrix} \dot{u} \\ \dot{v} \\ \dot{w} \end{Bmatrix} + \dot{C}^{UD} \begin{Bmatrix} 0 \\ e_{tqc} \\ 0 \end{Bmatrix} \tag{2.73}$$

Where e_{tqc} is the three quarter-chord position with respect to the elastic axis in the blade deformed frame D (positive toward leading edge). The angular velocity term ($\omega^{UI/U}$) in Eq. 2.66 has already been calculated in Eq. 2.57. The wind velocity ($v^{W/U}$) has contribution from the freestream and the induced flow:

$$v^{W/U} = C^{UH} C^{HW} C^{WI} v^{W/I} - C^{UH} \begin{Bmatrix} \lambda_{ix} \\ \lambda_{iy} \\ \lambda_{iz} \end{Bmatrix} \Omega R \tag{2.74}$$

Where $v^{W/I}$ is an input to the analysis and λ_i is the induced flow, which is calculated with the appropriate model. Typically, λ_{ix} and λ_{iy} are small compared to λ_{iz}.

2.7.2 Unsteady Thin Airfoil Theory

Unsteady thin airfoil theory models the effect of shed vortices due to pitching and plunging motion of the blade. The lift and the pitching moment are comprised of circulatory and noncirculatory terms. Equations for lift, drag, and pitching moment (acting on the elastic axis, which is assumed to coincide with the pitch axis) are given below.

$$L_1 = C\frac{1}{2}\rho(v_{2D})^2 cC_l(\alpha, M) \tag{2.75}$$

$$L_2 = -\pi\left(\frac{c}{2}\right)^2 \rho a_z^{MI/D} \tag{2.76}$$

$$L_3 = \pi\left(\frac{c}{2}\right)^2 \rho v_{2D}\omega_x^{DI/D} \tag{2.77}$$

$$D = \frac{1}{2}\rho(v_{2D})^2 cC_d(\alpha, M) \tag{2.78}$$

$$M = CL_1\left(a_h b + \frac{c}{4}\right) + L_2(a_h b) + L_3\left(a_h b - \frac{c}{4}\right) + \frac{1}{2}\rho(v_{2D})^2 c^2 C_m(\alpha, M) + M_{NC} \tag{2.79}$$

Where L_1 is circulatory lift, L_2 and L_3 are noncirculatory lift, ρ is density, c is chord, C is lift deficiency function, C_l is the lift coefficient, C_d is the drag coefficient, C_m is the moment coefficient, $a_z^{MI/D}$ is the acceleration at the mid-point with respect to the inertial frame I measured along the axes of the blade deformed frame D, M_{NC} is the noncirculatory pitching moment, and $a_h b$ is the position of the mid-chord with respect to the pitch axis (positive toward leading edge). Note that L_3 is the only source of torsion damping. Equation for the noncirculatory pitching moment is given below.

$$M_{NC} = -\frac{\pi\left(\frac{c}{2}\right)^4}{8}\rho\dot{\omega}_x^{DI/D} \tag{2.80}$$

The lift deficiency function is calculated using Robert Loewy's theory of returning wake (valid only for axial flight):

$$|C| = \frac{1}{1 + \frac{\pi}{4}\frac{\sigma}{\lambda}} \tag{2.81}$$

Where σ is the local solidity and λ is the inflow ratio. They are calculated as follows:

$$\sigma = \frac{N_b c}{\pi R} \tag{2.82}$$

$$\lambda = -\frac{v_z^{W/H}}{\Omega R} \tag{2.83}$$

The term $a_h b$ is calculated as follows:

$$a_h b = e_{tqc} + \frac{c}{4} \tag{2.84}$$

The term $a_z^{MI/D}$ is calculated as explained in Chapter 2.6.1, replacing e_{cg} by $a_h b$ in Eqs. 2.54 to 2.56. After that, a rotation from the blade undeformed frame U to the blade deformed frame D is applied. The terms $\omega_x^{DI/D}$ and $\dot{\omega}_x^{DI/D}$ have already been calculated in Eqs. 2.60 and 2.61.

The total lift is a summation of circulatory and noncirculatory terms:

$$L = L_1 + L_2 + L_3 \tag{2.85}$$

Lift and drag are in the wind frame. They are rotated to the blade deformed frame D as follows:

$$f_x^{D/D} = -D \tan \beta \tag{2.86}$$

$$f_y^{D/D} = L \sin \alpha - D \cos \alpha \tag{2.87}$$

$$f_z^{D/D} = L \cos \alpha + D \sin \alpha \tag{2.88}$$

$$m_x^{D/D} = M \tag{2.89}$$

Finally, the forces and pitching moment in the blade deformed frame D are rotated to the blade undeformed frame U:

$$
\begin{aligned}
f^{U/U} &= f^{D/U} = C^{UD} f^{D/D} \\
m^{U/U} &= m^{D/U} = C^{UD} m^{D/D}
\end{aligned}
\tag{2.90}
$$

2.7.3 Radial Flow Corrections

The boundary layer is affected due to radial flow, which is not included in the 2D airfoil tables. The change in the boundary layer can be significant at high advance ratio and for high blade sweep angles. Stall is delayed and drag is increased. The equations for radial flow corrections are given below. A detailed derivation is given in Ref. [77].

$$
\begin{aligned}
C_l &= \frac{1}{\cos^2\beta} C_l(\alpha \cos^2\beta, M) \\
C_d &= \frac{1}{\cos\beta} C_d(\alpha \cos\beta, M) \\
C_m &= \frac{1}{\cos^2\beta} C_m(\alpha \cos^2\beta, M)
\end{aligned}
\tag{2.91}
$$

2.7.4 Reverse Flow

Reverse flow may have a significant impact on blade aerodynamics at high-speed edgewise flight. It can be neglected up to an advance ratio of 0.5 (Ref. [77]). Modeling of reverse flow is not required for this work as the tiltrotor aircraft typically do not fly at high advance ratios; however, its effects are included due to the comprehensive nature of the developed solver.

Reverse flow check is performed on the section angle of attack; if the absolute value of the angle of attack is greater than $90°$, the section experiences reverse flow. It is taken into account by swapping the quarter-chord and three quarter-chord locations. Equation 2.91 is also modified as follows:

$$
\begin{aligned}
C_l &= \frac{1}{\cos^2\beta} C_l\Big(\big[(|\alpha| - \pi)\cos^2\beta + \pi\big]\,\mathbf{sign}(\alpha), M\Big) \\
C_d &= \frac{1}{\cos\beta} C_d\Big(\big[(|\alpha| - \pi)\cos\beta + \pi\big]\,\mathbf{sign}(\alpha), M\Big) \\
C_m &= \frac{1}{\cos^2\beta} C_m\Big(\big[(|\alpha| - \pi)\cos^2\beta + \pi\big]\,\mathbf{sign}(\alpha), M\Big)
\end{aligned}
\tag{2.92}
$$

2.7.5 Freewake Model

The primary elements of the freewake model is the vortex convection equation and the core-growth model. The vortex convection equation is given below. The equation is discretized using the Predictor-Corrector Second-Order Backward (PC2B) scheme (Refs. [80, 81]).

$$
\frac{\partial r}{\partial t} + \frac{\partial r}{\partial t_\phi} = v \tag{2.93}
$$

Where r is vortex position, t is time, t_ϕ is vortex age, and v is the fluid velocity at the vortex center. The core-growth model uses the following equation to model the viscous diffusion of vorticity:

$$
r_c^2 = r_{c0}^2 + 4(1.2564)(\nu + \nu_t)t_\phi \tag{2.94}
$$

Where r_c is the current core radius, r_{c0} is the initial core radius, ν is kinematic viscosity, and ν_t is additional viscosity due to turbulence in the vortex core. Squire (Ref. [82]) showed that ν_t can be approximated as follows:

$$\nu_t = a_1 \Gamma \tag{2.95}$$

Where Γ is the vortex strength and a_1 is a proportionality constant, which is an input to the analysis. Vatistas approximation of Lamb-Oseen model (Ref. [83]) is used for the vortex core. The equation for the resulting vortex velocity profile is as follows:

$$v = \frac{\Gamma}{2\pi r_v} \frac{r_v^2}{(r_v^{2n} + r_c^{2n})^{1/n}} \tag{2.96}$$

Where r_v is the distance from the center of the vortex. The induced flow at a point due to the vortex is calculated using Biot-Savart Law ($n = 1$ for Scully):

$$\begin{aligned} v &= \frac{\Gamma}{4\pi} l \cdot \left(\frac{r_1}{|r_1|} - \frac{r_2}{|r_2|} \right) \frac{r_1 \times r_2}{|l|^2 (h^2 + r_c^2)} \\ h &= \frac{|r_1 \times r_2|}{|l|} \end{aligned} \tag{2.97}$$

Where r_1 and r_2 are vectors from the vortex start and end points to the point where the induced velocity is to be calculated and l is a vector from vortex start to end point as shown in Fig. 2.3.

2.7.6 Nearwake Model

A nonlinear nearwake model is used. The nearwake model includes all the trailing vortices, but they are assumed to not interact with each other to save computation time. A rigid vortex geometry shown in Fig. 2.4 is formed (convected only due to freestream) to span a set azimuth until vortices are assumed to roll up to a single tip vortex.

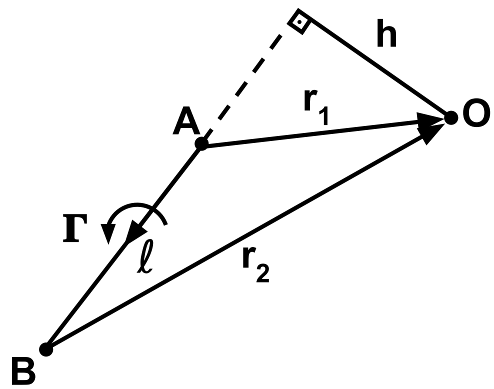

Figure 2.3: Induced velocity of vortex filament A-B at point O

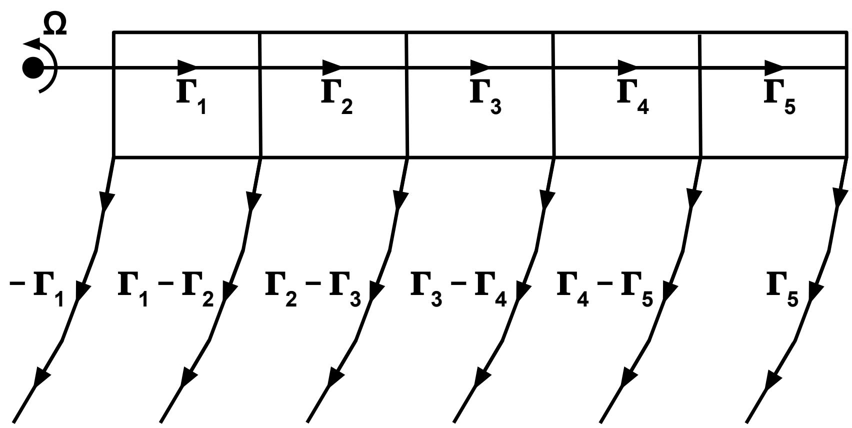

Figure 2.4: Nearwake geometry

First, bound circulation on each aerodynamic panel is calculated:

$$\Gamma = \frac{1}{2} v_{2D} c C_l(\alpha, M) \tag{2.98}$$

The vortices are trailed at each node. The trailed vortex strength is calculated from the bound circulation of the adjacent aerodynamic panels:

$$\Gamma_t = \Gamma_i - \Gamma_{i+1} \tag{2.99}$$

The induced flow due to the vortices on the blade is calculated using Eq. 2.97. After finding the induced flow, the new bound circulation distribution along the blade is calculated. This procedure is repeated until convergence is achieved.

2.8 Sectional Loads

Sectional loads can be calculated with two methods: force summation and deformation. For a converged solution with sufficient number of modes and spatial elements, the two methods result in identical loads, unless discontinuities in structural properties or airloads are present.

2.8.1 Loads by Force Summation

Force summation method integrates the loads from the tip to the section of interest. The equations for the undeformed frame loads are given below. Capital letters denote the integrated loads and small letters denote aerodynamic or inertial loads per span.

$$F_x(r) = \int_r^R f_x d\rho \tag{2.100}$$

$$F_y(r) = \int_r^R f_y d\rho \tag{2.101}$$

$$F_z(r) = \int_r^R f_z d\rho \tag{2.102}$$

$$M_x(r) = \int_r^R \Big(m_x + f_z \big[v - v(r) + y_{ea} - y_{ea}(r) \big] - f_y \big[w - w(r) + z_{ea} - z_{ea}(r) \big] \Big) d\rho \tag{2.103}$$

$$M_y(r) = \int_r^R \Big(m_y - f_z \big[x_{ea} - x_{ea}(r) \big] + f_x \big[w - w(r) + z_{ea} - z_{ea}(r) \big] \Big) d\rho \tag{2.104}$$

$$M_z(r) = \int_r^R \Big(m_z + f_y \big[x_{ea} - x_{ea}(r) \big] - f_x \big[v - v(r) + y_{ea} - y_{ea}(r) \big] \Big) d\rho \tag{2.105}$$

These loads can then be rotated to the deformed frame as follows:

$$\begin{aligned} F^D &= C^{DU} F^U \\ M^D &= C^{DU} M^U \end{aligned} \tag{2.106}$$

2.8.2 Loads by Deformation

The deformation method calculates the loads by integrating the stresses over the cross-section area. The equations for the loads in the deformed frame are given below.

$$\begin{aligned} F_\xi =& \iint_A \sigma_{\xi\xi} d\eta d\zeta \\ =& \iint_A E\epsilon_{\xi\xi} d\eta d\zeta \\ =& \iint_A E\Big[u_e' - \cancelto{0}{\lambda_T}(\hat{\phi}'' + w'v''' + w''v'') \\ & \qquad + (\eta^2+\zeta^2)\Big(\theta_0'\hat{\phi}' + \theta_0' w'v'' + \frac{\hat{\phi}'^2}{2} + \cancelto{\epsilon^4}{\frac{w'^2 v''^2}{2}} + \cancelto{\epsilon^3}{\hat{\phi}'w'v''}\Big) \\ & \qquad - v''(\eta\cos\theta - \cancelto{0}{\zeta}\sin\theta) - w''(\eta\sin\theta + \cancelto{0}{\zeta}\cos\theta)\Big] d\eta d\zeta \\ =& EAu_e' + EAK_A^2\Big(\theta_0'\hat{\phi}' + \theta_0' w'v'' + \frac{\hat{\phi}'^2}{2}\Big)\Big] \\ & - EAe_A\Big[v''\cos(\theta_0+\hat{\phi}) + w''\sin(\theta_0+\hat{\phi})\Big] \end{aligned} \tag{2.107}$$

$$
\begin{aligned}
M_\xi =& \iint_A \Big[\eta\sigma_{\xi\zeta} - \zeta\sigma_{\xi\eta} + \lambda_T\Big(\frac{\partial\sigma_{\xi\eta}}{\partial\eta} + \frac{\partial\sigma_{\xi\zeta}}{\partial\zeta}\Big)\Big] d\eta d\zeta + \frac{\partial}{\partial x}\iint_A \lambda_T\sigma_{\xi\xi} d\eta d\zeta \\
&+ (\theta_0' + \hat{\phi}') \iint_A (\eta^2+\zeta^2)\sigma_{\xi\xi} d\eta d\zeta \\
=& \iint_A G\Big[\eta\epsilon_{\xi\zeta} - \zeta\epsilon_{\xi\eta} + \lambda_T\Big(\frac{\partial\epsilon_{\xi\eta}}{\partial\eta} + \frac{\partial\epsilon_{\xi\zeta}}{\partial\zeta}\Big)\Big] d\eta d\zeta + \frac{\partial}{\partial x}\iint_A E\lambda_T\epsilon_{\xi\xi} d\eta d\zeta \\
&+ (\theta_0' + \hat{\phi}') \iint_A E(\eta^2+\zeta^2)\epsilon_{\xi\xi} d\eta d\zeta \\
=& \iint_A G\Big[\eta\hat{\eta}(\hat{\phi}' + w'v'') + \zeta\hat{\zeta}(\hat{\phi}' + w'v'') - \lambda_T\phi'\Big(\frac{\partial^2\lambda_T}{\partial\eta^2} + \frac{\partial^2\lambda_T}{\partial\zeta^2}\Big)\Big] d\eta d\zeta \\
&+ \frac{\partial}{\partial x}\iint_A E\lambda_T\Big[\cancelto{0}{u_e'} - \lambda_T(\hat{\phi}'' + \cancelto{\epsilon^4}{w'v'''} + \cancelto{\epsilon^4}{w''v''}) \\
&\qquad + \cancelto{0}{(\eta^2+\zeta^2)}\Big(\theta_0'\hat{\phi}' + \theta_0'w'v'' + \frac{\hat{\phi}'^2}{2} + \frac{w'^2v''^2}{2} + \hat{\phi}'w'v''\Big) \\
&\qquad - v''(\cancelto{0}{\eta}\cos\theta - \zeta\sin\theta) - w''(\cancelto{0}{\eta}\sin\theta_0 + \zeta\cos\theta)\Big] d\eta d\zeta \\
&+ \iint_A \Bigg(E(\eta^2+\zeta^2)\theta_0'\Big[u_e' - \cancelto{0}{\lambda_T}(\hat{\phi}'' + w'v''' + w''v'') \\
&\qquad + (\eta^2+\zeta^2)\Big(\theta_0'\hat{\phi}' + \theta_0'w'v'' + \cancelto{\epsilon^4}{\frac{\hat{\phi}'^2}{2}} + \cancelto{\epsilon^6}{\frac{w'^2v''^2}{2}} + \cancelto{\epsilon^5}{\hat{\phi}'w'v''}\Big) \\
&\qquad - v''(\eta\cos\theta - \cancelto{0}{\zeta}\sin\theta) - w''(\eta\sin\theta + \cancelto{0}{\zeta}\cos\theta)\Big] \\
&\quad + E(\eta^2+\zeta^2)\hat{\phi}'\Big[u_e' - \cancelto{0}{\lambda_T}(\hat{\phi}'' + w'v''' + w''v'') \\
&\qquad + \cancelto{\epsilon^3}{(\eta^2+\zeta^2)}\Big(\theta_0'\hat{\phi}' + \theta_0'w'v'' + \frac{\hat{\phi}'^2}{2} + \frac{w'^2v''^2}{2} + \hat{\phi}'w'v''\Big) \\
&\qquad - v''(\cancelto{\epsilon^3}{\eta}\cos\theta - \cancelto{0}{\zeta}\sin\theta) - w''(\cancelto{\epsilon^3}{\eta}\sin\theta + \cancelto{0}{\zeta}\cos\theta)\Big]\Bigg) d\eta d\zeta \\
=& GJ(\hat{\phi}' + w'v'') + \frac{\partial}{\partial x}\Big[-EC_1\hat{\phi}'' + EC_2\big(v''\sin(\theta_0+\hat{\phi}) - w''\cos(\theta_0+\hat{\phi})\big)\Big] \\
&+ EAK_A^2(\theta_0' + \hat{\phi}')u_e' + EB_1\theta_0'^2(\hat{\phi}' + w'v'') \\
&- EB_2\theta_0'\big(v''\cos(\theta_0+\hat{\phi}) + w''\sin(\theta_0+\hat{\phi})\big)
\end{aligned}
\tag{2.108}
$$

$$
\begin{aligned}
M_\eta &= \iint_A \zeta \sigma_{\xi\xi}\, d\eta d\zeta \\
&= \iint_A \zeta E \epsilon_{\xi\xi}\, d\eta d\zeta \\
&= \iint_A \zeta E \Big[\cancelto{0}{u'_e} - \lambda_T(\hat{\phi}'' + \cancelto{\epsilon^3}{w'v'''} + \cancelto{\epsilon^3}{w''v''}) \\
&\qquad + \cancelto{0}{(\eta^2+\zeta^2)}\Big(\theta'_0\hat{\phi}' + \theta'_0 w'v'' + \frac{\hat{\phi}'^2}{2} + \frac{w'^2v''^2}{2} + \hat{\phi}'w'v''\Big) \\
&\qquad - v''(\cancelto{0}{\eta}\cos\theta - \zeta\sin\theta) - w''(\cancelto{0}{\eta}\sin\theta + \zeta\cos\theta)\Big] d\eta d\zeta \\
&= -EC_2\hat{\phi}'' + EI_n\big(v''\sin(\theta_0+\hat{\phi}) - w''\cos(\theta_0+\hat{\phi})\big)
\end{aligned} \tag{2.109}
$$

$$
\begin{aligned}
M_\zeta &= -\iint_A \eta \sigma_{\xi\xi}\, d\eta d\zeta \\
&= -\iint_A \eta E \epsilon_{\xi\xi}\, d\eta d\zeta \\
&= -\iint_A \eta E \Big[u'_e - \cancelto{0}{\lambda_T}(\hat{\phi}'' + w'v''' + w''v'') \\
&\qquad + (\eta^2+\zeta^2)\Big(\theta'_0\hat{\phi}' + \cancelto{\epsilon^3}{\theta'_0 w'v''} + \cancelto{\epsilon^3}{\frac{\hat{\phi}'^2}{2}} + \cancelto{\epsilon^5}{\frac{w'^2v''^2}{2}} + \cancelto{\epsilon^4}{\hat{\phi}'w'v''}\Big) \\
&\qquad - v''(\eta\cos\theta - \cancelto{0}{\zeta}\sin\theta) - w''(\eta\sin\theta + \cancelto{0}{\zeta}\cos\theta)\Big] d\eta d\zeta \\
&= -EAe_A u'_e - EB_2\theta'_0\hat{\phi}' + EI_c\big(v''\cos(\theta_0+\hat{\phi}) + w''\sin(\theta_0+\hat{\phi})\big)
\end{aligned} \tag{2.110}
$$

2.9 Hub Loads

Hub loads excite the wing/pylon. They are calculated by first integrating the inertial and aerodynamic loads in the undeformed frame to the hub for each blade as shown below.

$$F_x^{H/U} = \int_0^R f_x d\rho \tag{2.111}$$

$$F_y^{H/U} = \int_0^R f_y d\rho \tag{2.112}$$

$$F_z^{H/U} = \int_0^R f_z d\rho \tag{2.113}$$

$$M_x^{H/U} = \int_0^R \Big[m_x + f_z(v + y_{ea}) - f_y(w + z_{ea}) \Big] d\rho \tag{2.114}$$

$$M_y^{H/U} = \int_0^R \Big[m_y - f_z x_{ea} + f_x(w + z_{ea}) \Big] d\rho \tag{2.115}$$

$$M_z^{H/U} = \int_0^R \Big[m_z + f_y x_{ea} - f_x(v + y_{ea}) \Big] d\rho \tag{2.116}$$

The hub loads in the nonrotating hub frame H can then be calculated by rotating from the blade undeformed frame U and summing for all the blades.

$$\begin{aligned} F^{H/H} &= \sum_{m=1}^{N_b} C_m^{HR} C^{RU} F_m^{H/U} \\ M^{H/H} &= \sum_{m=1}^{N_b} C_m^{HR} C^{RU} M_m^{H/U} \end{aligned} \tag{2.117}$$

2.10 Advanced Geometry Blades

Advanced geometry blades are modeled by introducing an intermediate frame between undeformed and deformed frames: element undeformed frame E. This frame rotates the blade undeformed frame U by the control angle, sweep, anhedral, and pretwist. The direction cosine matrix C^{EU} is given below. Here Λ_1 is pretwist, Λ_2 is anhedral, Λ_3 is sweep, and θ_c is the control angle. Note that the control angle is not taken into account in C^{DU} (now C^{DE}) anymore. Element undeformed frame E is attached to the inboard boundary of the element. The change in the pretwist angle between any point on the element and the inboard boundary is included in the C^{DU} calculation. Each element is still straight, so the same strain-displacement equations are applicable.

$$C^{EU} = \begin{bmatrix} 1 & 0 & 0 \\ 0 & \mathrm{c}\Lambda_1 & \mathrm{s}\Lambda_1 \\ 0 & -\mathrm{s}\Lambda_1 & \mathrm{c}\Lambda_1 \end{bmatrix} \begin{bmatrix} \mathrm{c}\Lambda_2 & 0 & -\mathrm{s}\Lambda_2 \\ 0 & 1 & 0 \\ \mathrm{s}\Lambda_2 & 0 & \mathrm{c}\Lambda_2 \end{bmatrix} \begin{bmatrix} \mathrm{c}\Lambda_3 & \mathrm{s}\Lambda_3 & 0 \\ -\mathrm{s}\Lambda_3 & \mathrm{c}\Lambda_3 & 0 \\ 0 & 0 & 1 \end{bmatrix} \begin{bmatrix} 1 & 0 & 0 \\ 0 & \mathrm{c}\theta_c & \mathrm{s}\theta_c \\ 0 & -\mathrm{s}\theta_c & \mathrm{c}\theta_c \end{bmatrix} \quad (2.118)$$

The quantities for the elastic axis positions in Eqs. 2.54 and 2.72 also change. They can be calculated for element j element for a simple case with zero torque offset and underslung as follows:

$$r_{ea} = \begin{Bmatrix} x_{ea} \\ y_{ea} \\ z_{ea} \end{Bmatrix} = \begin{Bmatrix} s \\ 0 \\ 0 \end{Bmatrix} + \sum_{i=1}^{j-1} C^{ji} \begin{Bmatrix} d_i \\ 0 \\ 0 \end{Bmatrix} \quad (2.119)$$

Where s is the distance from the inboard node of the element, d is the total element length, and C^{ji} relates the element undeformed frame E of the i^{th} element to that of j^{th} element as shown in Eq. 2.120. The final change is in the inter-element compatibility equations, which use C^{ji} for the assembly of the element matrices/forcing vector into the global matrices/forcing vector.

$$C^{ji} = C_j^{EU} C_i^{EU\top} \quad (2.120)$$

2.11 Finite Element Discretization

Finite Element discretization is used to obtain the governing equations of motion. Each beam is represented by 15 degrees of freedom. Flap and lag degrees of freedom are represented by displacements and rotations at the boundaries and they use third-order Hermite polynomials as shape functions (for continuity of displacement and slope). Axial and torsion degrees of freedom are represented by both boundary and internal degrees of freedom as shown in Fig. 2.5 and they use third- and second-order Lagrange polynomials, respectively (for continuity of displacement). The shape functions are given below. Linear variation of bending and torsion moments and quadratic variation of axial force within an element is ensured.

$$\begin{Bmatrix} u_e(x) \\ v(x) \\ w(x) \\ \hat{\phi}(x) \end{Bmatrix} = \begin{bmatrix} H_{u_e}^\top & 0 & 0 & 0 \\ 0 & H_v^\top & 0 & 0 \\ 0 & 0 & H_w^\top & 0 \\ 0 & 0 & 0 & H_{\hat{\phi}}^\top \end{bmatrix} q \tag{2.121}$$

$$H_{u_e} = \begin{Bmatrix} -4.5x^3 + 9x^2 - 5.5x + 1 \\ 13.5x^3 - 22.5x^2 + 9x \\ -13.5x^3 + 18x^2 - 4.5x \\ 4.5x^3 - 4.5x^2 + x \end{Bmatrix} \tag{2.122}$$

$$H_v = H_w = \begin{Bmatrix} 2x^3 - 3x^2 + 1 \\ (x^3 - 2x^2 + x)d \\ -2x^3 + 3x^2 \\ (x^3 - x^2)d \end{Bmatrix} \tag{2.123}$$

$$H_p = \begin{Bmatrix} 2x^2 - 3x + 1 \\ -4x^2 + 4x \\ 2x^2 - x \end{Bmatrix} \tag{2.124}$$

Where x is the nondimensional spanwise coordinate within the element ($0 \leq x \leq 1$), d is the element length, and q is an array of finite element degrees of freedom as shown below.

$$q = [u_{e1}, u_{e2}, u_{e3}, u_{e4}, v_1, v_1', v_2, v_2', w_1, w_1', w_2, w_2', \hat{\phi}_1, \hat{\phi}_2, \hat{\phi}_3]^\top \tag{2.125}$$

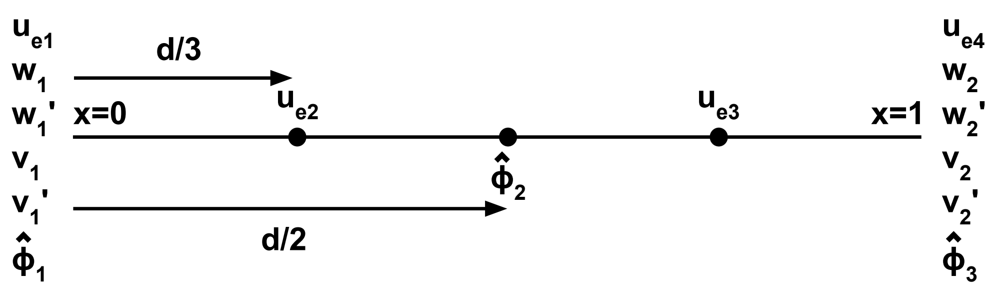

Figure 2.5: Finite element degrees of freedom

Rewriting Equation 2.8,

$$\int_{t_1}^{t_2} \delta(U - T - W) = 0 \tag{2.126}$$

The variation in kinetic energy is numerically calculated as virtual work by the inertial loads. Hence, Eq. 2.126 is modified as follows:

$$\int_{t_1}^{t_2} \delta(U - W_i - W_a) = 0 \tag{2.127}$$

Where W_i and W_a are virtual work done by inertial and aerodynamic loads. Using the shape functions, Eq. 2.127 is written in terms of the finite element degrees of freedom as follows:

$$\int_{t_1}^{t_2} \delta\Big(\frac{1}{2}q^\top K q - q^\top (Q_i + Q_a)\Big) dt = 0 \tag{2.128}$$

$$\int_{t_1}^{t_2} \delta q^\top (Kq - Q_i - Q_a) dt = 0 \tag{2.129}$$

$$Kq = Q_i + Q_a \tag{2.130}$$

The next section explains how mass, damping, and stiffness matrices can be extracted from the Q_i and Q_a terms, which will turn Eq 2.130 into the following form:

$$M\ddot{q} + C\dot{q} + Kq = Q \tag{2.131}$$

2.12 Numerical Extraction of Matrices

Numerical perturbation is used to extract the aerodynamic and inertial matrices. The principal source of damping for the blade motions is aerodynamics; hence the extraction of aerodynamic damping is essential for trim and stability solutions. The inertial terms are also important due to Coriolis coupling. This approach does not make any small-term assumptions and retains all the nonlinear terms. For illustration of the method, consider the virtual work of only the flapping degree of freedom as follows:

$$\delta W = \int_0^R \delta w f dr \tag{2.132}$$

Where $f(w, \dot{w}, \ddot{w}, w', \dot{w}', \ddot{w}')$ is the vertical force per span and includes both aerodynamic and inertial forces. The task then is to linearize f about deflection, slope, and corresponding velocity and accelerations. It is an easy task if the analytical form is known, but intractable with the addition of many types of motions as the model complexity increases. For numerical extraction, expand as Taylor Series considering only $f(\dot{w})$ for the sake of illustration:

$$f^{n+1} \simeq f^n + \left.\frac{\partial f}{\partial \dot{w}}\right|_n (\dot{w}^{n+1} - \dot{w}^n) \tag{2.133}$$

Where n is the given state and $n+1$ is the new state to be solved for. First, the deflections are perturbed to calculate the partial derivative as follows:

$$\dot{w}_2^n = \dot{w}_1^n + \delta\dot{w} \tag{2.134}$$

Where $\dot{w}_1^n$ is the quantity before perturbation, $\dot{w}_2^n$ is after perturbation, and $\delta\dot{w}$ is a small perturbation. Typically, $0.01R$ and $0.01\ \mathrm{rad}$ perturbation is sufficient for displacements and rotations, respectively. The partial derivative is then obtained numerically with finite difference approximation about the given state as shown below.

$$\left.\frac{\partial f}{\partial \dot{w}}\right|_n = \frac{f(\dot{w}_2^n) - f(\dot{w}_1^n)}{\dot{w}_2^n - \dot{w}_1^n} \tag{2.135}$$

These calculations are carried out for each element. The element damping matrix and forcing vector due to these terms are obtained as follows:

$$\begin{aligned}
C &= -\int_0^d H_w \frac{\partial f}{\partial \dot{w}}\bigg|_n H_w^\top dr \\
Q &= \int_0^d H_w \Big(f^n - \frac{\partial f}{\partial \dot{w}}\bigg|_n \dot{w}^n \Big) dr
\end{aligned} \tag{2.136}$$

This process is repeated for w, $\ddot{w}$, w', $\dot{w}'$, $\ddot{w}'$, etc. for all the degrees of freedom. The forcing f is calculated exactly and numerically, without the need for an analytical expression.

2.13 Fixed–Rotating Interface

The aerodynamic and inertial forces on the blade depend on the wing motions. Consider Eq. 2.133 again, but now suppose the wing torsion ($\hat{\phi}_w$) affects the forcing.

$$f^{n+1} \simeq f^n + \frac{\partial f}{\partial \dot{w}}\bigg|_n (\dot{w}^{n+1} - \dot{w}^n) + \frac{\partial f}{\partial \dot{\hat{\phi}}_w}\bigg|_n (\dot{\hat{\phi}}_w^{n+1} - \dot{\hat{\phi}}_w^n) \tag{2.137}$$

For this example, only damping coupling is present between the rotor flap and wing torsion motions. The coupling matrix is calculated as follows:

$$C_{rw} = -\int_0^d H_w \frac{\partial f}{\partial \dot{\hat{\phi}}} H_{\hat{\phi}}^\top \tag{2.138}$$

Where $H_{\hat{\phi}}$ is the wing shape function for torsion evaluated at the hub. Similarly, the forces on the wing depend on the blade motions as well as the wing motions. These motions change the aerodynamic and inertial loading on the blade and excites the wing through the hub loads.

Wing forcing due to blade motion perturbation results in M_{wr}, C_{wr}, and K_{wr}. Wing forcing due to wing perturbation gives M_{ww}, C_{ww}, and K_{ww}. These are added to the mass, damping, and stiffness matrices of an isolated wing.

The solver can use two methods to model the fixed structure and couple it with the rotor: direct finite element modeling and modal input methods. In the direct finite element approach, the fixed structure is modeled in the solver itself. This is a relatively simple task as the wing admits the same type of inputs as the rotor, only with zero rotation speed. Beams can be assembled in any way to model the fixed structure. In the modal input approach, the fixed structure is modeled in an external finite element code such as NASTRAN and the natural frequencies and mode shapes at the rotor hub are extracted. This is a case of practical importance since wing finite element groups are separate from rotor's in the industry. It also enables rapid evaluation of existing/legacy wings on which rotors are perhaps to be installed. The frequency and mode shape values are used as inputs to the solver which couples the wing with the rotor. This method may result in a more accurate model if the fixed structure is complicated and cannot be accurately modeled with beam elements; however, it includes an extra step with an external solver. The modal method is briefly explained below.

Consider the isolated wing system without damping for simplicity:

$$M\ddot{q} + Kq = Q \tag{2.139}$$

The degrees of freedom can be converted to modal space as follows:

$$q = P\eta \tag{2.140}$$

Where P is a matrix composed of eigenvectors and η is the modal coordinate. Substituting into Eq. 2.139 and premultiplying by $P^{\top}$,

$$P^\top MP\ddot{\eta} + P^\top KP\eta = P^\top Q \tag{2.141}$$

$$\bar{M}\ddot{\eta} + \bar{K}\eta = \bar{Q} \tag{2.142}$$

Eigenvectors are typically mass-normalized; mass matrix is a unit matrix and stiffness matrix is comprised of diagonal elements of squares of the natural frequencies:

$$\bar{M} = \begin{bmatrix} 1 & 0 & 0 \\ 0 & 1 & 0 \\ 0 & 0 & 1 \end{bmatrix} \qquad \bar{K} = \begin{bmatrix} \omega_1^2 & 0 & 0 \\ 0 & \omega_2^2 & 0 \\ 0 & 0 & \omega_3^2 \end{bmatrix} \tag{2.143}$$

The eigenvalues and eigenvectors only modal the isolated wing. The wing mass, damping, and stiffness matrices (M_{ww}, C_{ww}, and K_{ww}) due to rotor hub loads (all calculated with the perturbation method explained before) are added to above matrices after pre and postmultiplied by the wing eigenvectors. The coupling matrices are pre and postmultiplied by the rotor and wing eigenvectors. After solution of the equations of motion, the motion at the hub can be calculated using Eq. 2.140. Eigenvector outputs at more span stations is necessary to account for wing aerodynamics, which can be important for high-speed stability. Assuming SI system, the units for the mass-normalized eigenvectors are shown below. Here P_0 is the eigenvector matrix before mass-normalization and P is the matrix after.

$$\begin{aligned} P = \frac{P_0}{\sqrt{P_0^\top MP_0}} &: \frac{\mathrm{m}}{\sqrt{\mathrm{kg\,m^2}}} = \frac{\mathrm{m}}{\sqrt{\mathrm{N\,s^2\,m}}} \quad \text{(for translation)} \\ &: \frac{\mathrm{rad}}{\sqrt{\mathrm{kg\,m^2}}} = \frac{\mathrm{rad}}{\sqrt{\mathrm{N\,s^2\,m}}} \quad \text{(for rotation)} \end{aligned} \tag{2.144}$$

2.14 Joints

Joints are needed to model complicated root structures, hinges, bearings, and dampers, which do not have strains but provide constraints and allow large rotations between flexible parts. Joints can also be used for actuation of the pitch bearing to model the pilot control inputs. Figure 2.6 shows a schematic of two finite elements connected through a joint between them. Only planar motions and small angles are considered for illustration.

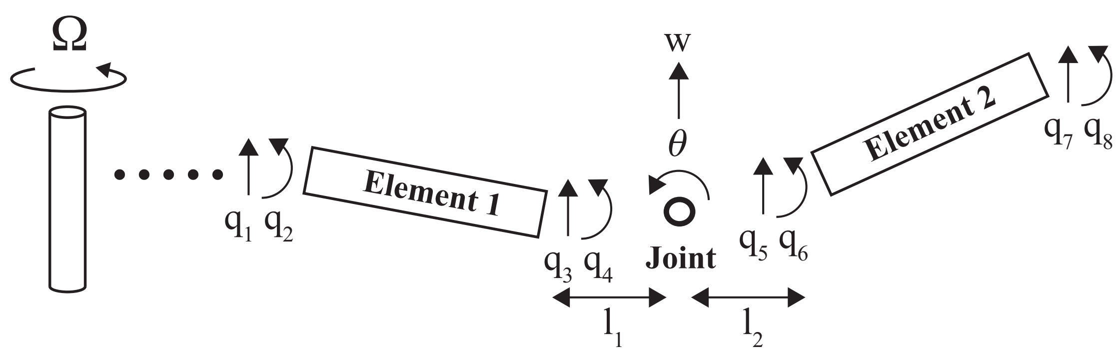

Figure 2.6: Joint schematic

The inter-element compatibility from element 1 to 2 are given as follows:

$$\begin{aligned} q_5 &= q_3 + l_1 \sin(q_4) + l_2 \sin(q_4 + \theta) + w \cos(q_4) \\ q_6 &= q_4 + \theta \end{aligned} \tag{2.145}$$

Where l_1 and l_2 are distances from elements 1 and 2. For sake of simplicity, consider $l_1 = l_2 = 0$ and a small q_4. Equation 2.145 then becomes:

$$\begin{aligned} q_5 &= q_3 + w \\ q_6 &= q_4 + \theta \end{aligned} \tag{2.146}$$

Then, q_5 and q_6 of element 2 can be reduced in terms of q_3, q_4, w, and θ. In matrix form:

$$\begin{Bmatrix} q_5 \\ q_6 \\ q_7 \\ q_8 \end{Bmatrix} = \begin{bmatrix} 1 & 0 & 0 & 0 & 1 & 0 \\ 0 & 1 & 0 & 0 & 0 & 1 \\ 0 & 0 & 1 & 0 & 0 & 0 \\ 0 & 0 & 0 & 1 & 0 & 0 \end{bmatrix} \begin{Bmatrix} q_3 \\ q_4 \\ q_7 \\ q_8 \\ w \\ \theta \end{Bmatrix} = Jq \tag{2.147}$$

Hence, for element 2,

$$w = HJq \tag{2.148}$$

The mass, damping, and stiffness matrices, and the forcing vector for an element that is touched by a joint are therefore modified as follows:

$$\begin{aligned} \hat{M} &= J^\top M J & \hat{C} &= J^\top C J \\ \hat{K} &= J^\top K J & \hat{Q} &= J^\top Q \end{aligned} \tag{2.149}$$

The small joint motion assumption can be easily removed, so the transformation is a nonlinear function of the joint states to be updated by the solution procedure. Equation 2.149 is applied to each element that is touched by a joint. This transformation results in expanded matrices (6×6 instead of 4×4 for flap only) for the joint element as they combine the motion of the joint as well as the motions of the connecting elements. Joints can connect to multiple elements. By using a connectivity matrix, rows and columns of the element matrices are added to the global mass, damping, and stiffness matrices. Hence, if a joint between the elements is locked, it will not be taken into account in the global matrices and the computation time will not increase unnecessarily.

Joint properties can be assigned by adding m, c, and k to the matrix entries for the w and θ degrees of freedom. These represent the mass, damping, and stiffness of the physical bearing. Joint actuation can be introduced by adding kw_{comm} or $k\theta_{comm}$ to the joint forcing where $comm$ is the commanded input. A joint stiffness is needed for commanded motion. A joint force can be introduced directly. Note that the simplification here is that the joint translational displacement is in the undeformed frame; in an actual structure the actuation would be in the deformed frame. This can be added by a simple axis transformation and a subsequent linearization of the nonlinear equations. The joint formulation is valid only to displacement elements with holonomic constraints between them. This is generally an adequate approximation for rotor blades. In summary, the element matrices of an element connected to a joint are modified.

2.15 System Matrices

Using the analytical strain energy terms and linearization of aerodynamic and inertial loads, the mass, damping, and stiffness matrices, and the forcing vector for each element are obtained.

2.15.1 Strain Energy

The equations for the system matrices due to strain energy are given below. The nonlinear terms are linearized with respect to each deflection quantity. The angle θ_0 should be replaced by the angle used to rotate the undeformed frame U to the deformed frame D for advanced geometry blades.

$$K_{u_e u_e} = \int_0^d EAH'_{u_e} H'^{\top}_{u_e} dr \tag{2.150}$$

$$K_{u_e v} = -\int_0^d EAe_A \cos\theta_0 H'_{u_e} H''^{\top}_{v} dr \tag{2.151}$$

$$K_{u_e w} = -\int_0^d EAe_A \sin\theta_0 H'_{u_e} H''^{\top}_{w} dr \tag{2.152}$$

$$K_{u_e \hat{\phi}} = \int_0^d EAK_A^2 \theta'_0 H'_{u_e} H'^{\top}_{\hat{\phi}} dr \tag{2.153}$$

$$K_{v u_e} = -\int_0^d EAe_A \cos\theta_0 H''_{v} H'^{\top}_{u_e} dr = K^{\top}_{u_e v} \tag{2.154}$$

$$K_{vv} = \int_0^d (EI_c \cos^2\theta_0 + EI_n \sin^2\theta_0) H''_{v} H''^{\top}_{v} dr \tag{2.155}$$

$$K_{vw} = \int_0^d (EI_c - EI_n) \sin\theta_0 \cos\theta_0 H''_{v} H''^{\top}_{w} dr \tag{2.156}$$

$$K_{v\hat{\phi}} = -\int_0^d EB_2 \theta'_0 \cos\theta_0 H''_{v} H'^{\top}_{\hat{\phi}} dr - \int_0^d EC_2 \sin\theta_0 H''_{v} H''^{\top}_{\hat{\phi}} dr \tag{2.157}$$

$$K_{w u_e} = -\int_0^d EAe_A \sin\theta_0 H''_{w} H'^{\top}_{u_e} dr = K^{\top}_{u_e w} \tag{2.158}$$

$$K_{wv} = \int_0^d (EI_c - EI_n) \sin\theta_0 \cos\theta_0 H''_{w} H''^{\top}_{v} dr = K^{\top}_{vw} \tag{2.159}$$

$$K_{ww} = \int_0^d (EI_n \cos^2\theta_0 + EI_c \sin^2\theta_0) H''_{w} H''^{\top}_{w} dr \tag{2.160}$$

$$K_{w\hat{\phi}} = -\int_0^d EB_2 \theta'_0 \sin\theta_0 H''_{w} H'^{\top}_{\hat{\phi}} dr + \int_0^d EC_2 \cos\theta_0 H''_{w} H''^{\top}_{\hat{\phi}} dr \tag{2.161}$$

$$K_{\hat{\phi} u_e} = \int_0^d EAK_A^2 \theta'_0 H'_{\hat{\phi}} H'^{\top}_{u_e} dr = K^{\top}_{u_e \hat{\phi}} \tag{2.162}$$

$$K_{\hat{\phi} v} = -\int_0^d EB_2 \theta'_0 \cos\theta_0 H'_{\hat{\phi}} H''^{\top}_{v} dr - \int_0^d EC_2 \sin\theta_0 H''_{\hat{\phi}} H''^{\top}_{v} dr = K^{\top}_{v\hat{\phi}} \tag{2.163}$$

$$K_{\hat{\phi} w} = -\int_0^d EB_2 \theta'_0 \sin\theta_0 H'_{\hat{\phi}} H''^{\top}_{w} dr + \int_0^d EC_2 \cos\theta_0 H''_{\hat{\phi}} H''^{\top}_{w} dr = K^{\top}_{w\hat{\phi}} \tag{2.164}$$

$$K_{\hat{\phi}\hat{\phi}} = \int_0^d (GJ + EB_1 \theta'^2_0) H'_{\hat{\phi}} H'^{\top}_{\hat{\phi}} dr + \int_0^d EC_1 H''_{\hat{\phi}} H''^{\top}_{\hat{\phi}} dr \tag{2.165}$$

$$Q_{u_e} = \int_0^d \Big[- EAK_A^2 \Big(\theta'_0 w' v'' + \frac{\hat{\phi}'^2}{2} \Big) + EAe_A(-v'' \hat{\phi} \sin\theta_0 + w'' \hat{\phi} \cos\theta_0) \Big] H'_{u_e} dr \tag{2.166}$$

$$Q_v = \int_0^d \Big[- EAK_A^2\theta_0' w' u_e' - (GJ + EB_1\theta_0'^2) w'\hat{\phi}' - EAe_A u_e'\hat{\phi}\sin\theta_0 + (EI_c - EI_n)v''\hat{\phi}^2\cos 2\theta_0 + (EI_c - EI_n)v''\hat{\phi}\sin 2\theta_0 + (EI_c - EI_n)w''\hat{\phi}^2\sin 2\theta_0 - (EI_c - EI_n)w''\hat{\phi}\cos 2\theta_0 \Big] H_v'' dr \tag{2.167}$$

$$Q_w = -\int_0^d \Big[EAK_A^2\theta_0' v'' u_e' + (GJ + EB_1\theta_0'^2) v''\hat{\phi}' \Big] H_w' dr + \int_0^d \Big[EAe_A u_e'\hat{\phi}\cos\theta_0 + (EI_c - EI_n)v''\hat{\phi}^2\sin 2\theta_0 - (EI_c - EI_n)v''\hat{\phi}\cos 2\theta_0 - (EI_c - EI_n)w''\hat{\phi}^2\cos 2\theta_0 - (EI_c - EI_n)w''\hat{\phi}\sin 2\theta_0 \Big] H_w'' dr \tag{2.168}$$

$$Q_{\hat{\phi}} = \int_0^d \Big[- (EI_c - EI_n)w''v''\cos 2\theta_0 + 2(EI_c - EI_n)w''v''\hat{\phi}\sin 2\theta_0 - (EI_c - EI_n)(w''^2 - v''^2)\sin\theta_0\cos\theta_0 - (EI_c - EI_n)(w''^2 - v''^2)\hat{\phi}\cos 2\theta_0 + EAe_A u_e'(w''\cos\theta_0 - v''\sin\theta_0) \Big] H_{\hat{\phi}} - \int_0^d \Big[EAK_A^2 u_e'\hat{\phi}' + GJw'v'' + EB_1\theta_0'^2 w'v'' \Big] H_{\hat{\phi}}' dr \tag{2.169}$$

The forcing is comprised of nonlinear terms. A first-order Taylor Series expansion is used to linearize:

$$Q^{n+1} = Q^n + \left.\frac{\partial Q}{\partial q}\right|_n (q^{n+1} - q^n) \tag{2.170}$$

Where q represents the degrees of freedom and their spatial derivatives. Substituting into the equation of motion,

$$M\ddot{q}^{n+1} + C\dot{q}^{n+1} + \Big(K - \left.\frac{\partial Q}{\partial q}\right|_n\Big) q^{n+1} = Q^n - \left.\frac{\partial Q}{\partial q}\right|_n q^n \tag{2.171}$$

The term $-\left.\frac{\partial Q}{\partial q}\right|_n$ results in the displacement Jacobian matrix given below.

$$K_{u_e u_e} = 0 \tag{2.172}$$

$$K_{u_e v} = \int_0^d (EAK_A^2 \theta_0' w' + EAe_a \hat{\phi} \sin\theta_0) H_{u_e}' H_v''^{\top} dr \tag{2.173}$$

$$K_{u_e w} = \int_0^d EAK_A \theta_0' v'' H_{u_e}' H_w'^{\top} dr - \int_0^d EAe_A \hat{\phi} cos\theta_0 H_{u_e}' H_w''^{\top} dr \tag{2.174}$$

$$K_{u_e \hat{\phi}} = \int_0^d EAK_A^2 \hat{\phi}' H_{u_e}' H_{\hat{\phi}}'^{\top} dr - \int_0^d EAe_A (w'' \cos\theta_0 - v'' \sin\theta_0) H_{u_e}' H_{\hat{\phi}}^{\top} dr \tag{2.175}$$

$$K_{v u_e} = \int_0^d (EAK_A^2 \theta_0' w' + EAe_a \hat{\phi} \sin\theta_0) H_v'' H_{u_e}'^{\top} dr = K_{u_e v}^{\top} \tag{2.176}$$

$$K_{vv} = -\int_0^d \Big[(EI_c - EI_n) \hat{\phi}^2 \cos 2\theta_0 - (EI_c - EI_n) \hat{\phi} \sin 2\theta_0 \Big] H_v'' H_v''^{\top} dr \tag{2.177}$$

$$\begin{aligned} K_{vw} = & \int_0^d \Big[EAK_A^2 \theta_0' u_e' + (GJ + EB_1 \theta_0'^2) \hat{\phi}' \Big] H_v'' H_w'^{\top} dr \\ & - \int_0^d \Big[(EI_c - EI_n) \hat{\phi}^2 \sin 2\theta_0 - (EI_c - EI_n) \hat{\phi} \cos\theta_0 \Big] H_v'' H_w''^{\top} dr \end{aligned} \tag{2.178}$$

$$\begin{aligned} K_{v\hat{\phi}} = & \int_0^d (GJ + EB_1 \theta_0'^2) w' H_v'' H_{\hat{\phi}}'^{\top} dr \\ & + \int_0^d \Big[EAe_A u_e' \sin\theta_0 - 2(EI_c - EI_n) v'' \hat{\phi} \cos 2\theta_0 - (EI_c - EI_n) v'' \sin 2\theta_0 \\ & \quad - 2(EI_c - EI_n) w'' \hat{\phi} \sin 2\theta_0 + (EI_c - EI_n) w'' \cos 2\theta_0 \Big] H_v'' H_{\hat{\phi}}^{\top} dr \end{aligned} \tag{2.179}$$

$$K_{w u_e} = \int_0^d EAK_A \theta_0' v'' H_w' H_{u_e}'^{\top} dr - \int_0^d EAe_A \hat{\phi} cos\theta_0 H_w'' H_{u_e}'^{\top} dr = K_{u_e w}^{\top} \tag{2.180}$$

$$K_{wv} = \int_0^d (EI_c - EI_n) \sin\theta_0 \cos\theta_0 H_w'' H_v''^{\top} dr = K_{vw}^{\top} \tag{2.181}$$

$$K_{ww} = \int_0^d \Big[(EI_c - EI_n) \hat{\phi}^2 \cos 2\theta_0 + (EI_c - EI_n) \hat{\phi} \sin 2\theta_0 \Big] H_w'' H_w''^{\top} dr \tag{2.182}$$

$$\begin{aligned} K_{w\hat{\phi}} = & \int_0^d (GJ + EB_1 \theta_0'^2) v'' H_w' H_{\hat{\phi}}'^{\top} dr \\ & - \int_0^d \Big[EAe_A u_e' \cos\theta_0 + 2(EI_c - EI_n) v'' \hat{\phi} \sin 2\theta_0 - (EI_c - EI_n) v'' \cos 2\theta_0 \\ & \quad - 2(EI_c - EI_n) w'' \hat{\phi} \cos 2\theta_0 - (EI_c - EI_n) w'' \sin 2\theta_0 \Big] H_w'' H_{\hat{\phi}}^{\top} dr \end{aligned} \tag{2.183}$$

$$K_{\hat{\phi}u_e} = \int_0^d EAK_A^2\hat{\phi}' H_{u_e}'^{\top} H_{\hat{\phi}}' dr$$

$$-\int_0^d EAe_A(w'' \cos\theta_0 - v'' \sin\theta_0) H_{\hat{\phi}} H_{u_e}'^{\top} dr = K_{u_e\hat{\phi}}^{\top} \quad (2.184)$$

$$K_{\hat{\phi}v} = \int_0^d (GJ + EB_1\theta_0'^2) w' H_{\hat{\phi}}' H_v''^{\top} dr$$

$$+\int_0^d \Big[EAe_A u_e' \sin\theta_0 - 2(EI_c - EI_n) v''\hat{\phi} \cos 2\theta_0 - (EI_c - EI_n) v'' \sin 2\theta_0$$

$$- 2(EI_c - EI_n) w''\hat{\phi} \sin 2\theta_0 + (EI_c - EI_n) w'' \cos 2\theta_0 \Big] H_{\hat{\phi}} H_v''^{\top} dr = K_{v\hat{\phi}}^{\top} \quad (2.185)$$

$$K_{\hat{\phi}w} = \int_0^d (GJ + EB_1\theta_0'^2) v'' H_{\hat{\phi}}' H_w'^{\top} dr$$

$$-\int_0^d \Big[EAe_A u_e' \cos\theta_0 + 2(EI_c - EI_n) v''\hat{\phi} \sin 2\theta_0 - (EI_c - EI_n) v'' \cos 2\theta_0$$

$$- 2(EI_c - EI_n) w''\hat{\phi} \cos 2\theta_0 - (EI_c - EI_n) w'' \sin 2\theta_0 \Big] H_{\hat{\phi}} H_w''^{\top} dr = K_{w\hat{\phi}}^{\top} \quad (2.186)$$

$$K_{\hat{\phi}\hat{\phi}} = \int_0^d \Big[- 2w''v''(EI_c - EI_n) \sin 2\theta_0 + (w''^2 - v''^2)(EI_c - EI_n) \cos 2\theta_0 \Big] H_{\hat{\phi}} H_{\hat{\phi}}^{\top} dr$$

$$+\int_0^d EAK_A^2 u_e' H_{\hat{\phi}}' H_{\hat{\phi}}'^{\top} dr \quad (2.187)$$

2.15.2 Aerodynamic/Inertial Loads

Isolated rotor and wing matrices due to aerodynamic/inertial loads are given below. The rotor/wing coupling matrices can be obtained by replacing the perturbation quantities with the wing deflections. The wing/rotor coupling matrices can be obtained by replacing the distributed forces/moments with the hub forces/moments. Finally, the wing matrices due to wing perturbation through the hub loads can be obtained by replacing the perturbation quantities with wing deflections as well as the distributed forces/moments with the hub loads. The shape functions are also evaluated accordingly.

$$M_{u_e u_e} = -\int_0^d H_{u_e} \frac{\partial f_x}{\partial \ddot{u}_e} H_{u_e}^\top dr \tag{2.188}$$

$$M_{u_e v} = -\int_0^d H_{u_e} \Big(\frac{\partial f_x}{\partial \ddot{v}} H_v^\top + \frac{\partial f_x}{\partial \ddot{v}'} H_v'^\top \Big) dr \tag{2.189}$$

$$M_{u_e w} = -\int_0^d H_{u_e} \Big(\frac{\partial f_x}{\partial \ddot{w}} H_w^\top + \frac{\partial f_x}{\partial \ddot{w}'} H_w'^\top \Big) dr \tag{2.190}$$

$$M_{u_e \hat{\phi}} = -\int_0^d H_{u_e} \frac{\partial f_x}{\partial \ddot{\hat{\phi}}} H_{\hat{\phi}}^\top dr \tag{2.191}$$

$$M_{v u_e} = -\int_0^d H_v \frac{\partial f_y}{\partial \ddot{u}_e} H_{u_e}^\top dr \quad - \int_0^d H_v' \frac{\partial m_z}{\partial \ddot{u}_e} H_{u_e}^\top dr \tag{2.192}$$

$$M_{vv} = -\int_0^d H_v \Big(\frac{\partial f_y}{\partial \ddot{v}} H_v^\top + \frac{\partial f_y}{\partial \ddot{v}'} H_v'^\top \Big) dr \quad - \int_0^d H_v' \Big(\frac{\partial m_z}{\partial \ddot{v}} H_v^\top + \frac{\partial m_z}{\partial \ddot{v}'} H_v'^\top \Big) dr \tag{2.193}$$

$$M_{vw} = -\int_0^d H_v \Big(\frac{\partial f_y}{\partial \ddot{w}} H_w^\top + \frac{\partial f_y}{\partial \ddot{w}'} H_w'^\top \Big) dr \quad - \int_0^d H_v' \Big(\frac{\partial m_z}{\partial \ddot{w}} H_w^\top + \frac{\partial m_z}{\partial \ddot{w}'} H_w'^\top \Big) dr \tag{2.194}$$

$$M_{v\hat{\phi}} = -\int_0^d H_v \frac{\partial f_y}{\partial \ddot{\hat{\phi}}} H_{\hat{\phi}}^\top dr \quad - \int_0^d H_v' \frac{\partial m_z}{\partial \ddot{\hat{\phi}}} H_{\hat{\phi}}^\top dr \tag{2.195}$$

$$M_{w u_e} = -\int_0^d H_w \frac{\partial f_z}{\partial \ddot{u}_e} H_{u_e}^\top dr \quad + \int_0^d H_w' \frac{\partial m_y}{\partial \ddot{u}_e} H_{u_e}^\top dr \tag{2.196}$$

$$M_{wv} = -\int_0^d H_w \Big(\frac{\partial f_z}{\partial \ddot{v}} H_v^\top + \frac{\partial f_z}{\partial \ddot{v}'} H_v'^\top \Big) dr \quad + \int_0^d H_w' \Big(\frac{\partial m_y}{\partial \ddot{v}} H_v^\top + \frac{\partial m_y}{\partial \ddot{v}'} H_v'^\top \Big) dr \tag{2.197}$$

$$M_{ww} = -\int_0^d H_w \Big(\frac{\partial f_z}{\partial \ddot{w}} H_w^\top + \frac{\partial f_z}{\partial \ddot{w}'} H_w'^\top \Big) dr \quad + \int_0^d H_w' \Big(\frac{\partial m_y}{\partial \ddot{w}} H_w^\top + \frac{\partial m_y}{\partial \ddot{w}'} H_w'^\top \Big) dr \tag{2.198}$$

$$M_{w\hat{\phi}} = -\int_0^d H_w \frac{\partial f_z}{\partial \ddot{\hat{\phi}}} H_{\hat{\phi}}^\top dr \quad + \int_0^d H_w' \frac{\partial m_y}{\partial \ddot{\hat{\phi}}} H_{\hat{\phi}}^\top dr \tag{2.199}$$

$$M_{\hat{\phi} u_e} = -\int_0^d H_{\hat{\phi}} \frac{\partial m_x}{\partial \ddot{u}_e} H_{u_e}^\top dr \tag{2.200}$$

$$M_{\hat{\phi} v} = -\int_0^d H_{\hat{\phi}} \Big(\frac{\partial m_x}{\partial \ddot{v}} H_v^\top + \frac{\partial m_x}{\partial \ddot{v}'} H_v'^\top \Big) dr \tag{2.201}$$

$$M_{\hat{\phi} w} = -\int_0^d H_{\hat{\phi}} \Big(\frac{\partial m_x}{\partial \ddot{w}} H_w^\top + \frac{\partial m_x}{\partial \ddot{w}'} H_w'^\top \Big) dr \tag{2.202}$$

$$M_{\hat{\phi}\hat{\phi}} = -\int_0^d H_{\hat{\phi}} \frac{\partial m_x}{\partial \ddot{\hat{\phi}}} H_{\hat{\phi}}^\top dr \tag{2.203}$$

$$C_{u_e u_e} = -\int_0^d H_{u_e} \frac{\partial f_x}{\partial \dot{u}_e} H_{u_e}^\top dr \tag{2.204}$$

$$C_{u_e v} = -\int_0^d H_{u_e} \Big(\frac{\partial f_x}{\partial \dot{v}} H_v^\top + \frac{\partial f_x}{\partial \dot{v}'} H_v'^\top \Big) dr \tag{2.205}$$

$$C_{u_e w} = -\int_0^d H_{u_e} \Big(\frac{\partial f_x}{\partial \dot{w}} H_w^\top + \frac{\partial f_x}{\partial \dot{w}'} H_w'^\top \Big) dr \tag{2.206}$$

$$C_{u_e \hat{\phi}} = -\int_0^d H_{u_e} \frac{\partial f_x}{\partial \dot{\hat{\phi}}} H_{\hat{\phi}}^\top dr \tag{2.207}$$

$$C_{v u_e} = -\int_0^d H_v \frac{\partial f_y}{\partial \dot{u}_e} H_{u_e}^\top dr - \int_0^d H_v' \frac{\partial m_z}{\partial \dot{u}_e} H_{u_e}^\top dr \tag{2.208}$$

$$C_{vv} = -\int_0^d H_v \Big(\frac{\partial f_y}{\partial \dot{v}} H_v^\top + \frac{\partial f_y}{\partial \dot{v}'} H_v'^\top \Big) dr - \int_0^d H_v' \Big(\frac{\partial m_z}{\partial \dot{v}} H_v^\top + \frac{\partial m_z}{\partial \dot{v}'} H_v'^\top \Big) dr \tag{2.209}$$

$$C_{vw} = -\int_0^d H_v \Big(\frac{\partial f_y}{\partial \dot{w}} H_w^\top + \frac{\partial f_y}{\partial \dot{w}'} H_w'^\top \Big) dr - \int_0^d H_v' \Big(\frac{\partial m_z}{\partial \dot{w}} H_w^\top + \frac{\partial m_z}{\partial \dot{w}'} H_w'^\top \Big) dr \tag{2.210}$$

$$C_{v\hat{\phi}} = -\int_0^d H_v \frac{\partial f_y}{\partial \dot{\hat{\phi}}} H_{\hat{\phi}}^\top dr - \int_0^d H_v' \frac{\partial m_z}{\partial \dot{\hat{\phi}}} H_{\hat{\phi}}^\top dr \tag{2.211}$$

$$C_{w u_e} = -\int_0^d H_w \frac{\partial f_z}{\partial \dot{u}_e} H_{u_e}^\top dr + \int_0^d H_w' \frac{\partial m_y}{\partial \dot{u}_e} H_{u_e}^\top dr \tag{2.212}$$

$$C_{wv} = -\int_0^d H_w \Big(\frac{\partial f_z}{\partial \dot{v}} H_v^\top + \frac{\partial f_z}{\partial \dot{v}'} H_v'^\top \Big) dr + \int_0^d H_w' \Big(\frac{\partial m_y}{\partial \dot{v}} H_v^\top + \frac{\partial m_y}{\partial \dot{v}'} H_v'^\top \Big) dr \tag{2.213}$$

$$C_{ww} = -\int_0^d H_w \Big(\frac{\partial f_z}{\partial \dot{w}} H_w^\top + \frac{\partial f_z}{\partial \dot{w}'} H_w'^\top \Big) dr + \int_0^d H_w' \Big(\frac{\partial m_y}{\partial \dot{w}} H_w^\top + \frac{\partial m_y}{\partial \dot{w}'} H_w'^\top \Big) dr \tag{2.214}$$

$$C_{w\hat{\phi}} = -\int_0^d H_w \frac{\partial f_z}{\partial \dot{\hat{\phi}}} H_{\hat{\phi}}^\top dr + \int_0^d H_w' \frac{\partial m_y}{\partial \dot{\hat{\phi}}} H_{\hat{\phi}}^\top dr \tag{2.215}$$

$$C_{\hat{\phi} u_e} = -\int_0^d H_{\hat{\phi}} \frac{\partial m_x}{\partial \dot{u}_e} H_{u_e}^\top dr \tag{2.216}$$

$$C_{\hat{\phi} v} = -\int_0^d H_{\hat{\phi}} \Big(\frac{\partial m_x}{\partial \dot{v}} H_v^\top + \frac{\partial m_x}{\partial \dot{v}'} H_v'^\top \Big) dr \tag{2.217}$$

$$C_{\hat{\phi} w} = -\int_0^d H_{\hat{\phi}} \Big(\frac{\partial m_x}{\partial \dot{w}} H_w^\top + \frac{\partial m_x}{\partial \dot{w}'} H_w'^\top \Big) dr \tag{2.218}$$

$$C_{\hat{\phi}\hat{\phi}} = -\int_0^d H_{\hat{\phi}} \frac{\partial m_x}{\partial \dot{\hat{\phi}}} H_{\hat{\phi}}^\top dr \tag{2.219}$$

$$K_{u_eu_e} = -\int_0^d H_{u_e}\frac{\partial f_x}{\partial u_e}H_{u_e}^\top dr \tag{2.220}$$

$$K_{u_ev} = -\int_0^d H_{u_e}\Big(\frac{\partial f_x}{\partial v}H_v^\top + \frac{\partial f_x}{\partial v'}H_v'^\top\Big)dr \tag{2.221}$$

$$K_{u_ew} = -\int_0^d H_{u_e}\Big(\frac{\partial f_x}{\partial w}H_w^\top + \frac{\partial f_x}{\partial w'}H_w'^\top\Big)dr \tag{2.222}$$

$$K_{u_e\hat{\phi}} = -\int_0^d H_{u_e}\frac{\partial f_x}{\partial \hat{\phi}}H_{\hat{\phi}}^\top dr \tag{2.223}$$

$$K_{vu_e} = -\int_0^d H_v\frac{\partial f_y}{\partial u_e}H_{u_e}^\top dr \quad -\int_0^d H_v'\frac{\partial m_z}{\partial u_e}H_{u_e}^\top dr \tag{2.224}$$

$$\begin{aligned} K_{vv} = & -\int_0^d H_v\Big(\frac{\partial f_y}{\partial v}H_v^\top + \frac{\partial f_y}{\partial v'}H_v'^\top\Big)dr \quad -\int_0^d H_v'\Big(\frac{\partial m_z}{\partial v}H_v^\top + \frac{\partial m_z}{\partial v'}H_v'^\top\Big)dr \\ & +\int_0^d H_v' T H_v'^\top dr \end{aligned} \tag{2.225}$$

$$K_{vw} = -\int_0^d H_v\Big(\frac{\partial f_y}{\partial w}H_w^\top + \frac{\partial f_y}{\partial w'}H_w'^\top\Big)dr \quad -\int_0^d H_v'\Big(\frac{\partial m_z}{\partial w}H_w^\top + \frac{\partial m_z}{\partial w'}H_w'^\top\Big)dr \tag{2.226}$$

$$K_{v\hat{\phi}} = -\int_0^d H_v\frac{\partial f_y}{\partial \hat{\phi}}H_{\hat{\phi}}^\top dr \quad -\int_0^d H_v'\frac{\partial m_z}{\partial \hat{\phi}}H_{\hat{\phi}}^\top dr \tag{2.227}$$

$$K_{wu_e} = -\int_0^d H_w\frac{\partial f_z}{\partial u_e}H_{u_e}^\top dr \quad +\int_0^d H_w'\frac{\partial m_y}{\partial u_e}H_{u_e}^\top dr \tag{2.228}$$

$$K_{wv} = -\int_0^d H_w\Big(\frac{\partial f_z}{\partial v}H_v^\top + \frac{\partial f_z}{\partial v'}H_v'^\top\Big)dr \quad +\int_0^d H_w'\Big(\frac{\partial m_y}{\partial v}H_v^\top + \frac{\partial m_y}{\partial v'}H_v'^\top\Big)dr \tag{2.229}$$

$$\begin{aligned} K_{ww} = & -\int_0^d H_w\Big(\frac{\partial f_z}{\partial w}H_w^\top + \frac{\partial f_z}{\partial w'}H_w'^\top\Big)dr \quad +\int_0^d H_w'\Big(\frac{\partial m_y}{\partial w}H_w^\top + \frac{\partial m_y}{\partial w'}H_w'^\top\Big)dr \\ & +\int_0^d H_w' T H_w'^\top dr \end{aligned} \tag{2.230}$$

$$K_{w\hat{\phi}} = -\int_0^d H_w\frac{\partial f_z}{\partial \hat{\phi}}H_{\hat{\phi}}^\top dr \quad +\int_0^d H_w'\frac{\partial m_y}{\partial \hat{\phi}}H_{\hat{\phi}}^\top dr \tag{2.231}$$

$$K_{\hat{\phi}u_e} = -\int_0^d H_{\hat{\phi}}\frac{\partial m_x}{\partial u_e}H_{u_e}^\top dr \tag{2.232}$$

$$K_{\hat{\phi}v} = -\int_0^d H_{\hat{\phi}}\Big(\frac{\partial m_x}{\partial v}H_v^\top + \frac{\partial m_x}{\partial v'}H_v'^\top\Big)dr \tag{2.233}$$

$$K_{\hat{\phi}w} = -\int_0^d H_{\hat{\phi}}\Big(\frac{\partial m_x}{\partial w}H_w^\top + \frac{\partial m_x}{\partial w'}H_w'^\top\Big)dr \tag{2.234}$$

$$K_{\hat{\phi}\hat{\phi}} = -\int_0^d H_{\hat{\phi}}\frac{\partial m_x}{\partial \hat{\phi}}H_{\hat{\phi}}^\top dr \tag{2.235}$$

$$
\begin{aligned}
Q_{u_e} = \; & \int_0^d H_{u_e}\Big(f_x - \frac{\partial f_x}{\partial \ddot{u}_e}\ddot{u}_e - \frac{\partial f_x}{\partial \ddot{v}}\ddot{v} - \frac{\partial f_x}{\partial \ddot{v}'}\ddot{v}' - \frac{\partial f_x}{\partial \ddot{w}}\ddot{w} - \frac{\partial f_x}{\partial \ddot{w}'}\ddot{w}' - \frac{\partial f_x}{\partial \ddot{\hat{\phi}}}\ddot{\hat{\phi}} \\
& - \frac{\partial f_x}{\partial \dot{u}_e}\dot{u}_e - \frac{\partial f_x}{\partial \dot{v}}\dot{v} - \frac{\partial f_x}{\partial \dot{v}'}\dot{v}' - \frac{\partial f_x}{\partial \dot{w}}\dot{w} - \frac{\partial f_x}{\partial \dot{w}'}\dot{w}' - \frac{\partial f_x}{\partial \dot{\hat{\phi}}}\dot{\hat{\phi}} \\
& - \frac{\partial f_x}{\partial u_e}u_e - \frac{\partial f_x}{\partial v}v - \frac{\partial f_x}{\partial v'}v' - \frac{\partial f_x}{\partial w}w - \frac{\partial f_x}{\partial w'}w' - \frac{\partial f_x}{\partial \hat{\phi}}\hat{\phi}\Big)dr
\end{aligned} \tag{2.236}
$$

$$
\begin{aligned}
Q_v = \; & \int_0^d H_v\Big(f_y - \frac{\partial f_y}{\partial \ddot{u}_e}\ddot{u}_e - \frac{\partial f_y}{\partial \ddot{v}}\ddot{v} - \frac{\partial f_y}{\partial \ddot{v}'}\ddot{v}' - \frac{\partial f_y}{\partial \ddot{w}}\ddot{w} - \frac{\partial f_y}{\partial \ddot{w}'}\ddot{w}' - \frac{\partial f_y}{\partial \ddot{\hat{\phi}}}\ddot{\hat{\phi}} \\
& - \frac{\partial f_y}{\partial \dot{u}_e}\dot{u}_e - \frac{\partial f_y}{\partial \dot{v}}\dot{v} - \frac{\partial f_y}{\partial \dot{v}'}\dot{v}' - \frac{\partial f_y}{\partial \dot{w}}\dot{w} - \frac{\partial f_y}{\partial \dot{w}'}\dot{w}' - \frac{\partial f_y}{\partial \dot{\hat{\phi}}}\dot{\hat{\phi}} \\
& - \frac{\partial f_y}{\partial u_e}u_e - \frac{\partial f_y}{\partial v}v - \frac{\partial f_y}{\partial v'}v' - \frac{\partial f_y}{\partial w}w - \frac{\partial f_y}{\partial w'}w' - \frac{\partial f_y}{\partial \hat{\phi}}\hat{\phi}\Big)dr \\
& + \int_0^d H_v'\Big(m_z - \frac{\partial m_z}{\partial \ddot{u}_e}\ddot{u}_e - \frac{\partial m_z}{\partial \ddot{v}}\ddot{v} - \frac{\partial m_z}{\partial \ddot{v}'}\ddot{v}' - \frac{\partial m_z}{\partial \ddot{w}}\ddot{w} - \frac{\partial m_z}{\partial \ddot{w}'}\ddot{w}' - \frac{\partial m_z}{\partial \ddot{\hat{\phi}}}\ddot{\hat{\phi}} \\
& - \frac{\partial m_z}{\partial \dot{u}_e}\dot{u}_e - \frac{\partial m_z}{\partial \dot{v}}\dot{v} - \frac{\partial m_z}{\partial \dot{v}'}\dot{v}' - \frac{\partial m_z}{\partial \dot{w}}\dot{w} - \frac{\partial m_z}{\partial \dot{w}'}\dot{w}' - \frac{\partial m_z}{\partial \dot{\hat{\phi}}}\dot{\hat{\phi}} \\
& - \frac{\partial m_z}{\partial u_e}u_e - \frac{\partial m_z}{\partial v}v - \frac{\partial m_z}{\partial v'}v' - \frac{\partial m_z}{\partial w}w - \frac{\partial m_z}{\partial w'}w' - \frac{\partial m_z}{\partial \hat{\phi}}\hat{\phi}\Big)dr
\end{aligned} \tag{2.237}
$$

$$
\begin{aligned}
Q_w = \; & \int_0^d H_w\Big(f_z - \frac{\partial f_z}{\partial \ddot{u}_e}\ddot{u}_e - \frac{\partial f_z}{\partial \ddot{v}}\ddot{v} - \frac{\partial f_z}{\partial \ddot{v}'}\ddot{v}' - \frac{\partial f_z}{\partial \ddot{w}}\ddot{w} - \frac{\partial f_z}{\partial \ddot{w}'}\ddot{w}' - \frac{\partial f_z}{\partial \ddot{\hat{\phi}}}\ddot{\hat{\phi}} \\
& - \frac{\partial f_z}{\partial \dot{u}_e}\dot{u}_e - \frac{\partial f_z}{\partial \dot{v}}\dot{v} - \frac{\partial f_z}{\partial \dot{v}'}\dot{v}' - \frac{\partial f_z}{\partial \dot{w}}\dot{w} - \frac{\partial f_z}{\partial \dot{w}'}\dot{w}' - \frac{\partial f_z}{\partial \dot{\hat{\phi}}}\dot{\hat{\phi}} \\
& - \frac{\partial f_z}{\partial u_e}u_e - \frac{\partial f_z}{\partial v}v - \frac{\partial f_z}{\partial v'}v' - \frac{\partial f_z}{\partial w}w - \frac{\partial f_z}{\partial w'}w' - \frac{\partial f_z}{\partial \hat{\phi}}\hat{\phi}\Big)dr \\
& - \int_0^d H_w'\Big(m_y - \frac{\partial m_y}{\partial \ddot{u}_e}\ddot{u}_e - \frac{\partial m_y}{\partial \ddot{v}}\ddot{v} - \frac{\partial m_y}{\partial \ddot{v}'}\ddot{v}' - \frac{\partial m_y}{\partial \ddot{w}}\ddot{w} - \frac{\partial m_y}{\partial \ddot{w}'}\ddot{w}' - \frac{\partial m_y}{\partial \ddot{\hat{\phi}}}\ddot{\hat{\phi}} \\
& - \frac{\partial m_y}{\partial \dot{u}_e}\dot{u}_e - \frac{\partial m_y}{\partial \dot{v}}\dot{v} - \frac{\partial m_y}{\partial \dot{v}'}\dot{v}' - \frac{\partial m_y}{\partial \dot{w}}\dot{w} - \frac{\partial m_y}{\partial \dot{w}'}\dot{w}' - \frac{\partial m_y}{\partial \dot{\hat{\phi}}}\dot{\hat{\phi}} \\
& - \frac{\partial m_y}{\partial u_e}u_e - \frac{\partial m_y}{\partial v}v - \frac{\partial m_y}{\partial v'}v' - \frac{\partial m_y}{\partial w}w - \frac{\partial m_y}{\partial w'}w' - \frac{\partial m_y}{\partial \hat{\phi}}\hat{\phi}\Big)dr
\end{aligned} \tag{2.238}
$$

$$
\begin{aligned}
Q_{\hat{\phi}} =& \int_0^d H_{\hat{\phi}} \Big(m_x - \frac{\partial m_x}{\partial \ddot{u}_e}\ddot{u}_e - \frac{\partial m_x}{\partial \ddot{v}}\ddot{v} - \frac{\partial m_x}{\partial \ddot{v}'}\ddot{v}' - \frac{\partial m_x}{\partial \ddot{w}}\ddot{w} - \frac{\partial m_x}{\partial \ddot{w}'}\ddot{w}' - \frac{\partial m_x}{\partial \ddot{\hat{\phi}}}\ddot{\hat{\phi}} \\
& - \frac{\partial m_x}{\partial \dot{u}_e}\dot{u}_e - \frac{\partial m_x}{\partial \dot{v}}\dot{v} - \frac{\partial m_x}{\partial \dot{v}'}\dot{v}' - \frac{\partial m_x}{\partial \dot{w}}\dot{w} - \frac{\partial m_x}{\partial \dot{w}'}\dot{w}' - \frac{\partial m_x}{\partial \dot{\hat{\phi}}}\dot{\hat{\phi}} \\
& - \frac{\partial m_x}{\partial u_e}u_e - \frac{\partial m_x}{\partial v}v - \frac{\partial m_x}{\partial v'}v' - \frac{\partial m_x}{\partial w}w - \frac{\partial m_x}{\partial w'}w' - \frac{\partial m_x}{\partial \hat{\phi}}\hat{\phi} \Big) dr
\end{aligned} \tag{2.239}
$$

Where T is the centrifugal force acting on the cross-section:

$$
T = \int_r^R f_x d\rho \tag{2.240}
$$

2.16 Multiblade Coordinate Transformation (MCT)

Multiblade Coordinate Transformation (MCT) enables constant coefficient approximation for the calculation of the stability roots. The transformation of equations from rotating coordinates to multiblade (fixed) coordinates (MBC) are given in Eqs. 2.241 to 2.244. The reverse transformation from multiblade coordinates to rotating coordinates for the flap degree of freedom is given in Eq. 2.245.

$$
B_0 \text{ equation } = \frac{1}{N_b}\sum_{m=1}^{N_b}(ode) \tag{2.241}
$$

$$
B_{1c} \text{ equation } = \frac{2}{N_b}\sum_{m=1}^{N_b}(ode)\cos n\psi_m \tag{2.242}
$$

$$
B_{1s} \text{ equation } = \frac{2}{N_b}\sum_{m=1}^{N_b}(ode)\sin n\psi_m \tag{2.243}
$$

$$
B_d \text{ equation } = \frac{1}{N_b}\sum_{m=1}^{N_b}(ode)(-1)^m \tag{2.244}
$$

$$
\beta^m(\psi) = B_0(\psi) + \sum_n \left[B_{nc}\cos(n\psi_m) + B_{ns}\sin(n\psi_m)\right] + B_d(-1)^m \tag{2.245}
$$

Where m is the blade number, $n = 1, 2, \ldots, (N_b-2)/2$ if N_b is even, and $n = 1, 2, \ldots, (N_b-1)/2$ if N_b is odd. Eq. 2.244 is required only if N_b is even.

Consider the set of ordinary differential equations for blade m together with the wing/pylon coupling terms:

$$M_{rr,m}\ddot{q}_{r,m} + C_{rr,m}\dot{q}_{r,m} + K_{rr,m}q_{r,m} + M_{rw,m}\ddot{q}_w + C_{rw,m}\dot{q}_w + K_{rw,m}q_w = Q_{r,m} \tag{2.246}$$

Where $q_{r,m}$ represents the degrees of freedom for blade m. The relationship between the fixed and rotating coordinates can be written in matrix form as follows:

$$q_{r,m} = A_m q_{rf} \tag{2.247}$$

A single degree of freedom (for a single blade) in rotating coordinates is converted to N_b degrees of freedom in fixed coordinates. Hence, for p number of degrees of freedom in the rotating coordinates, there are pN_b fixed coordinates.

$$q_{rf} = \begin{Bmatrix} q_{rf}^{(1)} \\ q_{rf}^{(2)} \\ \vdots \\ q_{rf}^{(p)} \end{Bmatrix}_{pN_b\times 1} \qquad q_{rf}^{(k)} = \begin{Bmatrix} q_{rf0} \\ q_{rf1c} \\ \vdots \\ q_{rfnc} \\ q_{rf1s} \\ \vdots \\ q_{rfns} \\ q_{rfd} \end{Bmatrix}^{(k)}_{N_b\times 1} \tag{2.248}$$

$$A_m = \begin{bmatrix} a_m & 0 & 0 & \dots & 0 \\ 0 & a_m & 0 & \dots & 0 \\ 0 & 0 & a_m & \dots & 0 \\ \vdots & \vdots & \vdots & \ddots & \\ 0 & 0 & 0 & & a_m \end{bmatrix}_{p \times pN_b} \tag{2.249}$$

$$a_m = \begin{cases} [1, \cos\psi_m, \dots, \cos n\psi_m, \sin\psi_m, \dots, \sin n\psi_m, (-1)^m]_{1\times N_b} & \text{if } N_b \text{ is even} \\ [1, \cos\psi_m, \dots, \cos n\psi_m, \sin\psi_m, \dots, \sin n\psi_m]_{1\times N_b} & \text{if } N_b \text{ is odd} \end{cases} \tag{2.250}$$

Taking the derivative of Eq. 2.247 with respect to time,

$$\dot{q}_{r,m} = \dot{A}_m q_{rf} + A_m \dot{q}_{rf} \tag{2.251}$$

$$\ddot{q}_{r,m} = \ddot{A}_m q_{rf} + 2\dot{A}_m \dot{q}_{rf} + A_m \ddot{q}_{rf} \tag{2.252}$$

Substituting Eqs. 2.247, 2.251, and 2.252 into Eq. 2.246,

$$\begin{aligned} M_{rr,m} A \ddot{q}_{rf} + (C_{rr,m} A_m + 2M_{rr,m} \dot{A}_m)\dot{q}_{rf} + (K_{rr,m} A_m + C_{rr,m} \dot{A}_m + M_{rr,m} \ddot{A}_m) q_{rf} \\ + M_{rw,m} \ddot{q}_w + C_{rw,m} \dot{q}_w + K_{rw,m} q_w = Q_{rf} \end{aligned} \tag{2.253}$$

Finally, the set ordinary differential equations is transformed to the fixed frame using Eqs. 2.241 to 2.244 as follows:

$$M_{rrf} \ddot{q}_{rf} + C_{rrf} \dot{q}_{rf} + K_{rrf} q_{rf} + M_{rwf} \ddot{q}_w + C_{rwf} \dot{q}_w + K_{rwf} q_w = Q_{rf} \tag{2.254}$$

$$M_{rrf} = \frac{1}{N_b}\sum_{m=1}^{N_b} H_m M_{rr,m} A_m \tag{2.255}$$

$$C_{rrf} = \frac{1}{N_b}\sum_{m=1}^{N_b} H_m (C_{rr,m} A_m + 2M_{rr,m}\dot{A}_m) \tag{2.256}$$

$$K_{rrf} = \frac{1}{N_b}\sum_{m=1}^{N_b} H_m (K_{rr,m} A_m + C_{rr,m}\dot{A}_m + M_{rr,m}\ddot{A}_m) \tag{2.257}$$

$$M_{rwf} = \frac{1}{N_b}\sum_{m=1}^{N_b} H_m M_{rw,m} \tag{2.258}$$

$$C_{rwf} = \frac{1}{N_b}\sum_{m=1}^{N_b} H_m C_{rw,m} \tag{2.259}$$

$$K_{rwf} = \frac{1}{N_b}\sum_{m=1}^{N_b} H_m K_{rw,m} \tag{2.260}$$

$$Q_{rf} = \frac{1}{N_b}\sum_{m=1}^{N_b} H_m Q_{r,m} \tag{2.261}$$

The matrix H_m is calculated as follows:

$$H_m = \begin{bmatrix} h_m & 0 & 0 & \dots & 0 \\ 0 & h_m & 0 & \dots & 0 \\ 0 & 0 & h_m & \dots & 0 \\ \vdots & \vdots & \vdots & \ddots & \\ 0 & 0 & 0 & & h_m \end{bmatrix}_{pN_b \times p} \tag{2.262}$$

$$h_m = \begin{cases} [1, 2\cos\psi_m, \dots, 2\cos n\psi_m, 2\sin\psi_m, \dots, 2\sin n\psi_m, (-1)^m]^\top_{1\times N_b} & \text{if } N_b \text{ is even} \\ [1, 2\cos\psi_m, \dots, 2\cos n\psi_m, 2\sin\psi_m, \dots, 2\sin n\psi_m]^\top_{1\times N_b} & \text{if } N_b \text{ is odd} \end{cases} \tag{2.263}$$

The wing equation with the rotor coupling terms is given as follows:

$$M_{ww}\ddot{q}_w + C_{ww}\dot{q}_w + K_{ww}q_w + \sum_{m=1}^{N_b}(M_{wr,m}\ddot{q}_{r,m} + C_{wr,m}\dot{q}_{r,m} + K_{wr,m}q_{r,m}) = 0 \tag{2.264}$$

This equation is already in the fixed frame, only the rotor degrees of freedom are transformed to fixed coordinates as follows:

$$M_{ww}\ddot{q}_w + C_{ww}\dot{q}_w + K_{ww}q_w + M_{wrf}\ddot{q}_{rf} + C_{wrf}\dot{q}_{rf} + K_{wrf}q_{rf} = 0 \tag{2.265}$$

Where

$$M_{wrf} = \sum_{m=1}^{N_b} M_{wr,m}A_m \tag{2.266}$$

$$C_{wrf} = \sum_{m=1}^{N_b} C_{wr,m}A_m + 2M_{wr,m}\dot{A}_m \tag{2.267}$$

$$K_{wrf} = \sum_{m=1}^{N_b} K_{wr,m}A_m + C_{wr,m}\dot{A}_m + M_{wr,m}\ddot{A}_m \tag{2.268}$$

2.17 Solution Methods

Trim solution can be obtained with two methods: Finite Element in Time (FET) or time marching. FET requires solution of a large system of equations, but the periodic solution is obtained directly. On the other hand, time marching requires computation until the initial conditions die out and the solution settles down to periodic response, which can be computationally heavy as solution for at least a few revolutions is required. After trim, a transient analysis can be performed for time-varying controls with the time marching solution.

2.17.1 Finite Element in Time

Finite Element in Time (FET) is similar to finite element in space, only this time the elements are temporal instead of spatial. FET was first introduced by Argyris and Scharpf in nuclear engineering (Ref. [84]). The first application on a rotorcraft problem was by Borri in 1986 (Ref. [85]). Boundary conditions are periodic. Lagrange shape functions are used. A period is divided into N temporal elements as shown in Fig. 2.7.

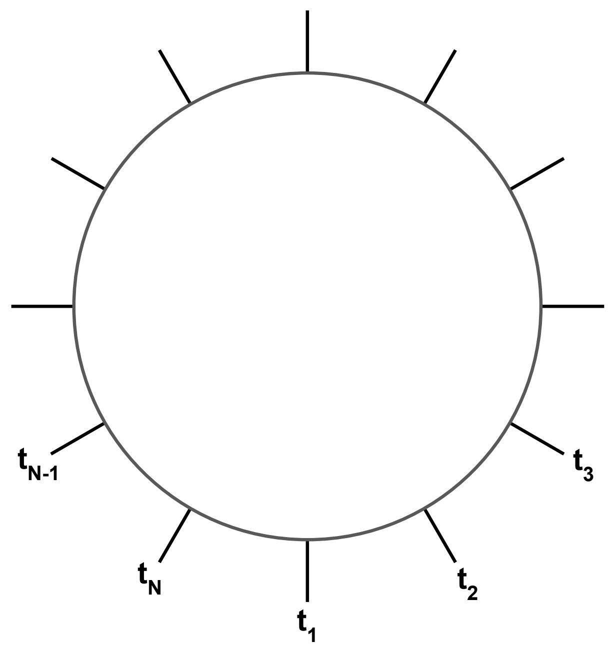

Figure 2.7: Finite element in time

Within each element, the degrees of freedom are allowed to change. Derivation of Lagrange polynomials for a third-order polynomial is illustrated below.

$$q(t) = \alpha_1 + \alpha_2 t + \alpha_3 t^2 + \alpha_4 t^3 \tag{2.269}$$

The nodal values are used to find the constants:

$$
\begin{aligned}
q_1 &= q(0) = \alpha_1 \\
q_2 &= q(h) = \alpha_1 + \alpha_2 h + \alpha_3 h^2 + \alpha_4 h^3 \\
q_3 &= q(2h) = \alpha_1 + 2\alpha_2 h + 4\alpha_3 h^2 + 8\alpha_4 h^3 \\
q_4 &= q(3h) = \alpha_1 + 3\alpha_2 h + 9\alpha_3 h^2 + 27\alpha_4 h^3
\end{aligned}
\tag{2.270}
$$

Where $h = 2\pi/N$. Solving for the constants,

$$
\begin{aligned}
\alpha_1 &= q_1 \\
\alpha_2 &= \frac{-11q_1 + 18q_2 - 9q_3 + 2q_4}{6h} \\
\alpha_3 &= \frac{2q_1 - 5q_2 + 4q_3 - q_4}{2h^2} \\
\alpha_4 &= \frac{-q_1 + 3q_2 - 3q_3 + q_4}{6h^3}
\end{aligned}
$$

Substituting into Eq. 2.269,

$$
\begin{aligned}
q(t) =& \Big(\frac{t^2}{h^2} - \frac{11t}{6h} - \frac{t^3}{6h^3} + 1\Big)q_1 + \Big(\frac{3t}{h} - \frac{5t^2}{2h^2} + \frac{t^3}{2h^3}\Big)q_2 \\
&+ \Big(\frac{2t^2}{h^2} - \frac{3t}{2h} - \frac{t^3}{2h^3}\Big)q_3 + \Big(\frac{t}{3h} - \frac{t^2}{2h^2} + \frac{t^3}{6h^3}\Big)q_4
\end{aligned}
\tag{2.271}
$$

$$
q(t) = H_1(t)q_1 + H_2(t)q_2 + H_3(t)q_3 + H_4(t)q_4 = H^\top q \tag{2.272}
$$

$$
\begin{aligned}
H_1(t) =& -\frac{t^3}{6h^3} + \frac{t^2}{h^2} - \frac{11t}{6h} + 1 \\
H_2(t) =& \frac{t^3}{2h^3} - \frac{5t^2}{2h^2} + \frac{3t}{h} \\
H_3(t) =& -\frac{t^3}{2h^3} + \frac{2t^2}{h^2} - \frac{3t}{2h} \\
H_4(t) =& \frac{t^3}{6h^3} - \frac{t^2}{2h^2} + \frac{t}{3h}
\end{aligned}
\tag{2.273}
$$

The equations for the FET solution is derived below. First, the governing equations are transformed into a variational form:

$$
\int_{t_1}^{t_{N+1}} \delta q^\top (M\ddot{q} + C\dot{q} + Kq - Q)dt = 0 \tag{2.274}
$$

Assuming M is not time dependent, the first term can be written as follows:

$$
\int_{t_1}^{t_{N+1}} \delta q^\top M\ddot{q}dt = \delta q^\top M\dot{q}\Big|_{t_1}^{t_{N+1}} - \int_{t_1}^{t_{N+1}} \delta\dot{q}^\top M\dot{q}dt \tag{2.275}
$$

Due to periodicity,

$$
\delta q^\top M\dot{q}\Big|_{t_1}^{t_{N+1}} = 0 \tag{2.276}
$$

$$
\int_{t_1}^{t_{N+1}} \delta q^\top M\ddot{q}dt = -\int_{t_1}^{t_{N+1}} \delta\dot{q}^\top M\dot{q}dt \tag{2.277}
$$

Eq. 2.274 is rewritten as follows:

$$
I = \int_{t_1}^{t_{N+1}} (-\delta\dot{q}^\top M\dot{q} + \delta q^\top C\dot{q} + \delta q^\top Kq - \delta q^\top Q)dt = 0 \tag{2.278}
$$

Using Eq. 2.272,

$$-\int_{t_1}^{t_{N+1}}(\delta q^\top \dot{H} M \dot{H}^\top q)dt + \int_{t_1}^{t_{N+1}}(\delta q^\top H C \dot{H}^\top q)dt$$
$$+ \int_{t_1}^{t_{N+1}}(\delta q^\top H K H^\top q)dt - \int_{t_1}^{t_{N+1}}(\delta q^\top H Q)dt = 0 \qquad (2.279)$$

Which can also be written as,

$$\delta q^\top A q - \delta q^\top B = 0 \qquad (2.280)$$

$$\delta q^\top (Aq - B) = 0 \qquad (2.281)$$

$$Aq = B \qquad (2.282)$$

Where

$$A = -\int_{t_1}^{t_{N+1}} \dot{H} M \dot{H}^\top dt + \int_{t_1}^{t_{N+1}} H C \dot{H}^\top dt + \int_{t_1}^{t_{N+1}} H K H^\top dt \qquad (2.283)$$
$$B = \int_{t_1}^{t_{N+1}} HQdt \qquad (2.284)$$

The ordinary differential equations are thus converted to a set of algebraic equations. The discretization of the integral for a first-order shape function and $N = 4$ is illustrated below.

$$I = I_1 + I_2 + I_3 + I_4 = \int_{t_1}^{t_2}(...)dt + \int_{t_2}^{t_3}(...)dt + \int_{t_3}^{t_4}(...)dt + \int_{t_4}^{t_1}(...)dt = 0 \qquad (2.285)$$

$$
\begin{aligned}
I_1 &= \begin{Bmatrix} \delta q_1 \\ \delta q_2 \end{Bmatrix}^\top \begin{bmatrix} A_{11} & A_{12} \\ A_{21} & A_{22} \end{bmatrix}_1 \begin{Bmatrix} \delta q_1 \\ \delta q_2 \end{Bmatrix} - \begin{Bmatrix} \delta q_1 \\ \delta q_2 \end{Bmatrix}^\top \begin{Bmatrix} B_1 \\ B_2 \end{Bmatrix}_1 \\
I_2 &= \begin{Bmatrix} \delta q_1 \\ \delta q_2 \end{Bmatrix}^\top \begin{bmatrix} A_{11} & A_{12} \\ A_{21} & A_{22} \end{bmatrix}_2 \begin{Bmatrix} \delta q_1 \\ \delta q_2 \end{Bmatrix} - \begin{Bmatrix} \delta q_1 \\ \delta q_2 \end{Bmatrix}^\top \begin{Bmatrix} B_1 \\ B_2 \end{Bmatrix}_2 \\
I_3 &= \begin{Bmatrix} \delta q_1 \\ \delta q_2 \end{Bmatrix}^\top \begin{bmatrix} A_{11} & A_{12} \\ A_{21} & A_{22} \end{bmatrix}_3 \begin{Bmatrix} \delta q_1 \\ \delta q_2 \end{Bmatrix} - \begin{Bmatrix} \delta q_1 \\ \delta q_2 \end{Bmatrix}^\top \begin{Bmatrix} B_1 \\ B_2 \end{Bmatrix}_3 \\
I_4 &= \begin{Bmatrix} \delta q_1 \\ \delta q_2 \end{Bmatrix}^\top \begin{bmatrix} A_{11} & A_{12} \\ A_{21} & A_{22} \end{bmatrix}_4 \begin{Bmatrix} \delta q_1 \\ \delta q_2 \end{Bmatrix} - \begin{Bmatrix} \delta q_1 \\ \delta q_2 \end{Bmatrix}^\top \begin{Bmatrix} B_1 \\ B_2 \end{Bmatrix}_4
\end{aligned}
\tag{2.286}
$$

Combining the integrals,

$$
\begin{Bmatrix} \delta q_1 \\ \delta q_2 \\ \delta q_3 \\ \delta q_4 \end{Bmatrix}^\top \begin{bmatrix} A_{11} & A_{12} & A_{13} & A_{14} \\ A_{21} & A_{22} & A_{23} & A_{24} \\ A_{31} & A_{32} & A_{33} & A_{34} \\ A_{41} & A_{42} & A_{43} & A_{44} \end{bmatrix} \begin{Bmatrix} q_1 \\ q_2 \\ q_3 \\ q_4 \end{Bmatrix} = \begin{Bmatrix} \delta q_1 \\ \delta q_2 \\ \delta q_3 \\ \delta q_4 \end{Bmatrix}^\top \begin{Bmatrix} B_1 \\ B_2 \\ B_3 \\ B_4 \end{Bmatrix}
\tag{2.287}
$$

$$
\begin{bmatrix} A_{11} & A_{12} & A_{13} & A_{14} \\ A_{21} & A_{22} & A_{23} & A_{24} \\ A_{31} & A_{32} & A_{33} & A_{34} \\ A_{41} & A_{42} & A_{43} & A_{44} \end{bmatrix} = \begin{bmatrix} (A_{11})_1 + (A_{22})_4 & (A_{12})_1 & 0 & (A_{21})_4 \\ (A_{21})_1 & (A_{22})_1 + (A_{11})_2 & (A_{12})_2 & 0 \\ 0 & (A_{21})_2 & (A_{22})_2 + (A_{11})_3 & (A_{12})_3 \\ (A_{12})_4 & 0 & (A_{21})_3 & (A_{22})_3 + (A_{11})_4 \end{bmatrix}
\tag{2.288}
$$

$$\begin{Bmatrix} B_1 \\ \\ B_2 \\ \\ B_3 \\ \\ B_4 \end{Bmatrix} = \begin{Bmatrix} (B_1)_1 + (B_2)_4 \\ \\ (B_2)_1 + (B_1)_2 \\ \\ (B_2)_2 + (B_1)_3 \\ \\ (B_2)_3 + (B_1)_4 \end{Bmatrix} \tag{2.289}$$

2.17.2 Time Marching

Two points backwards Euler scheme is used for time marching. It ensures algorithmic stability. First, equilibrium is satisfied at time $n+1$:

$$M^{n+1}\ddot{q}^{n+1} + C^{n+1}\dot{q}^{n+1} + K^{n+1}q^{n+1} = Q^{n+1} \tag{2.290}$$

The finite difference equations are given below.

$$\dot{q}^{n+1} = \frac{1}{\Delta t}(q^{n+1} - q^n) \tag{2.291}$$

$$\ddot{q}^{n+1} = \frac{1}{\Delta t^2}(q^{n+1} - 2q^n + q^{n-1}) \tag{2.292}$$

Substituting into Eq. 2.290:

$$M^{n+1}\frac{1}{\Delta t^2}(q^{n+1} - 2q^n + q^{n-1}) + C^{n+1}\frac{1}{\Delta t}(q^{n+1} - q^n) + K^{n+1}q^{n+1} = Q^{n+1} \tag{2.293}$$

Hence,

$$q^{n+1} = \Big[\frac{M^{n+1}}{\Delta t^2} + \frac{C^{n+1}}{\Delta t} + K^{n+1}\Big]^{-1}\Big[q^n\Big(2\frac{M^{n+1}}{\Delta t^2} + \frac{C^{n+1}}{\Delta t}\Big) - q^{n-1}\frac{M^{n+1}}{\Delta t^2} + Q^{n+1}\Big] \tag{2.294}$$

Once q^{n+1} is calculated, $\dot{q}^{n+1}$ and $\ddot{q}^{n+1}$ can be found using Eqs. 2.291 and 2.292.

Note that the problem is nonlinear; the matrices M^{n+1}, C^{n+1}, K^{n+1}, and the forcing vector Q^{n+1} depend on the solution itself. The equation should either be solved with sub-iterations for every time step, or small time steps should be used for accuracy.

2.18 Aeroelastic Stability

The stability of the rotor/pylon/wing system can be calculated with two methods: eigenanalysis or transient response. Eigenanalysis applies numerical perturbation to extract the mass, damping, and stiffness matrices due to aerodynamic and inertial forces. Eigenvalues then give the frequency and damping of the coupled system. A constant coefficient approximation is used in this method as it is valid and accurate for airplane mode axial flight. Floquet theory need not be invoked. Stability roots are obtained in the fixed frame after applying a numerical multiblade coordinate transformation. Transient response perturbs the rotor controls and the solution is obtained with time marching solution. After the excitation stops, the Moving-Block method (Ref. [78]) is used on the decaying signal to extract the frequency and the damping of a chosen mode.

Transient response is a simulation of the test. The gimbal motion can be modeled exactly, but all the blades must be included. Eigenanalysis is computationally faster; however, it can only simulate a gimbal using collective and cyclic modes in an approximate manner. In this dissertation, the hingeless rotor stability results were obtained with eigenanalysis and gimbal-free results were obtained with transient response. The results with the two methods are identical for a hingeless or articulated configuration.

2.18.1 Eigenanalysis

First, the right-hand side of the system of equations is set to zero for stability solution:

$$M\ddot{q} + C\dot{q} + Kq = 0 \tag{2.295}$$

Equation 2.295 is then converted to the first order form substituting $y_1 = q$ and $y_2 = \dot{q}$:

$$\begin{Bmatrix} \dot{y}_1 \\ \dot{y}_2 \end{Bmatrix} = \begin{bmatrix} 0 & I \\ -M^{-1}K & -M^{-1}C \end{bmatrix} \begin{Bmatrix} y_1 \\ y_2 \end{Bmatrix} \tag{2.296}$$

$$\dot{y} = Ay \tag{2.297}$$

Complex eigenvalues of matrix A give the stability roots. The eigenvalues are of the following form:

$$s = -\zeta\omega_n \pm i\sqrt{\omega_n^2 - (\zeta\omega_n)^2} \tag{2.298}$$

The natural frequency ω_n, damped frequency ω_d, and critical damping ratio ζ are calculated as follows:

$$\omega_n = |s| \tag{2.299}$$

$$\omega_d = Im(s) \tag{2.300}$$

$$\zeta = -\frac{Re(s)}{|s|} \tag{2.301}$$

2.18.2 Transient Response

The procedure for the transient response method is illustrated with an example. Consider a rotor/pylon/wing with traditional swashplate controls. Wing beam mode is excited with rotor longitudinal cyclic for 40 revolutions as shown in Fig. 2.8a, and then released. Transient solution is run for a total of 80 revolutions. The response of the wing is shown in Fig. 2.8b with a solid black line. The decay in the signal contains the aerodynamic and algorithmic damping, which need to be separated. This is achieved by performing the same solution once more, but this time setting the density to zero right when the excitation stops (red dashed lines). The damping in this signal is only the algorithmic damping. The solution for the algorithmic damping only needs to be performed once, and it is independent of rotor or flight speed.

The Moving-Block method can be used to calculate the frequency and the damping of the decaying signal. It is a useful method to analyze a response that contains multiple well-separated frequencies. The damping for each frequency that makes up the response can be determined. For this simple example where the response is comprised of only one frequency, a simple Fourier transform for the damped frequency and the logarithmic decrement method for the damping is sufficient and computationally faster.

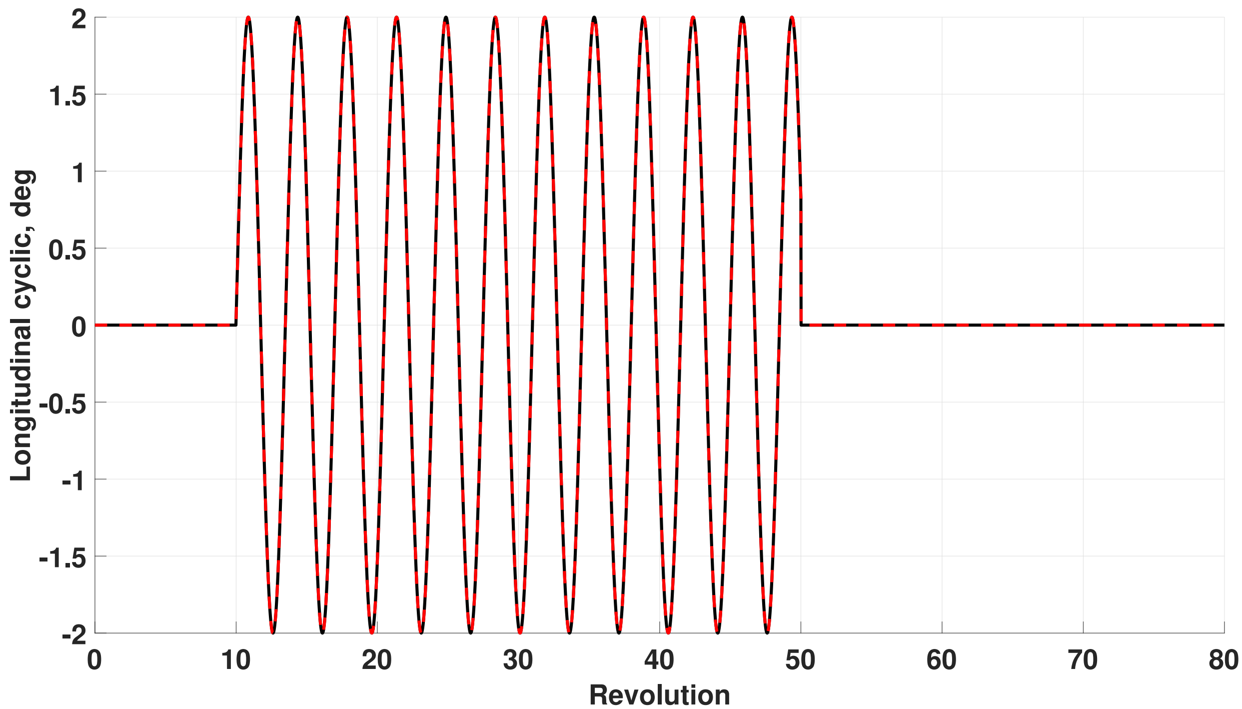

(a) Longitudinal cyclic

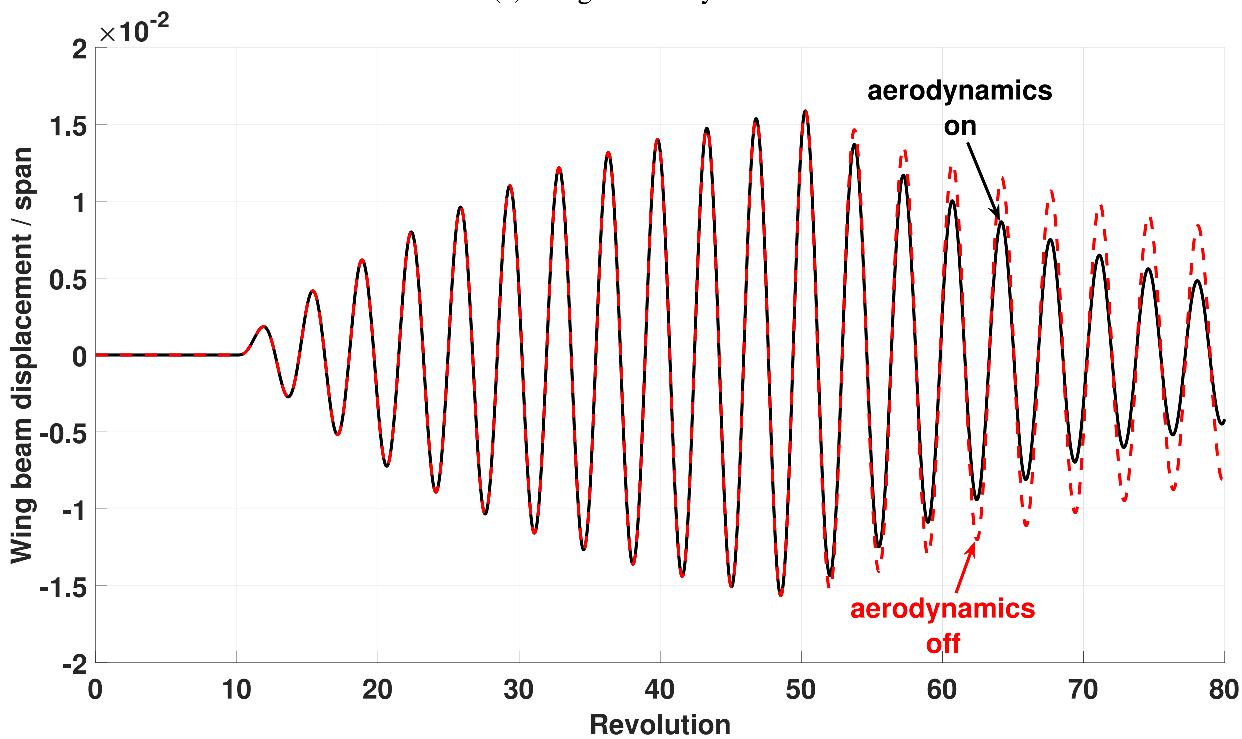

(b) Nondimensional wing beam displacement

Figure 2.8: Transient response method

Chapter 3: Verification with U.S. Army Hypothetical Case

Yeo and Kreshock (Ref. [19]) investigated whirl flutter characteristics of hypothetical hingeless hubs with various blade frequency options and established code-to-code consistency among CAMRAD II (Refs. [17, 18]) and RCAS (Refs. [31, 32]) solvers.

The present analysis was verified with this work. Rotor models that exhibit different flap, lag, and torsion frequencies were combined with a simple rigid pylon with root springs and dampers (Fig. 3.1) and a generic NASTRAN wing/pylon model (Fig. 3.2). In the Army paper (Ref. [19]), the NASTRAN wing/pylon was modeled with frequency and mode shape inputs to the comprehensive analysis. In the present work, the model was built into the solver instead of direct inputs and coupled with the rotor. Properties of the rigid pylon are given in Table 3.1. The frequency and mass-normalized mode shapes of the NASTRAN wing/pylon are given in Table 3.2. The terms X, Y, and Z denote translations at the rotor hub, and θ_X, θ_Y, and θ_Z denote rotations. Table 3.3 shows principal rotor characteristics. Table 3.4 shows the rotor frequencies. The slowed rotor is essentially a hyper-stiff in-plane hingeless rotor with a high flap frequency.

Table 3.1: U.S. Army rigid pylon properties (Ref. [19])

Mast length	4 ft
Mass per length	0.00373 slug/ft
Pitch spring stiffness	7000 lbf ft/rad
Yaw spring stiffness	7000 lbf ft/rad
Pitch damping	8.7 lbf ft s/rad
Yaw damping	8.7 lbf ft s/rad

Table 3.2: U.S. Army hypothetical generic NASTRAN wing/pylon frequencies and mass-normalized mode shapes at the rotor hub (Ref. [19])

Mode	**Frequency Hz**	**X***	**Y***	**Z***	$\theta_{\mathbf{X}}{}^\dagger$	$\theta_{\mathbf{Y}}{}^\dagger$	$\theta_{\mathbf{Z}}{}^\dagger$
Wing beam	3.43	0.000	0.000	-2.673	-0.025	-0.015	0.000
Wing chord	6.83	-2.024	-1.593	0.000	0.000	0.000	0.033
Wing torsion	8.63	0.000	0.000	3.954	-0.020	0.116	0.000
Pylon yaw	14.67	-0.720	4.480	0.000	0.000	0.000	-0.093

* Unit: $\sqrt{\mathrm{in}}/\sqrt{\mathrm{lbf\,s^2}}$

† Unit: $\mathrm{rad}/\sqrt{\mathrm{lbf\,s^2\,in}}$

Table 3.3: U.S. Army hypothetical hingeless rotor properties (Ref. [19])

Number of blades	3
Radius	4 ft
Chord	0.5 ft
Precone	2.5°
Twist	-40°, linear
Pitch bearing location	5%
Airfoil lift curve slope	5.7
Airfoil drag coefficient	0.0095
Airfoil moment coefficient	0
Structural damping	1%

Table 3.4: U.S. Army hypothetical hingeless rotor frequencies (Ref. [19])

Type	**Rotor speed rpm**	**Flap frequency /rev**	**Lag frequency /rev**	**Torsion frequency /rev**
Soft in-plane	742	1.19	0.76	7.49
Stiff in-plane 1	742	1.48	1.20	7.49
Stiff in-plane 2	742	1.87	1.54	7.49
Slowed rotor	532.8	2.42	3.16	13.38

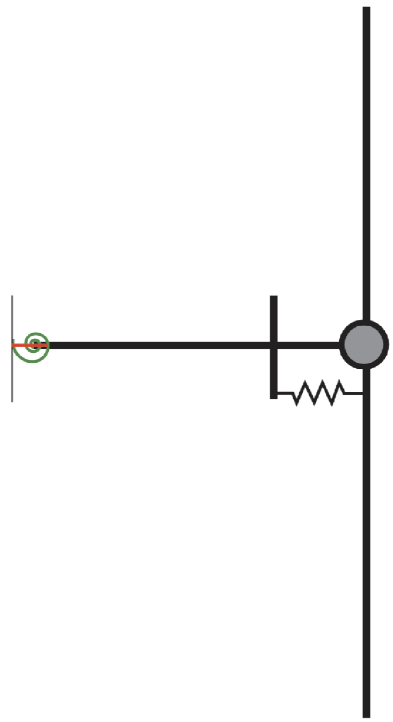

Figure 3.1: U.S. Army hypothetical rigid pylon model (Ref. [19])

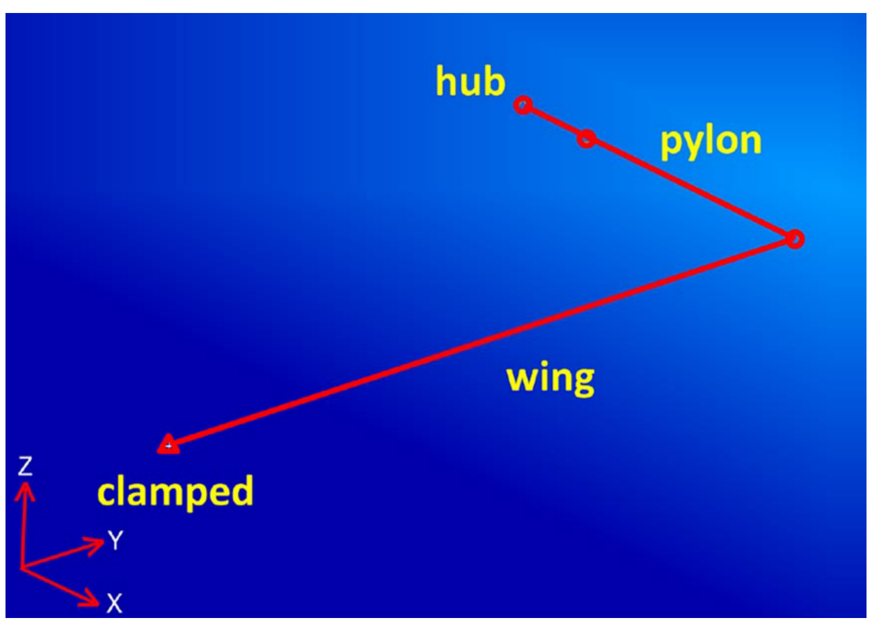

Figure 3.2: U.S. Army hypothetical generic NASTRAN wing/pylon model (Ref. [19])

3.1 Rigid Pylon Results

First, trim solution was obtained for freewheeling condition. Freewheeling results in conservative whirl flutter boundary while achieving near representative collective as powered flight. Next, the frequency and damping of coupled modes were calculated with the eigenanalysis method. Figures 3.3 to 3.7 show the predictions with respect to airspeed and comparison with CAMRAD II and RCAS for the different types of hingeless rotors. Pylon has two degrees of freedom: clockwise (CW) and counterclockwise (CCW) rotation. The pylon CW mode goes unstable (damping goes negative) for the simple rigid rotor (Fig. 3.3). For the soft in-plane rotor (Fig. 3.4), pylon CCW mode is already unstable even at low speeds. For the stiff in-plane rotors (Figs. 3.5 and 3.6), pylon CCW mode goes unstable when it starts coalescing with the low-frequency lag ($\zeta - 1$) mode (Figs. 3.5a and 3.6a). For the slowed rotor (Fig. 3.7), pylon CW is the critical mode. The agreement for the rigid rotor (Fig. 3.3) is excellent. Small differences in both frequency and damping are observed for the elastic rotor cases (Figs. 3.4 to 3.7), but the trends are correctly captured, and the agreement is satisfactory.

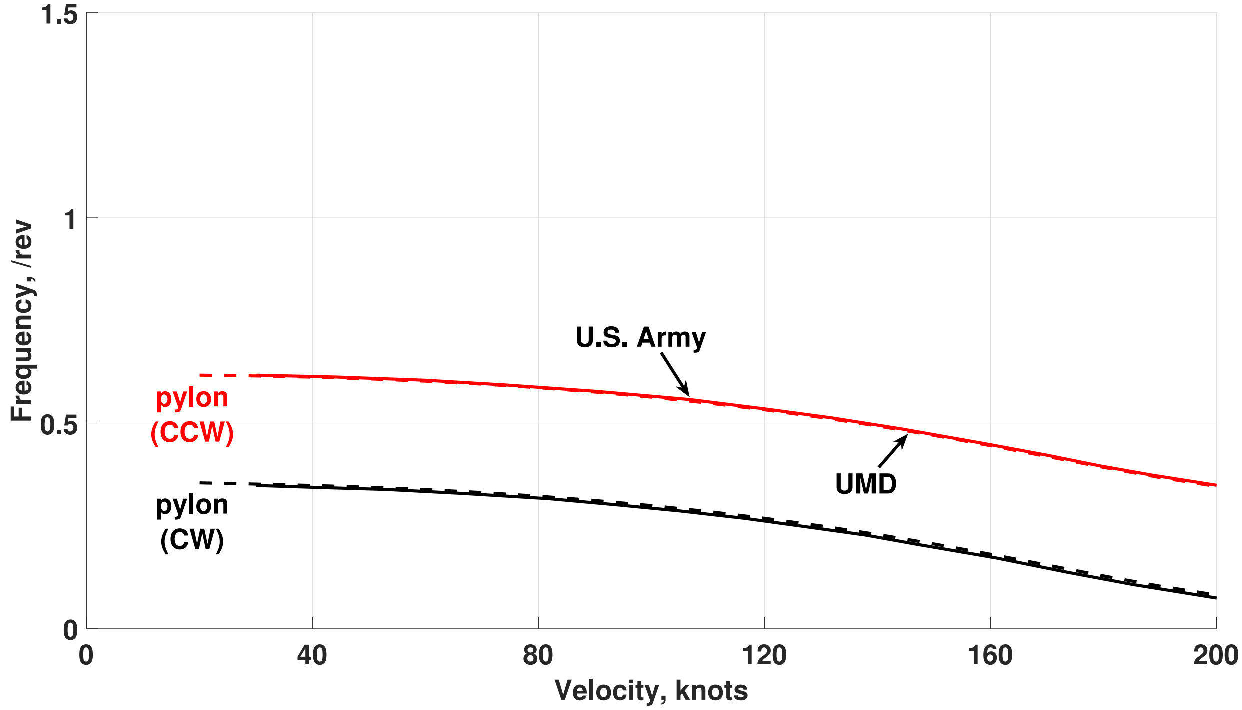

(a) Frequency

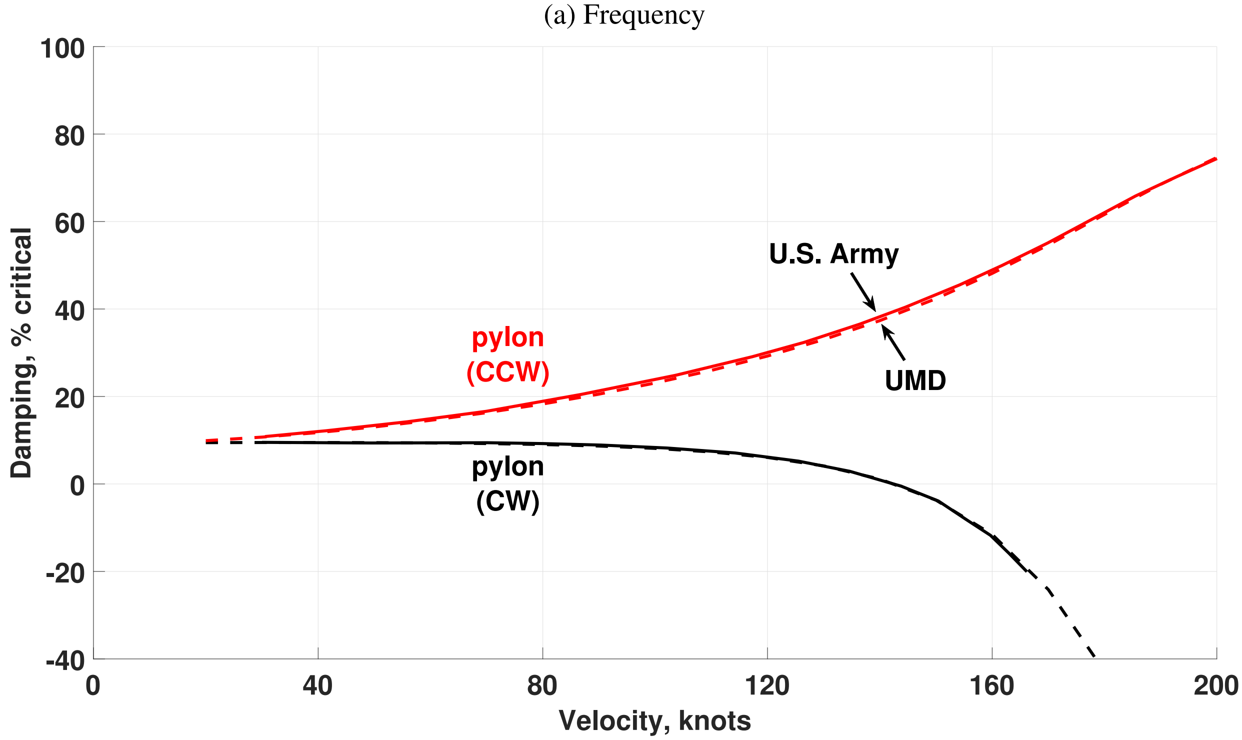

(b) Damping

Figure 3.3: Aeroelastic stability verification for rigid pylon and rigid rotor (solid: U.S. Army predictions with CAMRAD II and RCAS (Ref. [19]), dash: UMD predictions with UMARC-II)

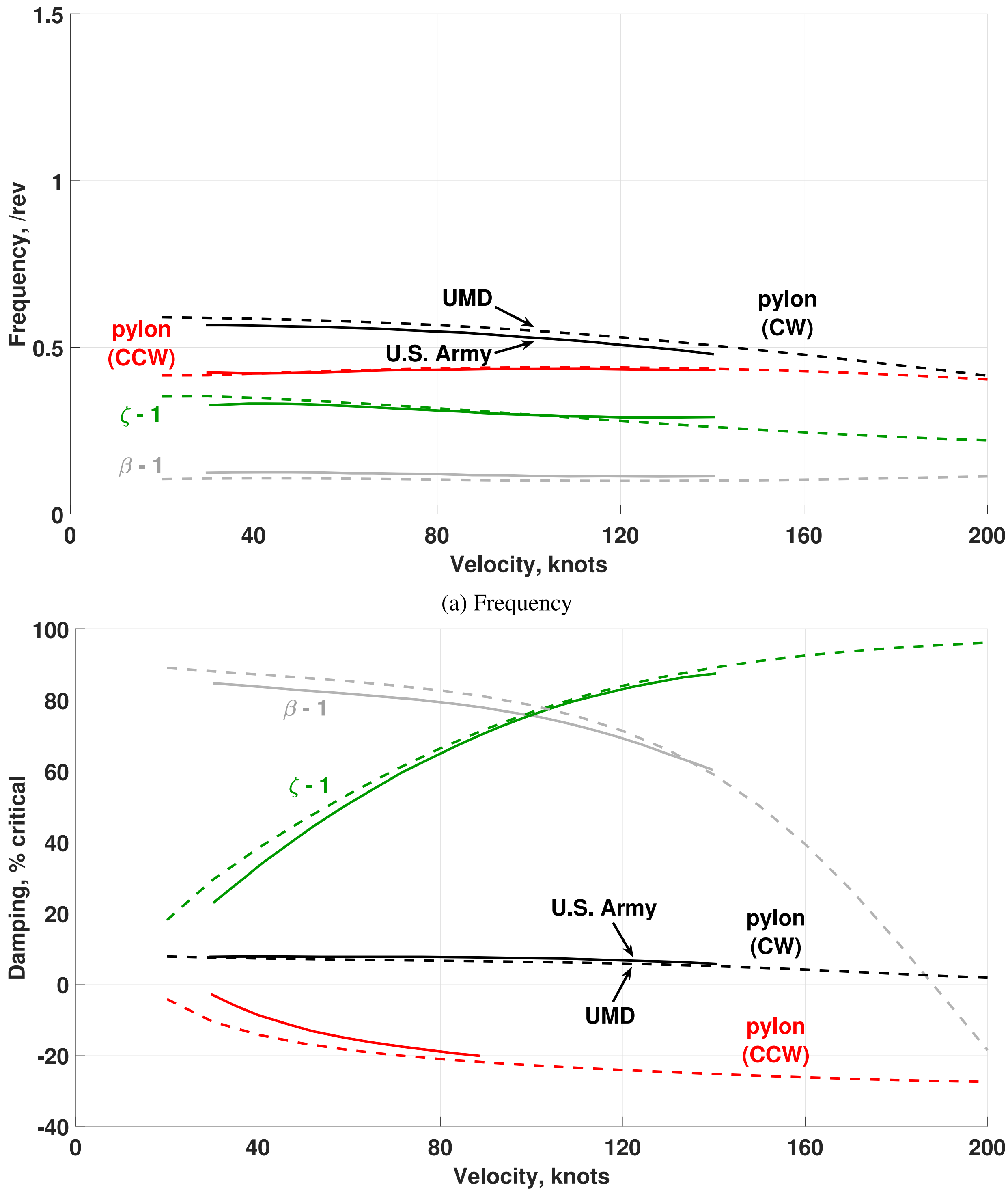

(a) Frequency

(b) Damping

Figure 3.4: Aeroelastic stability verification for rigid pylon and soft in-plane rotor (solid: U.S. Army predictions with CAMRAD II and RCAS (Ref. [19]), dash: UMD predictions with UMARC-II)

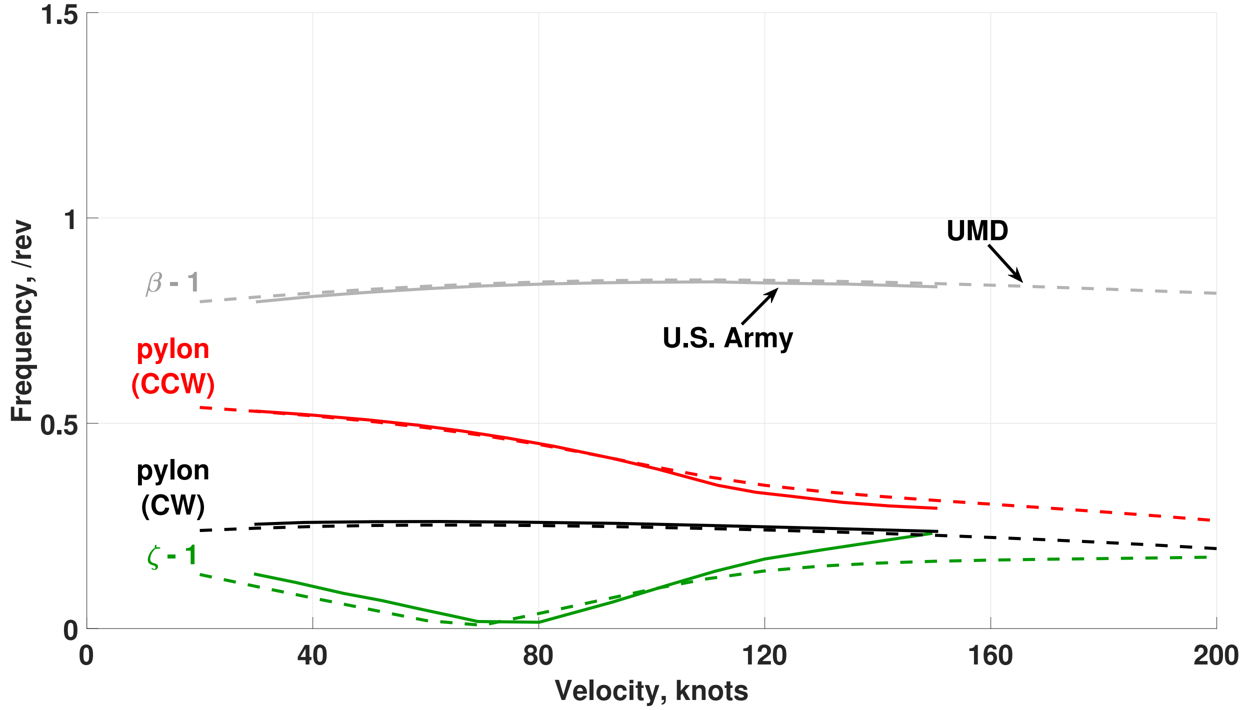

(a) Frequency

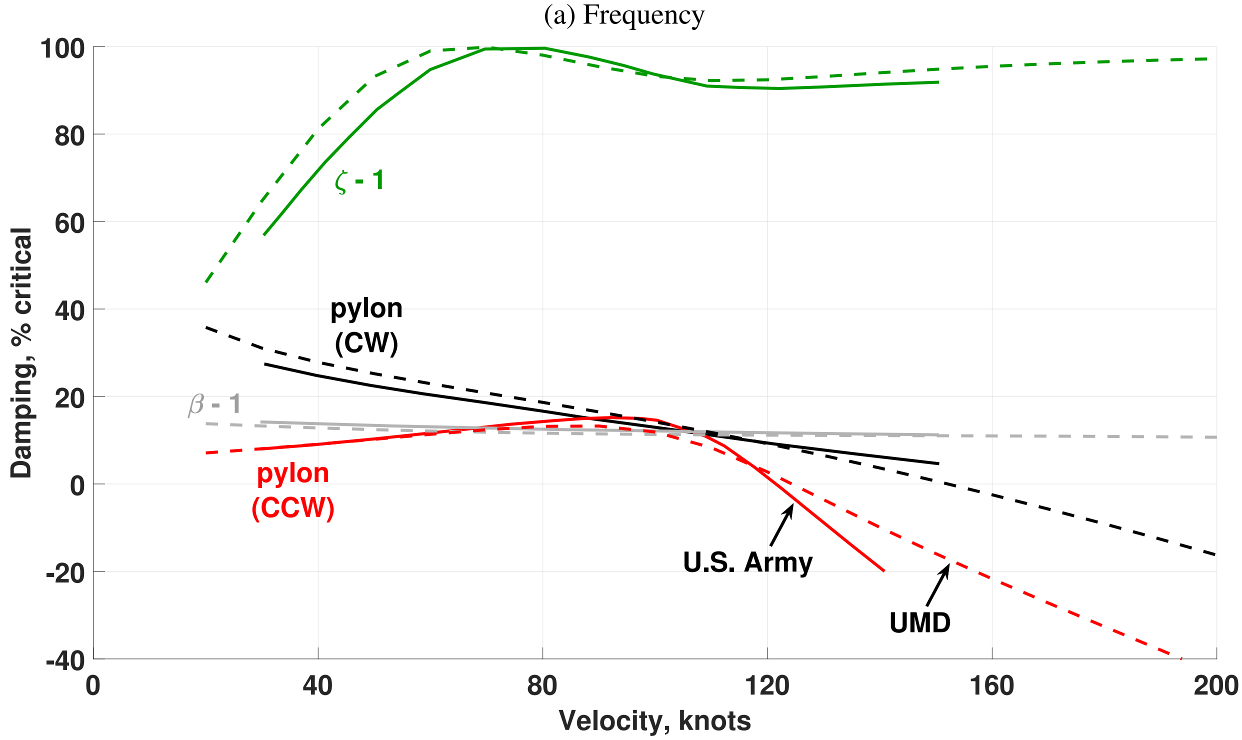

(b) Damping

Figure 3.5: Aeroelastic stability verification for rigid pylon and stiff in-plane 1 rotor (solid: U.S. Army predictions with CAMRAD II and RCAS (Ref. [19]), dash: UMD predictions with UMARC-II)

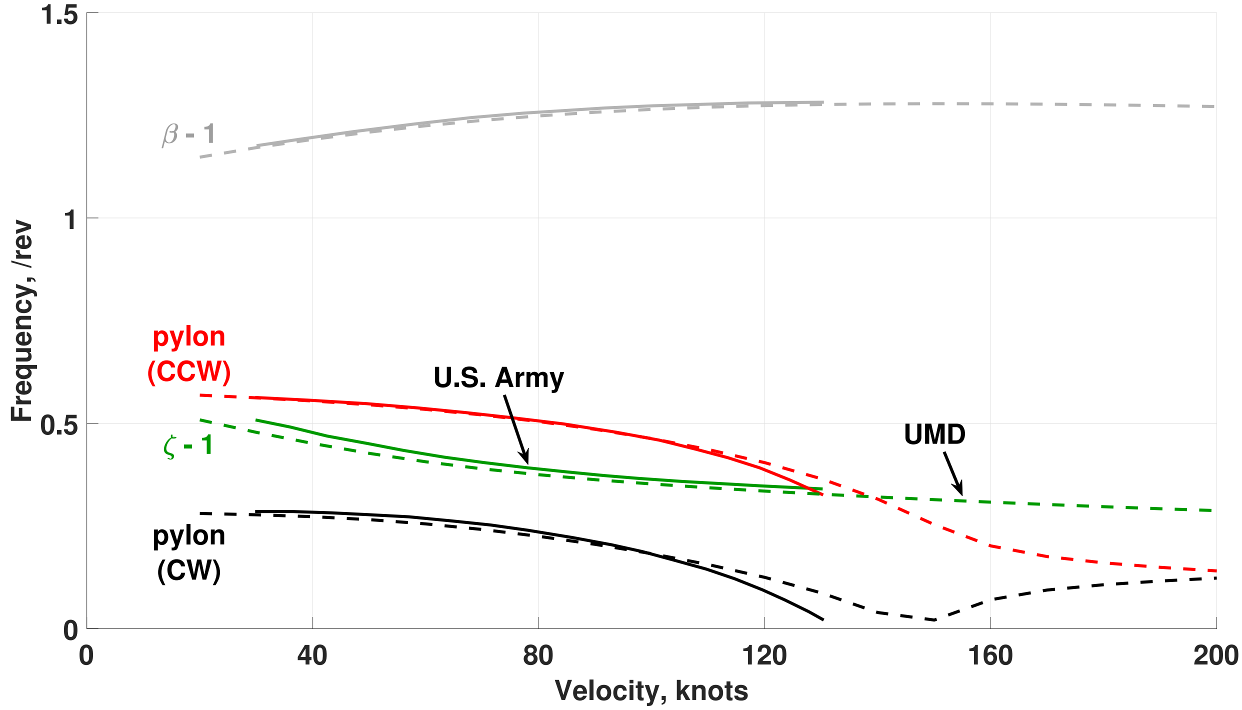

(a) Frequency

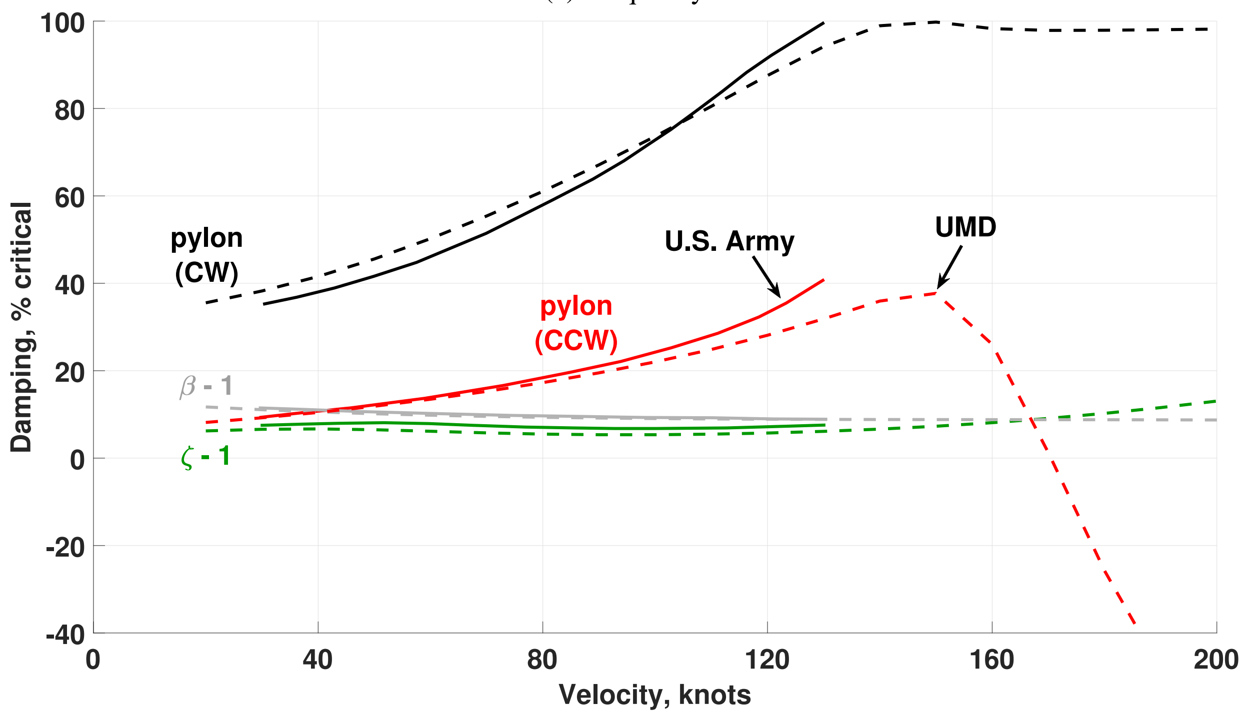

(b) Damping

Figure 3.6: Aeroelastic stability verification for rigid pylon and stiff in-plane 2 rotor (solid: U.S. Army predictions with CAMRAD II and RCAS (Ref. [19]), dash: UMD predictions with UMARC-II)

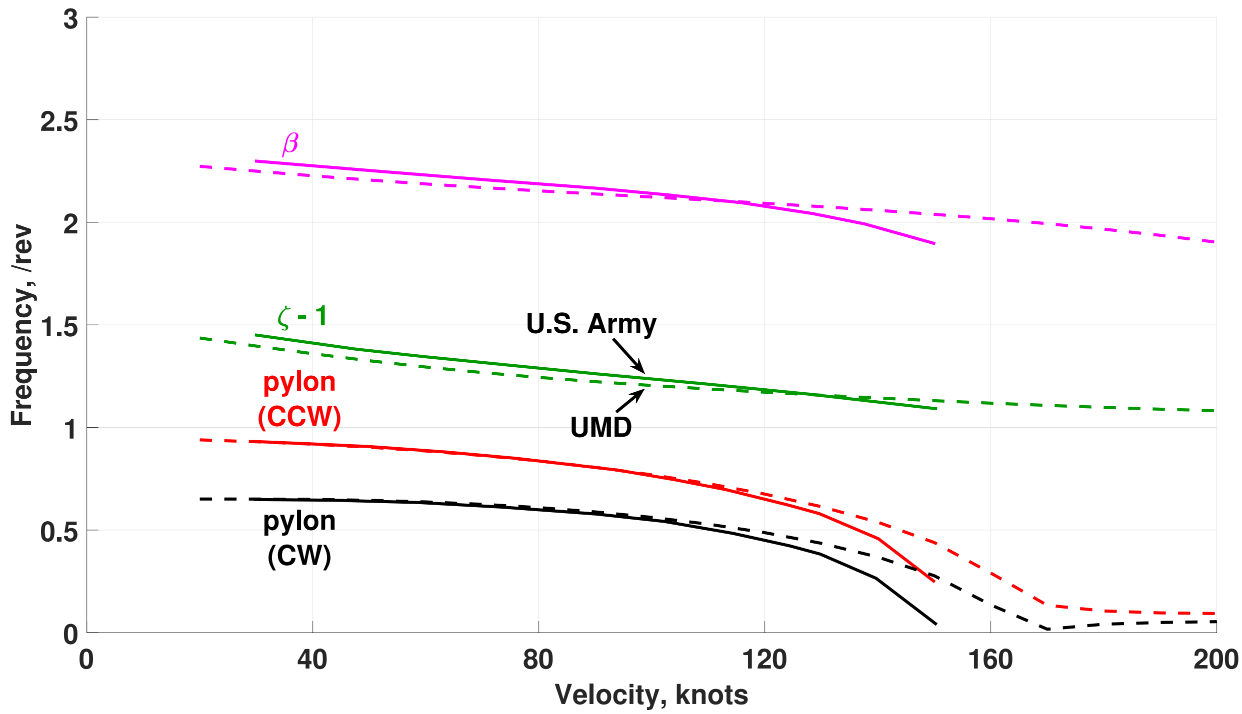

(a) Frequency

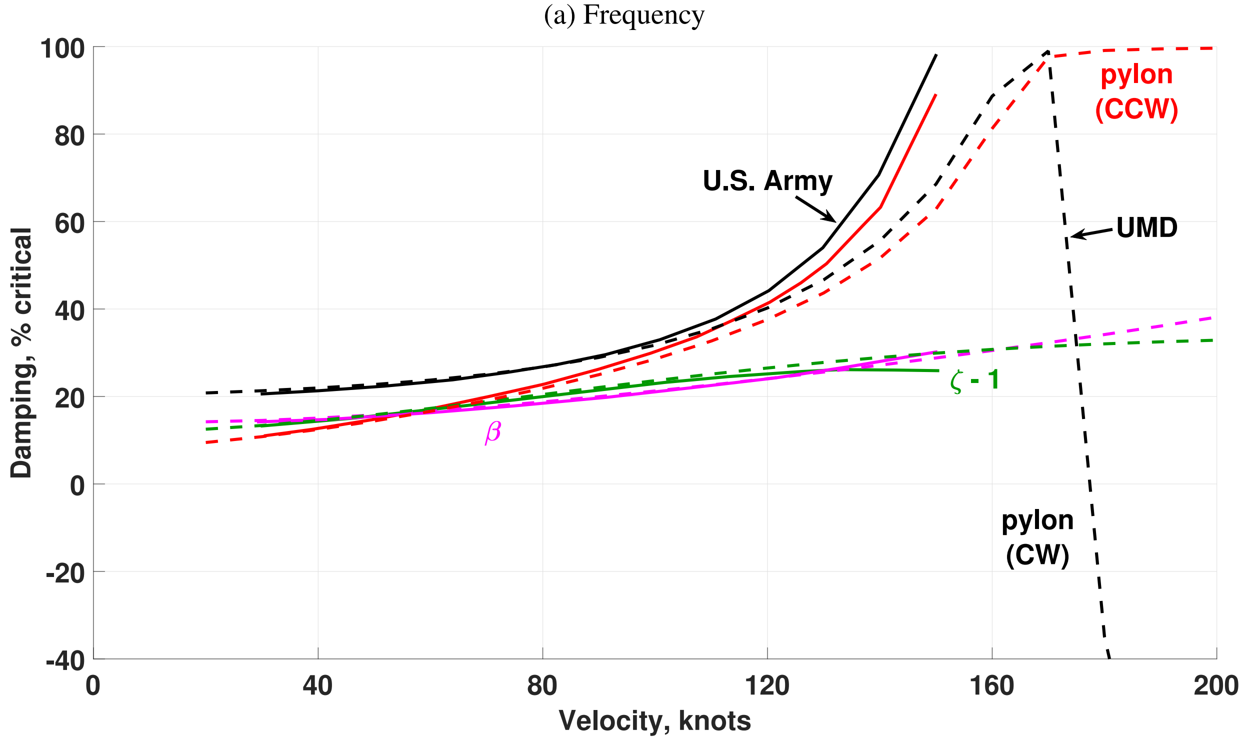

(b) Damping

Figure 3.7: Aeroelastic stability verification for rigid pylon and slowed rotor (solid: U.S. Army predictions with CAMRAD II and RCAS (Ref. [19]), dash: UMD predictions with UMARC-II)

3.2 Generic Wing/Pylon Results

Figures 3.8 to 3.11 show comparison of predictions for the generic NASTRAN wing/pylon cases. For the soft in-plane rotor (Fig. 3.8), the wing chord (q_2) mode goes unstable at around $80\ \mathrm{knots}$ when it coalesces with the collective lag (ζ) mode. Wing beam (q_1) mode is already unstable at low speeds. For the stiff in-plane 1 rotor (Fig. 3.9), wing beam (q_1) mode is critical and the instability speed is around $140\ \mathrm{knots}$. Wing beam (q_1) mode is again the critical mode for the stiff in-plane 2 rotor (Fig. 3.10); this time the instability speed is $175\ \mathrm{knots}$. Finally, for the slowed rotor (Fig. 3.11), no instability is observed up to $200\ \mathrm{knots}$. The instability speed seems to increase with higher rotor frequencies. There are some discrepancies between UMD and U.S. Army predictions. UMD predictions show a slower change for the frequency of the low-frequency lag ($\zeta - 1$) mode with respect to airspeed for all the cases, which impacts the coalescence of the modes and subsequently the damping values. The source of this discrepancy is unclear; however, the trends were predicted for both frequency and damping.

3.3 Summary and Conclusions

The developed solver was verified with U.S. Army's CAMRAD II and RCAS predictions. The stability of a total of nine hypothetical cases was studied. Rotors that exhibit different natural frequencies were modeled. The pylon model was varied from a rigid pylon with root springs and dampers to a generic NASTRAN wing/pylon. A better agreement was observed for the rigid pylon cases compared to the NASTRAN wing/pylon cases. Some discrepancies in the magnitudes are present, but the predictions captured the general trends, which means that the physical phenomenon was modeled correctly.

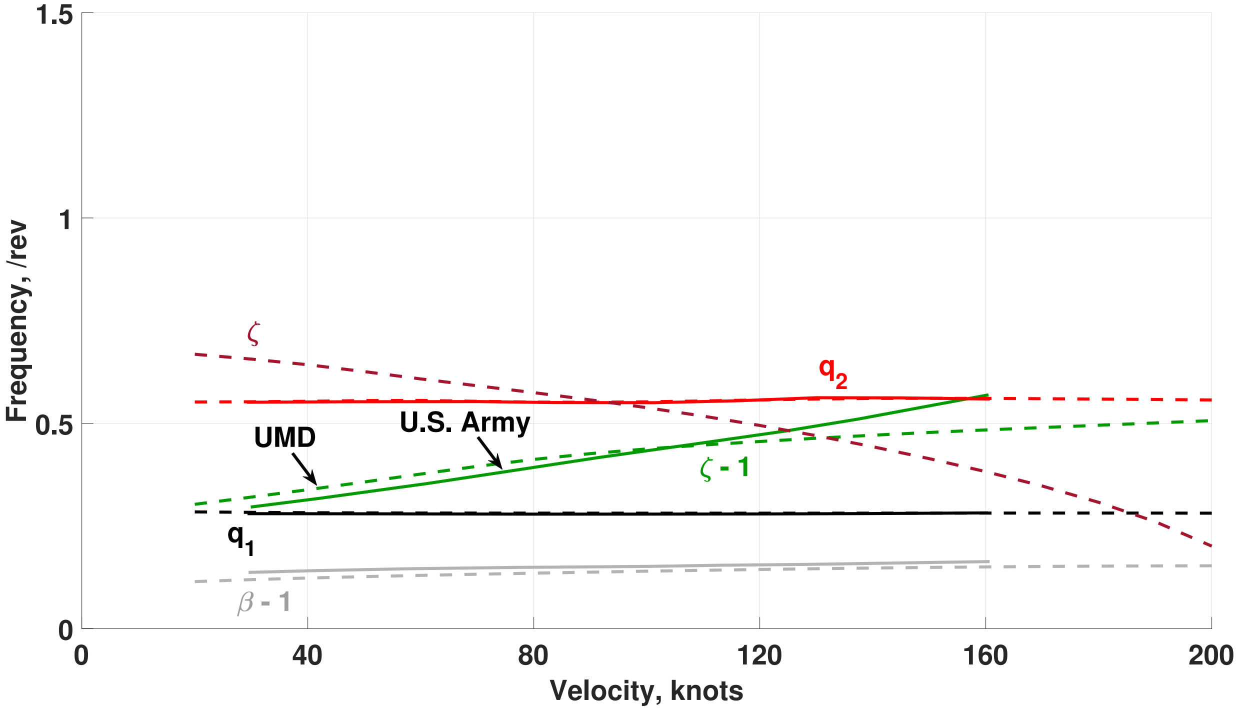

(a) Frequency

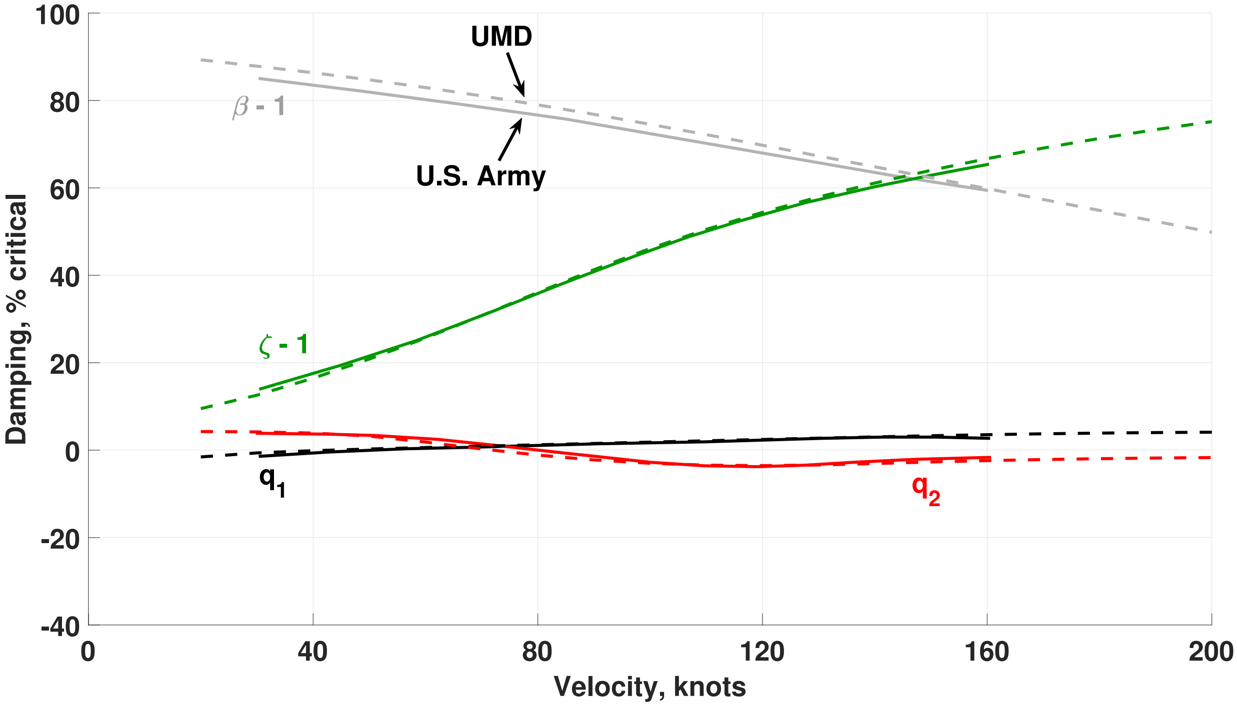

(b) Damping

Figure 3.8: Aeroelastic stability verification for generic wing/pylon and soft in-plane rotor (solid: U.S. Army predictions with CAMRAD II and RCAS (Ref. [19]), dash: UMD predictions with UMARC-II)

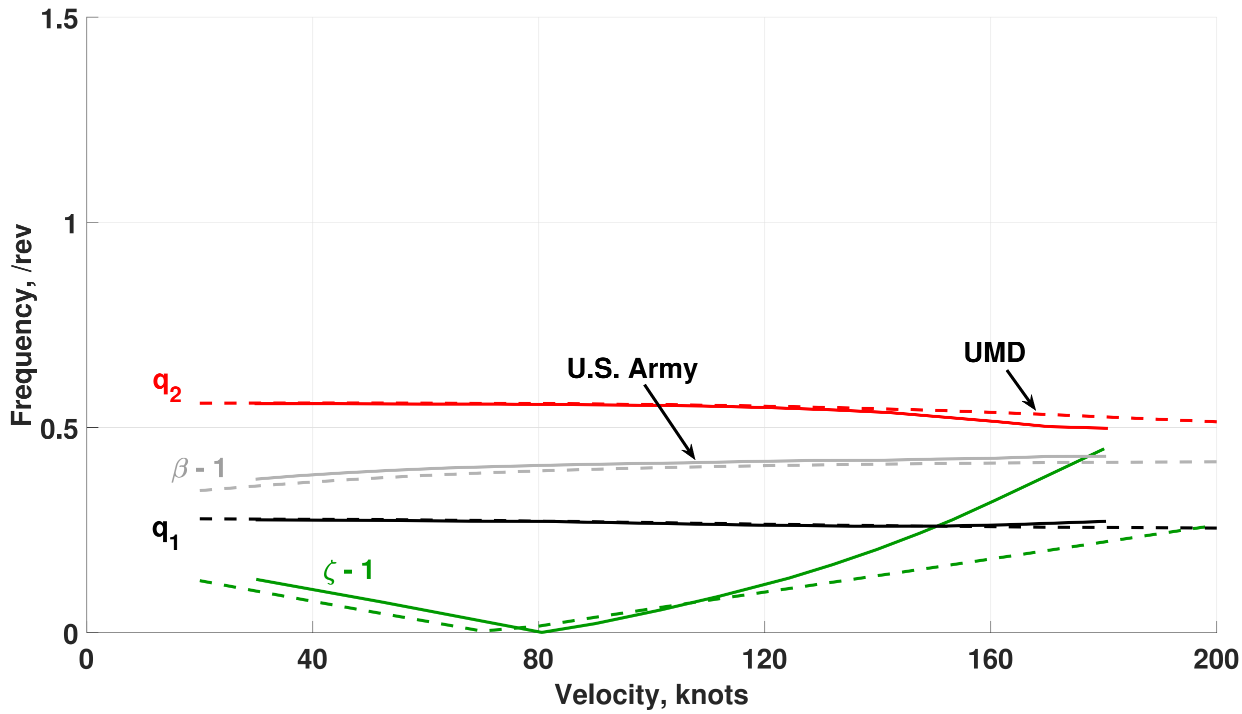

(a) Frequency

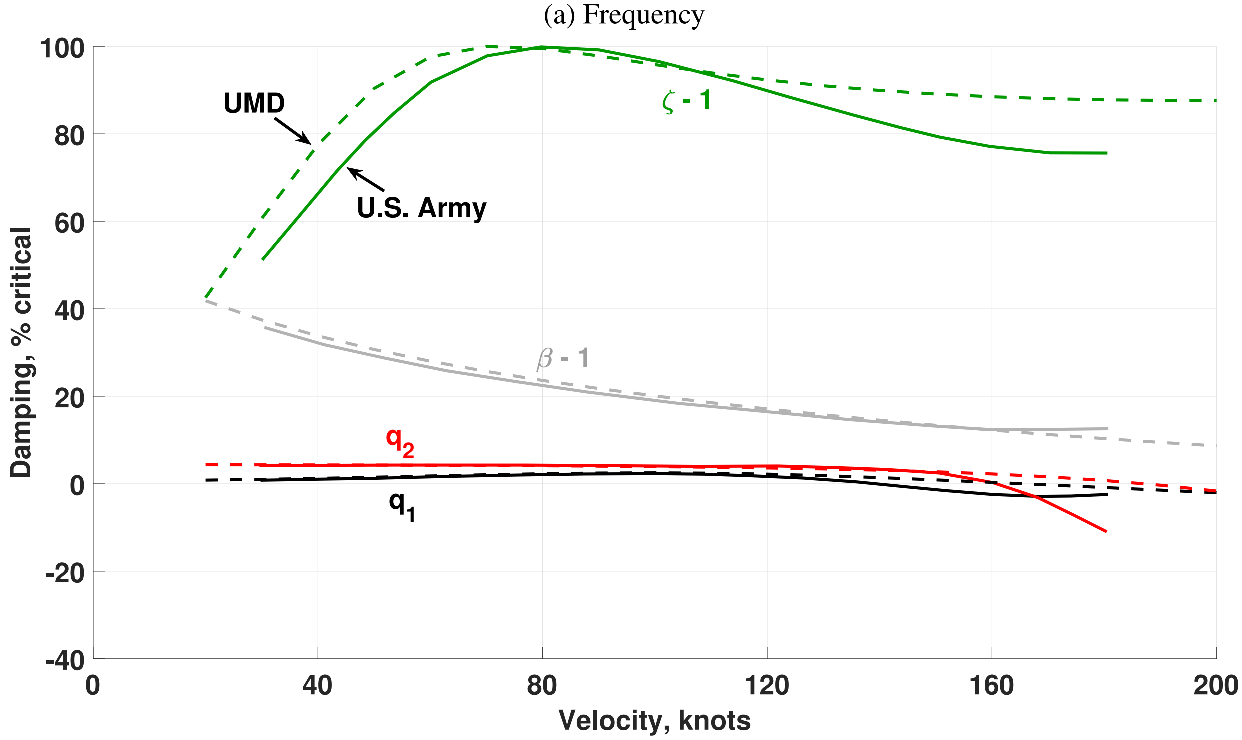

(b) Damping

Figure 3.9: Aeroelastic stability verification for generic wing/pylon and stiff in-plane 1 rotor (solid: U.S. Army predictions with CAMRAD II and RCAS (Ref. [19]), dash: UMD predictions with UMARC-II)

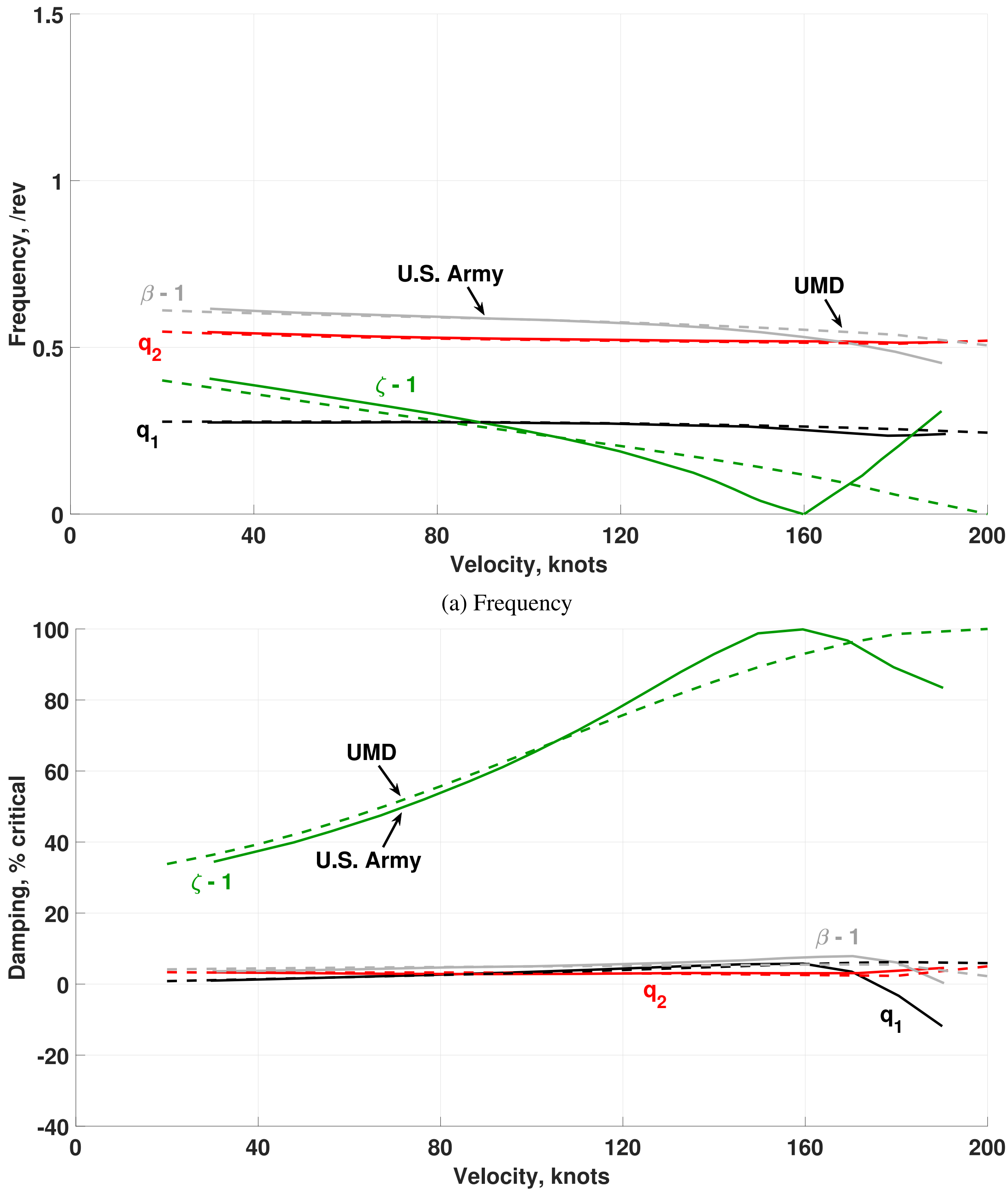

(a) Frequency

(b) Damping

Figure 3.10: Aeroelastic stability verification for generic wing/pylon and stiff in-plane 2 rotor (solid: U.S. Army predictions with CAMRAD II and RCAS (Ref. [19]), dash: UMD predictions with UMARC-II)

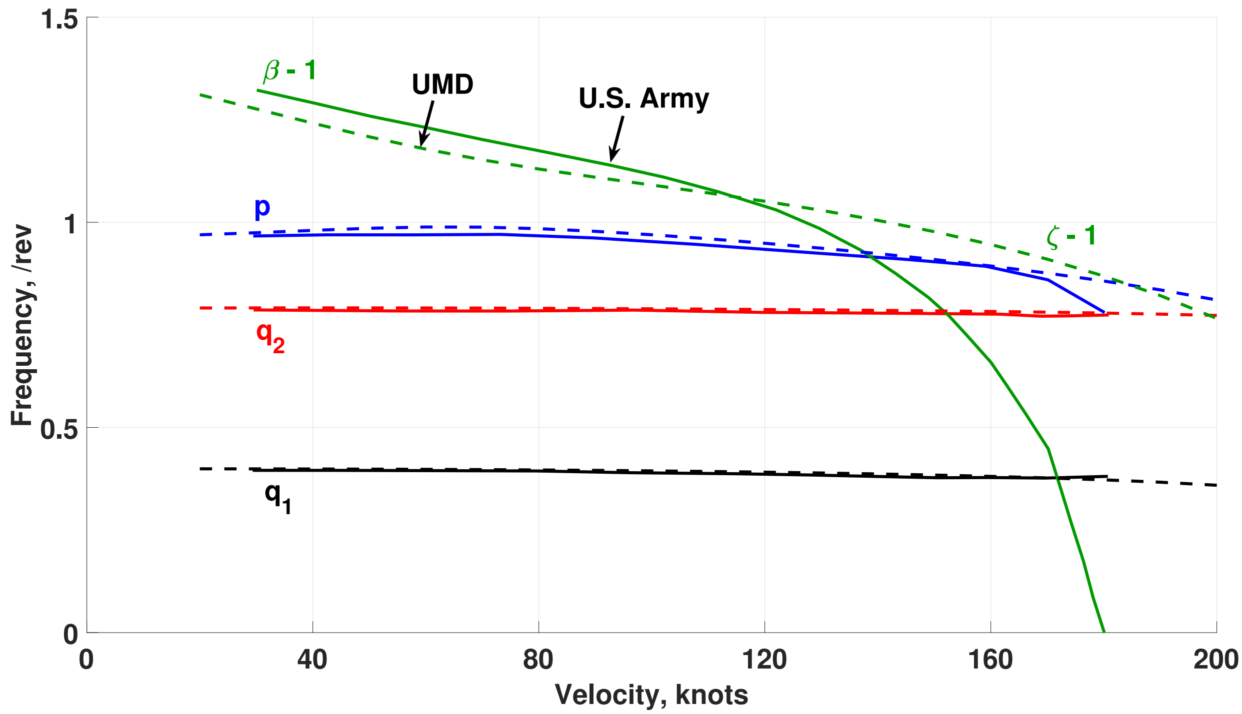

(a) Frequency

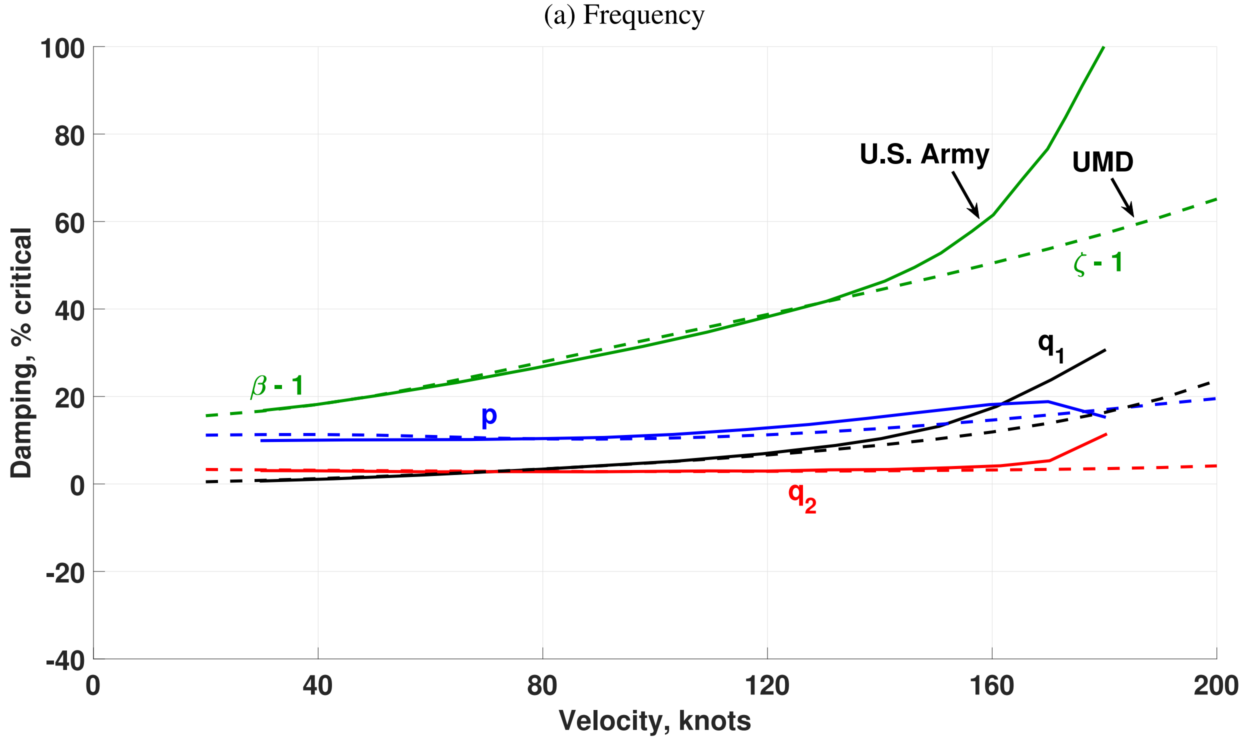

(b) Damping

Figure 3.11: Aeroelastic stability verification for generic wing/pylon and slowed rotor (solid: U.S. Army predictions with CAMRAD II and RCAS (Ref. [19]), dash: UMD predictions with UMARC-II)

Chapter 4: Validation with Full-Scale Boeing M222 Test and Fundamental Understanding

A full-scale Boeing M222 rotor was tested in the NASA Ames $40\text{-ft} \times 80\text{-ft}$ wind tunnel in 1972. Performance, loads, and stability of the rotor/pylon/wing system were measured. These tests provided the only available validation data for soft in-plane hingeless hub stability.

4.1 Boeing M222 Rotor

The Boeing M222 tiltrotor aircraft utilized a 26-ft diameter rotor with a soft in-plane hingeless hub. Two types of tests were conducted: unpowered (freewheeling) rotor on two vertically mounted semi-span wings (full- and quarter-stiffness NASA dynamic wing test stands, Fig. 1.11a) and powered rotor on an isolated propeller test rig (Fig. 1.11b). The principal characteristics of the rotor and the full-stiffness NASA dynamic wing test stand are given in Tables 4.1 and 4.2. The test points are shown in Table 4.3.

The stability of the rotor/pylon/wing system was measured at multiple rotor and tunnel speeds but only up to 192 knots (200 knots was the maximum speed of the $40\text{-ft} \times 80\text{-ft}$ tunnel at the time). Although the maximum tunnel speed was limited and away from any instability, the tip speed was varied at set tunnel speeds until proprotor air resonance behavior was observed. The purpose of testing the rotor on the quarter-stiffness wing, which exhibited half the natural

Table 4.1: Boeing M222 rotor properties

Number of blades	3
Radius	13 ft
Chord	1.57 ft
Precone	2.5°
Torque offset	0.65 in (lead)
Solidity	0.115
Twist	-41°
Rotor speed – helicopter	551 rpm
Rotor speed – airplane	386 rpm
Rotation direction	counterclockwise
Airfoil (10%R)	NACA 23021
Airfoil (45%R-100%R)	Boeing-Vertol 23010-1.58
Root cutout	10%
Pitch bearing location	7.2%
Swashplate phase angle	20°

Table 4.2: Full-stiffness NASA dynamic wing test stand properties

Span	165 in
Thickness	13.5%
Chord	5.17 ft
Pylon length	43.2 in (28%R)
Pylon mass (without blades)	2000 lb
Pylon c.g. offset	10.8 in (6.9%R, fwd.)

frequencies of the full-stiffness wing, was to simulate an inflow ratio equivalence of 400 knots (the rotor operated at half the design rotation speed). However, the simulation of the blade frequencies was not satisfactory at this rotor speed due to the first bending frequency (lag mode) being close to $1/\text{rev}$. This not only had an influence on the dynamics but also meant large vibrations and blade loads. The model was excited with a shaker vane mounted outboard of the nacelle, which could oscillate at various amplitudes and at frequencies ranging from 2 Hz to 20 Hz. Two sets of strain gauges were installed on the wing: one set near the root to measure flap bending, chord bending, and torsion moments, and another near the tip to measure chord bending and torsion moments, and normal and chordwise forces. Flap and chord bending moments along

Table 4.3: Boeing M222 test points

Test	Run	Condition	V knots	i_N deg	Ω rpm	M_{tip}
416	6	Hover	0^*	0	var	var
416	$7^\dagger$, 15	Hover	0^*	0	551	0.67
416	16	Shutdown	0^*	66	var	var
416	19	Transition	45	85	500	0.61
416	22	Transition	76	83	500	0.61
416	21	Transition	80	66	550	0.67
416	20	Transition	80	66	500	0.61
416	$9^\dagger$	Transition	105	27	551	0.67
416	13	Transition	140	27	551	0.67
416	$11^\dagger$	Cruise	140	10	386	0.47
416	14	Cruise	170	10	386	0.47
410	$(3 – 7)^\dagger$	Freewheeling	50	0	var	var
410	$8^\dagger$	Freewheeling	60	0	var	var
410	$(9, 10)^\dagger$	Freewheeling	100	0	var	var
410	$(12, 17)^\dagger$	Freewheeling	140	0	var	var
410	$(14, 15)^\dagger$	Freewheeling	192	0	var	var

* Effectively in climb due to tunnel recirculation
† Conditions analyzed

the blade were measured at multiple span stations. Control loads were collected on a pitch link and on the longitudinal actuator ground point bolt. One historical importance of this test is that another related model, the Bell Model 300 rotor with a gimballed, stiff in-plane hub, was also tested with the same wings in the same wind tunnel. Therefore, this test marked the first interchangeable hub tiltrotor wind tunnel test.

The rotor/pylon/wing model built in the present solver is shown in Fig. 4.1. The model uses ten elastic rotor modes, uniform inflow or freewake options, and appropriate airfoil decks for both the rotor and the wing. The rotor airfoil decks were obtained with in-house 2D CFD – TURNS (Ref. [86]). Linear interpolation was used for the airfoil transition region ($10\%R$ – $45\%R$). Stability results were obtained in freewheeling mode operation. Freewheeling means an unpowered rotor; hence allows for rotor speed perturbation. This model was built by stitching the properties given in Refs. [4, 33, 71]. The rotor section properties are given in Fig. 4.2. The full-stiffness wing was modeled. The wing/pylon model uses orthogonal frequency and mass-normalized mode shape inputs along the wing span, pylon, and hub, as reported in Tables 4.4 to 4.6. The modal damping values given in Tables 4.4 to 4.6 were obtained experimentally with blades off at 100-knots tunnel speed; they include structural and aerodynamic damping. The mode shape points and the axis system are shown in Fig. 4.3.

Figure 4.4 shows the rotor frequencies together with the test data. Predictions are shown for $8.8°$ (solid lines) and $40°$ (dashed lines) collective angles. Test data is shown for $0°$, $8.8°$, $23°$, $24.7°$, and $40°$ collectives. The nonrotating and rotating frequencies are accurately predicted.

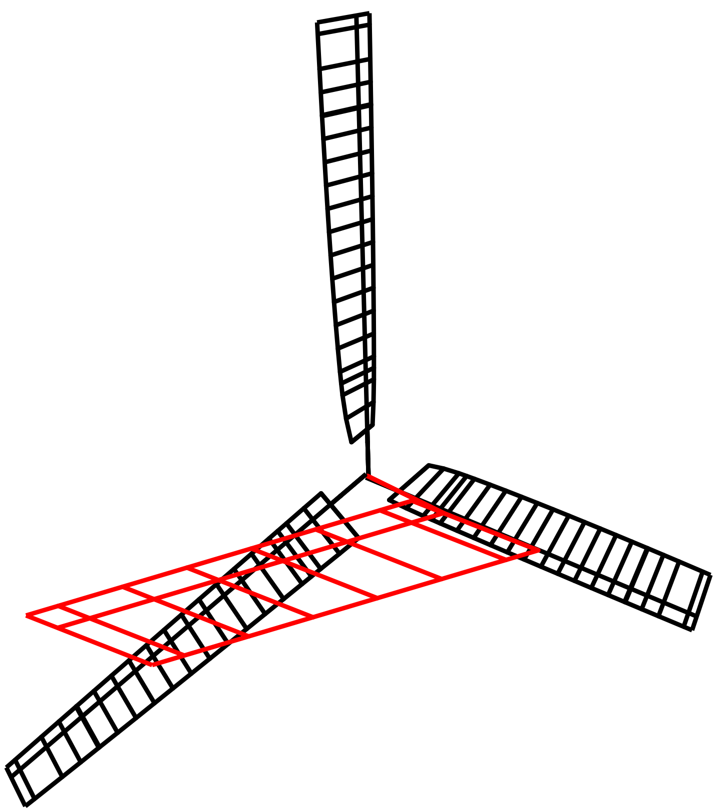

Figure 4.1: UMARC-II model of the Boeing M222 tiltrotor
(rotor, pylon, and wing are beams, panels show aerodynamic segments)

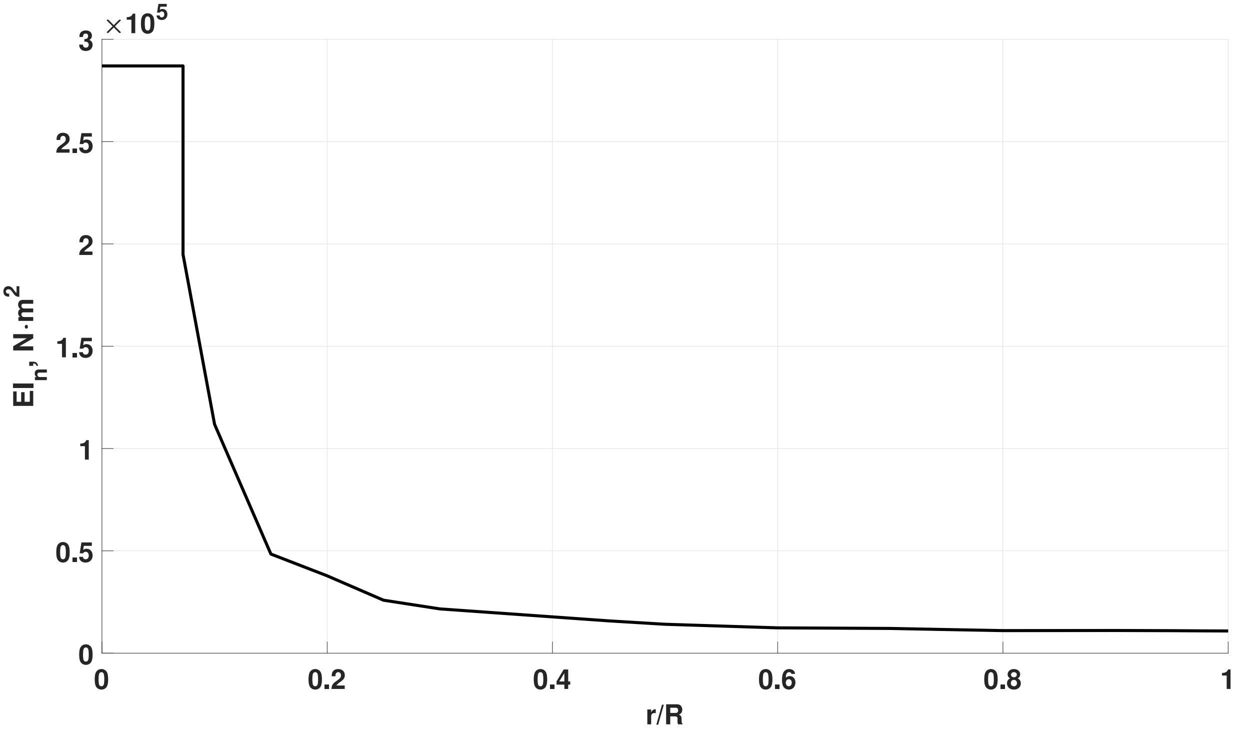

(a) Rotor normal stiffness

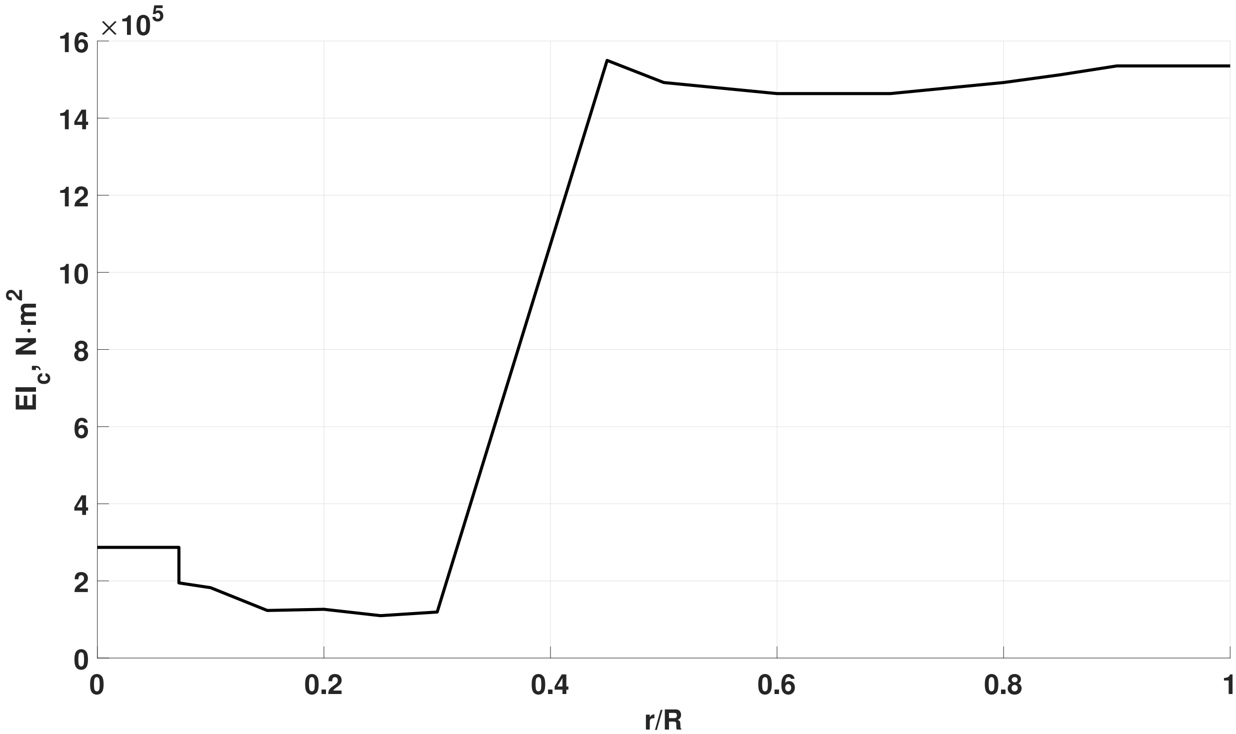

(b) Rotor chordwise stiffness

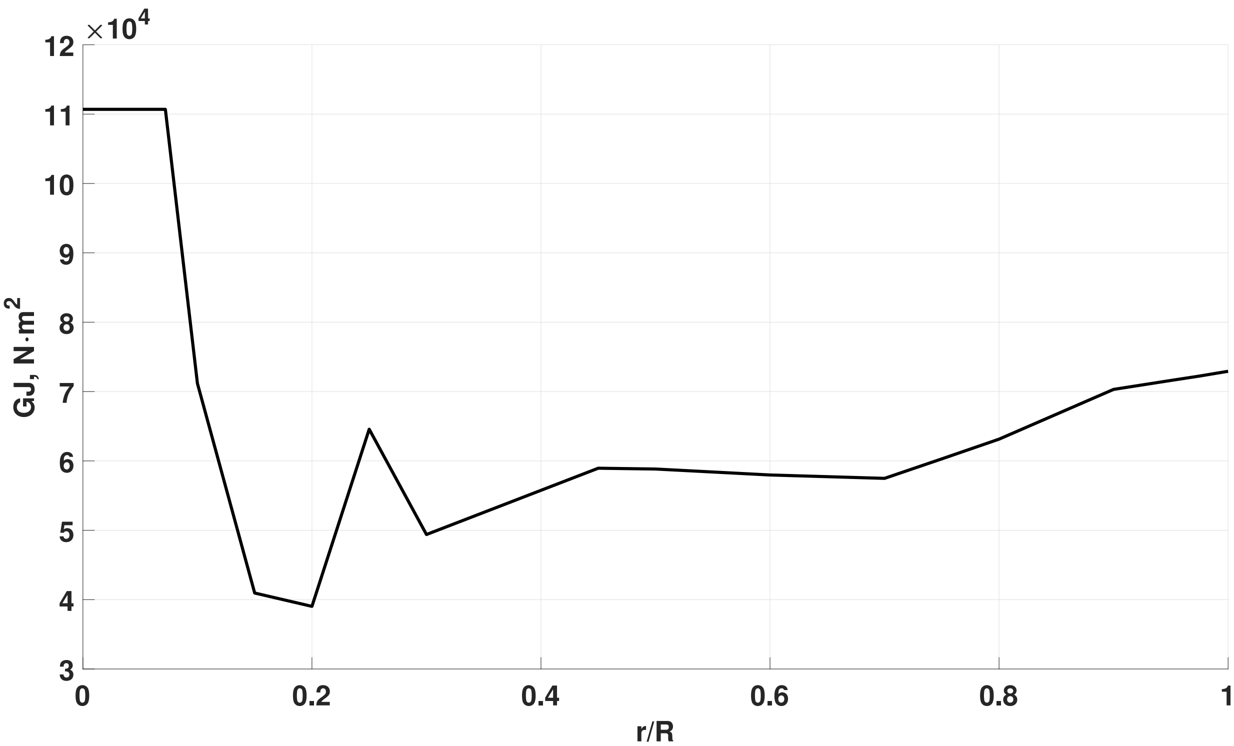

(c) Rotor torsional stiffness

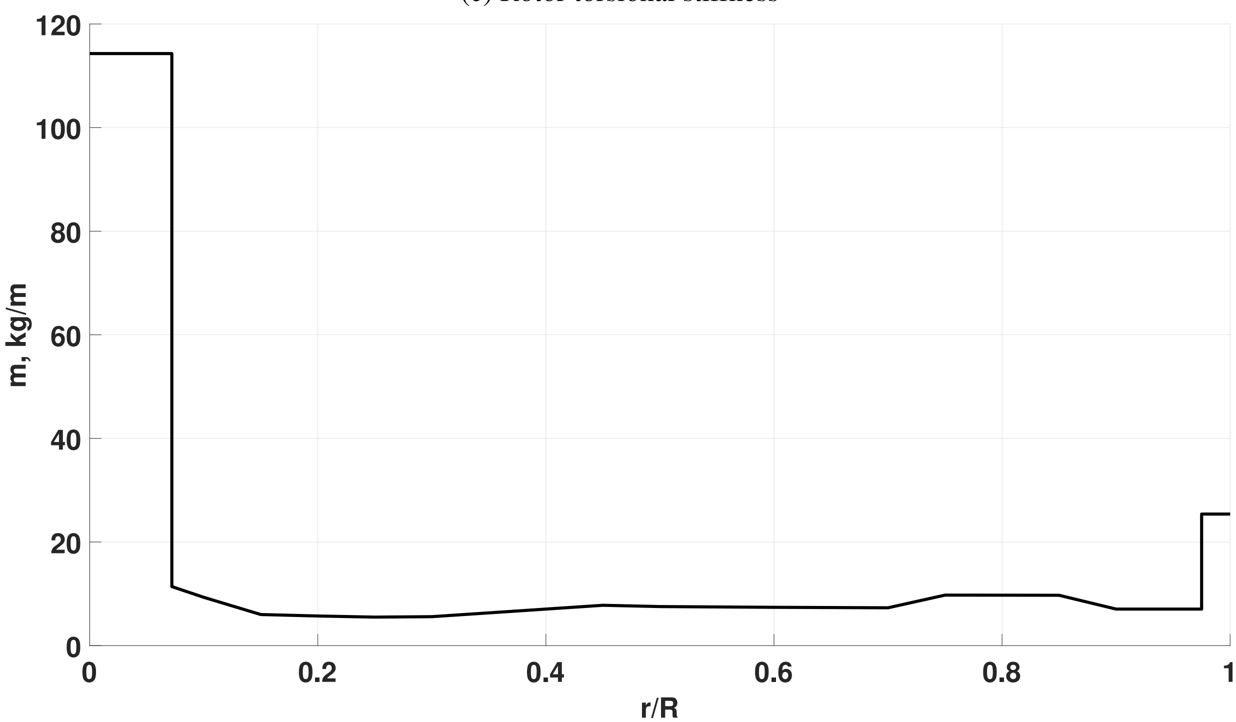

(d) Rotor mass per length

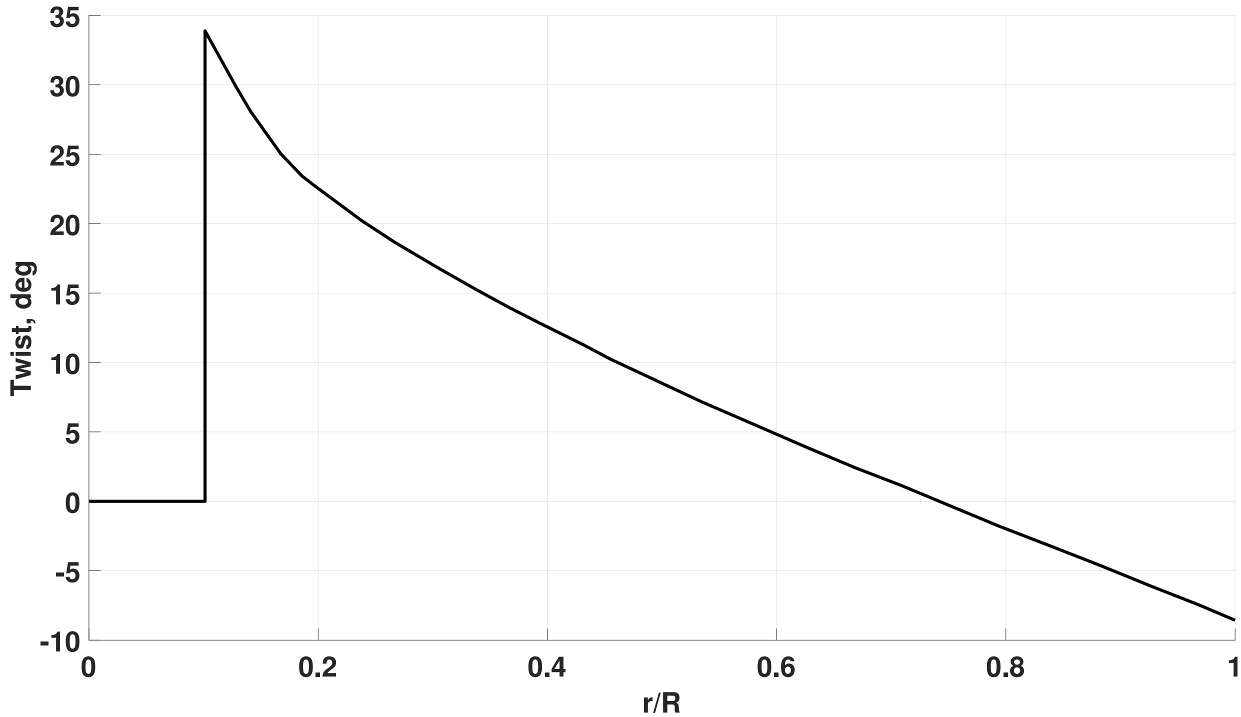

(e) Rotor twist

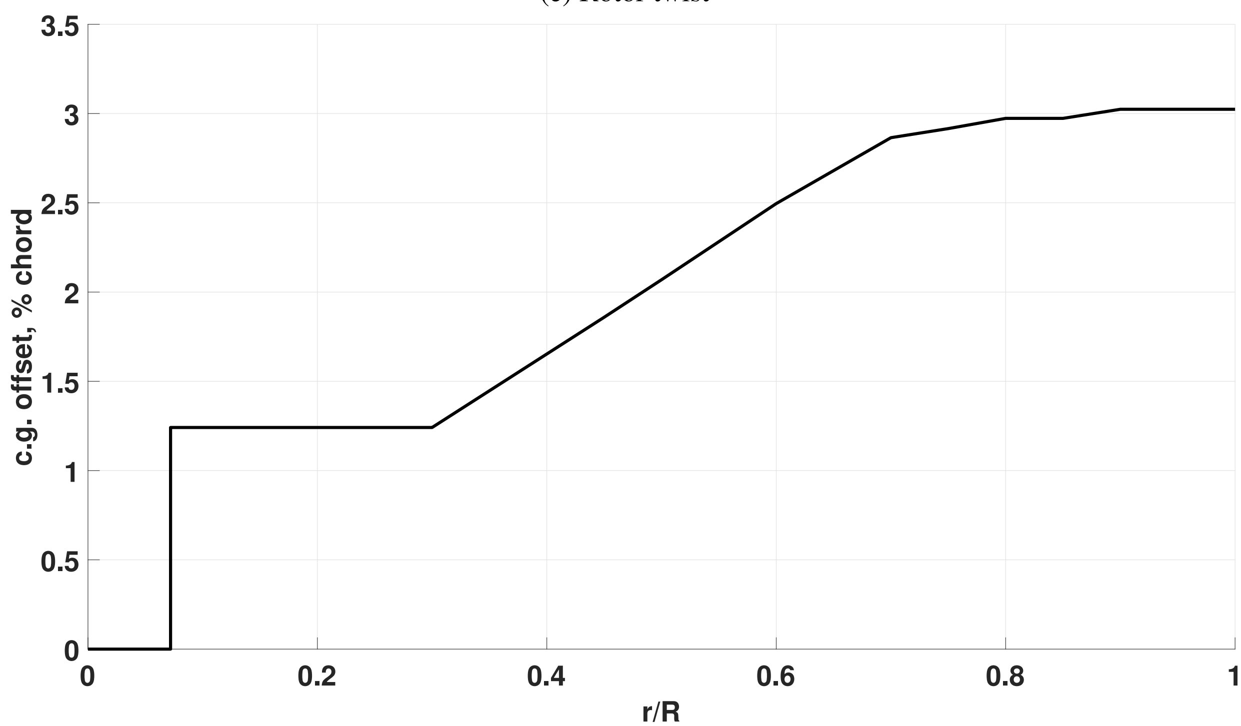

(f) Rotor center of gravity offset from elastic axis (positive toward trailing edge)

Figure 4.2: Boeing M222 rotor properties

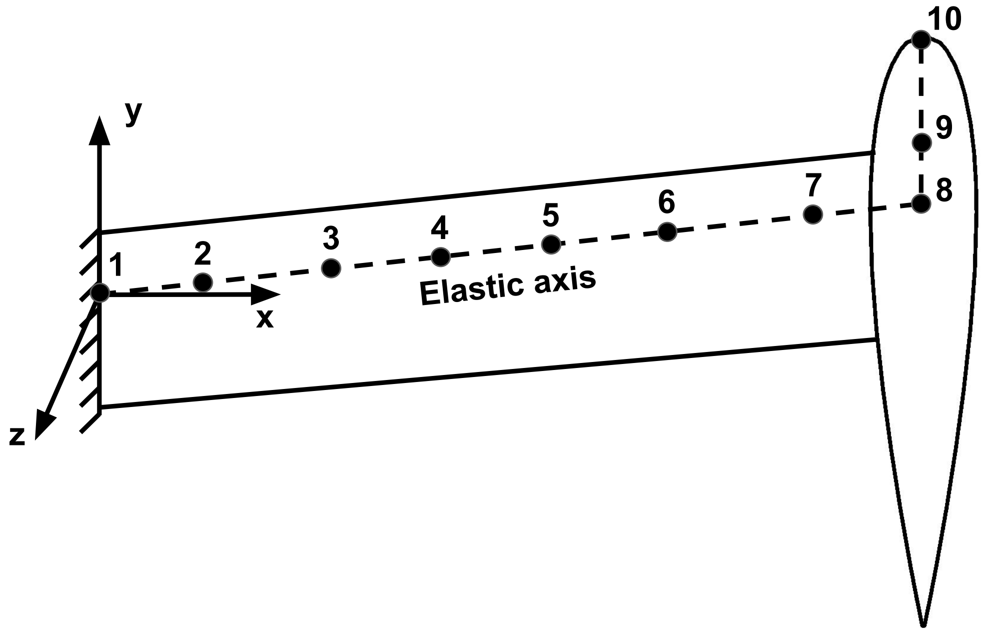

Figure 4.3: Boeing M222 mode shape points

Table 4.4: Boeing M222 wing beam mode
mass-normalized mode shape (Ref. [71])

Frequency = 2.5 Hz
Damping = 1%

Point	**r, in**	$\mathbf{x}^*$	$\mathbf{y}^*$	$\mathbf{z}^*$	$\theta_\mathbf{x}{}^\dagger$	$\theta_\mathbf{y}{}^\dagger$	$\theta_\mathbf{z}{}^\dagger$
1	0	0	0	0	0	0	0
2	13.75	0	0	0.005	0	0.001	0
3	41.25	0	-0.001	0.040	0	0.002	0
4	68.75	0	-0.002	0.104	-0.001	0.003	0
5	96.25	0	-0.004	0.191	-0.001	0.003	0
6	123.75	0.001	-0.006	0.293	-0.001	0.004	0
7	151.25	0.001	-0.008	0.405	-0.001	0.004	0
8	165	0.001	-0.009	0.463	-0.001	0.004	0
9	175.76	0.002	-0.009	0.475	-0.001	0.004	0
10	208.22	0.005	-0.009	0.511	-0.001	0.004	0

* Unit: $\sqrt{\mathrm{in}}/\sqrt{\mathrm{lbf\,s^2}}$
† Unit: $\mathrm{rad}/\sqrt{\mathrm{lbf\,s^2\,in}}$

Table 4.5: Boeing M222 wing chord mode mass-normalized mode shape (Ref. [71])

Frequency = 4.6 Hz
Damping = 0.64%

Point	**r, in**	$\mathbf{x}^*$	$\mathbf{y}^*$	$\mathbf{z}^*$	$\theta_\mathbf{x}{}^\dagger$	$\theta_\mathbf{y}{}^\dagger$	$\theta_\mathbf{z}{}^\dagger$
1	0	0	0	0	0	0	0
2	13.75	0.001	-0.005	0	0	0	0.001
3	41.25	0.005	-0.039	-0.001	0	0	0.002
4	68.75	0.012	-0.103	-0.002	0	0	0.003
5	96.25	0.022	-0.188	-0.004	0	0	0.003
6	123.75	0.033	-0.290	-0.006	0	0	0.004
7	151.25	0.046	-0.402	-0.008	0	0	0.004
8	165	0.053	-0.460	-0.009	0	0	0.004
9	175.76	0.099	-0.460	-0.009	0	0	0.004
10	208.22	0.236	-0.460	-0.011	0	0	0.004

* Unit: $\sqrt{\mathrm{in}}/\sqrt{\mathrm{lbf\,s^2}}$
† Unit: $\mathrm{rad}/\sqrt{\mathrm{lbf\,s^2\,in}}$

Table 4.6: Boeing M222 wing torsion mode mass-normalized mode shape (Ref. [71])

Frequency = 11.4 Hz
Damping = 1.74%

Point	**r, in**	$\mathbf{x}^*$	$\mathbf{y}^*$	$\mathbf{z}^*$	$\theta_\mathbf{x}{}^\dagger$	$\theta_\mathbf{y}{}^\dagger$	$\theta_\mathbf{z}{}^\dagger$
1	0	0	0	0	0	0	0
2	13.75	0	0	-0.005	-0.002	-0.001	0
3	41.25	0	0	-0.036	-0.007	-0.002	0
4	68.75	0	0	-0.089	-0.011	-0.003	0
5	96.25	0	0	-0.153	-0.016	-0.004	0
6	123.75	0	0	-0.217	-0.020	-0.005	0
7	151.25	0	-0.001	-0.276	-0.025	-0.005	0
8	165	0	-0.001	-0.301	-0.027	-0.005	0
9	175.76	0	-0.001	-0.012	-0.027	0	0
10	208.22	0.001	-0.001	-0.866	-0.027	0	0

* Unit: $\sqrt{\mathrm{in}}/\sqrt{\mathrm{lbf\,s^2}}$
† Unit: $\mathrm{rad}/\sqrt{\mathrm{lbf\,s^2\,in}}$

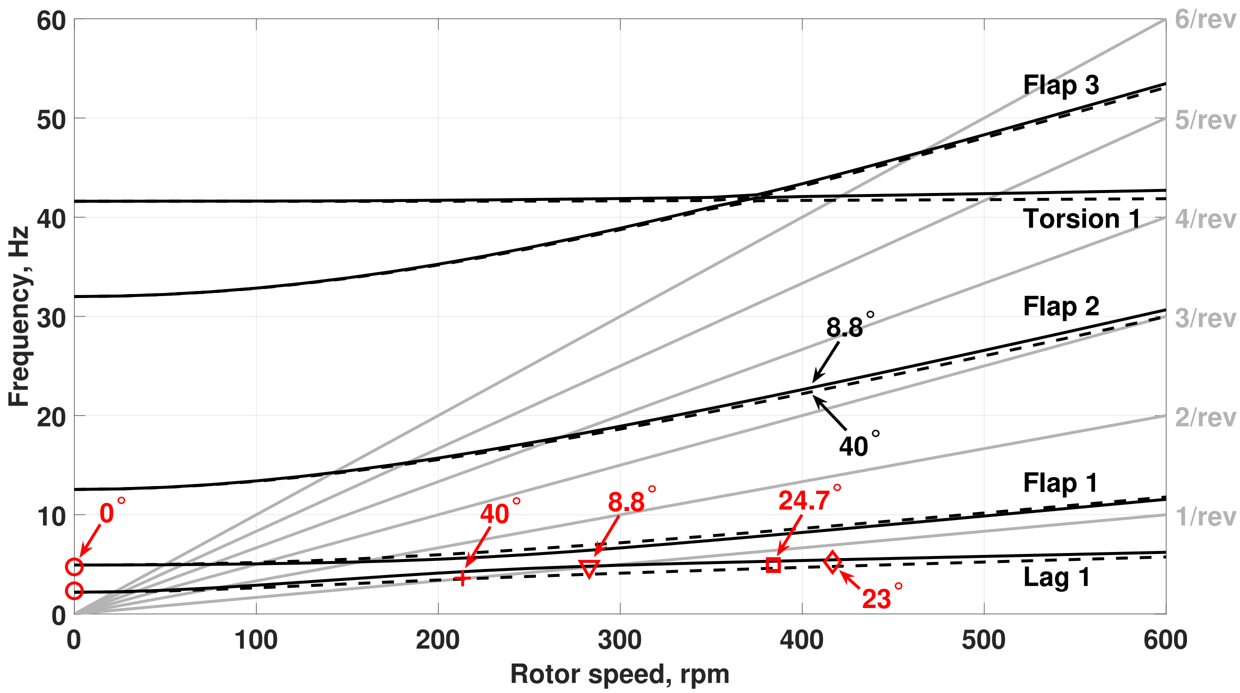

Figure 4.4: Boeing M222 fanplot
(solid: predictions for $8.8°$ collective, dash: predictions for $40°$ collective, symbols: test data)

4.2 Performance

Gross aerodynamics was validated through rotor thrust and power coefficient comparisons for hover, transition, and cruise. These were all powered runs. Prediction of freewheeling collective versus rotor speed was also validated.

4.2.1 Hover

The rotor had a $0°$ nacelle incidence angle (airplane mode) for the hover tests as shown in Fig. 1.11b. The tunnel was driven by the rotor up to 30 knots which made the test run effectively a cruise (axial climb) condition. For some test points, reverse fan was used in order to reduce the circulation in the tunnel. Figure 4.5 shows the change of rotor thrust and power coefficients with respect to inflow ratio for different collective angles (test 416, run 7). The rotor cyclic angles were set to zero for all test points. Predictions are acceptable and show the correct trends.

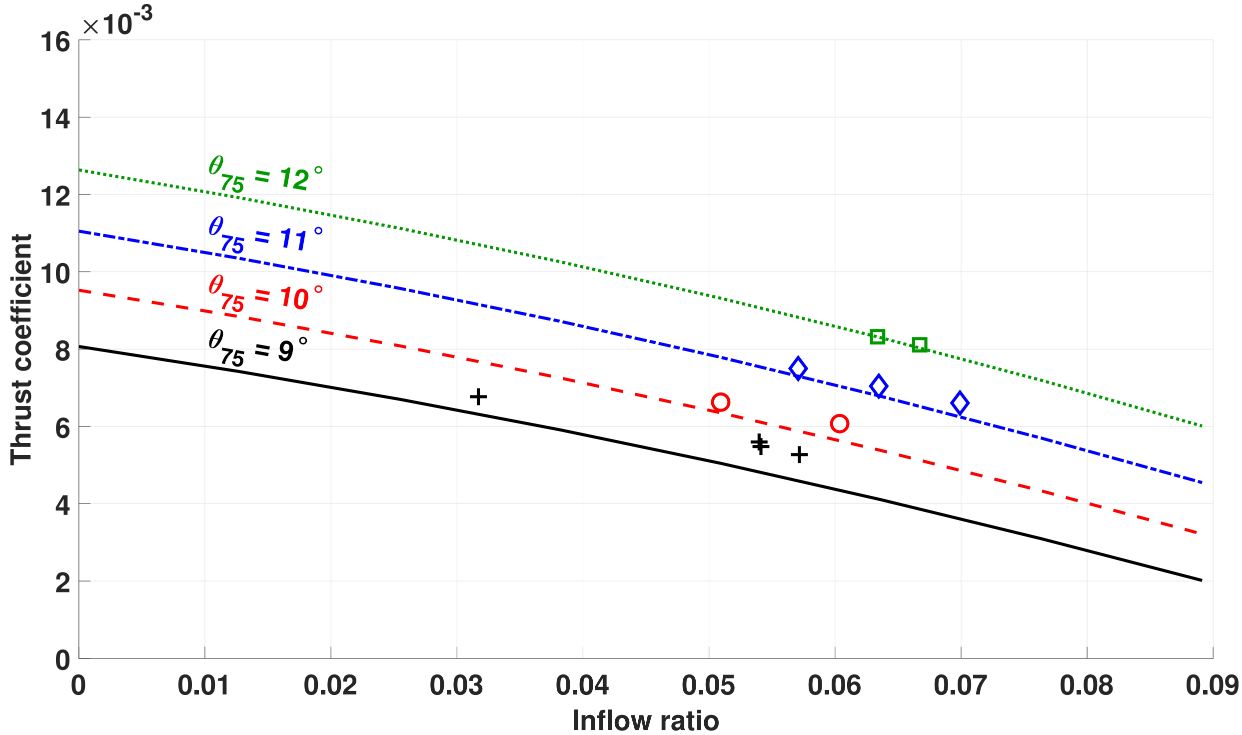

(a) Thrust coefficient

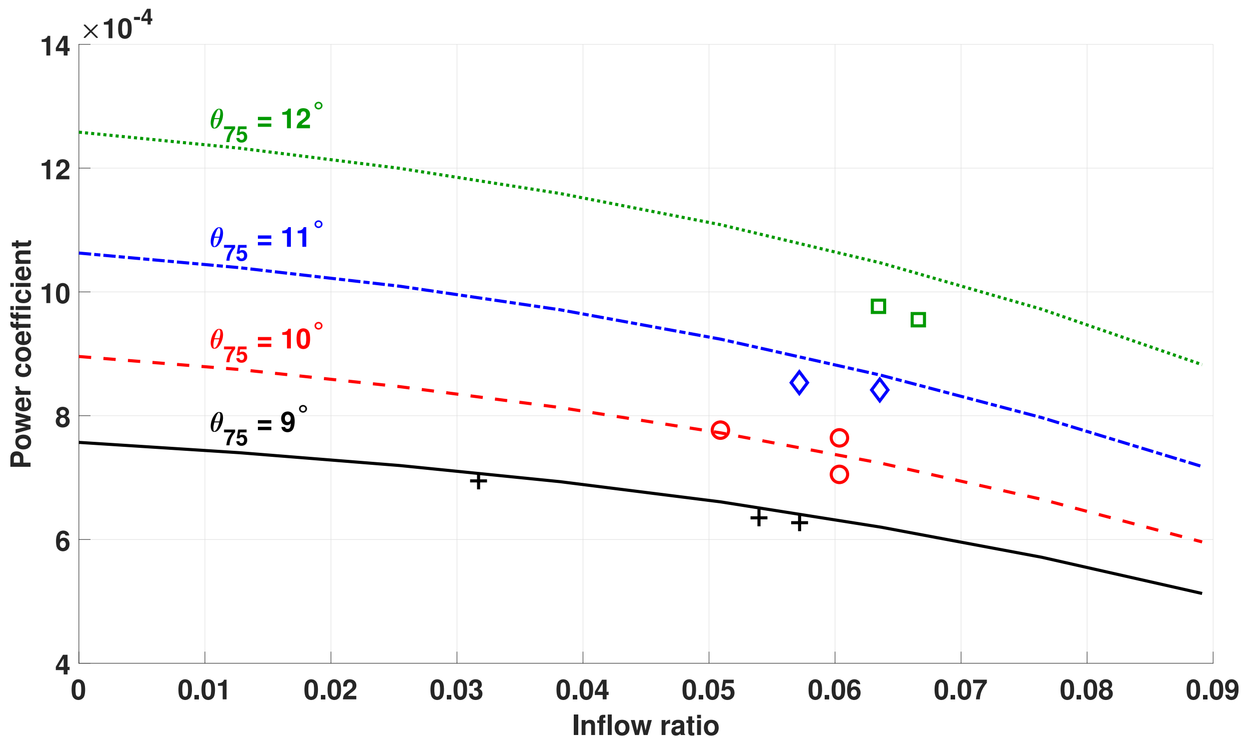

(b) Power coefficient

Figure 4.5: Comparison of hover thrust and power coefficient predictions with Boeing M222 test data (lines: predictions, symbols: test data)

4.2.2 Transition

Figure 4.6 shows the change of rotor power coefficient with respect to the thrust coefficient for a 105-knots transition run (test 416, run 9). The control angles were set to $\theta_{1c} = 2.16°$ and $\theta_{1s} = -2.56°$. The advance ratio and inflow ratio were $\mu = 0.11$ and $\lambda_c = 0.21$. The rotor was at $27°$ incidence nose up from the flow. Predictions match with the test data.

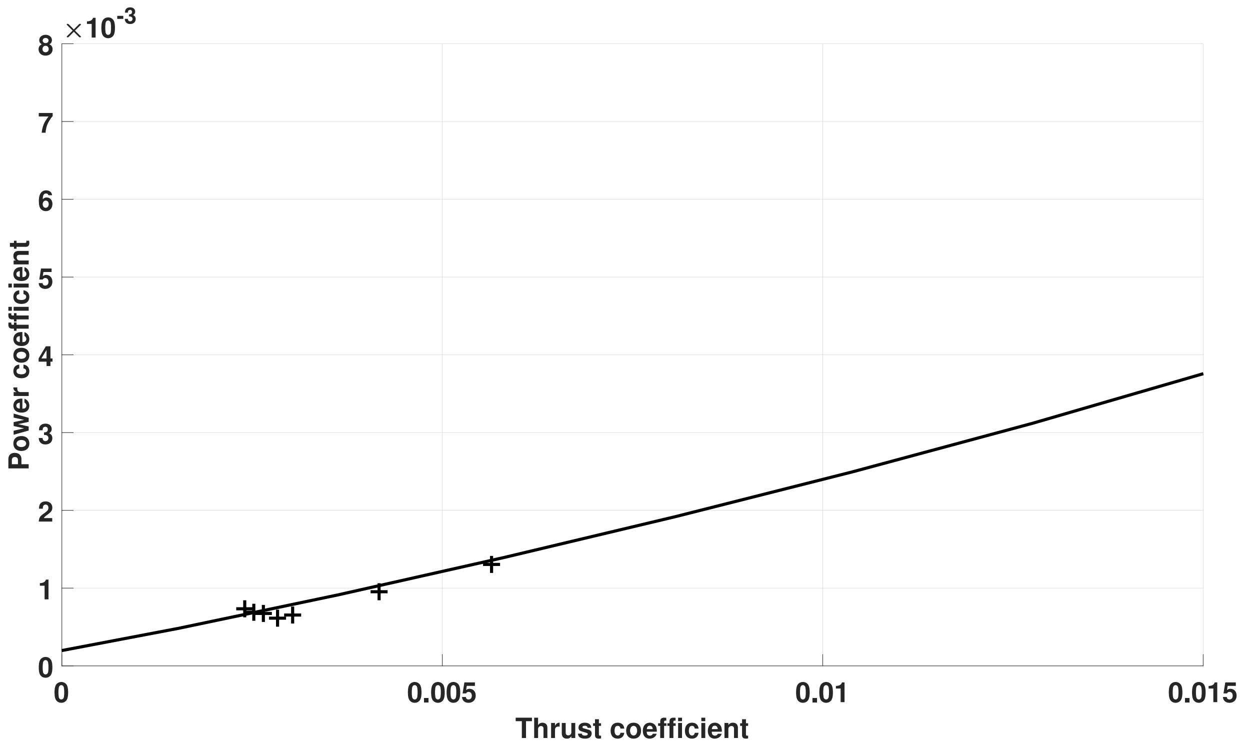

Figure 4.6: Comparison of 105-knots transition power versus thrust coefficient predictions with Boeing M222 test data ($\mu = 0.11$, $\lambda_c = 0.21$, $i_N = 27°$ from the flow) (lines: predictions, symbols: test data)

4.2.3 Cruise

Figure 4.7 shows the change of rotor power coefficient with respect to the thrust coefficient for a 140-knots cruise run (test 416, run 11). The control angles were set to $\theta_{1c} = 2.62°$ and $\theta_{1s} = -2.31°$. The advance ratio and inflow ratio were $\mu = 0.08$ and $\lambda_c = 0.44$. The rotor was at $10°$ incidence nose up from the flow. Cruise power coefficient is 95% higher than transition (for $C_T = 0.01$). Predictions show good agreement.

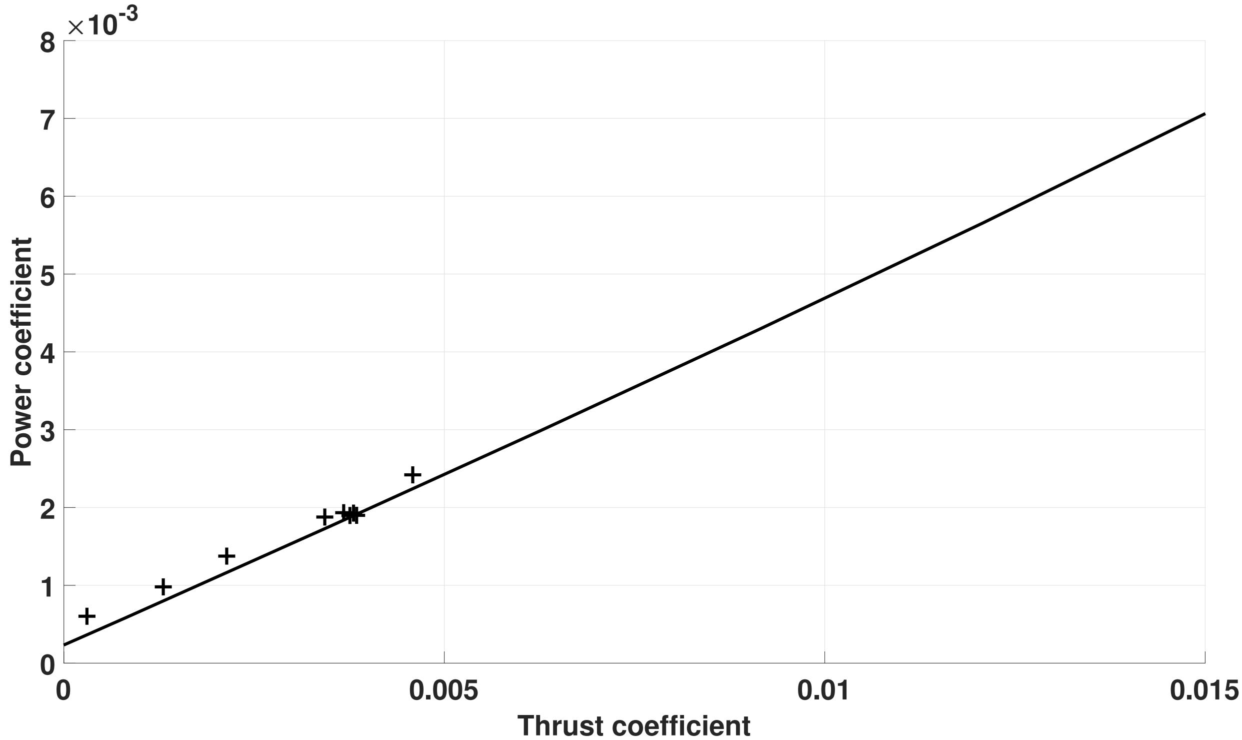

Figure 4.7: Comparison of 140-knots cruise power versus thrust coefficient predictions with Boeing M222 test data ($\mu = 0.08$, $\lambda_c = 0.44$, $i_N = 10°$ from the flow)
(lines: predictions, symbols: test data)

4.2.4 Freewheeling

Stability tests were carried out in freewheeling condition (test 410). This is typical of whirl flutter tests, as freewheeling decouples special features of the drivetrain, and also generally results in conservative whirl flutter boundary while achieving near representative collective as powered flight. Testing in freewheeling mode also reduces the complexity of the test that may arise due to powerplant stalling. Accurately predicting the rotor speed versus collective at a given tunnel speed is crucial for whirl flutter because of the effect of blade pitch angle on the coupling of flap and lag modes.

Figure 4.8 shows a comparison of the freewheeling predictions with the test data. The lower side below $10°$ collective shows reverse stall. Boeing tests have no data there because the higher side is more representative of the actual flight. Some small offset is observed for higher pitch settings, but there is generally a good agreement considering that the performance validates gross characteristics. The next step is to validate the structural loads.

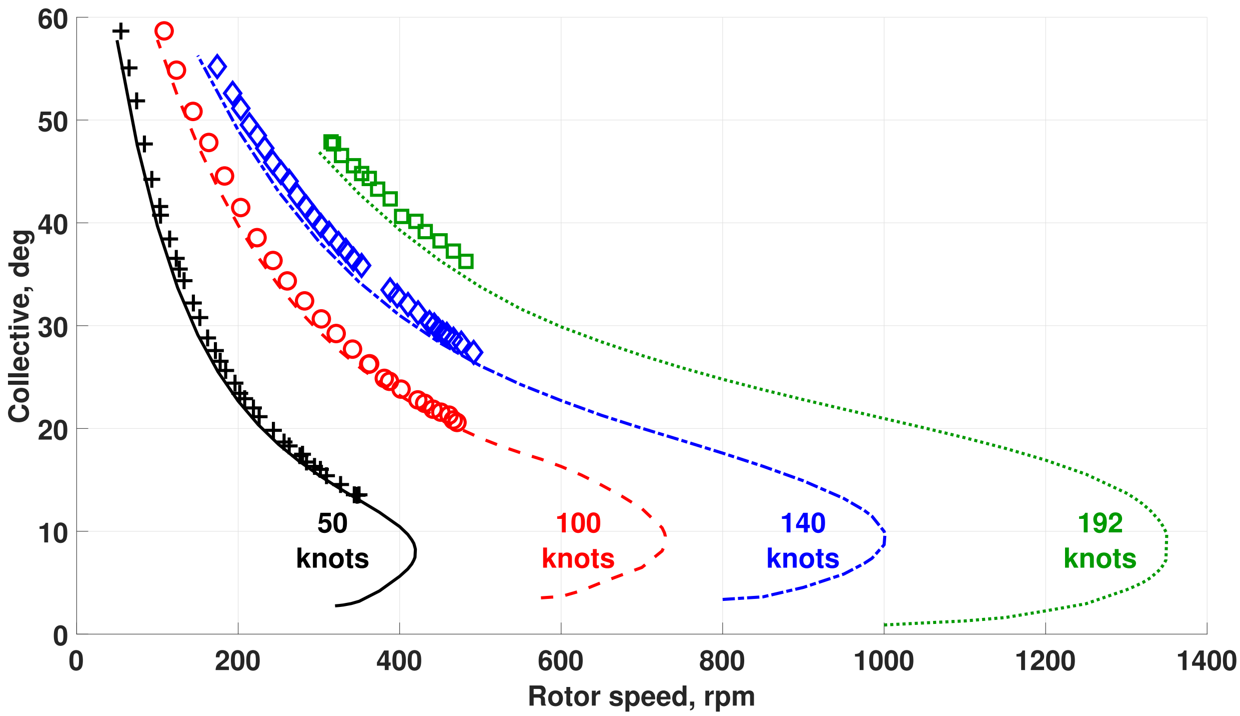

Figure 4.8: Comparison of freewheeling collective predictions with Boeing M222 test data (lines: predictions, symbols: test data)

4.3 Blade Loads

Structural loads on the blades were measured in hover, transition, and cruise. The tests were performed by keeping two out of three rotor controls (collective and cyclics) constant and varying the other in a set flight condition (defined by tunnel speed, incidence angle, and rotor speed). Blade loads were recorded in directions normal and parallel to the local chord except for the hub barrel gauges at $r/R = 3.9\%$, where the loads were measured in out-of-plane and in-plane directions.

The loads analysis was carried out both using the reported control angles (solid lines) and trimming to the hub moments (dotted lines). The Maryland Freewake was used with a single rolled-up tip vortex and a nearwake extending 30° behind. Induced flow and wake geometry were converged for each solution.

4.3.1 Hover

Figure 4.9 shows the variation of half peak-to-peak (HPP) flapwise and chordwise bending moments with respect to longitudinal cyclic for the hover run (test 416, run 7). The corresponding hub moments are given in Fig. 4.10. This rotor was effectively in 24-knots axial climb due to the tunnel recirculation. The collective and lateral cyclic were $\theta_{75} = 9^\circ$ and $\theta_{1c} = 0^\circ$.

4.3.2 Transition

Transition generates high oscillatory loads which dominate the structural design. Figure 4.11 shows the variation of half peak-to-peak flapwise and chordwise bending moments with respect to lateral cyclic for the 105-knots transition run (test 416, run 9). The corresponding hub moments are given in Fig. 4.12. The collective and longitudinal cyclic were $\theta_{75} = 18.9^\circ$ and $\theta_{1s} = -2.56^\circ$.

4.3.3 Cruise

Figure 4.13 shows the variation of half peak-to-peak flapwise and chordwise bending moments with respect to longitudinal cyclic for the 140-knots cruise run (test 416, run 11). The corresponding hub moments are given in Fig. 4.14. The collective and lateral cyclic were $\theta_{75} = 35.1^\circ$ and $\theta_{1c} = 2.66^\circ$. Note that even though it is called cruise, it is in fact an edgewise flight, not cruise as in a propeller aircraft. The nacelle is not fully down but tilted slightly up 10° from the flow. It is a difficult condition to predict as well as to measure, as is clear from the data and validation.

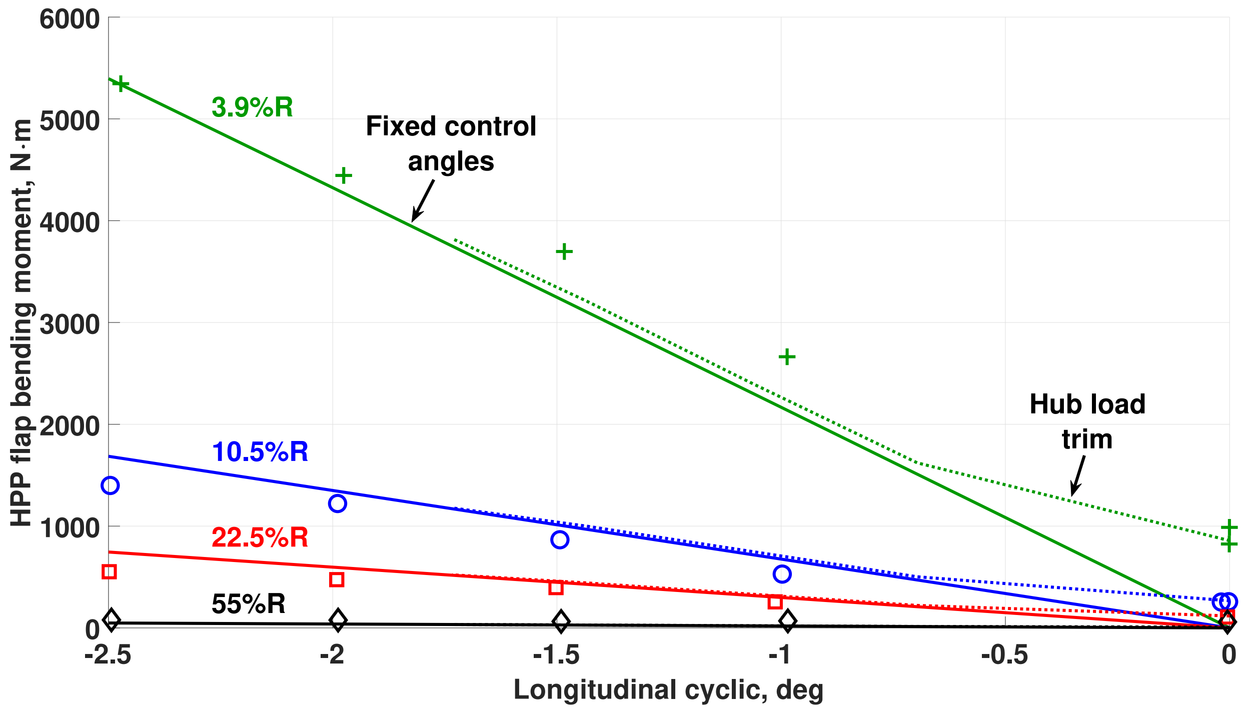

(a) Flapwise

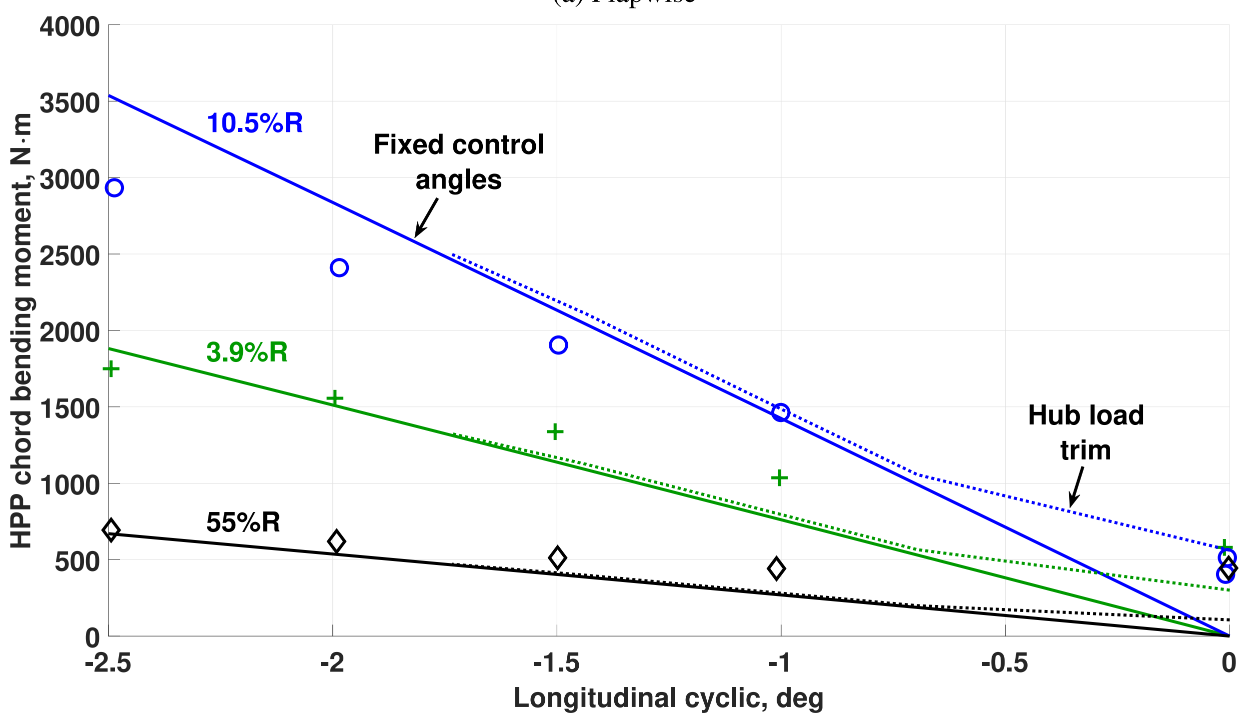

(b) Chordwise

Figure 4.9: Comparison of hover alternating bending moment predictions with Boeing M222 test data
(solid: predictions with control angles, dot: predictions with hub load trim, symbols: test data)

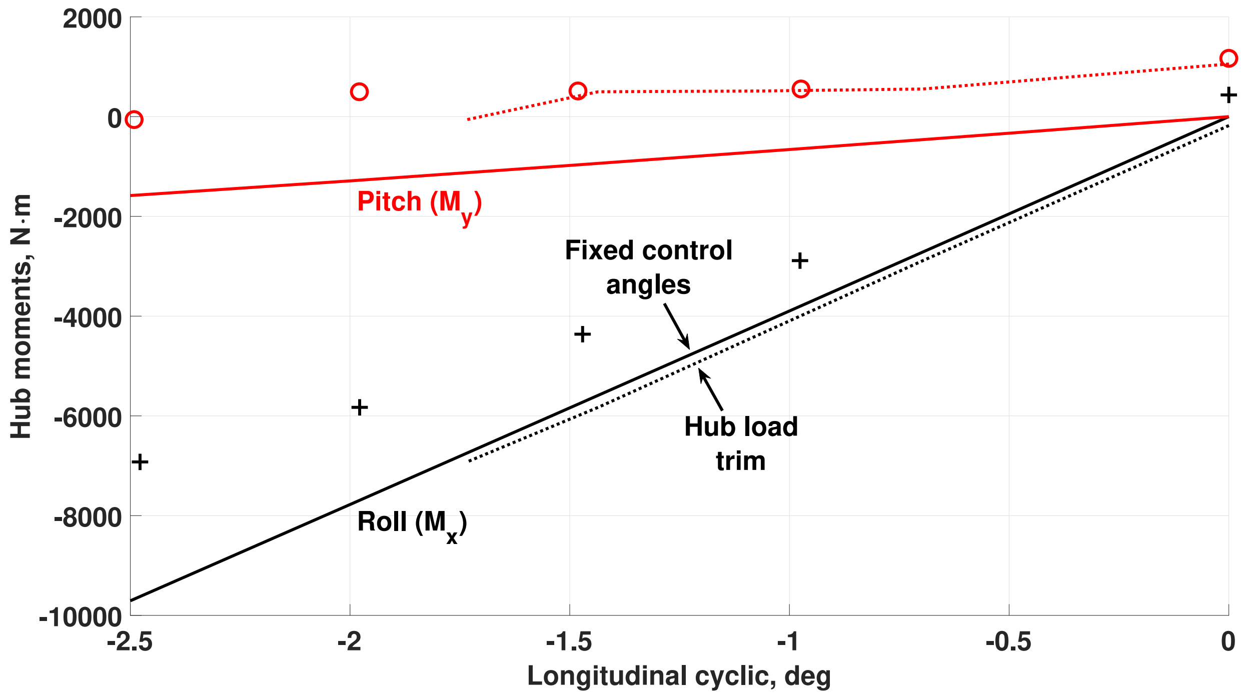

Figure 4.10: Comparison of hover hub moment predictions with
Boeing M222 test data
(solid: predictions with control angles, dot: predictions with hub load trim, symbols: test data)

Figures 4.9, 4.11, and 4.13 show that the solver can estimate the blade loads within acceptable errors. Offsets in the cyclics are observed, which are also apparent in the hub load predictions (Figs. 4.10, 4.12, and 4.14). Similar observations and offset values (changing between $0.66°$ and $1.12°$ with different methods) were reported for the 105-knots transition case in Ref. [34], where the loads were calculated with vortex wake, Viscous Vortex Particle Method (VVPM) (Refs. [87, 88]), and Helios™ (CFD) (Ref. [89]). Blade load predictions are much better for cruise with the trim solution (dotted lines). General trends were predicted for all the cases, but some difference in the magnitudes is present. The minimum load point in transition and cruise (Figs. 4.11 and 4.13) is due to the edgewise flow component; there exists a set of cyclics that alleviates the oscillatory loads because of the edgewise flow. The differences can be due to measurement errors, incorrect model properties, or errors in the analysis. It is difficult to pin

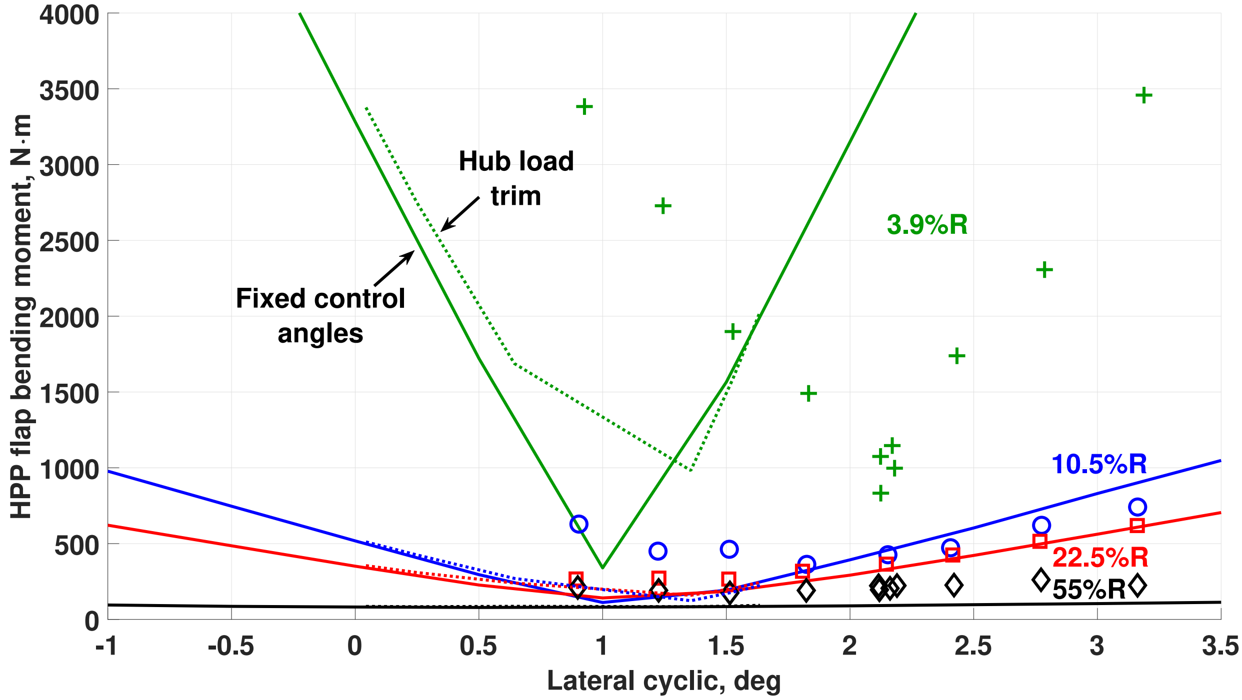

(a) Flapwise

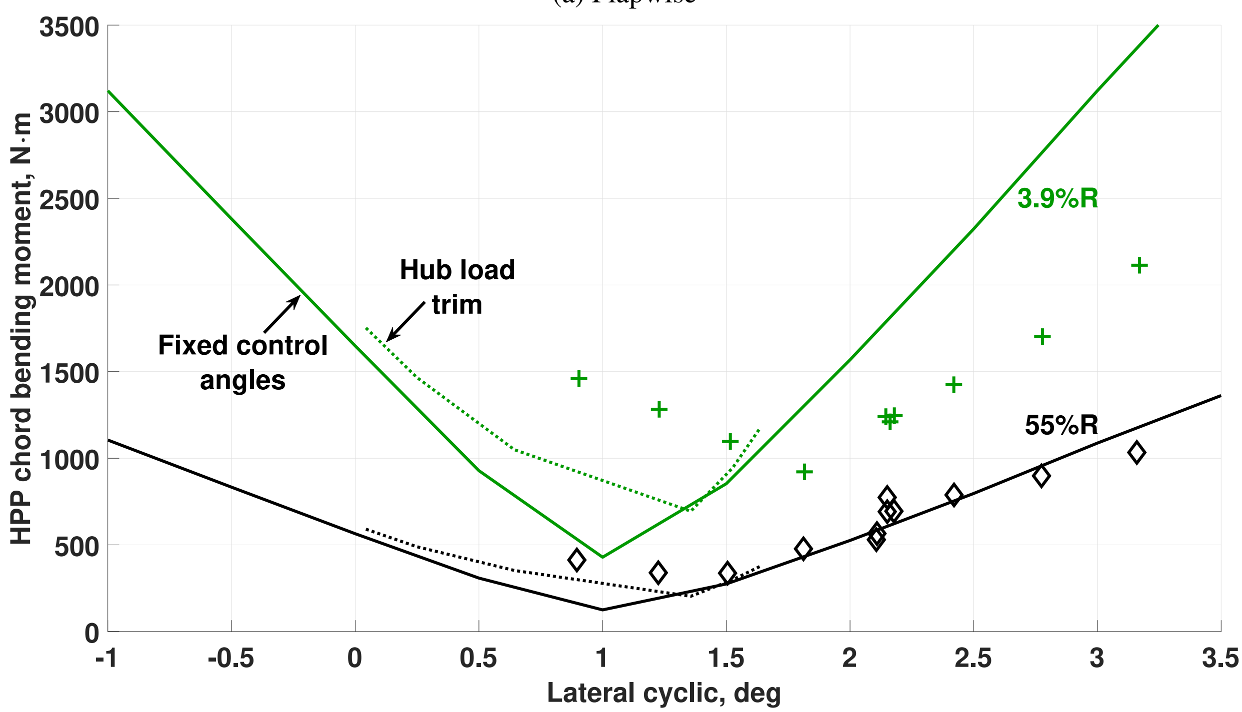

(b) Chordwise

Figure 4.11: Comparison of 105-knots transition alternating bending moment predictions with Boeing M222 test data ($\mu = 0.11$, $\lambda_c = 0.21$, $i_N = 27°$ from the flow)
(solid: predictions with control angles, dot: predictions with hub load trim, symbols: test data)

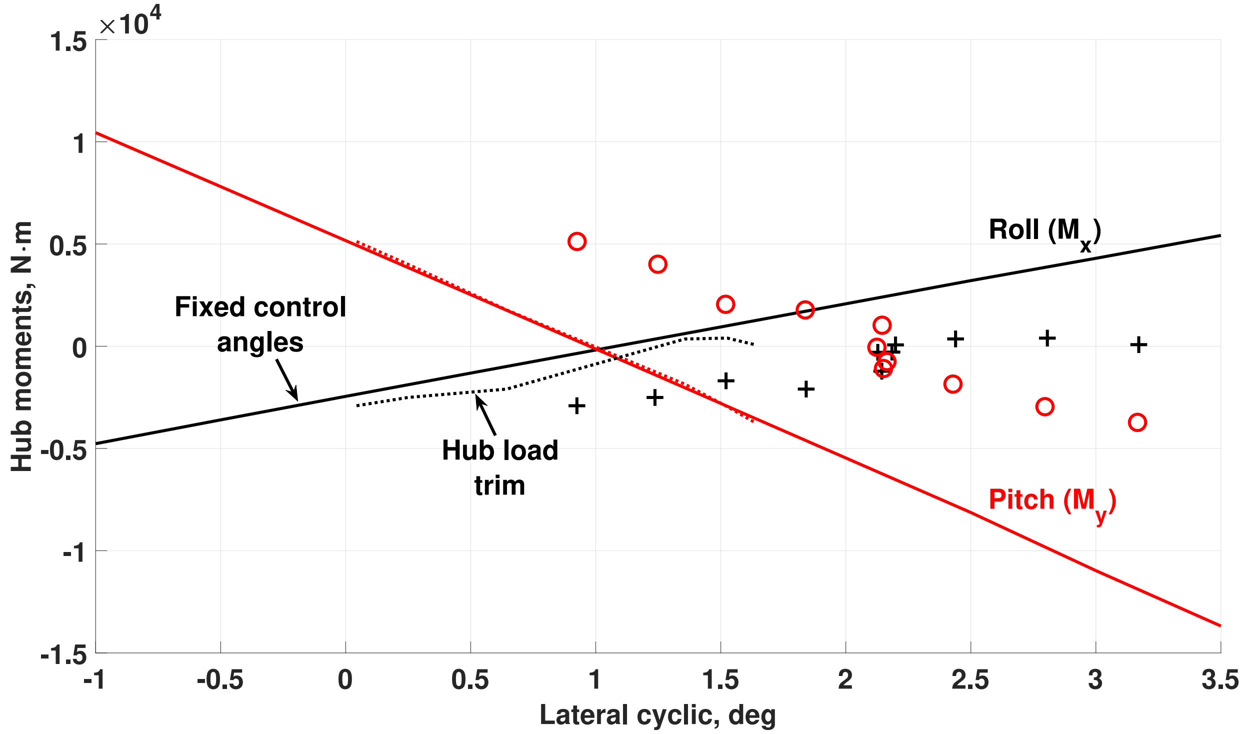

Figure 4.12: Comparison of 105-knots transition hub moment predictions with Boeing M222 test data ($\mu = 0.11$, $\lambda_c = 0.21$, $i_N = 27°$ from the flow) (solid: predictions with control angles, dot: predictions with hub load trim, symbols: test data)

down the source without high-quality test data and consistent properties. In general, sufficient confidence in the accuracy of the loads predictions could be established in order to proceed to more involved aeroelastic stability validation.

4.4 Aeroelastic Stability

First, the physical phenomena are explained. Stability of the isolated rotor, isolated wing, and the rotor/pylon/wing system was analyzed. Then, predictions were validated with the test data. Only essential features were retained in the model. Uniform inflow was used for the rotor. Wing aerodynamics did not include an induced flow model for simplicity. Figure 4.15 shows frequency and damping predictions for the isolated Boeing M222 rotor with respect to airspeed. The modes are labeled with the principal degree of freedom. Damping of the high-frequency

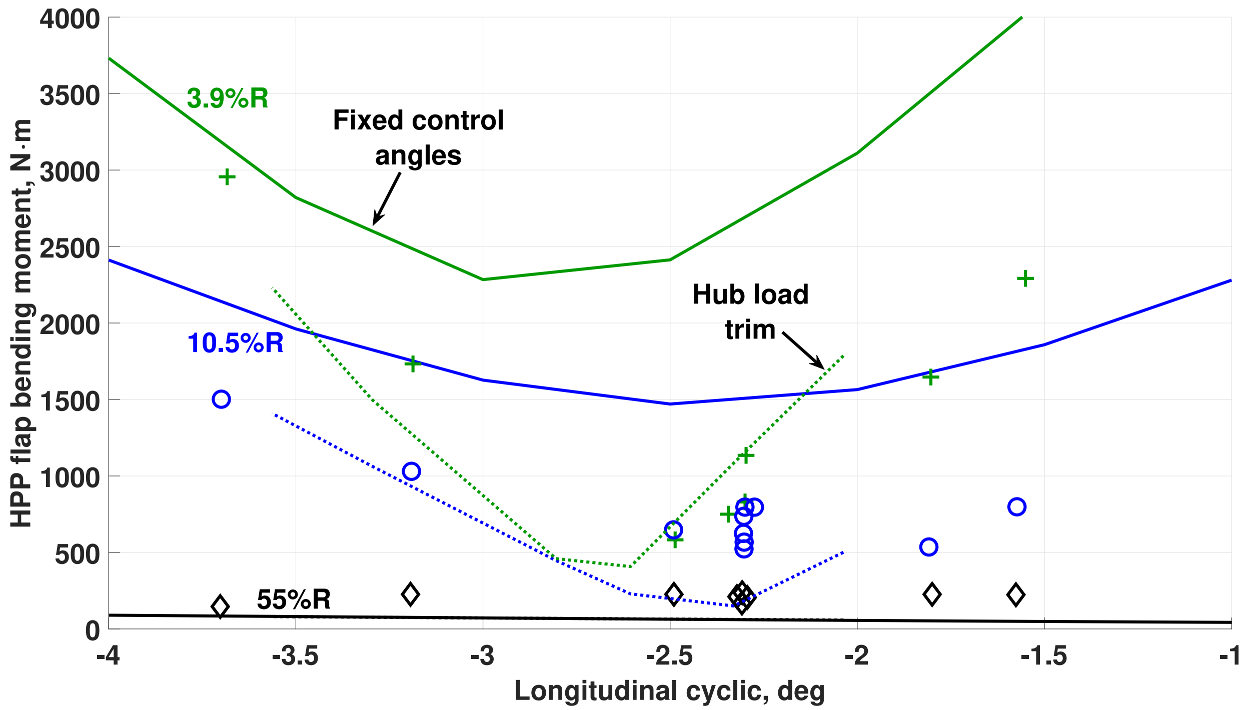

(a) Flapwise

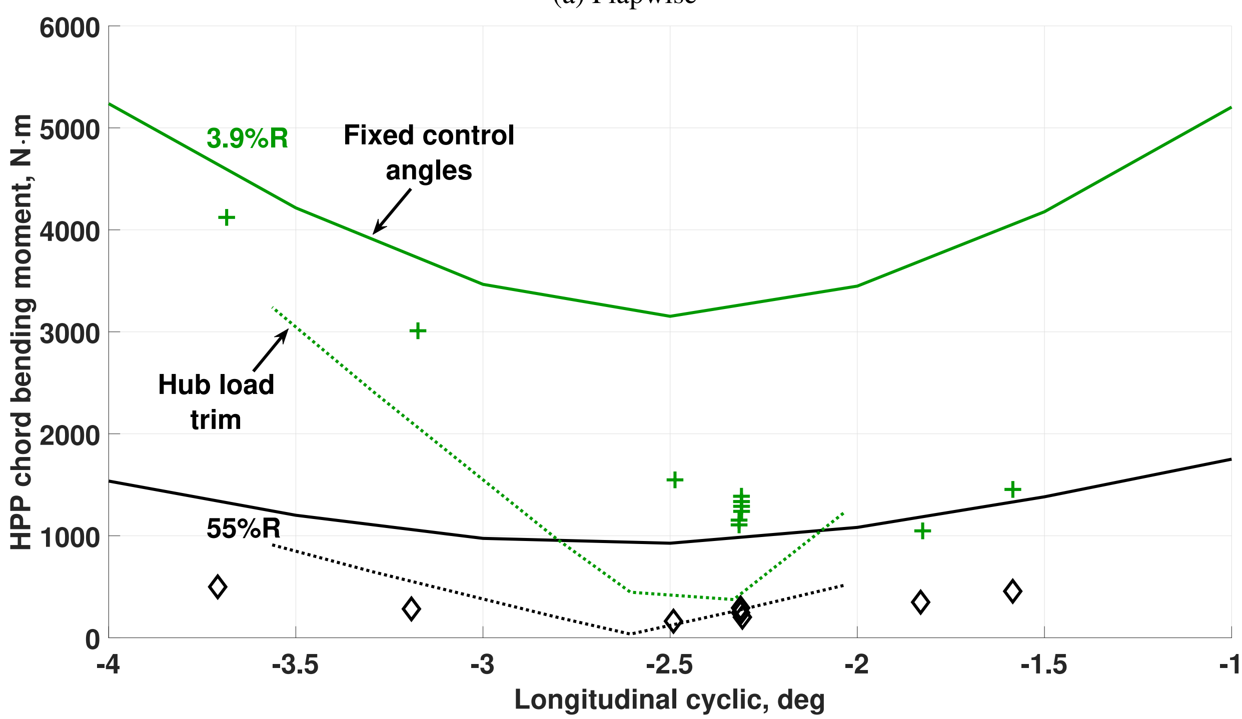

(b) Chordwise

Figure 4.13: Comparison of 140-knots cruise alternating bending moment predictions with Boeing M222 test data ($\mu = 0.08$, $\lambda_c = 0.44$, $i_N = 10^\circ$ from the flow)
(solid: predictions with control angles, dot: predictions with hub load trim, symbols: test data)

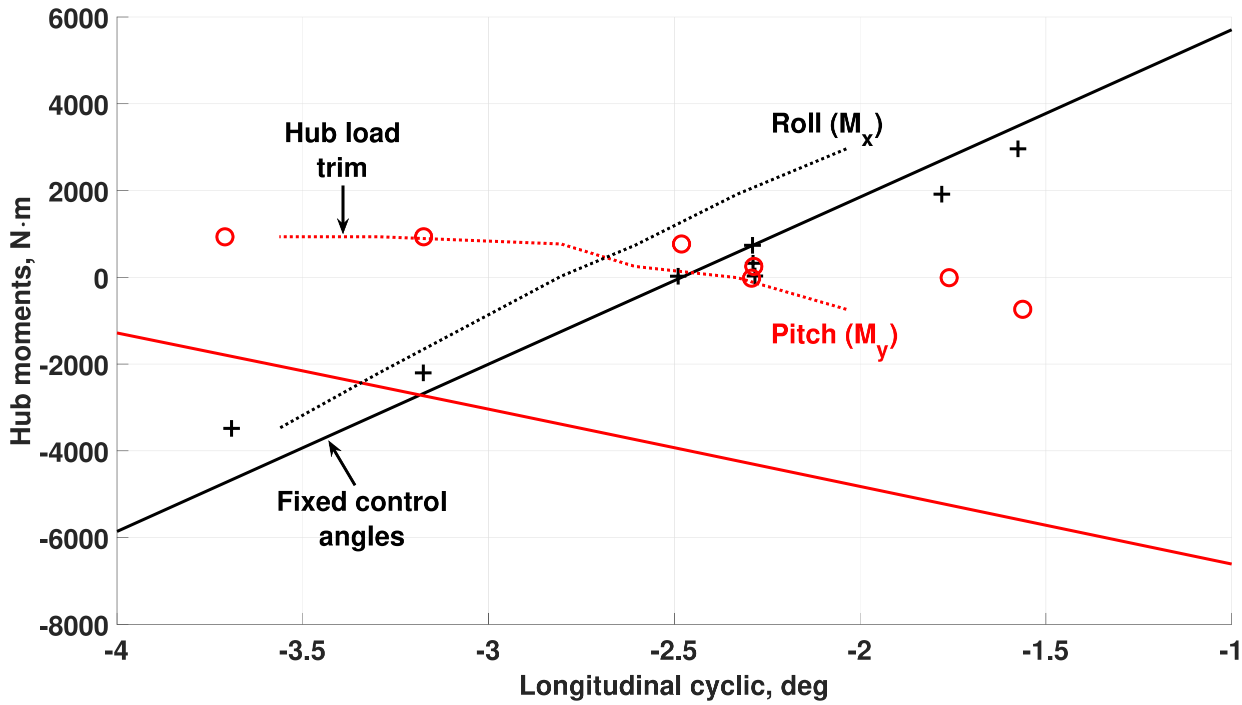

Figure 4.14: Comparison of 140-knots cruise hub moment predictions with Boeing M222 test data ($\mu = 0.08$, $\lambda_c = 0.44$, $i_N = 10°$ from the flow) (solid: predictions with control angles, dot: predictions with hub load trim, symbols: test data)

rotor flap ($\beta+1$) mode shows a gradual decrease with airspeed, but the rotor is stable even at high speeds (4% damping at 400 knots). Figure 4.16 shows the stability roots of the isolated NASA dynamic test stand. Solution was obtained up to 1000 knots, which is well beyond the accuracy limitation of the aerodynamic model. This was to demonstrate the coupling of the modes at high speed. Wing beam (q_1) and torsion (p) modes couple and damping of the wing torsion (p) mode shows a dramatic drop. This is the classical fixed-wing flutter. The isolated wing/pylon exhibits high stability where the aerodynamic model is valid (until about 500 knots). Figure 4.17 installs the stable rotor on the stable wing/pylon and shows the frequency and damping of the coupled system. After an initial drop in the wing chord (q_2) mode damping at around 150 – 200 knots due to coupling with the collective lag (ζ) mode, it is stabilized at higher speeds. Wing beam (q_1) mode is stable for all the flight speeds. After 250 knots, damping of the wing torsion (p)

mode decreases precipitately and goes unstable at $327\ \mathrm{knots}$. This is the proprotor air resonance phenomenon that was explained in Chapter 1.2. This instability occurs due to the soft in-plane hub ($\nu_\zeta < 1/\mathrm{rev}$) and the coupling of the low-frequency lag ($\zeta - 1$) and wing torsion (p) modes, despite the stable isolated rotor and wing/pylon. Figure 4.18 shows the time vector representation of this mode at 50 and $325\ \mathrm{knots}$. The eigenvector set for a given mode rotates counterclockwise at the damped frequency and the magnitudes decrease exponentially at a rate determined by the damping ratio. The projection of each line on the real axis gives the participation of the corresponding degree of freedom during the damped oscillation of the system. The terms β_{1c}, β_{1s} are the flap degrees of freedom and ζ_{1c} and ζ_{1s} are the lag degrees of freedom in the fixed frame. The wing torsion (p) mode is coupled with the wing beam (q_1) mode for all speeds due to high pylon mass ($2000\ \mathrm{lb}$ without blades) and pylon c.g. offset ($10.8\ \mathrm{in}$ ($6.9\%R$) forward of wing elastic axis), but mostly assumes a lag mode shape (dominant ζ_{1c} and ζ_{1s}) near instability as shown in Fig. 4.18b.

Figures 4.19 and 4.20 show the test data and predictions with respect to rotor speed at various tunnel speeds. Frequencies are reported for $100\ \mathrm{knots}$ to show the coupling of the modes. Damping results are presented for the q_1 mode as the test data is only available for this mode. Bowen-Davies also reports these predictions in Ref. [33] to validate the RCAS model of the Boeing M222 rotor, which are included in the plots (dotted lines) for additional verification. These were obtained using the measured modal damping given in Tables 4.4 to 4.6 instead of a wing aerodynamic model. A simplified set of predictions that used the same modal damping values is therefore also included in the damping plots (dashed-dotted lines) to compare with Ref. [33]. In reality, wing aerodynamic damping increases with the tunnel speed; hence, one set of values cannot be valid for every test speed.

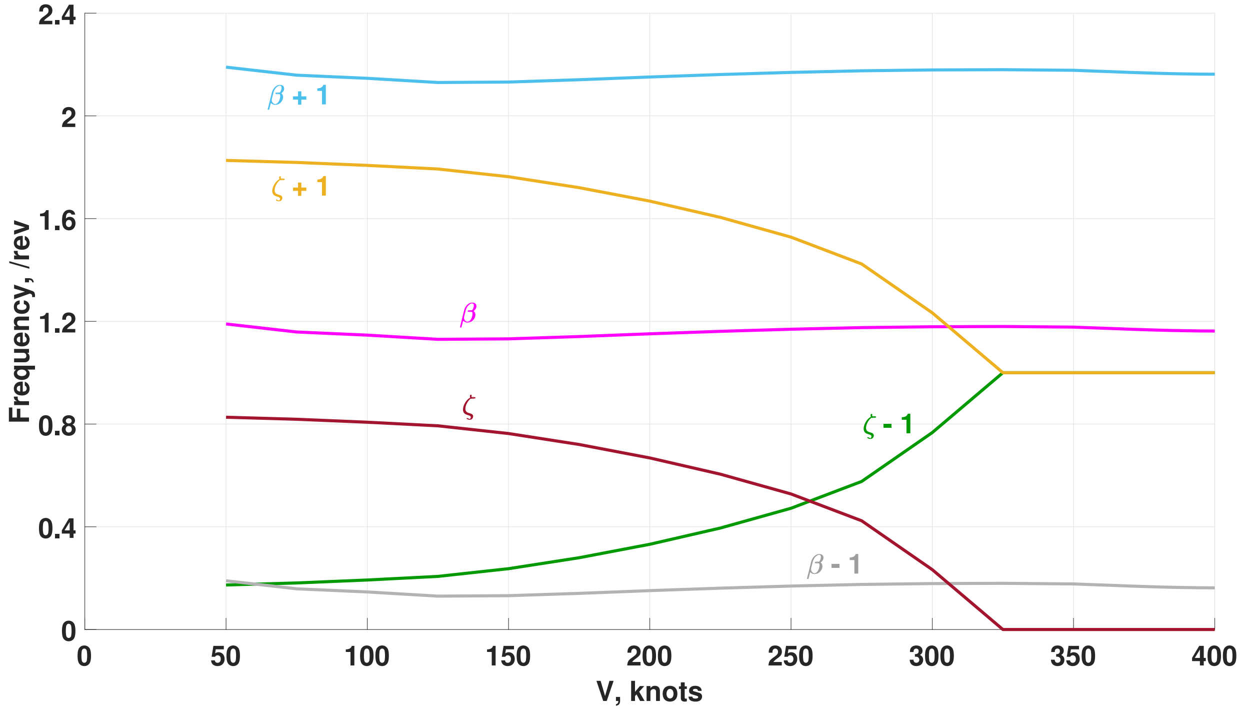

(a) Frequency

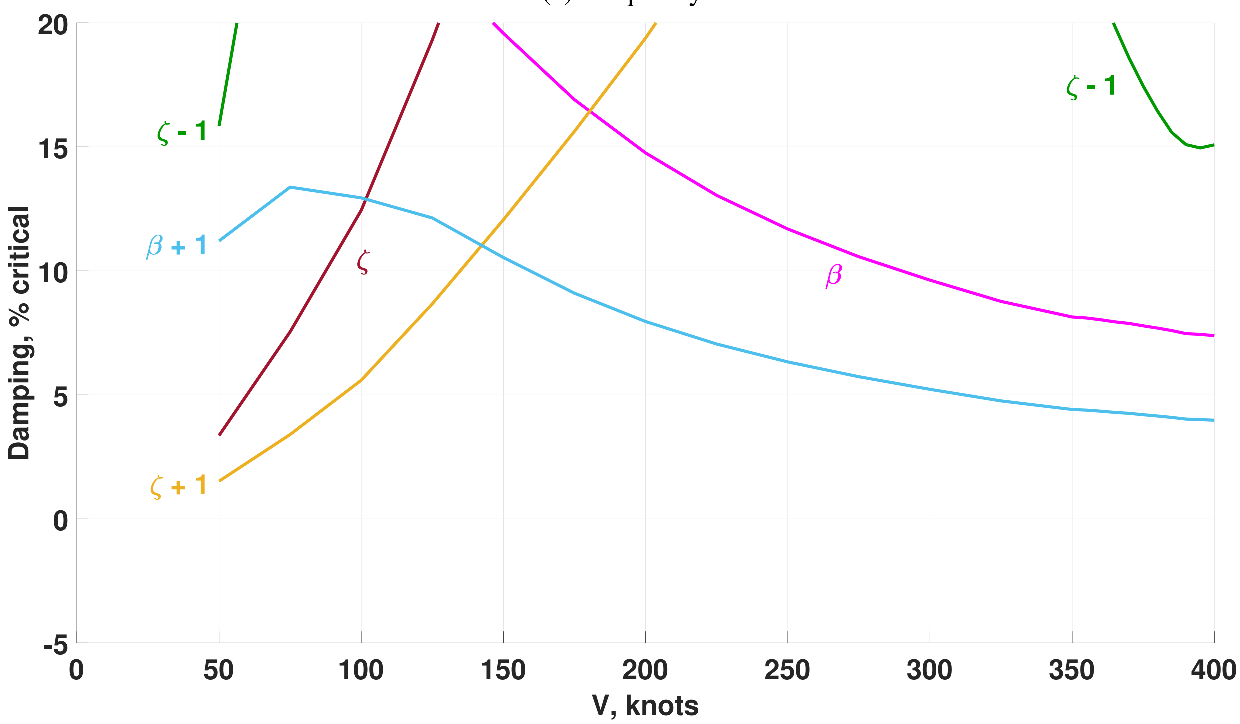

(b) Damping

Figure 4.15: Stability roots of isolated rotor modes at the design rotor speed ($386\ \mathrm{rpm}$)

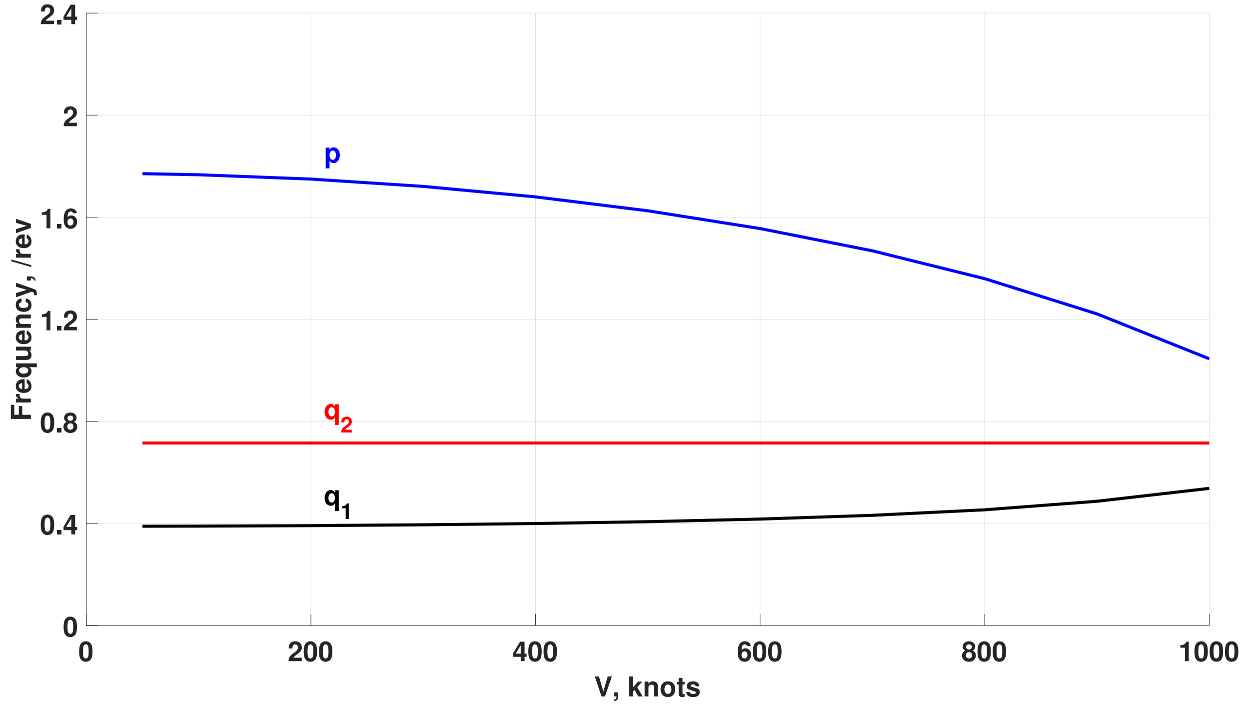

(a) Frequency

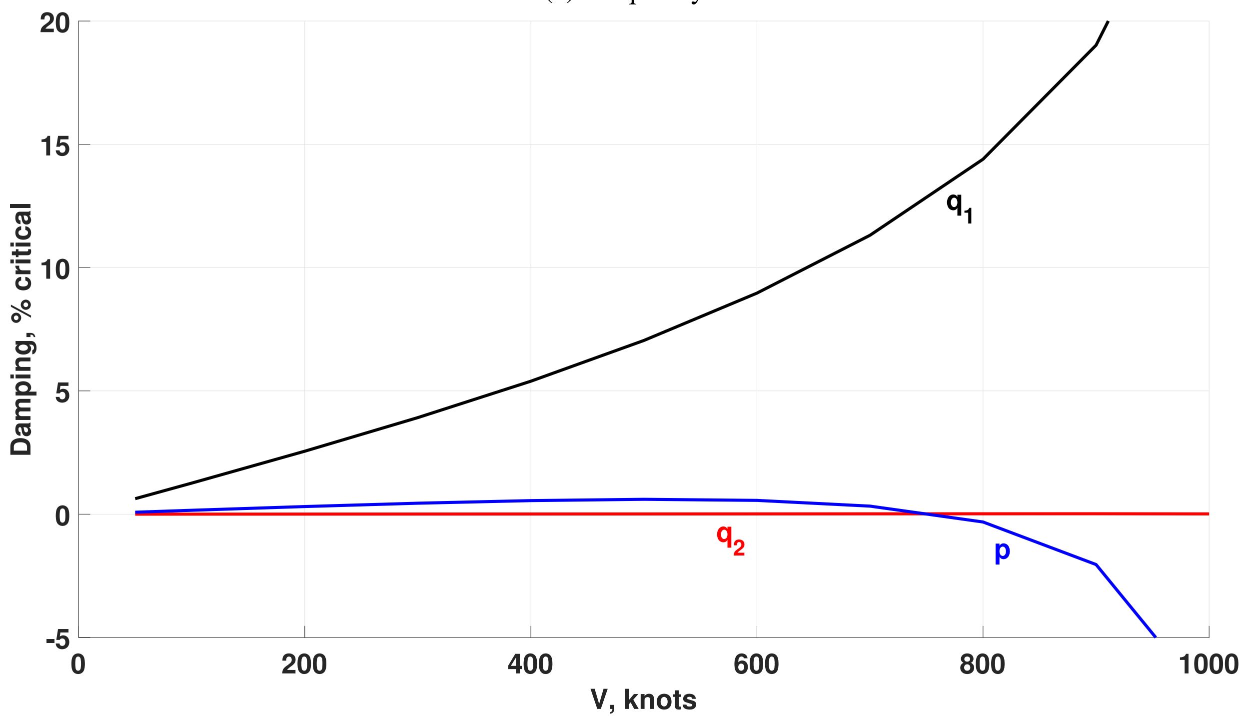

(b) Damping

Figure 4.16: Stability roots of isolated wing modes

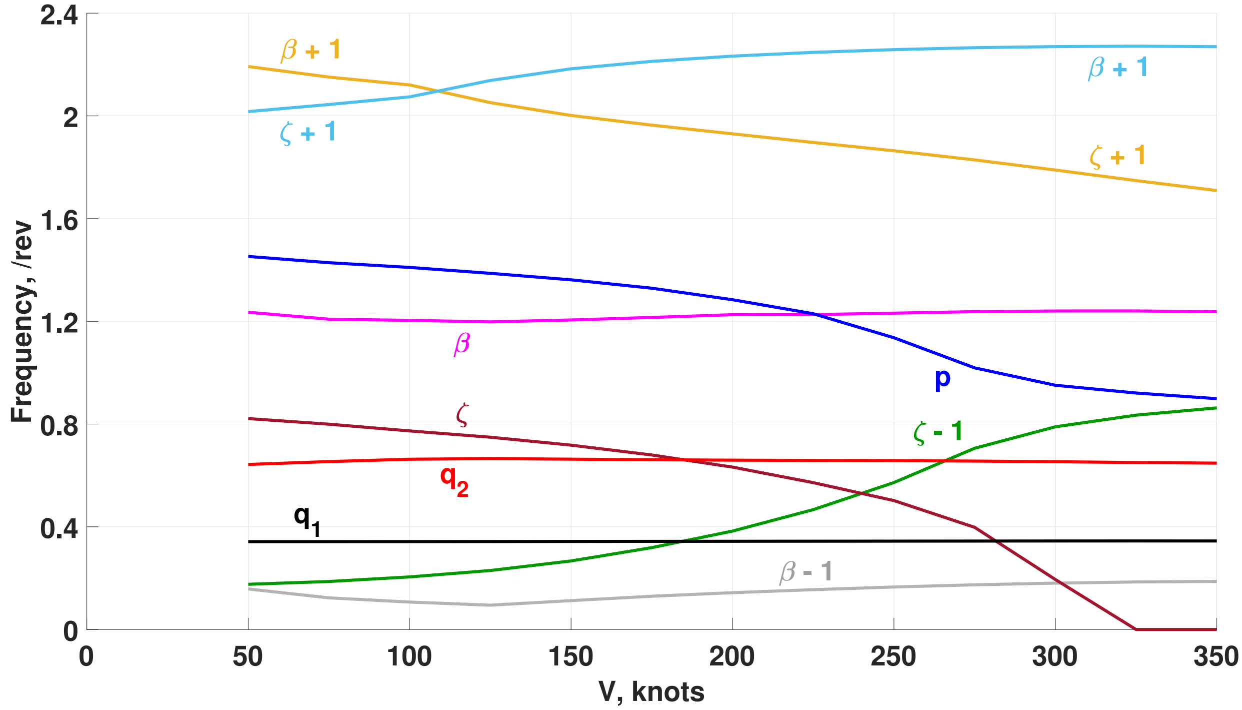

(a) Frequency

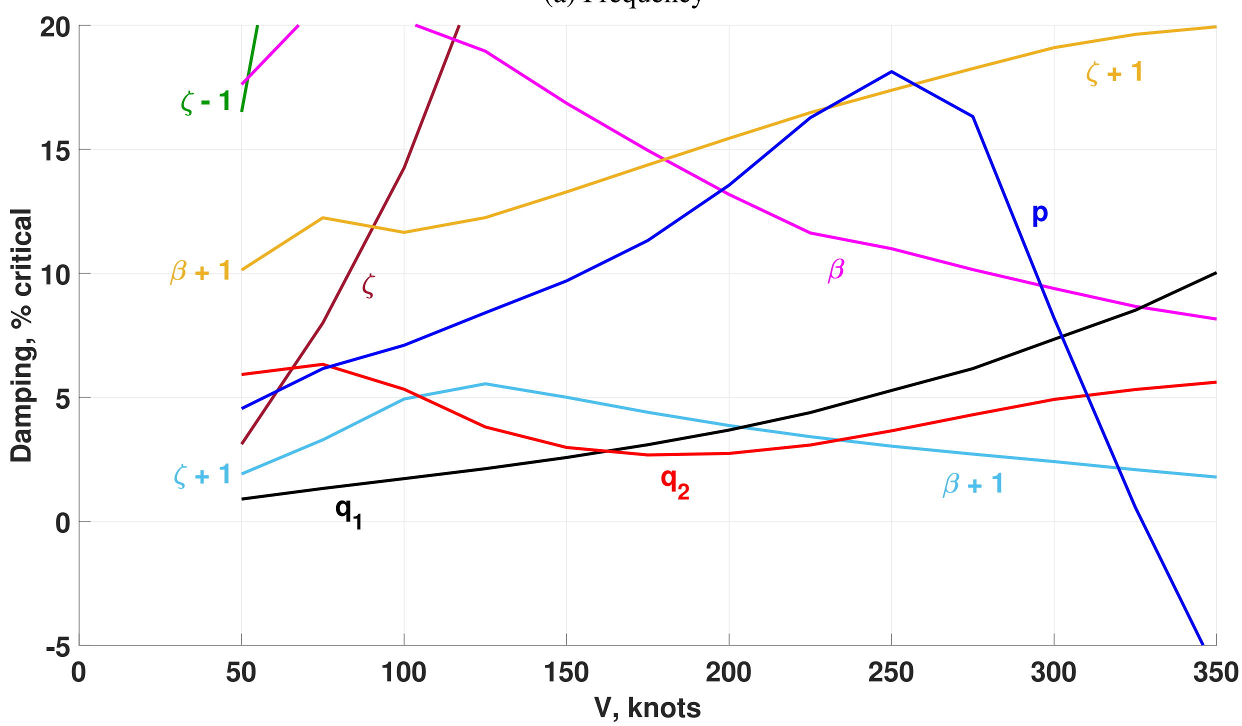

(b) Damping

Figure 4.17: Stability roots of coupled modes at the design rotor speed (386 rpm)

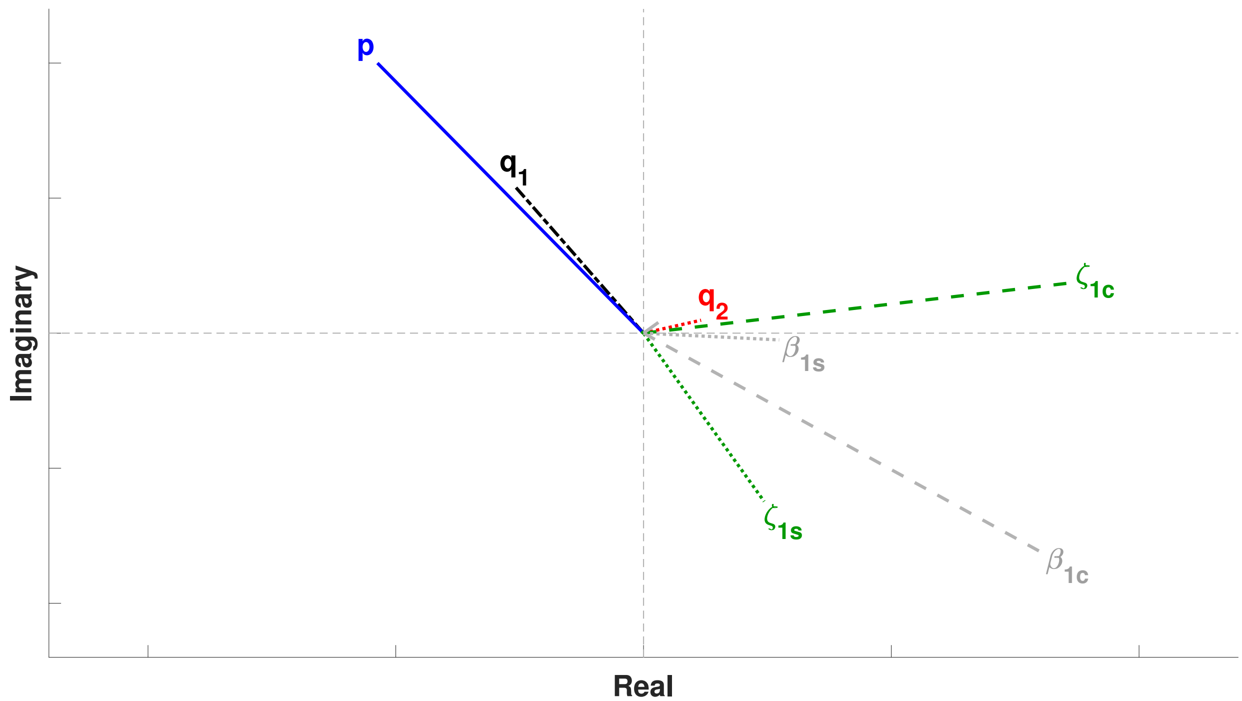

(a) 50 knots

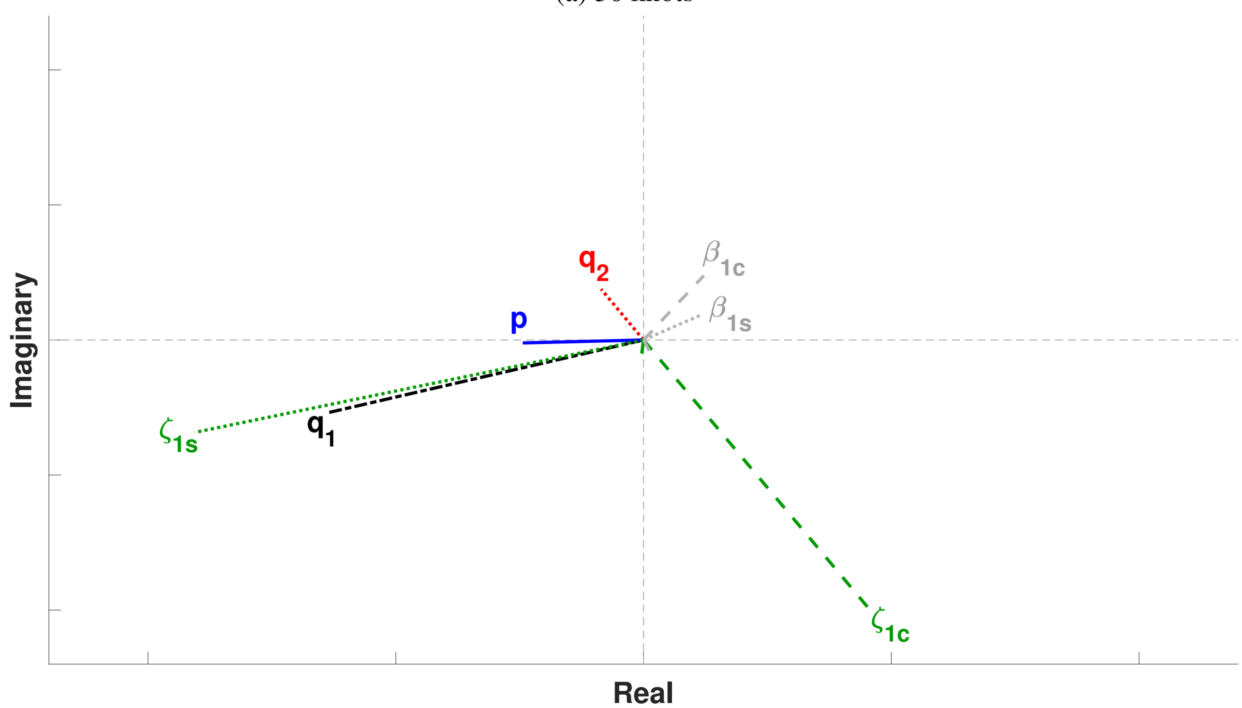

(b) 325 knots

Figure 4.18: Eigenvectors for the wing torsion mode

Figure 4.19 shows that damping of the q_1 mode first exhibits some change near 200 rpm when it is coupled with the $\beta - 1$ mode and then decreases dramatically at around 450 rpm. This is again the proprotor air resonance, this time due to the coupling of the $\zeta - 1$ and q_1 modes. The test data should be compared with the predictions that model proper wing aerodynamics. The agreement is satisfactory for low speeds, but some offset is observed for the damping at 140 and 192 knots. The instability at 100 and 192 knots was not captured at all, although the behavior for 100 knots was generally predicted. The discrepancies might be attributed to inaccurate modeling of physics, incorrect model inputs, or possible measurement uncertainties with the equipment used in the 1970s, but the cause remains unknown. An interesting behavior is that even though the drop in the damping with the rotor speed is still present, the q_1 mode is stabilized as the tunnel speed increases due to higher aerodynamic damping in rotor lag and wing beam motions, but only until 192 knots (Fig. 4.20). At 192 knots, the damping data shows an unexpected decrease. This trend was captured neither by UMD nor by RCAS.

Generally, UMD and RCAS predictions agree well with each other when modal damping is used. The highest discrepancy is for 100 knots (Fig. 4.19b), where maximum 0.7% difference in the damping and 20 rpm in the air resonance rotor speed is observed. The sources of the small differences between the two sets of predictions are not clear. UMD predictions with wing aerodynamics and modal damping show similar results for 100 knots, which verifies the wing aerodynamic model. Higher damping values were predicted for 140 and 192 knots with a wing aerodynamic model, which is expected. The predictions for 50 and 60 knots do not reach as high rotor speeds as RCAS because the rotor achieves maximum speed before stalling as shown in Fig. 4.8.

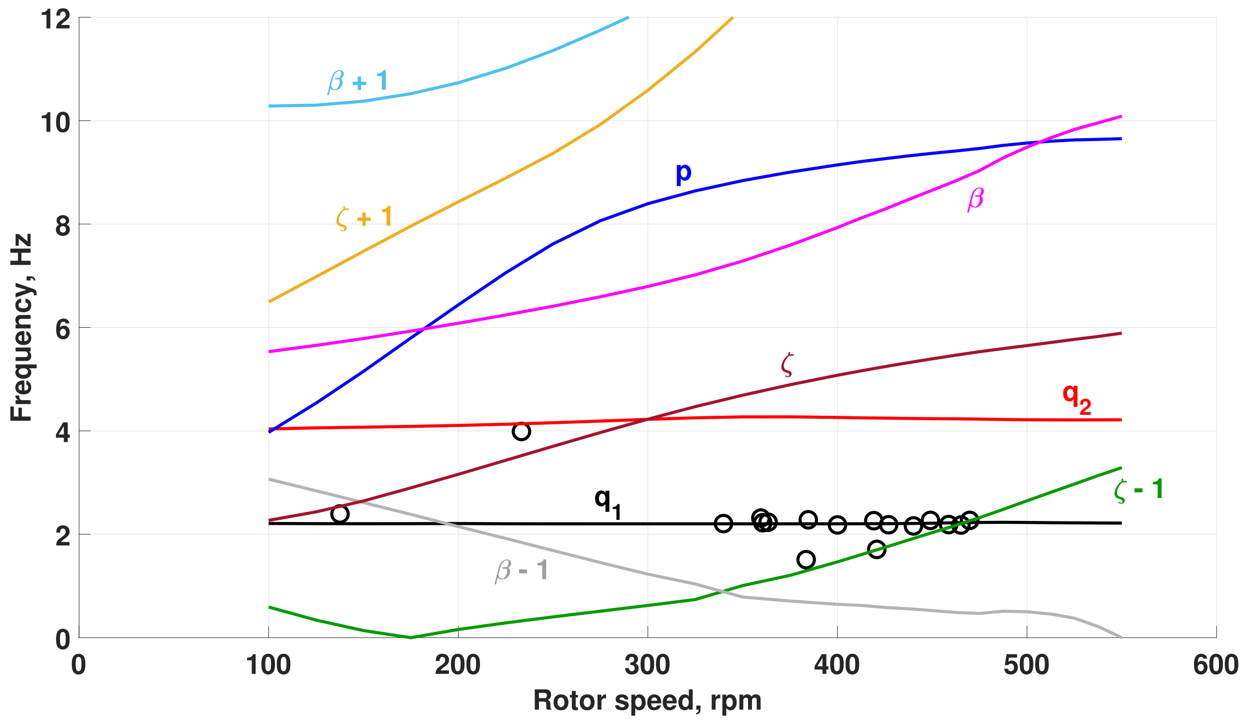

(a) Frequency

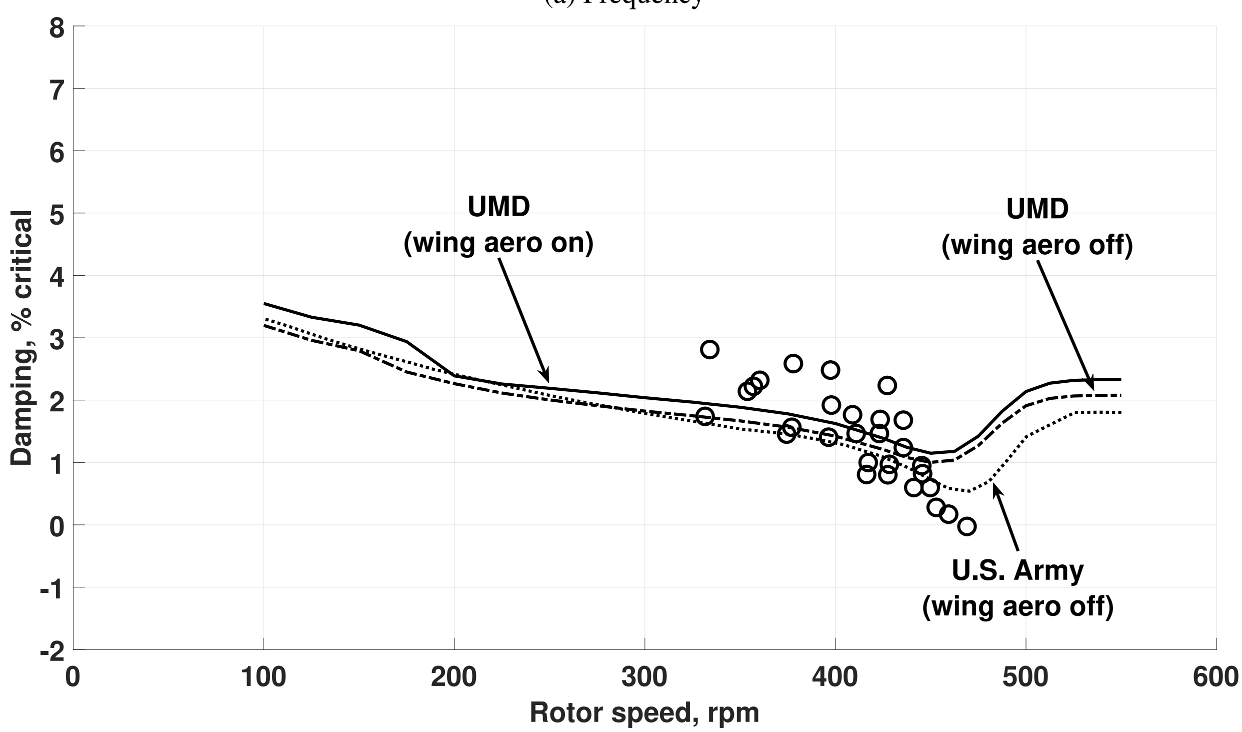

(b) Wing beam mode damping

Figure 4.19: Stability roots of coupled modes at 100-knots
(lines: UMD (UMARC-II) and U.S. Army (RCAS, Ref. [33]) predictions, symbols: test data)

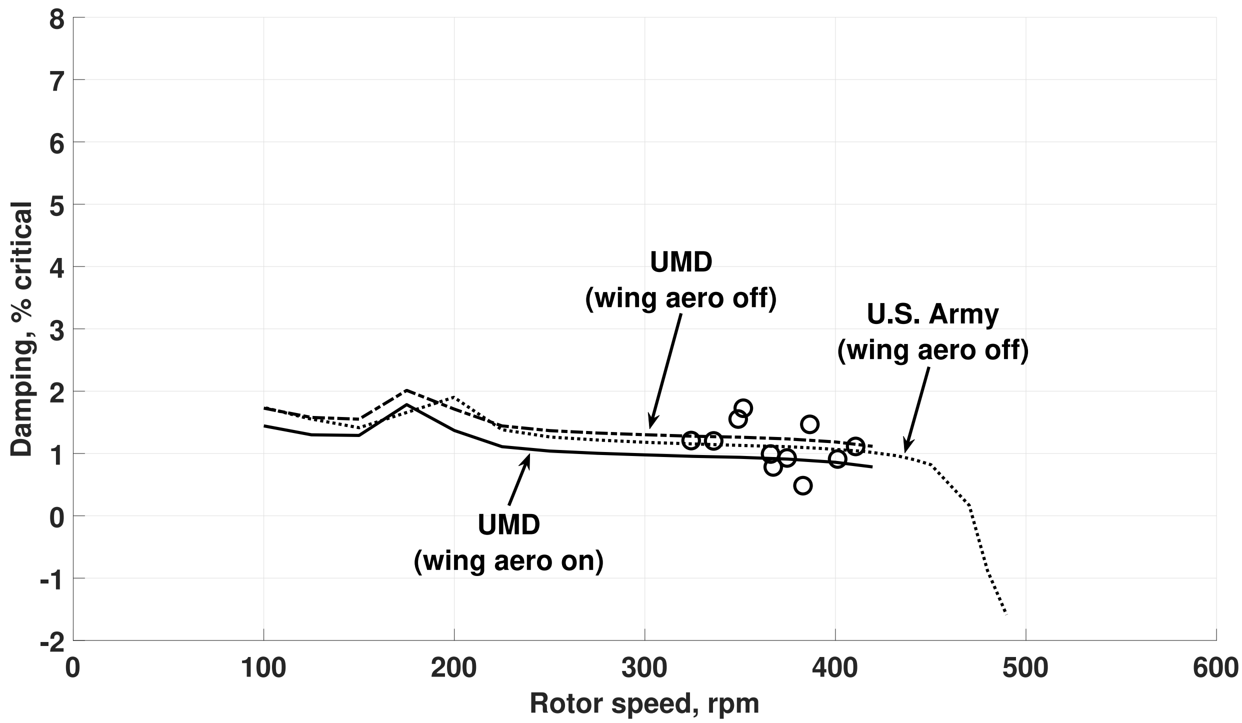

(a) 50 knots

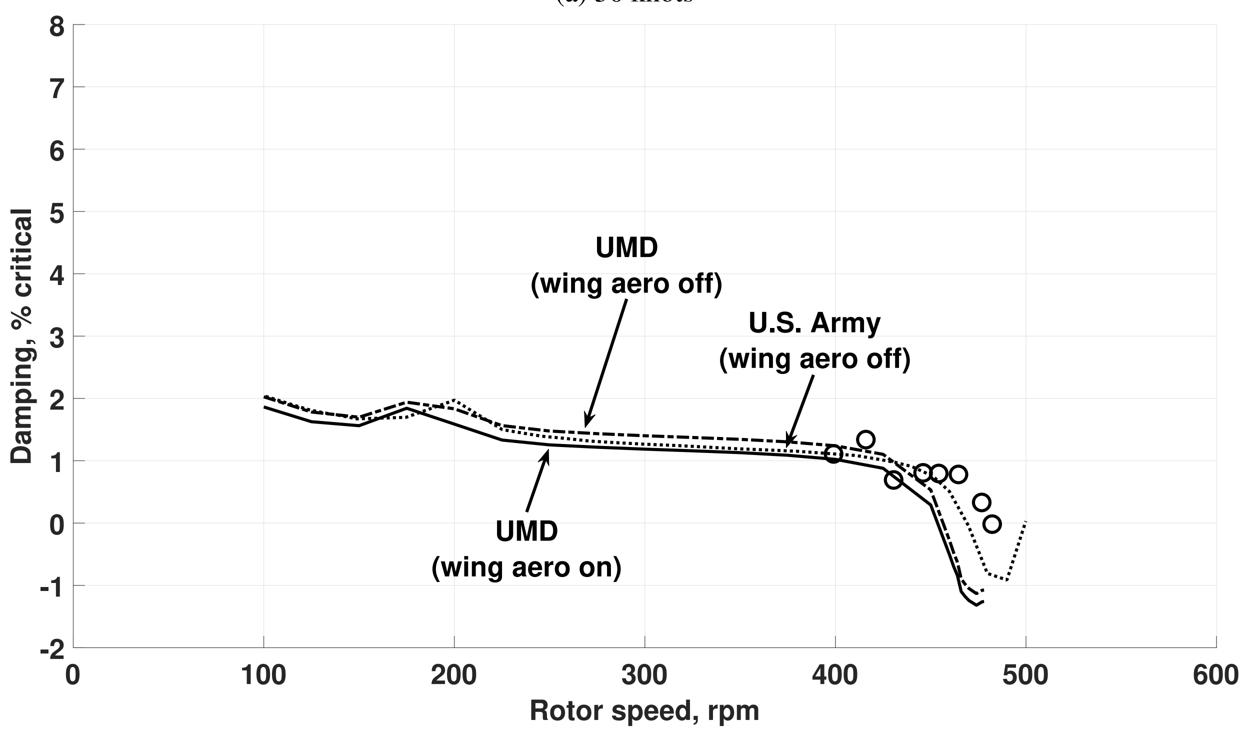

(b) 60 knots

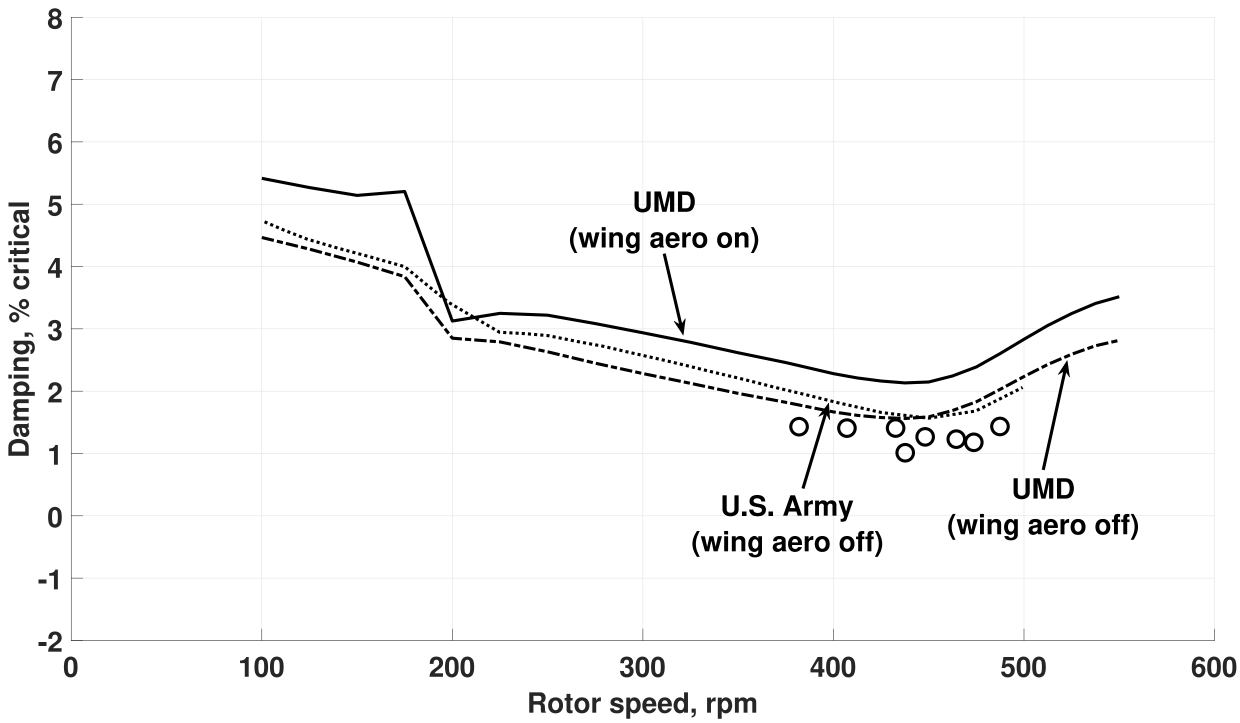

(c) 140 knots

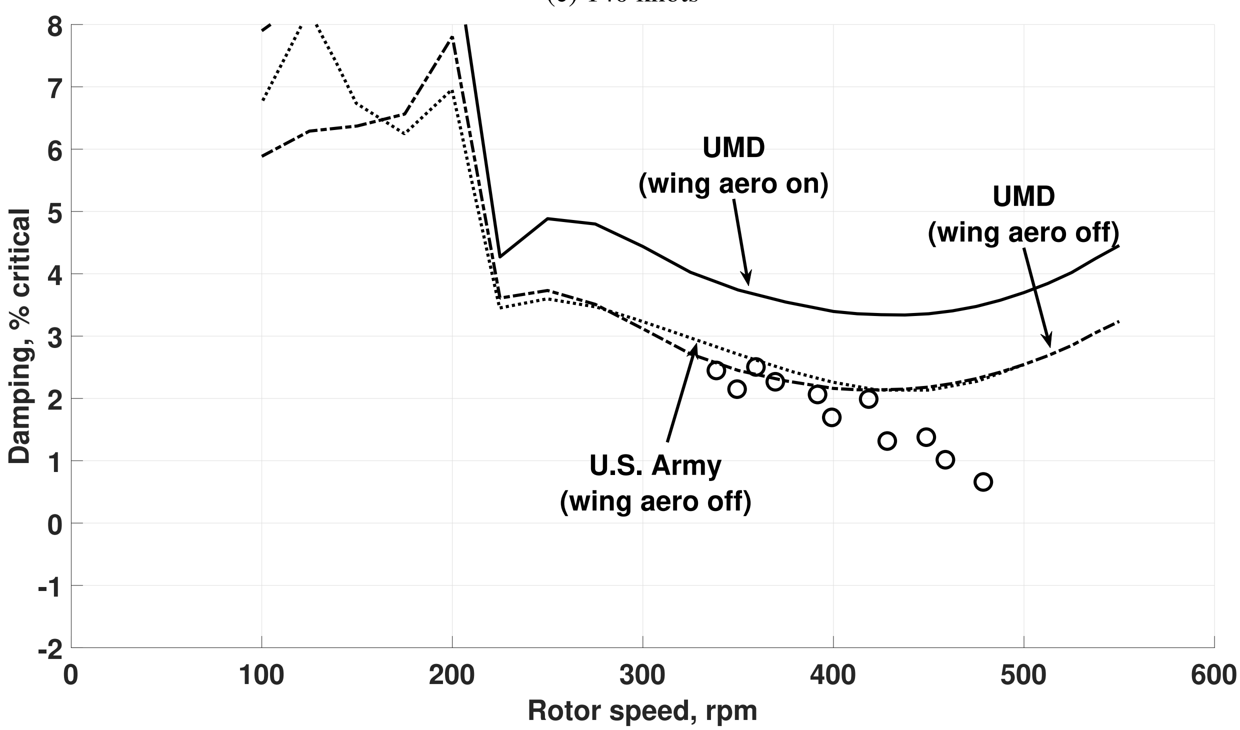

(d) 192 knots

Figure 4.20: Wing beam mode damping
(lines: UMD (UMARC-II) and U.S. Army (RCAS, Ref. [33]) predictions, symbols: test data)

4.5 Fundamental Understanding

This section presents a sensitivity analysis of stability predictions to model complexity. It is aimed at establishing modeling and testing requirements, and shedding further light on the physical phenomena. The highly damped rotor modes are not included in the figures for readability. The following are studied one by one: (1) effect of induced flow model, (2) effect of rotor speed perturbation and powered mode operation, (3) effect of rotor modes, (4) effect of blade airloads model, (5) effect of wing aerodynamics, and finally (6) effect of periodic solution before stability analysis.

Figure 4.21 shows the effect of the rotor induced flow model. Freewake geometry was converged for the trim solution and kept constant as the states were perturbed for the stability solution. This is because the change of trailed vorticity due to perturbation of states is insignificant. Shed vorticity, on the other hand, may be significant which was taken into account with unsteady thin airfoil theory for all the induced flow models. Figure 4.21 shows that the predictions with uniform inflow, no induced flow, and freewake with a single tip vortex and full-span nearwake are almost indistinguishable. This is because the induced flow is insignificant compared to the flight speed and the wake is quickly washed away from the rotor in high-speed flight. The inflow ratio (λ_c) varies from 0.16 to 1.12 from 50 to 350 knots.

Figure 4.22 shows the effect of rotor speed perturbation and powered mode operation. The dashed lines removed the joint at the rotor hub (in rotation direction) but the rotor still operates in freewheeling mode. The dotted line, in addition to removing the joint, also took into account the actual flight of the Boeing M222 aircraft by considering the parasite drag at the corresponding flight speed; a flat plate area of $6.279\ \mathrm{ft}^2$ was used based on Ref. [90] and the rotor was trimmed to produce half of this drag (two rotors on the aircraft). When the engine is considered ideal (dashed lines), which is perhaps closer to an electric drive, damping of q_1 mode increases compared to the baseline but p mode stays mostly unaffected. When the rotor is also trimmed in powered mode (dotted lines), an interesting behavior is observed for air resonance. Coupling of $\zeta - 1$ and p modes becomes more dominant; as a result, the damping of p mode drops much earlier. This is one of the fundamental differences of soft in-plane hingeless hub tiltrotors from their stiff in-plane gimballed counterparts where air resonance is not observed. These predictions show that it is important to perform stability predictions for both freewheeling mode with rotor speed perturbation and powered mode for these kinds of hubs. The most conservative results can then be used for design or testing purposes.

Figures 4.23 to 4.25 show the effect of rotor modes. The solver can apply modal reduction by taking into account a set number of modes for the rotor and the wing. Using only the first three rotor modes (flap, lag, and torsion, Fig. 4.23) resulted in relatively close air resonance predictions to the baseline model where ten rotor modes were used. The highest difference is in $\beta + 1$ mode. When the torsion mode was removed, significantly higher p damping was predicted at high speeds (coupling of $\zeta - 1$ and p modes is delayed). This is mostly because the rotor torsion deflection due to the propeller and aerodynamic pitching moments has a direct effect on the collective angle required to trim the rotor, which in turn introduces coupling between rotor flap and lag modes. Using only the rotor flap mode (Fig. 4.24) did not capture air resonance at all. Using only the rotor lag mode (Fig. 4.25) still predicted the air resonance phenomenon, but with high error; the critical mode becomes q_2, which goes unstable before p mode due to coupling with ζ mode.

Figures 4.26 and 4.27 show the effect of the blade airloads model. Omitting the unsteady terms (Fig. 4.26) did not have a significant impact on the solution. Further simplifying the model by replacing the airfoil tables with a linear aerodynamic model that used $C_{l_\alpha} = 5.73$, $C_{d_0} = 0.01$, and Glauert correction for compressibility resulted in significantly higher damping for p mode at high speeds again due to the delayed coupling of the modes. Removing the Glauert correction (Fig. 4.27) predicted even higher damping for p mode. Airfoil decks seem necessary for correct prediction of the proprotor air resonance instability. This means numerical perturbation is required; simple analytical equations should not be used.

Figures 4.28 and 4.29 show the effect of the wing aerodynamic model. As expected, when unsteady terms are not taken into account (Fig. 4.28), damping for p mode is slightly lower (L_3 term given in Eq. 2.77). This is the only source of torsion damping for an isolated wing, but is insignificant for a coupled rotor/pylon/wing system. Using an incompressible linear aerodynamic model without the unsteady terms changed high-speed predictions for the q_1 mode, but not significantly. The most important conclusion here is the necessity of a wing aerodynamic model if q_1 is the critical mode. When it is omitted (Fig. 4.29), this mode has significantly lower damping. This may result in too conservative stability predictions. In such a case, wing aerodynamics should use the correct airfoil decks if possible. But in this case where air resonance is critical, wing aerodynamics is not important at all.

Figures 4.30 and 4.31 show the effect of the periodic solution before stability calculations. Solid lines found the periodic solution for the rotor/pylon/wing system before the stability analysis. The dashed lines skipped the periodic solution step while using the same freewheeling collective angles; it essentially assumed zero deflections for the rotor and the wing in order to save computation time. Similar results were obtained for the freewheeling mode. This is expected as the deflections are small. However, for the powered mode, the instability speed was over-predicted when periodic solution is skipped. Damping of the q_1 mode was also over-predicted at high speeds.

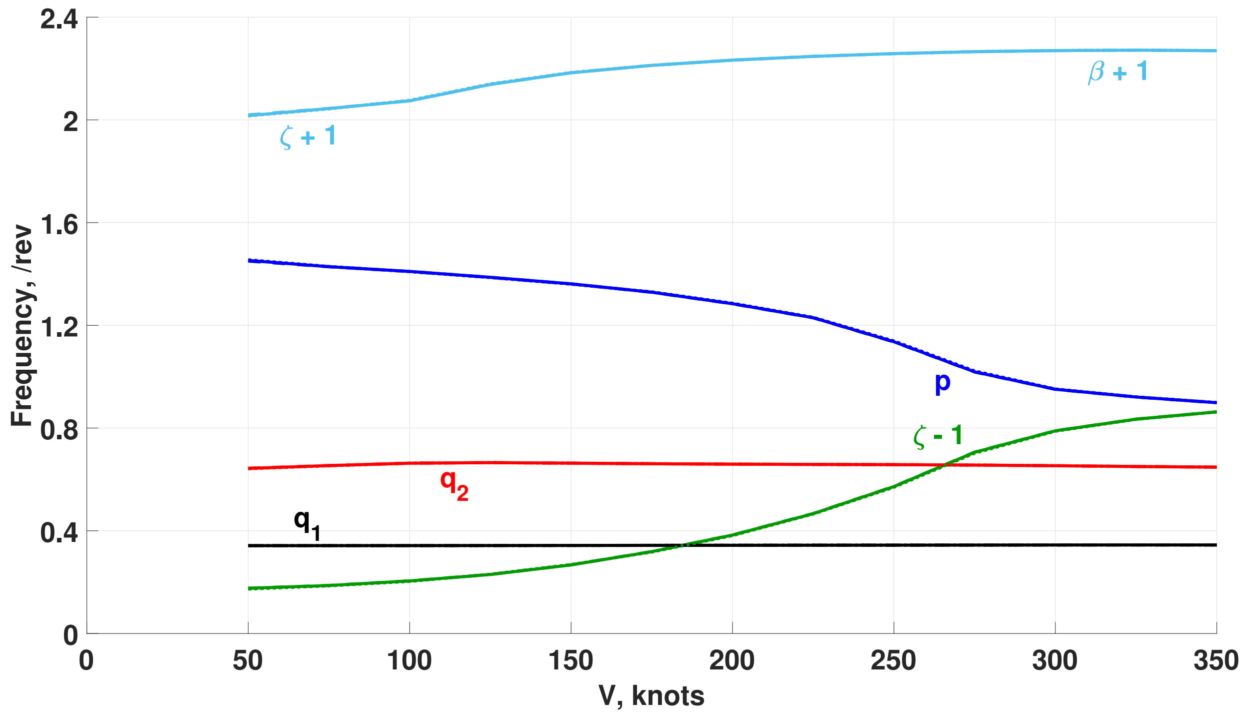

(a) Frequency

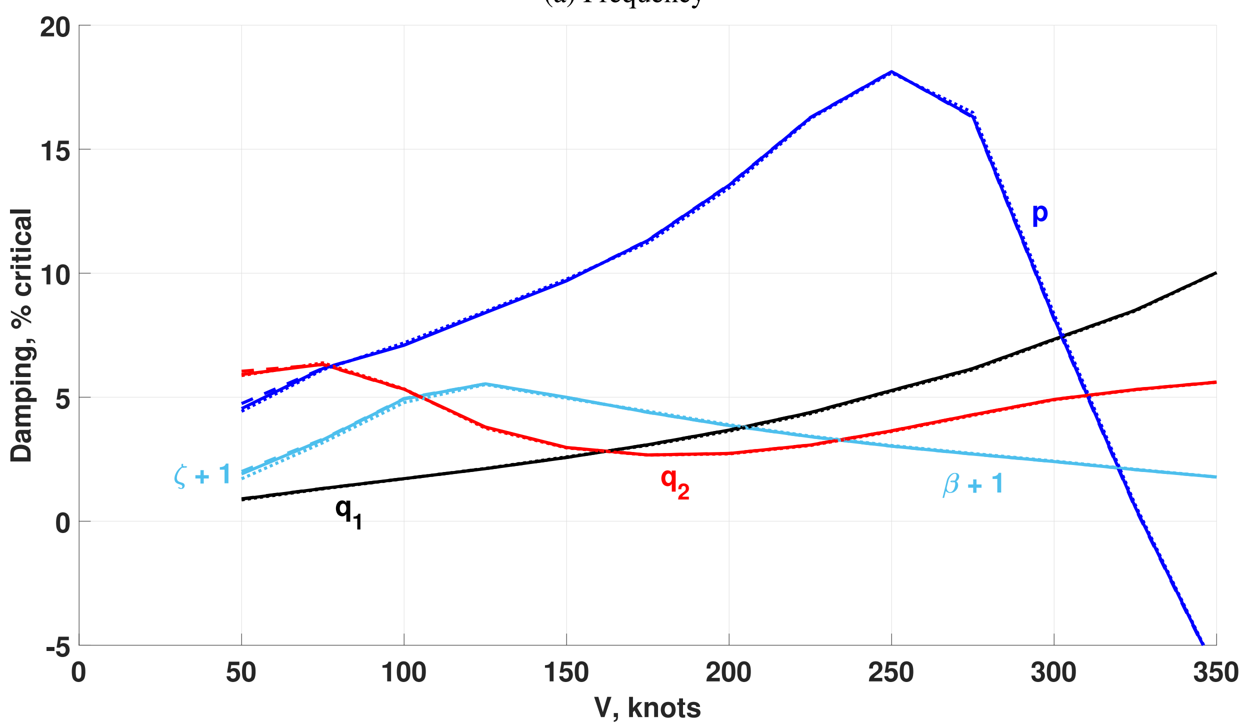

(b) Damping

Figure 4.21: Effect of induced flow
(solid: uniform inflow – baseline, dash: no induced flow, dot: Maryland Freewake)

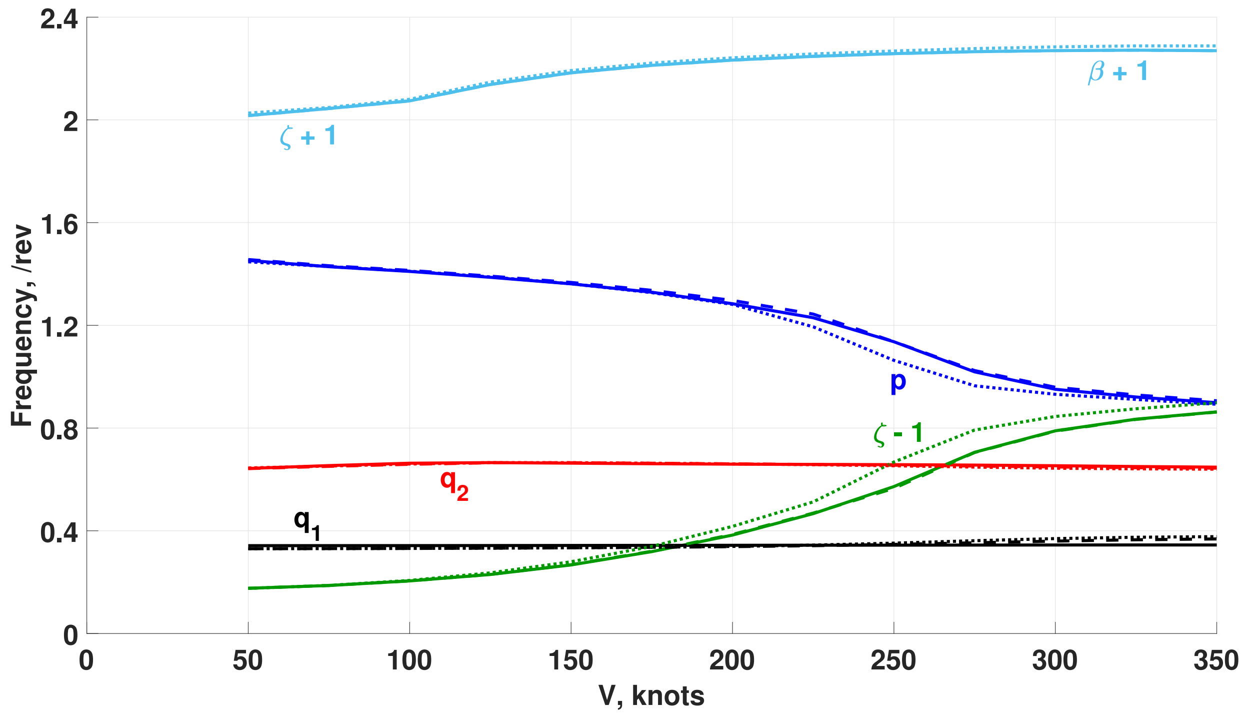

(a) Frequency

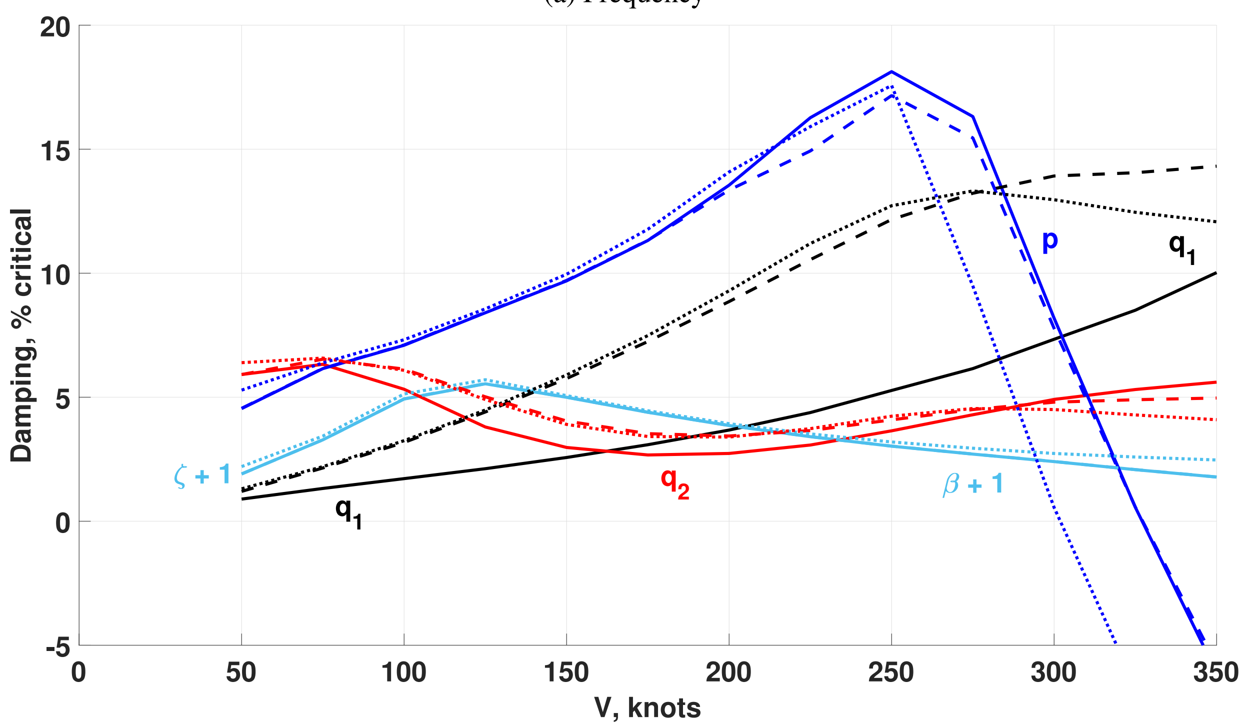

(b) Damping

Figure 4.22: Effect of rotor speed perturbation and powered mode operation (solid: freewheeling with rotor speed perturbation – baseline, dash: freewheeling with constant rotor speed (ideal engine), dot: powered with constant rotor speed (ideal engine))

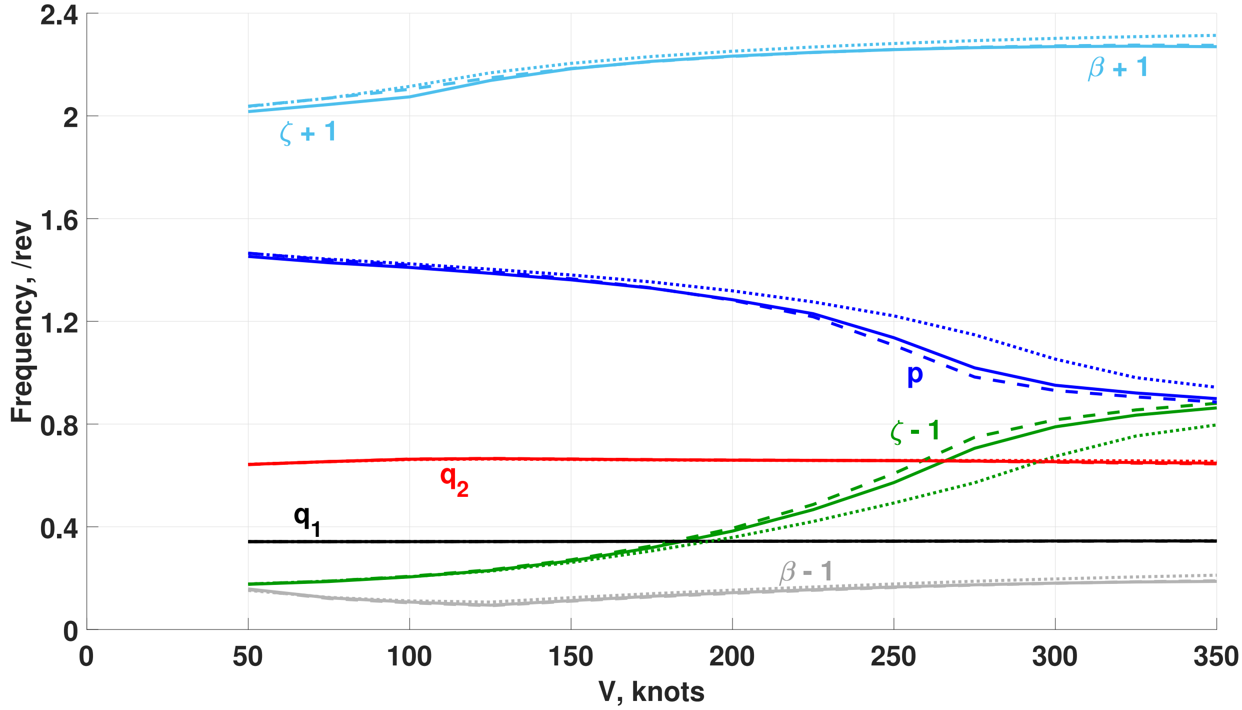

(a) Frequency

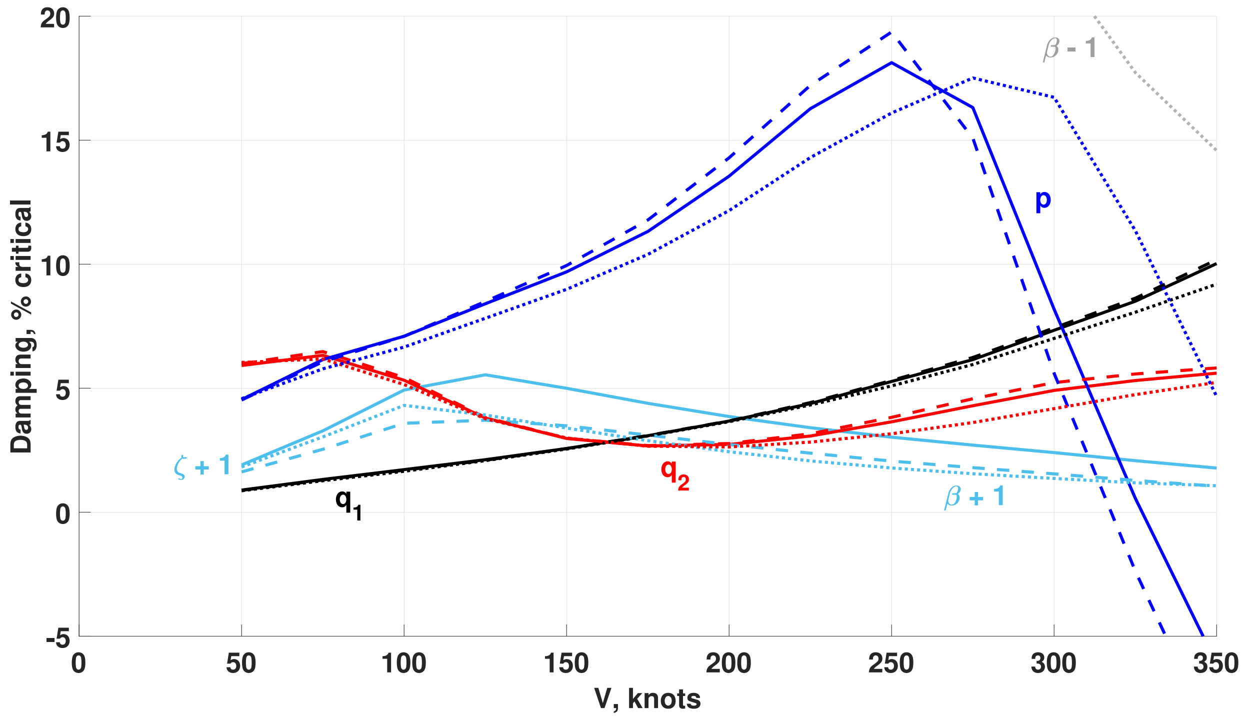

(b) Damping

Figure 4.23: Effect of rotor modes (solid: first 10 modes – baseline, dash: first flap, lag, and torsion modes, dot: first flap and lag modes)

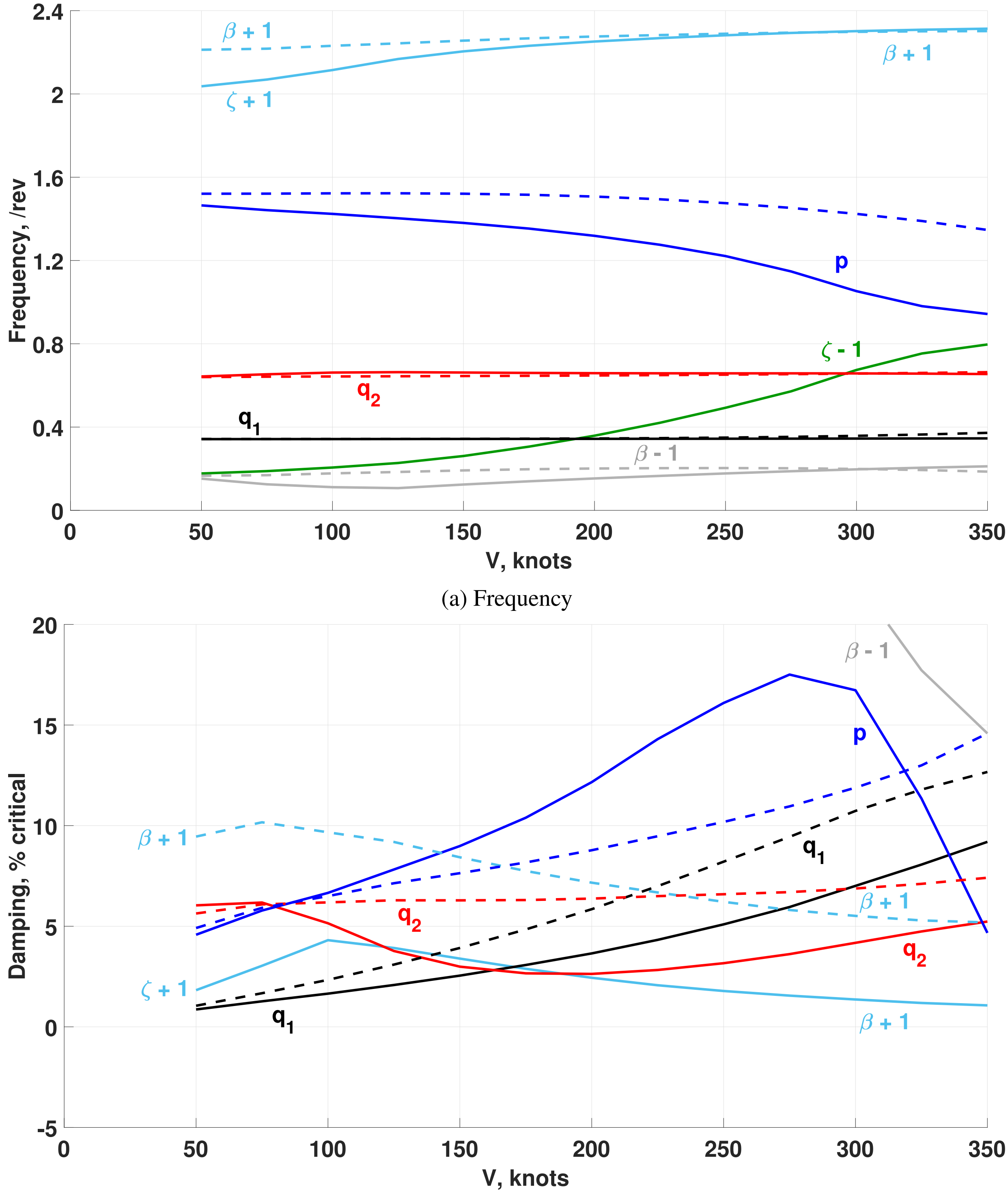

(a) Frequency

(b) Damping

Figure 4.24: Effect of rotor modes (solid: first flap and lag modes, dash: first flap mode only)

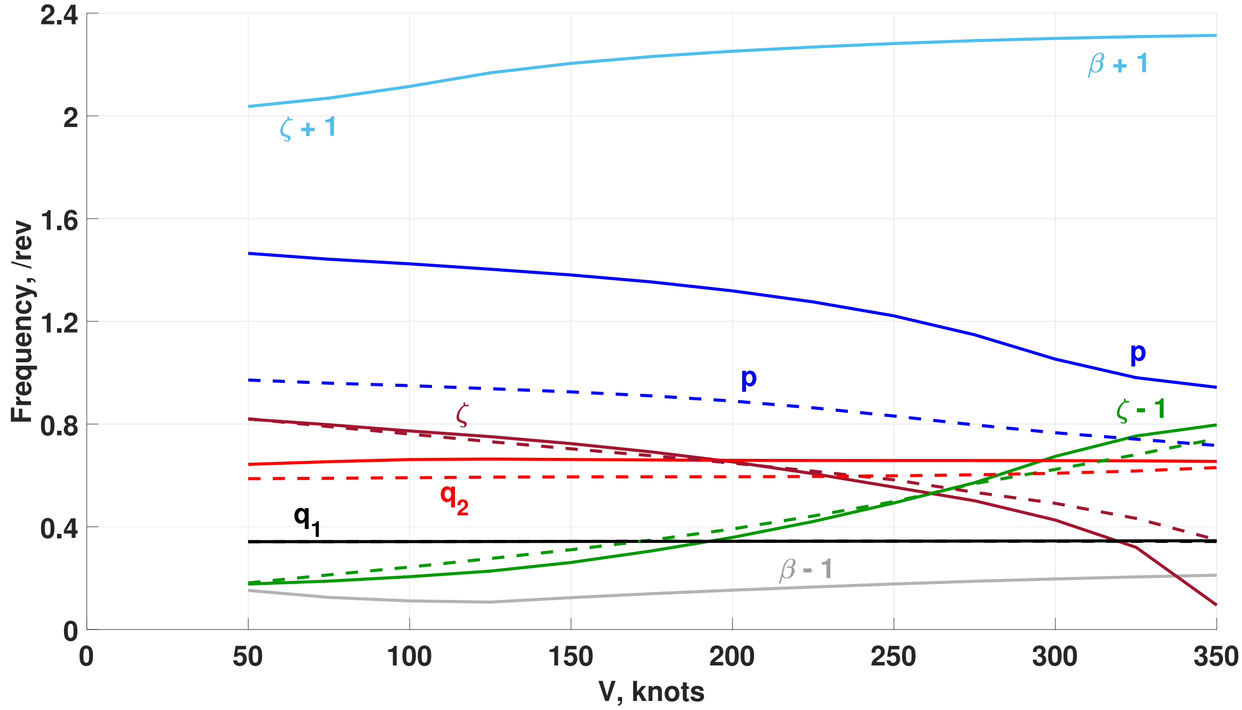

(a) Frequency

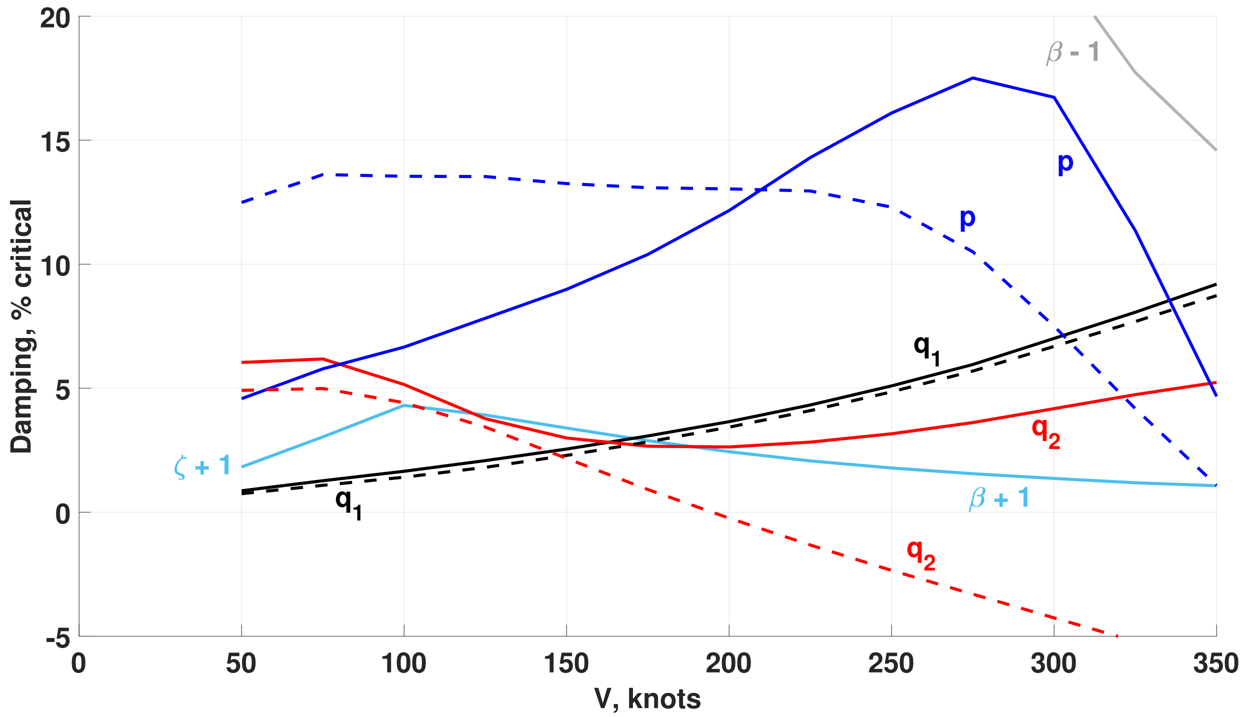

(b) Damping

Figure 4.25: Effect of rotor modes (solid: first flap and lag modes, dash: first lag mode only)

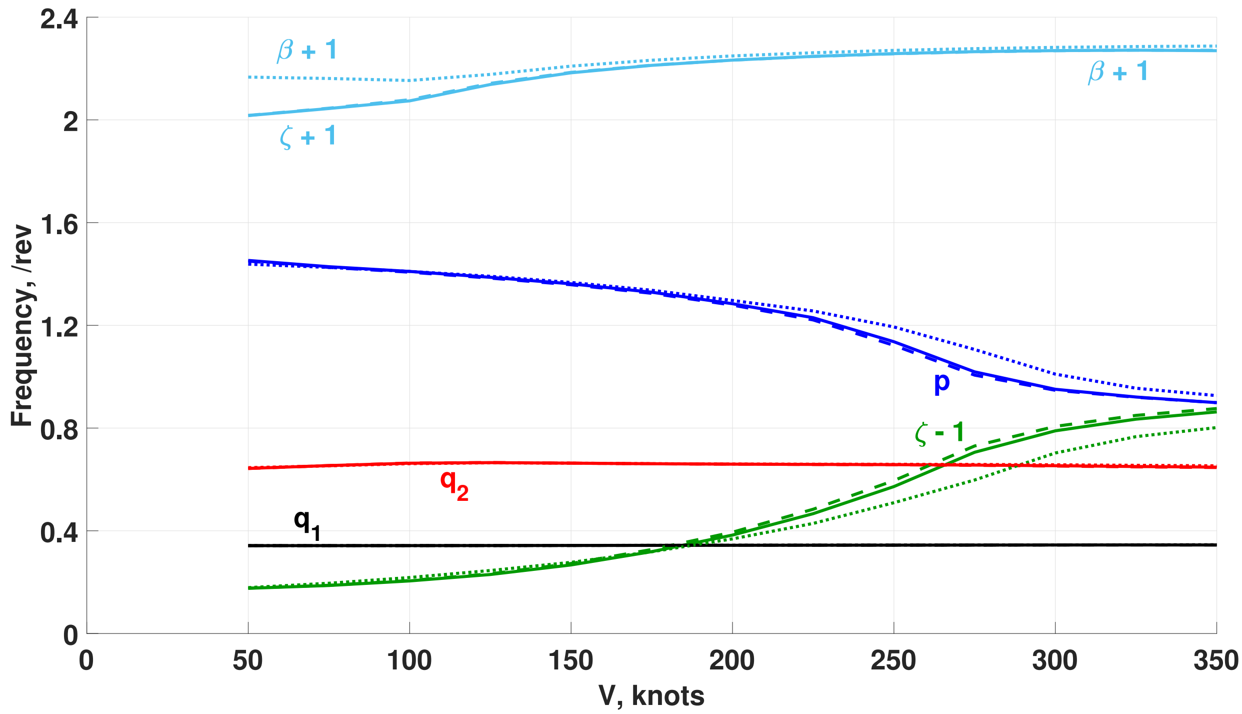

(a) Frequency

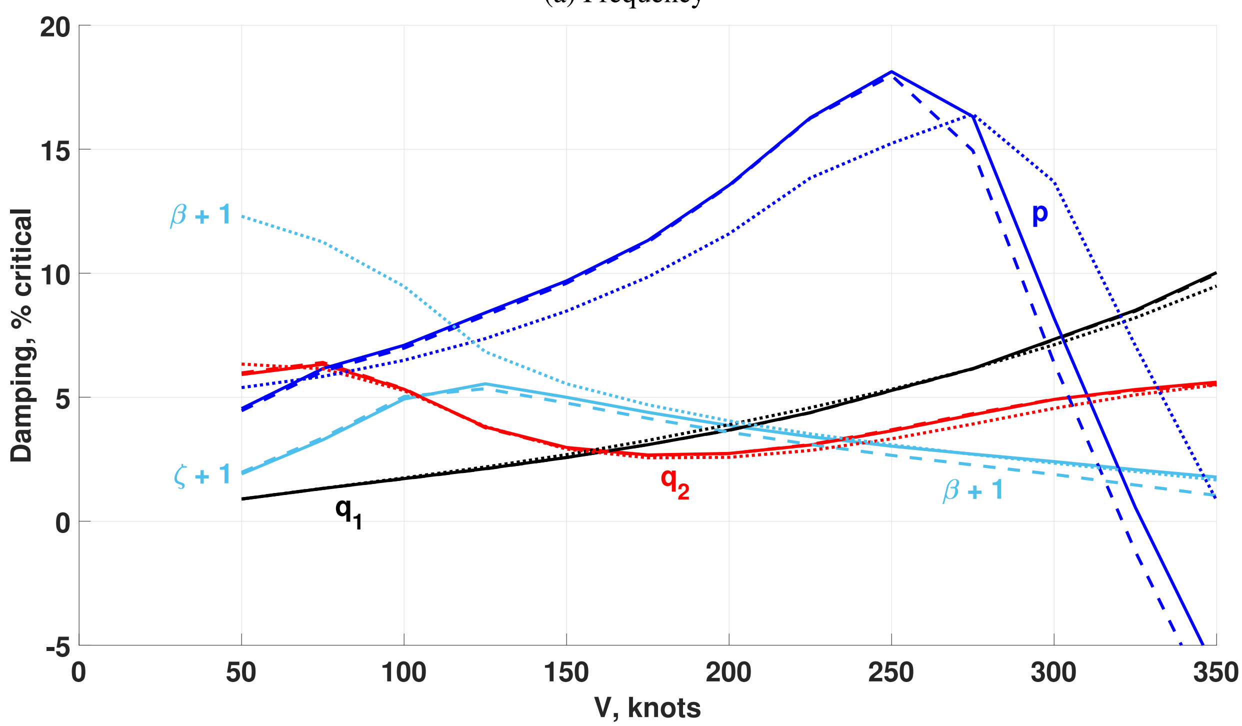

(b) Damping

Figure 4.26: Effect of blade airloads model
(solid: C81 airfoil decks with unsteady terms – baseline, dash: C81 airfoil decks without unsteady terms, dot: linear aerodynamics with Glauert correction)

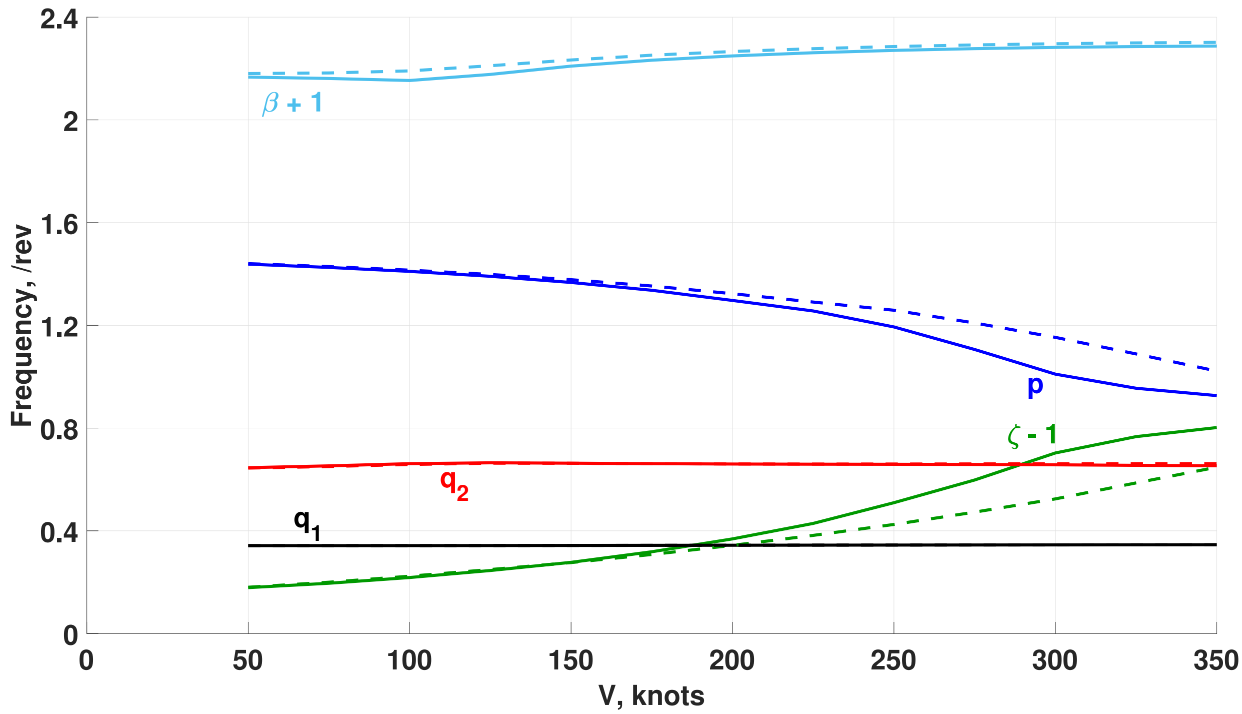

(a) Frequency

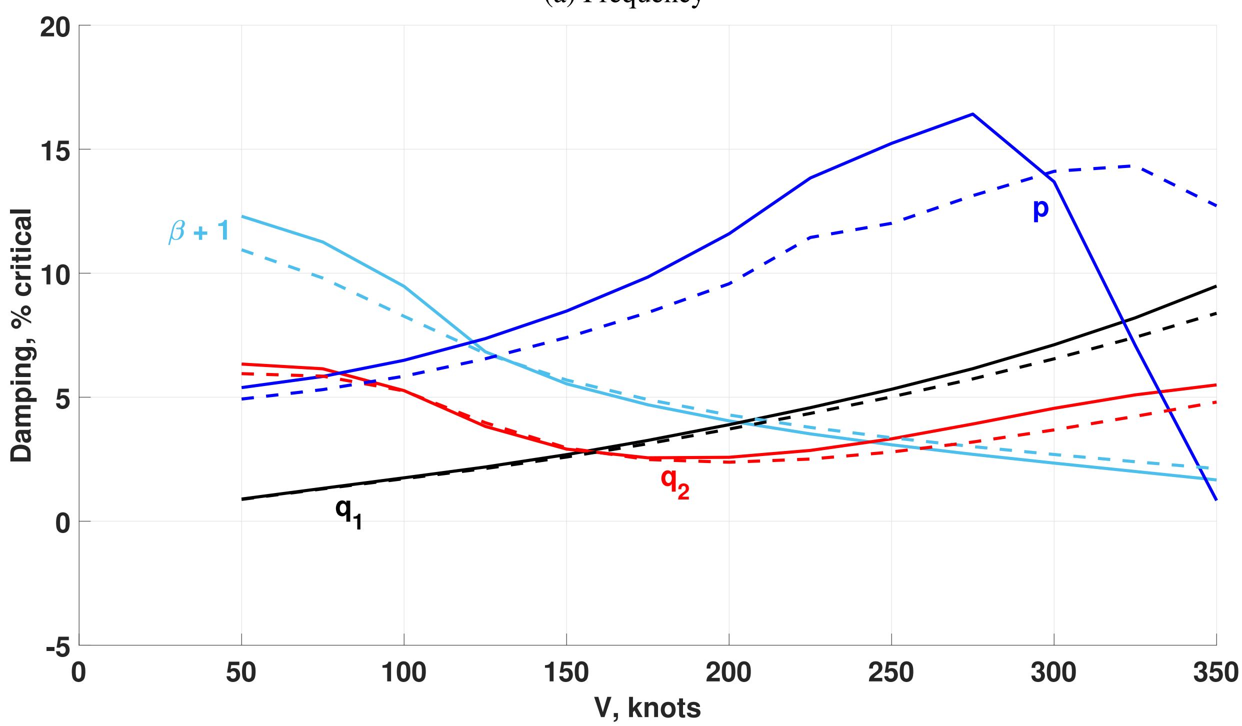

(b) Damping

Figure 4.27: Effect of blade airloads model
(solid: linear aerodynamics with Glauert correction, dash: incompressible linear aerodynamics)

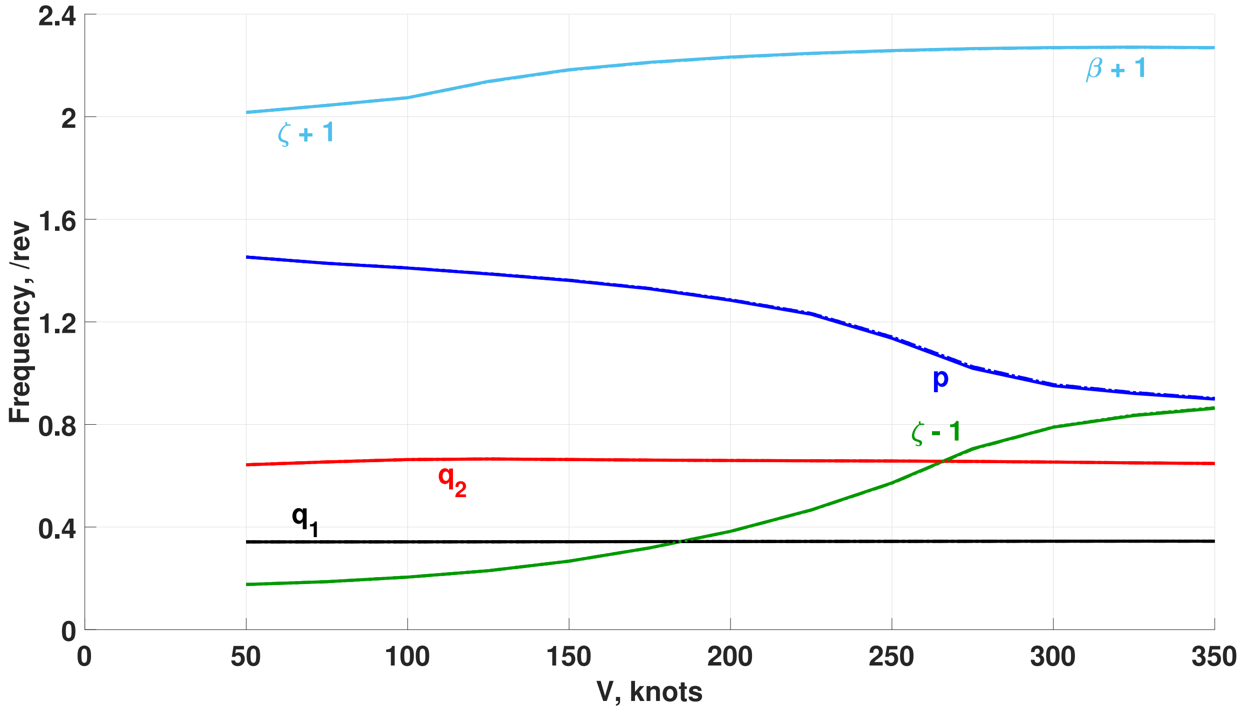

(a) Frequency

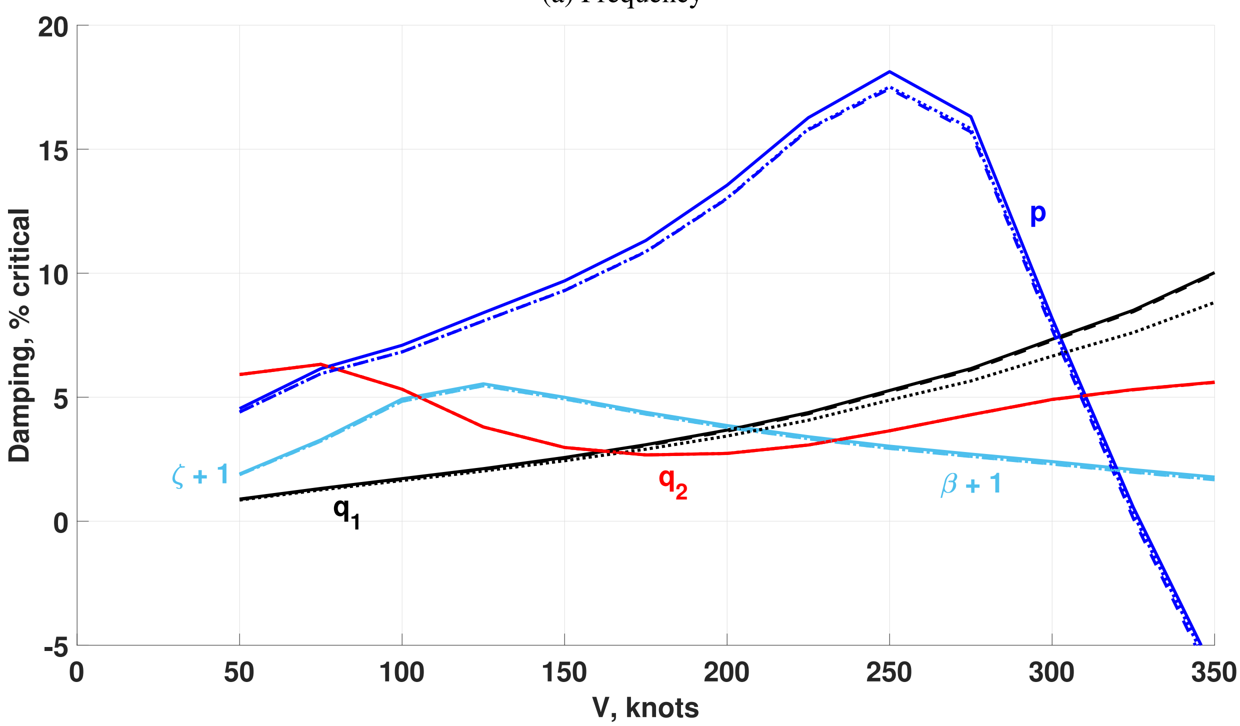

(b) Damping

Figure 4.28: Effect of wing aerodynamic model (solid: C81 airfoil deck – baseline, dash: C81 airfoil decks without unsteady terms, dot: incompressible linear aerodynamics)

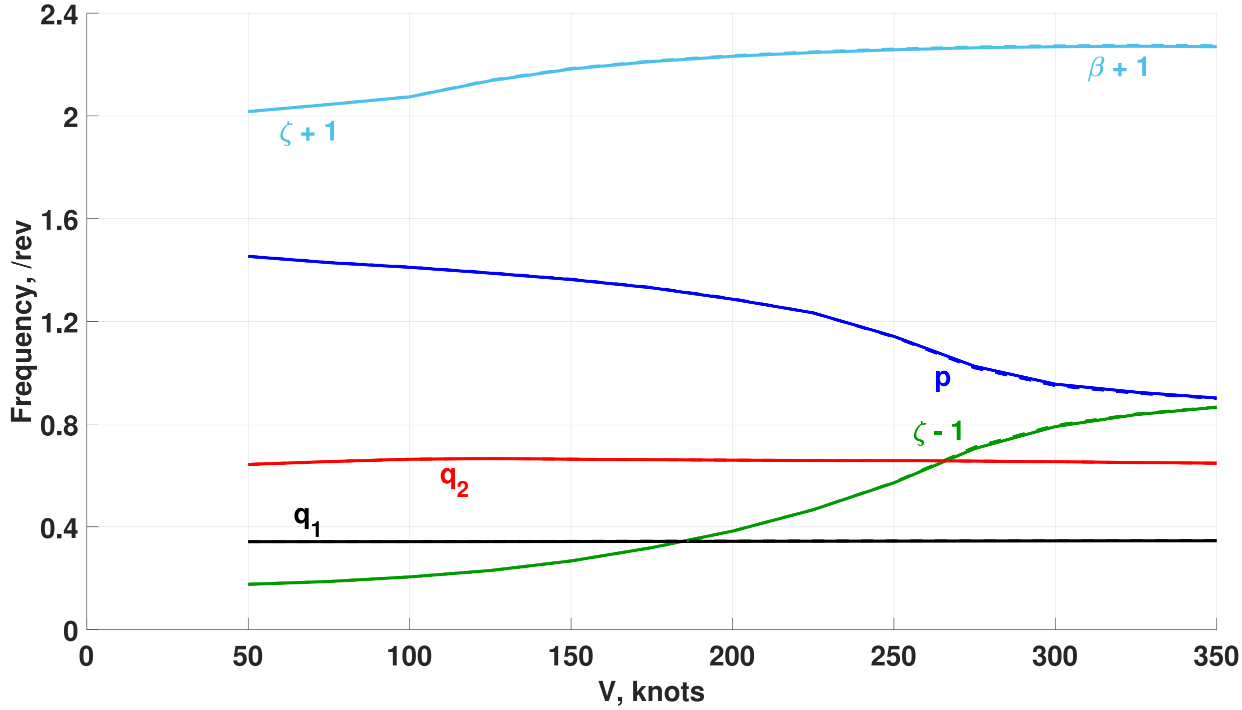

(a) Frequency

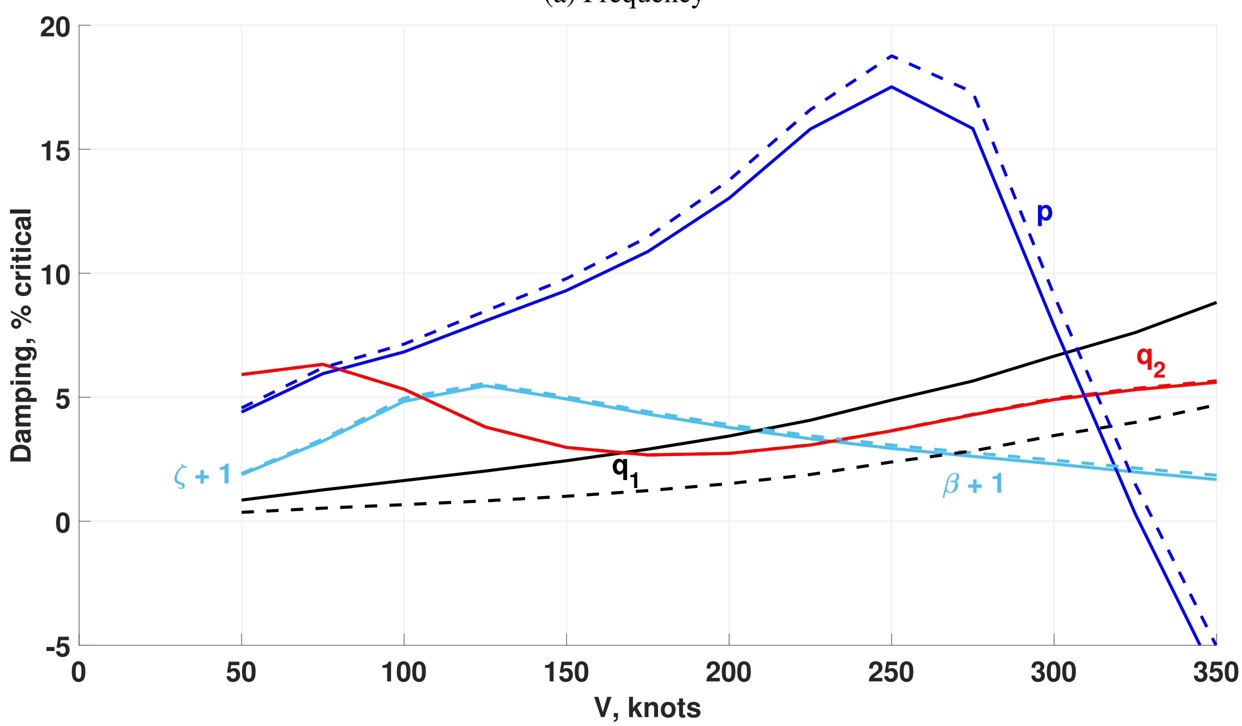

(b) Damping

Figure 4.29: Effect of wing aerodynamic model
(solid: incompressible linear aerodynamics, dash: no aerodynamics)

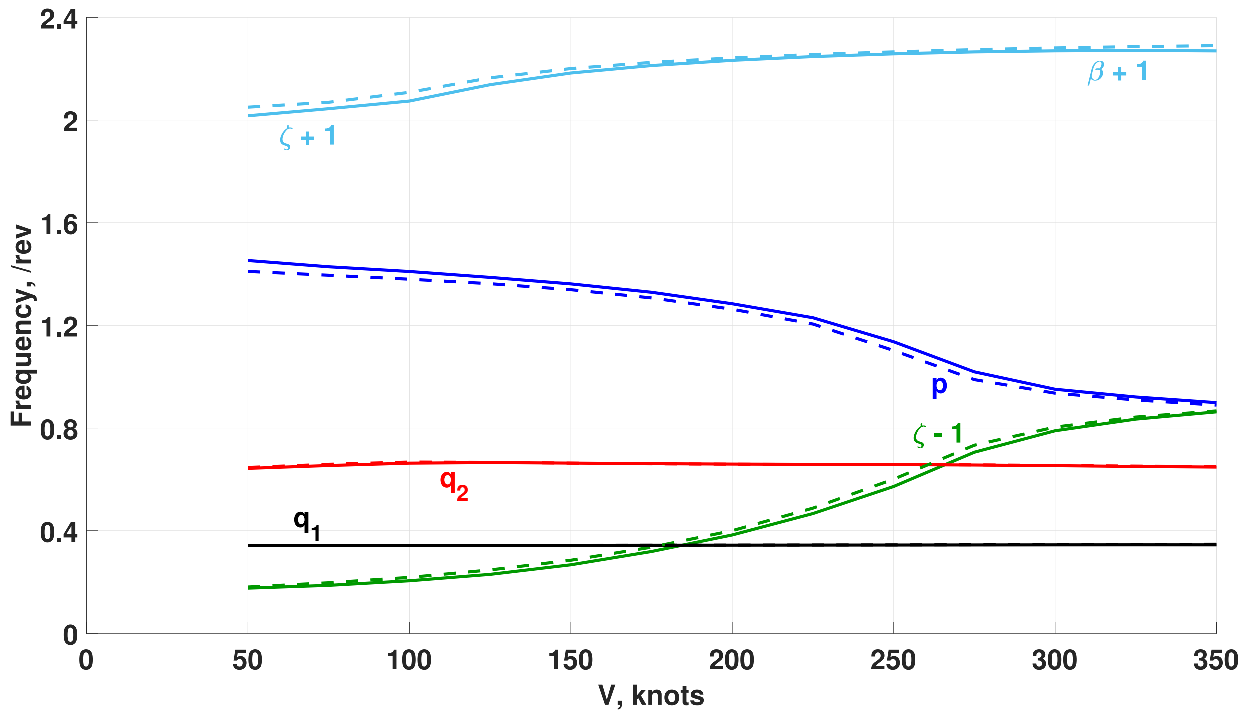

(a) Frequency

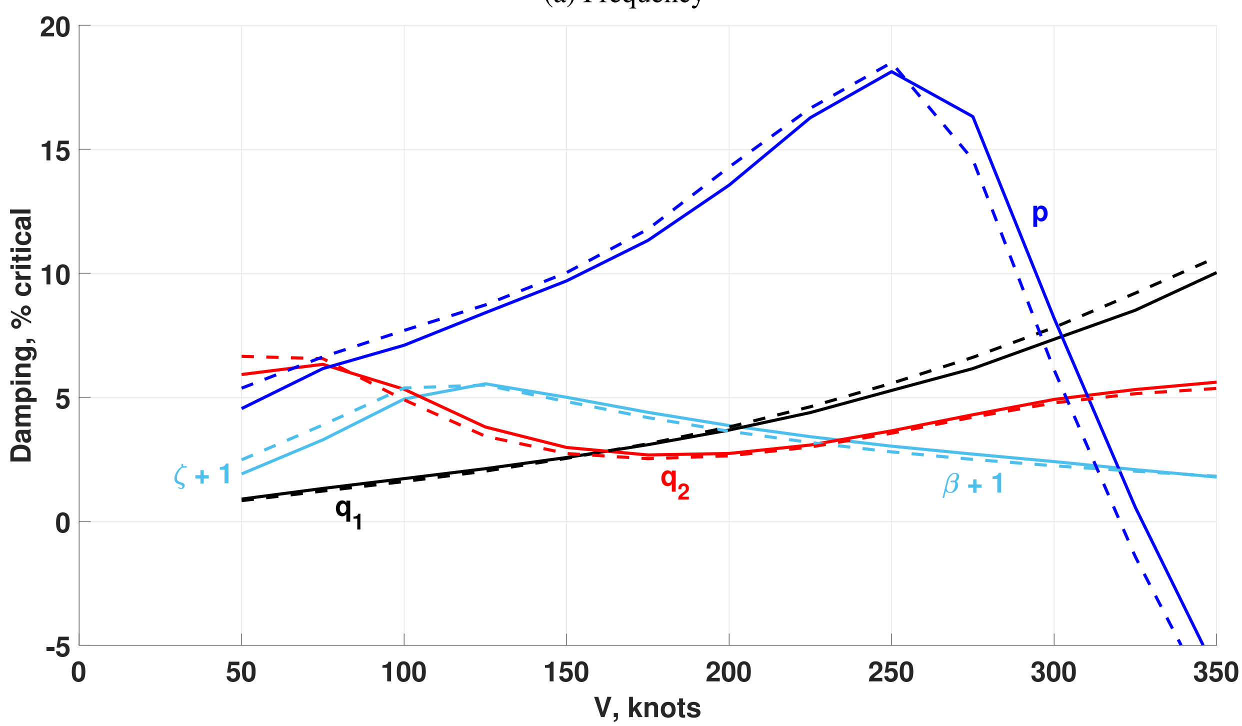

(b) Damping

Figure 4.30: Effect of periodic solution for freewheeling
(solid: baseline, dash: no periodic solution)

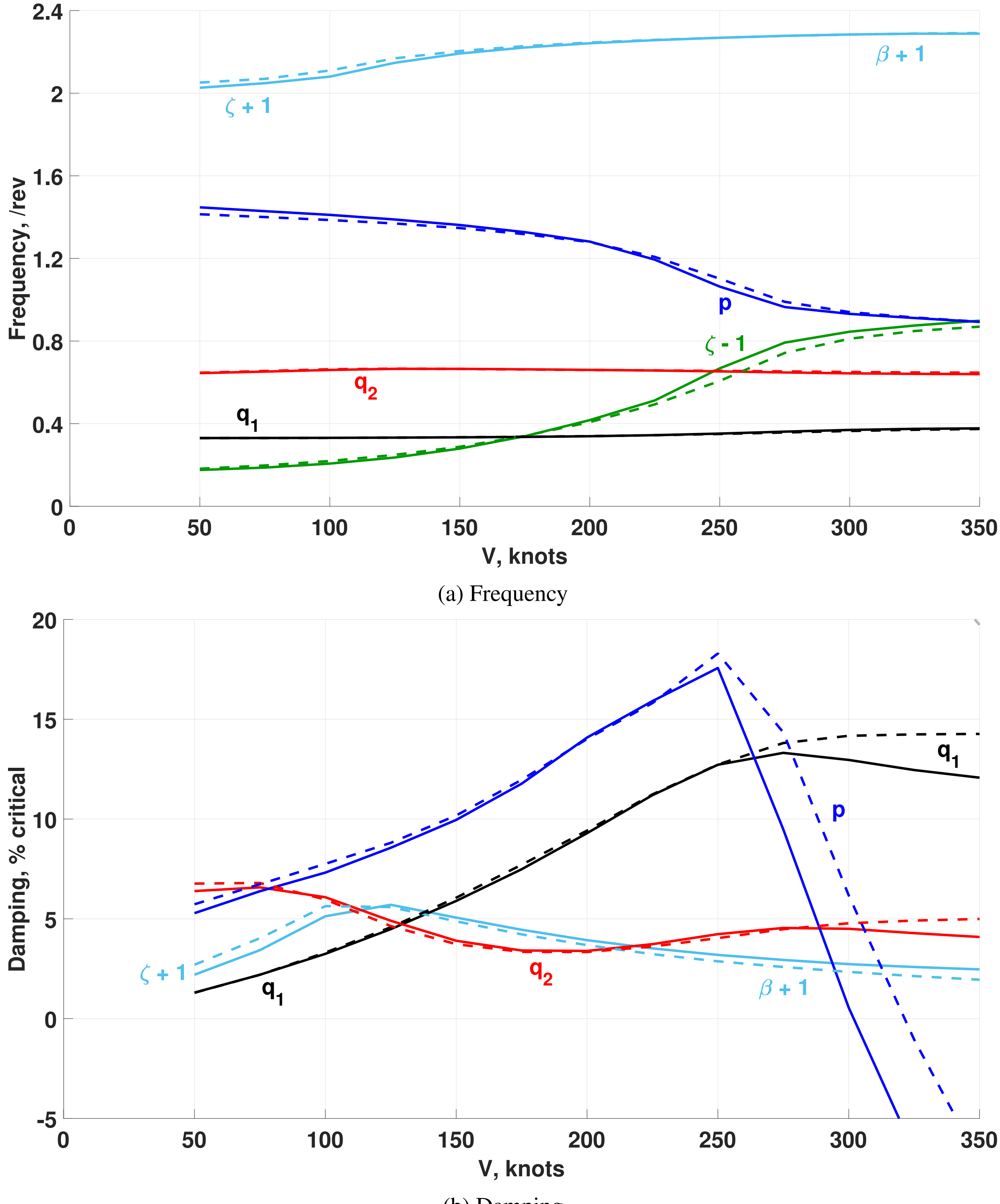

(a) Frequency

(b) Damping

Figure 4.31: Effect of periodic solution for powered mode
(solid: powered mode, dash: powered mode with no periodic solution)

4.6 Summary and Conclusions

The newly developed solver was validated with the full-scale Boeing M222 test data. Validation was carried out for performance, loads, and stability. A fundamental understanding of the physics of hingeless hub tiltrotor instabilities was gained. The key conclusions are as follows:

1. Good agreement was observed between performance predictions and test data.

2. The hover, transition, and cruise loads were predicted within the correct trends but some differences in the magnitudes remained.

3. Proprotor air resonance is the critical instability for the Boeing M222 rotor due to the soft in-plane hingeless hub, not whirl flutter. Air resonance occurs with the coupling of wing torsion (p) and low-frequency lag ($\zeta - 1$) modes at high speeds. The mode shape is mostly lag near instability.

4. Air resonance predictions agreed well with U.S. Army's RCAS predictions. The agreement with the test data was good for low speeds, but some offset in the damping levels was observed for 140 and 192 knots.

5. Induced flow bears no significance for high-speed stability predictions. Freewake is not required; a simple uniform inflow model is sufficient. Not using an inflow model is also acceptable at high speeds.

6. Predictions should be performed for both freewheeling with rotor speed perturbation and powered mode in actual flight with an ideal engine (no rotor speed perturbation) as air resonance can be more critical for the powered mode.

7. At least the first rotor flap, lag, and torsion modes must be included in the analysis.

8. Airfoil decks should be used for both the rotor and the wing. The wing aerodynamic model is only important if the wing beam mode is critical.

9. Periodic solution for freewheeling mode can be skipped before stability analysis to save computation time, provided the correct collective angle is used. However, periodic solution should be carried out for powered mode where deflections are larger.

Chapter 5: Validation with Maryland Tiltrotor Rig and Parametric Study

University of Maryland's Maryland Tiltrotor Rig (MTR) was tested in the Naval Surface Warfare Center Carderock Division $8\text{-ft} \times 10\text{-ft}$ subsonic wind tunnel on October 26 – November 2, 2021. Stability data was collected for eight different configurations. Configuration changes provided valuable data for validation and parametric study.

5.1 Maryland Tiltrotor Rig (MTR)

MTR is a new tiltrotor test facility at the University of Maryland (UMD) developed over the last six years. It is an optionally powered semi-span rig that supports interchangeable hubs (gimballed and hingeless), blades (straight and swept-tip), and wing spars in order to allow for a systematic variation of components that are important for whirl flutter. The rig consists of the wing assembly, motor drive, rotor shaft, hub, swashplate (three-bladed), and instrumentation.

MTR was initiated in January 2016. The requirements and conceptual design were completed in August 2016. Calspan Corporation was contracted to fabricate the MTR and supporting equipment in February 2017. The composite blades and wing spars were designed and fabricated in-house at UMD. The design and fabrication were planned in two phases; Phase-I for the gimballed hub and Phase-II for the interchangeable hingeless hub. The Preliminary Design Review was completed on June 28, 2017. The Critical Design Review of the gimballed hub was completed on October 6, 2017. The gimballed hub MTR was completed in March 2019.

After extensive instrumentation and characterization tests, it was transferred to UMD on August 20, 2019. Throughout this time, blade design and fabrication proceeded in parallel. The first checkout entry of the full rig with blades on was conducted at the Glenn L. Martin wind tunnel on September 10 – 13, 2019. This entry did not acquire research data. The second entry was on November 4 – 8, 2019. Stability data was not collected in this test. Soon after, the wind tunnel closed due to COVID-19. To expedite the acquisition of research data, the MTR was installed at the Carderock wind tunnel instead, and tested on October 26 – November 2, 2021. Concurrently, the development of the hingeless hub picked up post-COVID. The Critical Design Review was completed on September 21, 2021.

The design of the MTR is reported in Ref. [66]. The fabrication and instrumentation of the gimballed hub are presented in Ref. [91]. The design analysis for the hingeless hub is reported in Ref. [92]. The design and fabrication of the blades are described in Ref. [93] for straight blades and in Ref. [94] for swept-tip blades. The straight (Fig. 5.2a) and the swept-tip (Fig. 5.2b) blades have the same twist. The straight blades consisted of two sets; the first was the blades used in the 2019 checkout run (same as Ref. [93]), which had strain gauges in flap and torsion directions, and the second was a new set fabricated with strain gauges in flap and chord directions. The sweep angle is $20°$, starting at $80\%R$.

The MTR installed in the Carderock wind tunnel is shown in Fig. 1.9. UMARC-II model of the MTR is shown in Fig. 5.1. Principal characteristics of the rig are given in Tables 5.1 and 5.2. The rotor section properties are given in Fig. 5.3. The wing/pylon section properties are given in Fig. 5.4. Note that R in Fig 5.4 is the total of the wing span and the pylon length (a total length of 1.1705 m). So, the pylon ($r/R = 79.2\%$ – 100%) is included as well. Frequency, structural damping, and mass-normalized mode shapes for the wing beam, chord, and torsion modes are given in Tables 5.3 to 5.5, where r represents distance along the elastic axis of the wing and pylon. The structural damping values were measured with rap tests. Note that the chord mode shows higher structural damping when the wing fairings are on. The dynamics of the fixed structure is otherwise unaffected by the fairings. The corresponding mode shape points and the axis system are shown in Fig. 5.5. The UMARC-II model of the MTR includes a full-wing and pylon model; however, the frequencies, mode shapes, and structural damping values are sufficient to model the fixed frame for any future validation study.

Fanplots for straight and swept-tip blades are shown in Fig. 5.6. Both the predictions and the test data are for $0°$ collective. Good agreement with the nonrotating frequency measurements is observed. Swept-tip blades exhibit higher frequencies. This is because of the lower blade mass due to the lack of spar in the swept region.

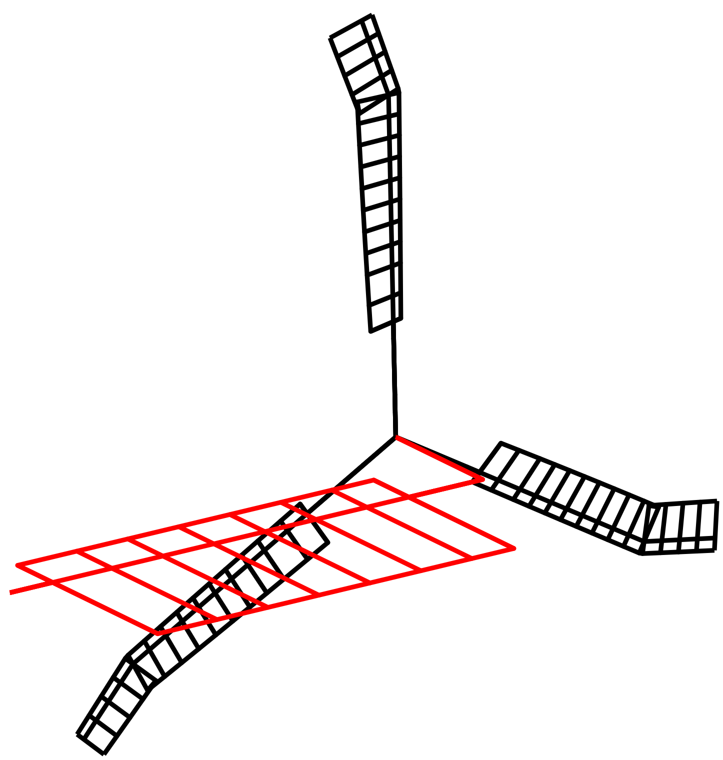

Figure 5.1: UMARC-II model of the MTR
(rotor, pylon, and wing are beams, panels show aerodynamic segments)

Table 5.1: MTR rotor properties

Number of blades	3
Radius	0.724 m
Chord	0.08 m
Precone	2°
δ_3	-15°
Solidity	0.106
Twist	-37°
Rotor speed (Froude-scaled Bell XV-15)	1050 rpm
Rotation direction	counterclockwise
Airfoil	VR-7
Root cutout	27%
Pitch bearing location	23%

Table 5.2: MTR wing/pylon properties

Wing span	0.927 m
Wing chord	0.392 m
Wing airfoil	NACA 0018
Pylon length	0.243 m (34%R)
Pylon mass (without rotating components)	28.53 kg
Pylon c.g. offset (without rotating components)	0.07 m (9.7%R, bwd.)

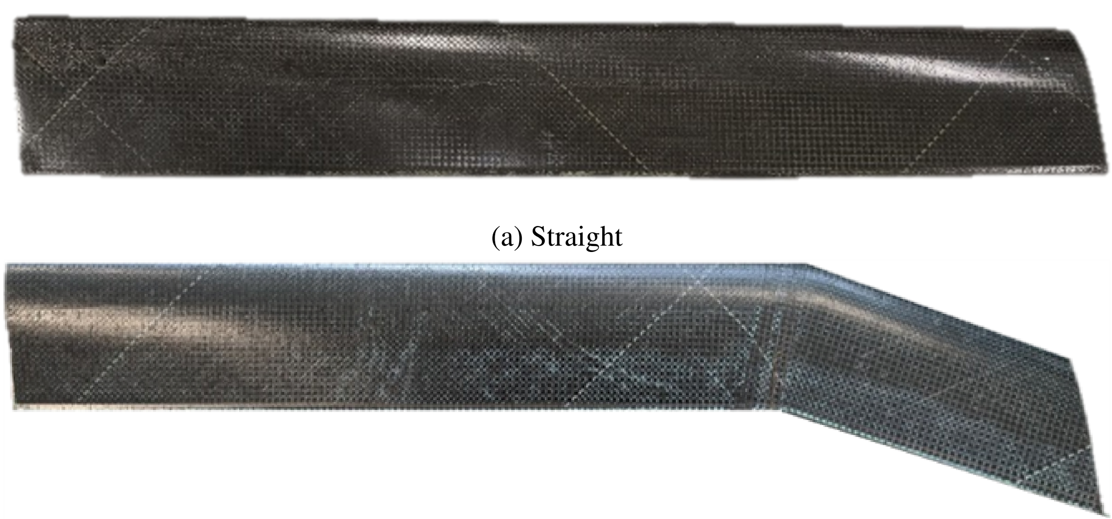

(a) Straight

(b) Swept-tip

Figure 5.2: MTR blades

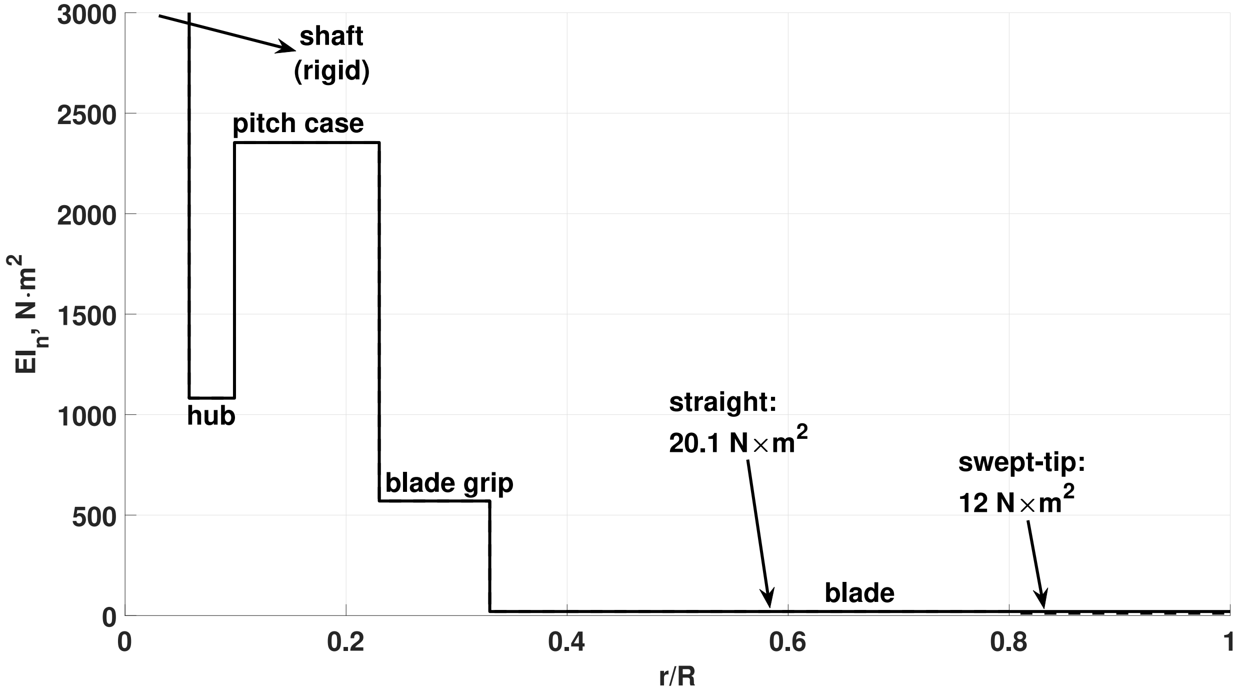

(a) Rotor normal stiffness

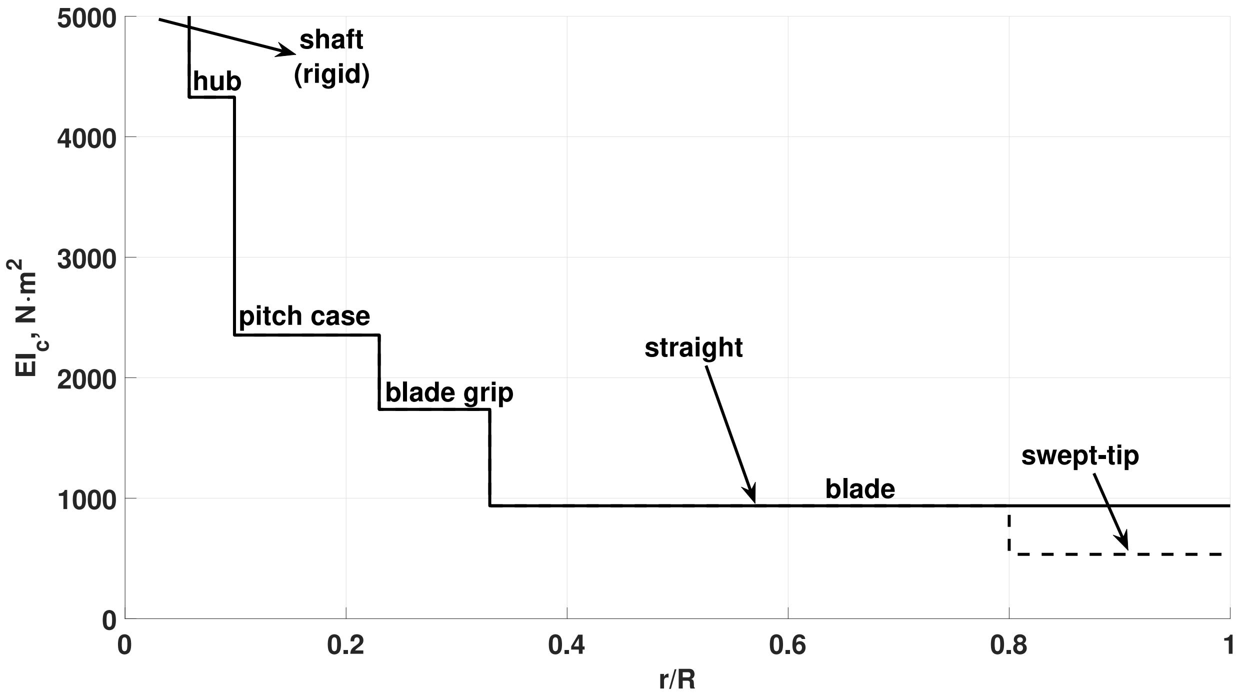

(b) Rotor chordwise stiffness

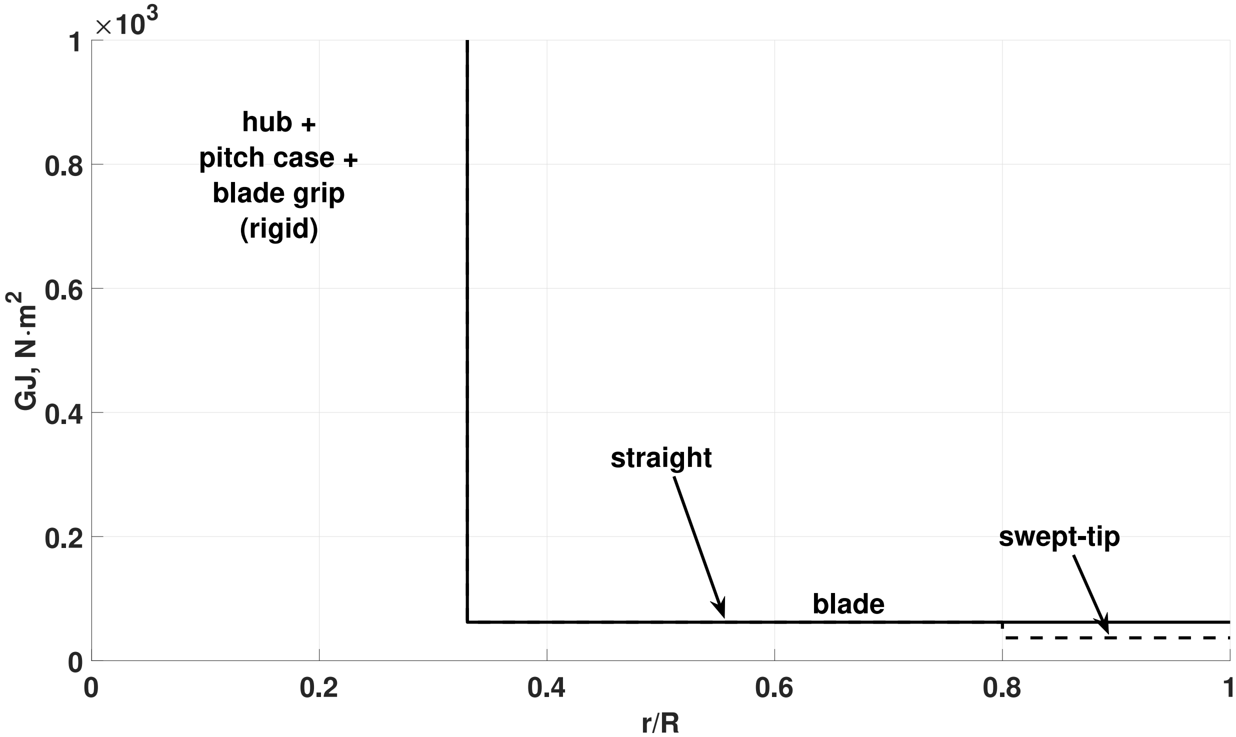

(c) Rotor torsional stiffness

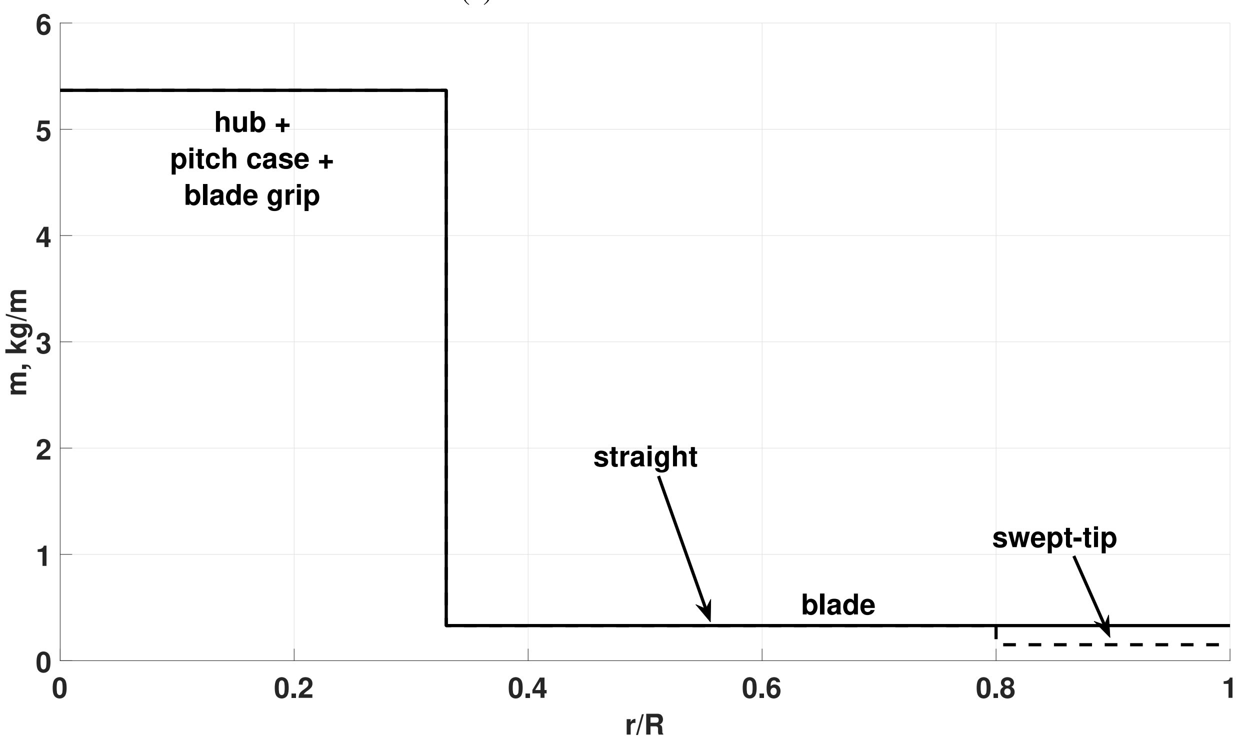

(d) Rotor mass per length

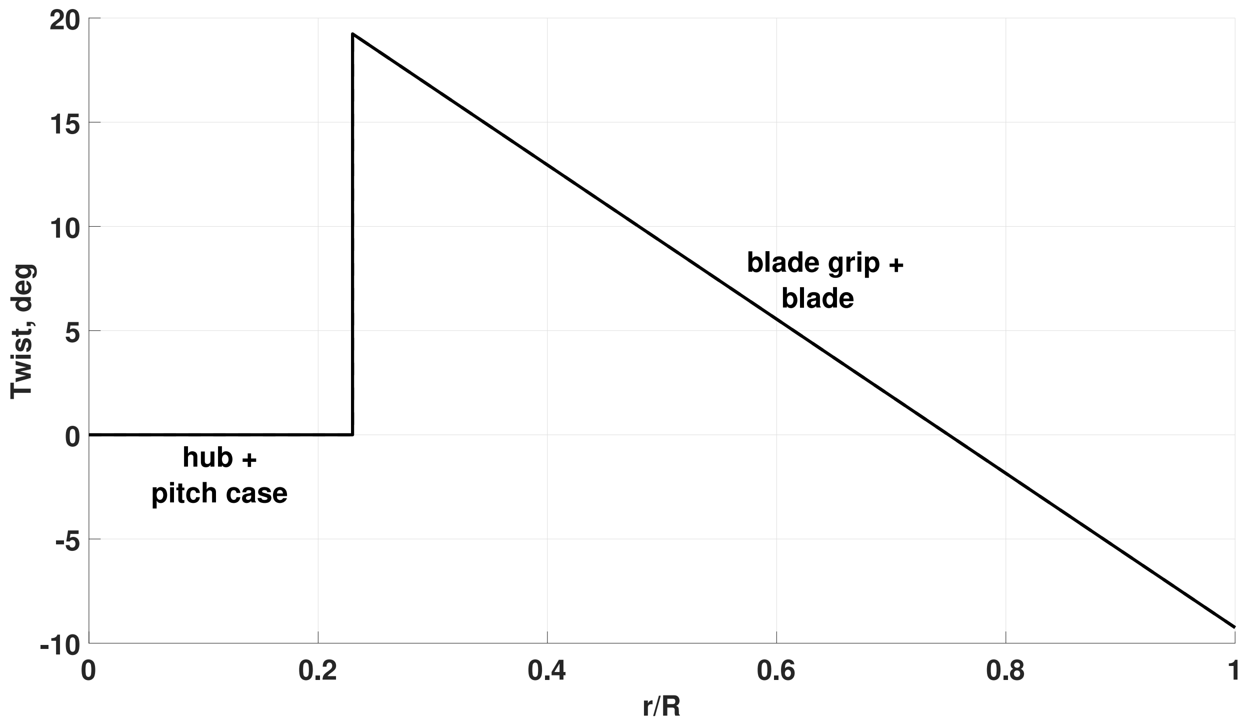

(e) Rotor twist

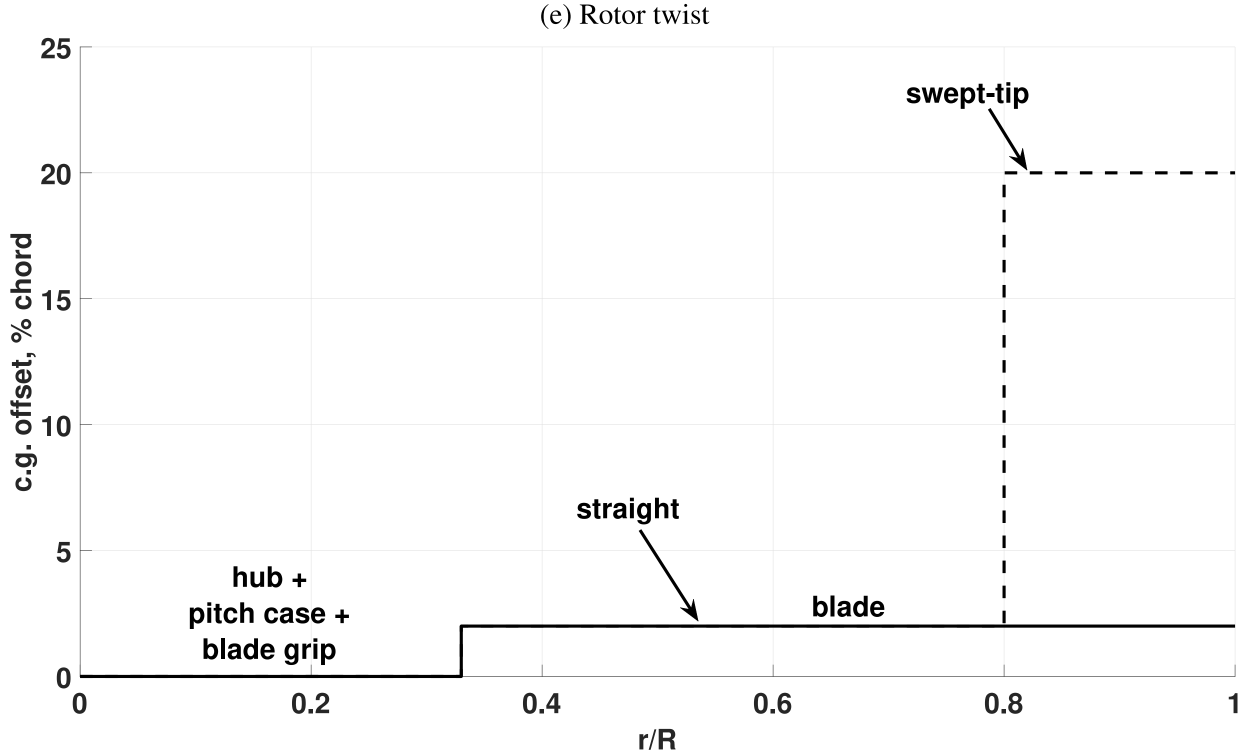

(f) Rotor center of gravity offset from elastic axis (positive toward trailing edge)

Figure 5.3: MTR rotor properties

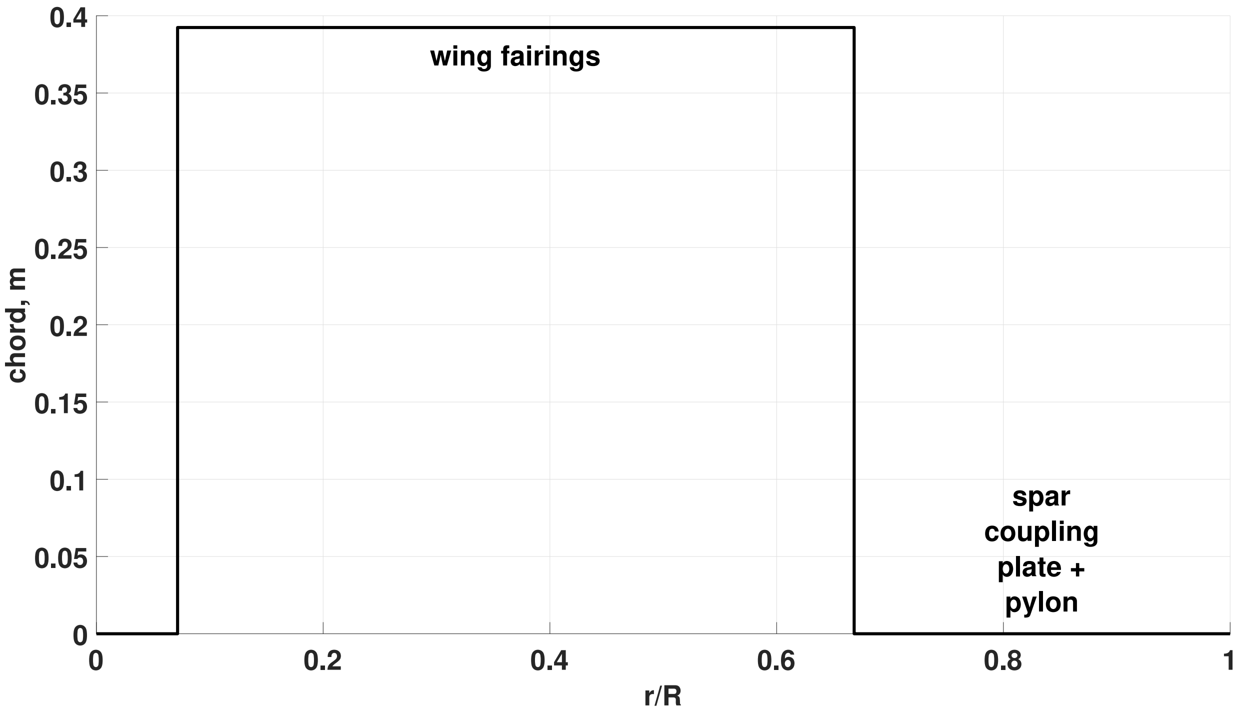

(a) Wing chord

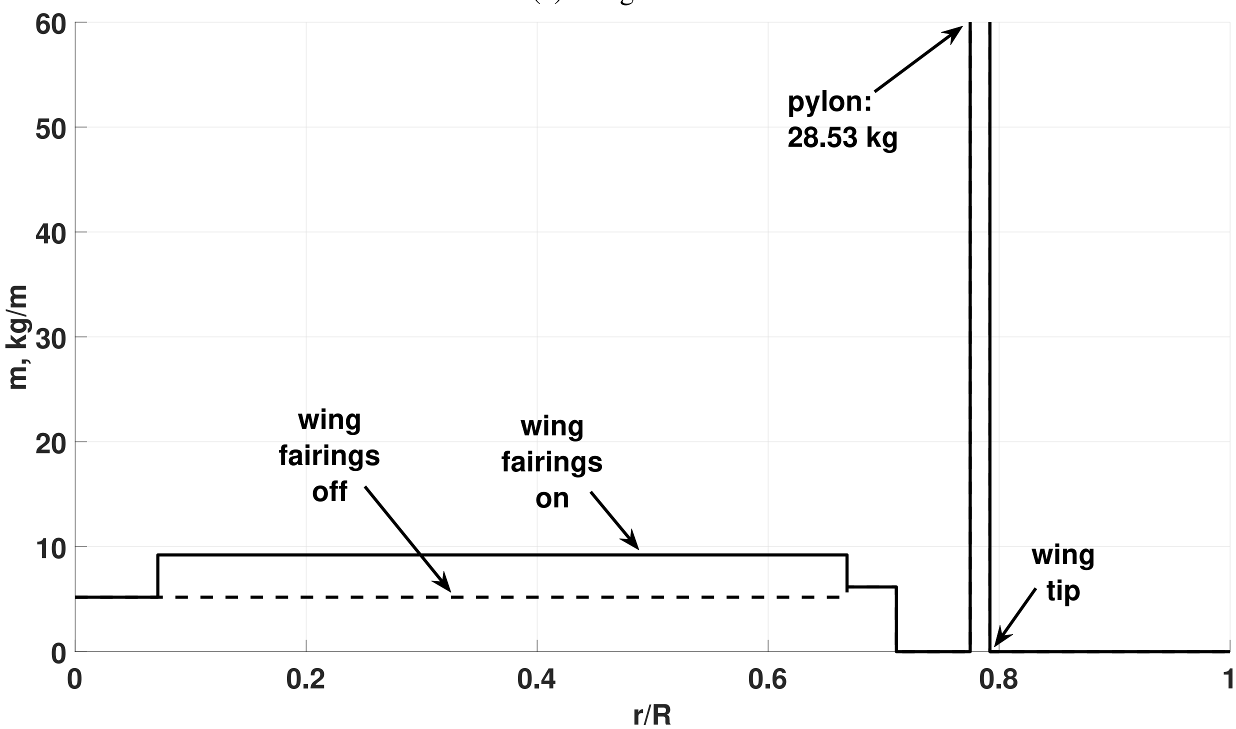

(b) Wing mass per length

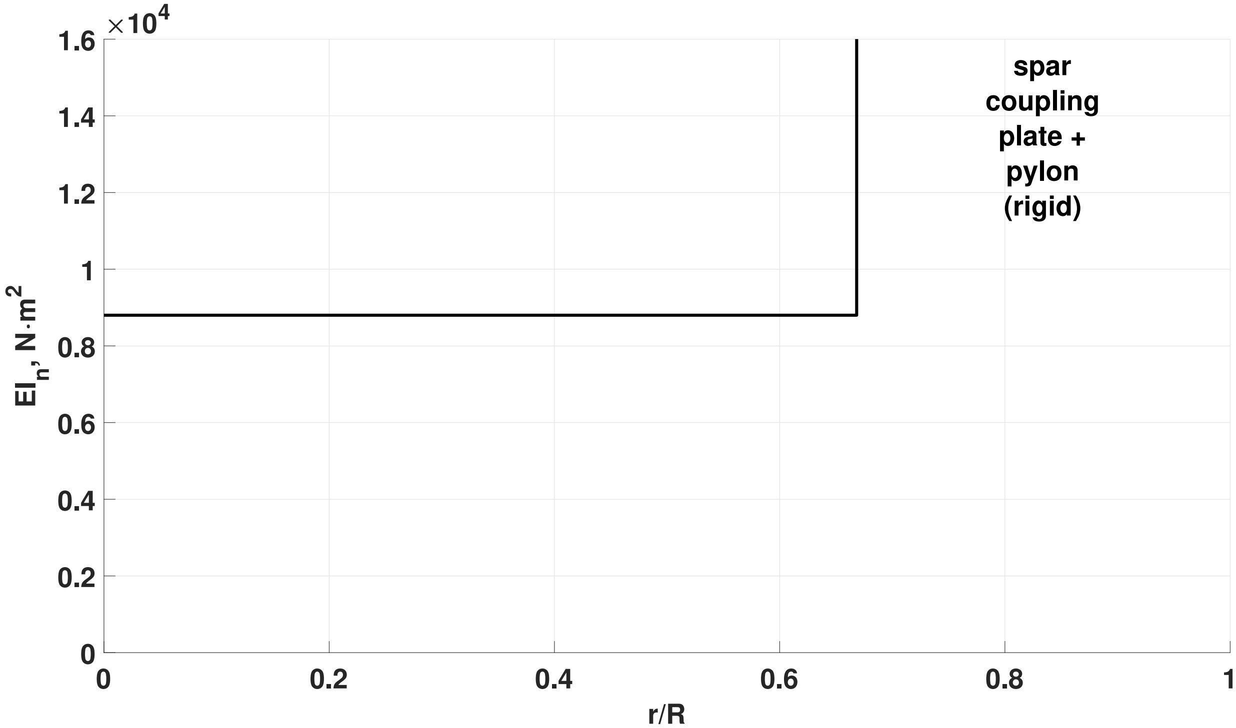

(c) Wing normal stiffness

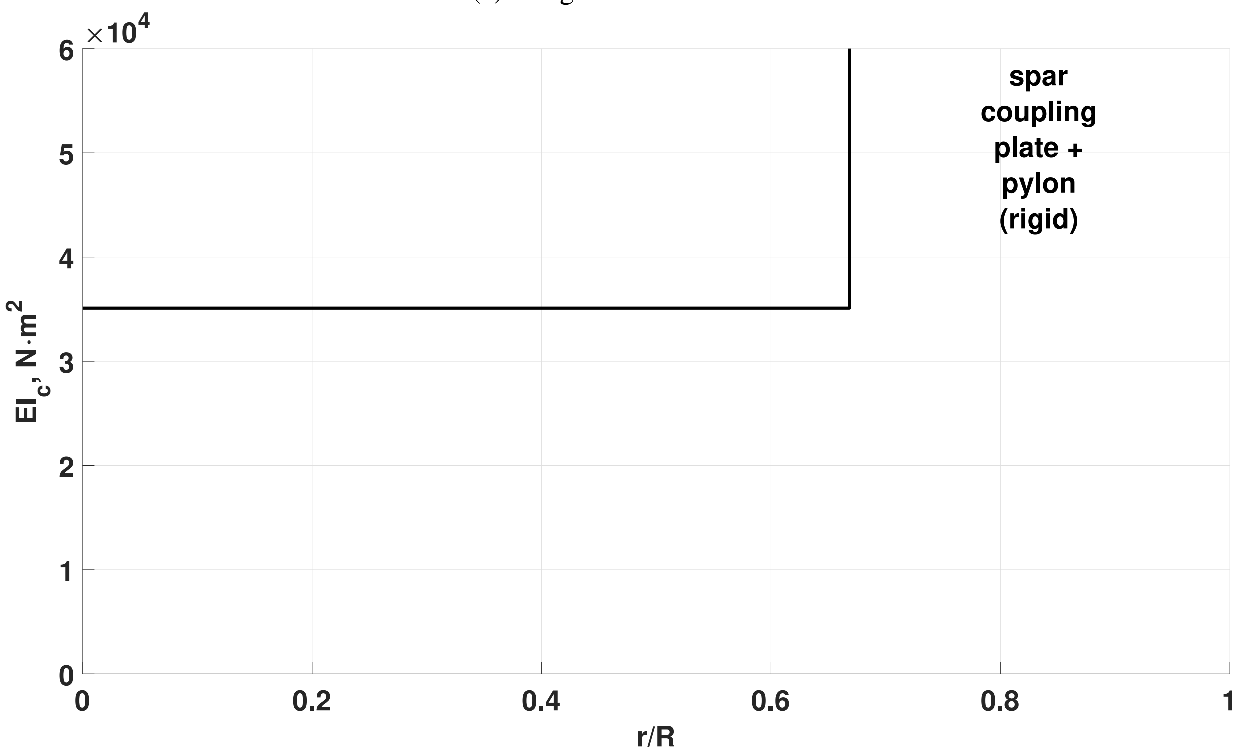

(d) Wing chordwise stiffness

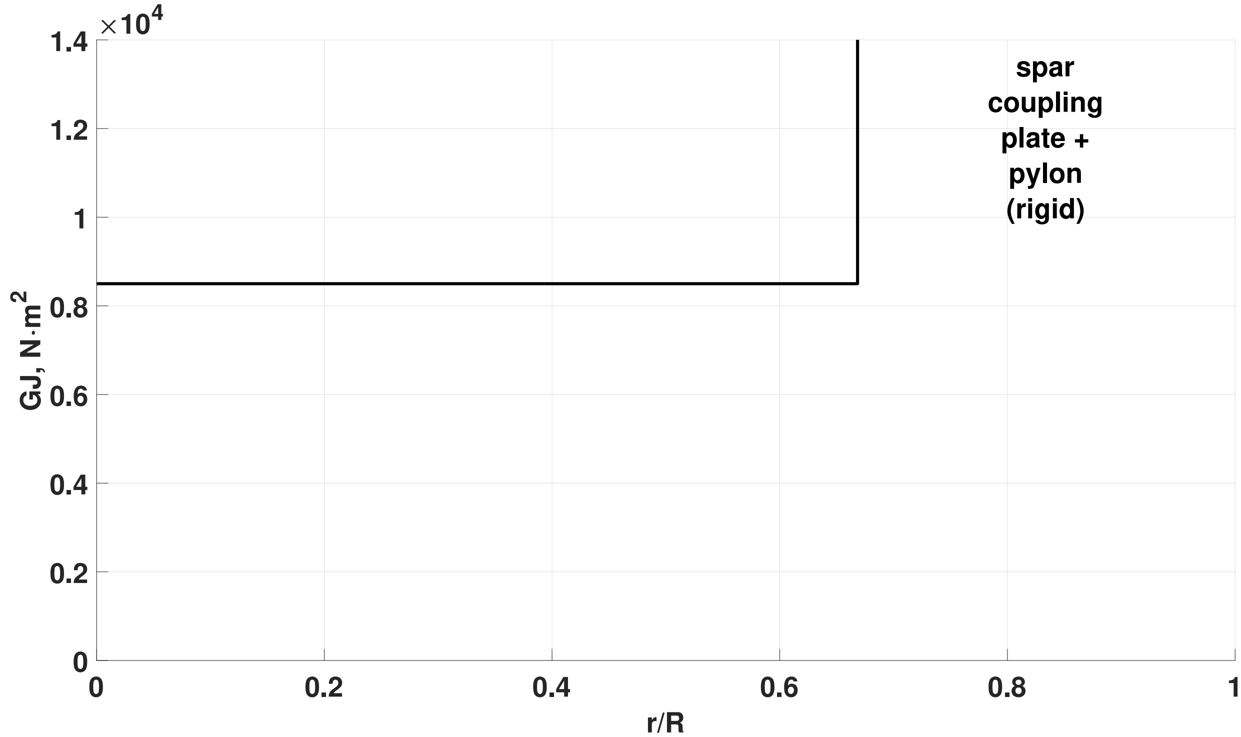

(e) Wing torsional stiffness

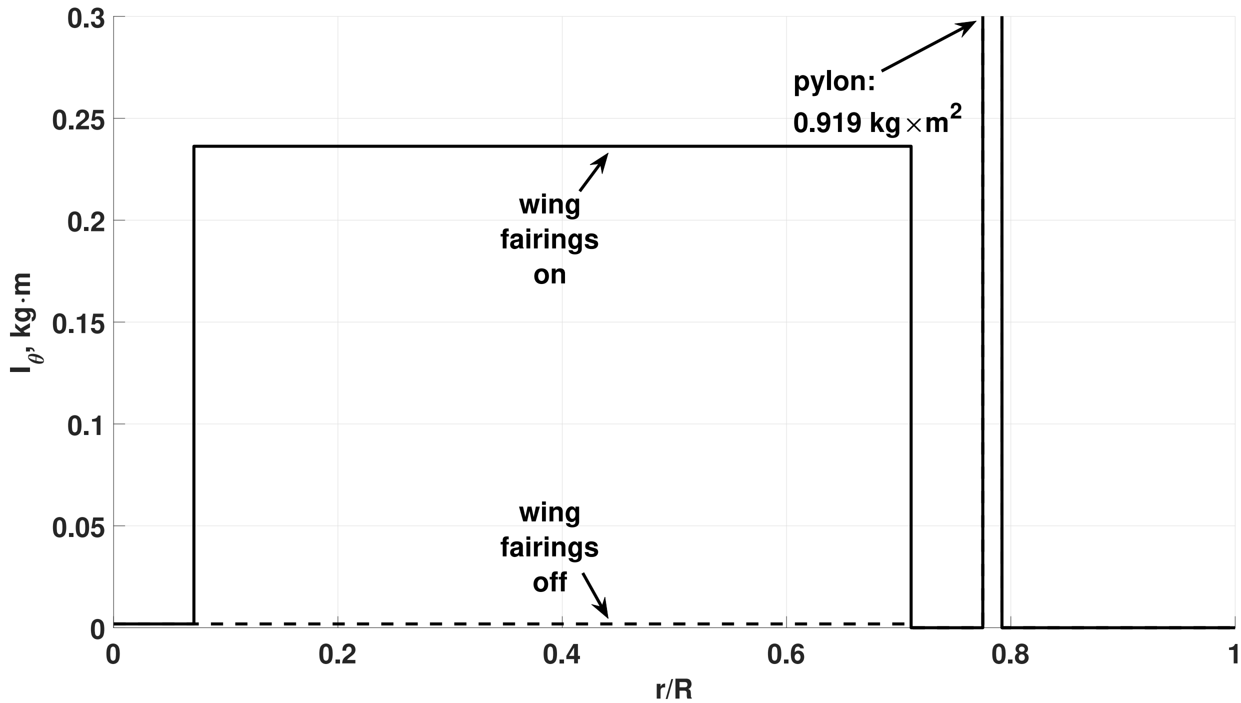

(f) Wing torsional moment of inertia,
with respect to section c.g.

Figure 5.4: MTR wing/pylon properties

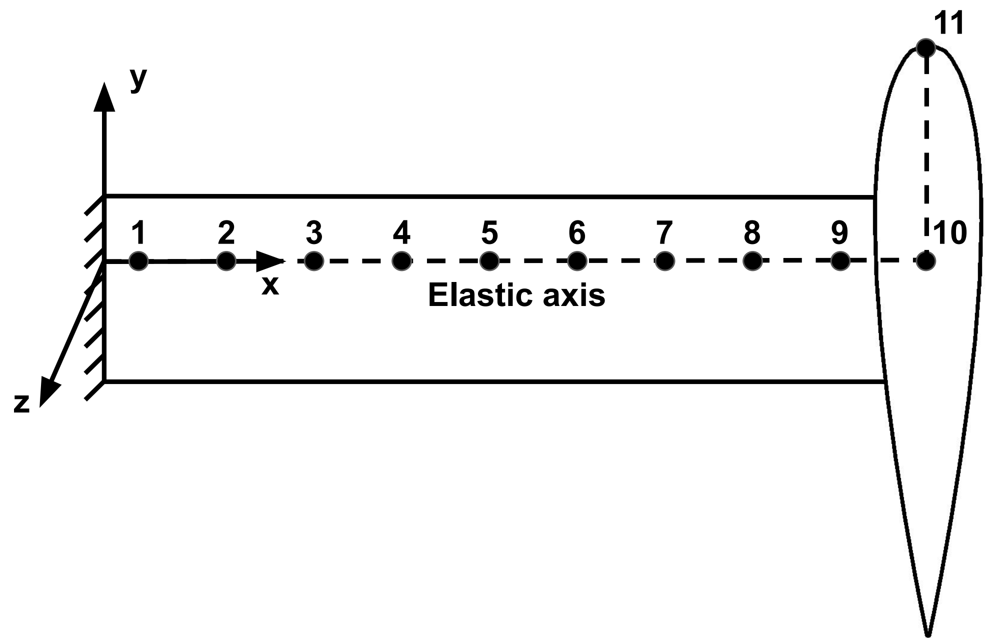

Figure 5.5: MTR mode shape points

Table 5.3: MTR wing beam mode
mass-normalized mode shape

Frequency = 5.1 Hz
Structural damping = 0.4%

Point	**r, m**	$\mathbf{x}^*$	$\mathbf{y}^*$	$\mathbf{z}^*$	$\theta_\mathbf{x}{}^\dagger$	$\theta_\mathbf{y}{}^\dagger$	$\theta_\mathbf{z}{}^\dagger$
1	0	0	0	0	0	0	0
2	0.0838	0	0	0.0022	-0.0047	-0.0520	0
3	0.2	0	0	0.0121	-0.0111	-0.1157	0
4	0.3	0	0	0.0260	-0.0166	-0.1627	0
5	0.4	0	0	0.0443	-0.0221	-0.2023	0
6	0.5	0	0	0.0663	-0.0276	-0.2348	0
7	0.6	0	0	0.0911	-0.0331	-0.2601	0
8	0.7	0	0	0.1181	-0.0386	-0.2784	0
9	0.7823	0	0	0.1414	-0.0431	-0.2882	0
10	0.9271	0	0	0.1831	-0.0431	-0.2882	0
11	1.1705	0	0	0.1727	-0.0431	-0.2882	0

* Unit: $\mathrm{m}/\sqrt{\mathrm{kg\,m^2}}$
† Unit: $\mathrm{rad}/\sqrt{\mathrm{kg\,m^2}}$

Table 5.4: MTR wing chord mode
mass-normalized mode shape

Frequency	= 9.7 Hz
Structural damping	= 0.57% (wing fairings on) = 0.36% (wing fairings off)

Point	**r, m**	$\mathbf{x}^*$	$\mathbf{y}^*$	$\mathbf{z}^*$	$\theta_\mathbf{x}{}^\dagger$	$\theta_\mathbf{y}{}^\dagger$	$\theta_\mathbf{z}{}^\dagger$
1	0	0	0	0	0	0	0
2	0.0838	0	0.0021	0	0	0	0.0491
3	0.2	0	0.0114	0	0	0	0.1098
4	0.3	0	0.0247	0	0	0	0.1550
5	0.4	0	0.0422	0	0	0	0.1938
6	0.5	0	0.0632	0	0	0	0.2262
7	0.6	0	0.0872	0	0	0	0.2523
8	0.7	0	0.1135	0	0	0	0.2720
9	0.7823	0	0.1364	0	0	0	0.2837
10	0.9271	0	0.1775	0	0	0	0.2837
11	1.1705	-0.0690	0.1775	0	0	0	0.2837

* Unit: $\mathrm{m}/\sqrt{\mathrm{kg\,m^2}}$
† Unit: $\mathrm{rad}/\sqrt{\mathrm{kg\,m^2}}$

Table 5.5: MTR wing torsion mode
mass-normalized mode shape

Frequency	= 14.4 Hz
Structural damping	= 2%

Point	**r, m**	$\mathbf{x}^*$	$\mathbf{y}^*$	$\mathbf{z}^*$	$\theta_\mathbf{x}{}^\dagger$	$\theta_\mathbf{y}{}^\dagger$	$\theta_\mathbf{z}{}^\dagger$
1	0	0	0	0	0	0	0
2	0.0838	0	0	-0.0010	-0.1105	0.0233	0
3	0.2	0	0	-0.0054	-0.2633	0.0509	0
4	0.3	0	0	-0.0115	-0.3940	0.0704	0
5	0.4	0	0	-0.0193	-0.5234	0.0861	0
6	0.5	0	0	-0.0285	-0.6511	0.0981	0
7	0.6	0	0	-0.0388	-0.7767	0.1068	0
8	0.7	0	0	-0.0498	-0.8999	0.1124	0
9	0.7823	0	0	-0.0592	-0.9991	0.1152	0
10	0.9271	0	0	-0.0759	-0.9991	0.1152	0
11	1.1705	0	0	-0.3190	-0.9991	0.1152	0

* Unit: $\mathrm{m}/\sqrt{\mathrm{kg\,m^2}}$
† Unit: $\mathrm{rad}/\sqrt{\mathrm{kg\,m^2}}$

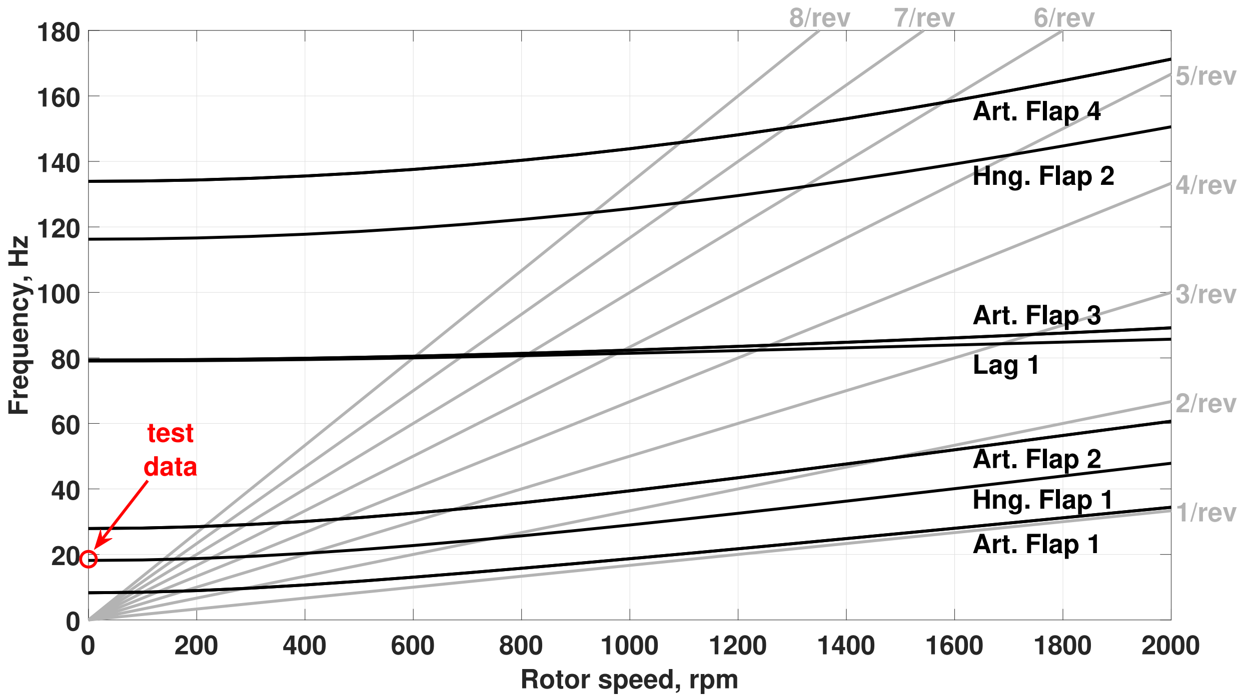

(a) Straight

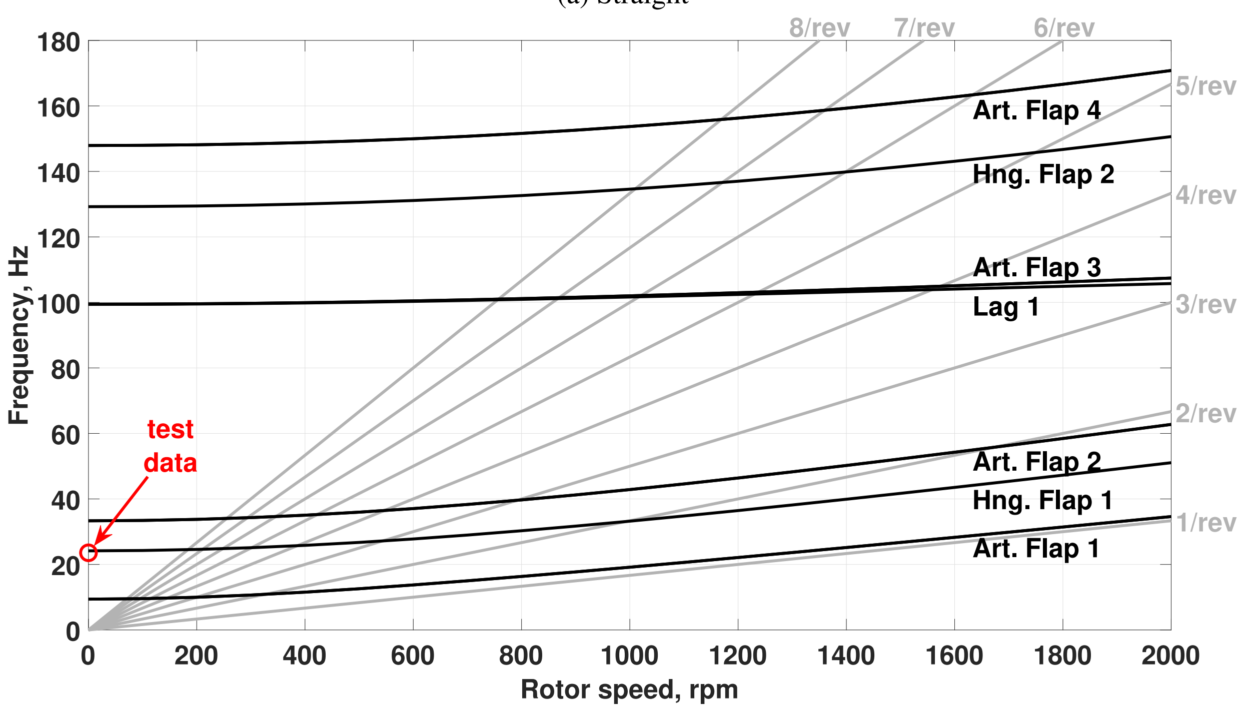

(b) Swept-tip

Figure 5.6: MTR fanplot
(solid: predictions, symbols: test data)

5.2 Testing Procedure

Flutter frequency and damping data was collected up to 100 knots for wing beam and chord modes. 100 knots was a safety restriction from the wind tunnel. Torsion mode frequency and damping were too high to be excited. Baseline data is gimbal-free, freewheeling mode, wing fairings on with straight and swept-tip blades. Gimbal-locked (essentially a hyper stiff in-plane hingeless hub with a high flap frequency), powered mode, and wing fairings off data was also collected, all with straight and swept-tip blades. The test conditions are shown in Table 5.6.

The rotor was trimmed to 1050 rpm (Froude-scaled XV-15 rotor speed) at any given tunnel speed. Analysis guided the test to find the trim collective. Then, the wing modes were excited with the high-bandwidth swashplate actuators. Wing beam mode was excited by oscillating the longitudinal cyclic at the beam frequency and the wing chord mode was excited by oscillating the collective at the chord frequency. After the excitation stopped, the decay in the signal was recorded and the Moving-Block method was used to extract the damping value. Analysis also helped here to ensure tunnel safety during the stability tests. At least three trials were performed for each wing mode. A detailed description of the test setup and the testing procedure is given in Ref. [67].

5.3 Freewheeling

Figure 5.7 shows the change of freewheeling collective with respect to tunnel speed at 1050 rpm. The UMARC-II predictions are provided with UMD and NASA VR-7 airfoil decks. Measurements with the two sets of straight blades are very close to each other, which signals consistency. Swept-tip blade collectives are slightly higher than straight blades. The predictions are satisfactorily close to the measurements, which validates the gross aerodynamic model.

Table 5.6: Flutter test conditions

Sweep	Tunnel speed knots	Collective deg	Gimbal	Mode	Wing fairings
Straight blades					
Set 2					
1	30, 40, 50, 60, 65, 70, 74, 78, 82, 86, 89, 92, 96, 100	9.9, 17.6, 22.3, 26.7, 28.2, 30.0, 31.2, 32.8, 34.1, 35.4, 36.8, 37.5, 38.8, 39.8	Free	Freewheel	On
2	30, 40, 50, 60, 65, 70, 74, 78, 82, 86, 89, 92, 96, 100	10.4, 17.3, 22.4, 26.5, 28.6, 30.5, 31.7, 33.4, 34.6, 35.9, 36.8, 37.9, 39.1, 40.1	Free	Freewheel	Off
Set 1					
3	30, 40, 50, 60	11.3, 17.2, 22.1, 26.4	Locked	Freewheel	Off
4	4, 20, 30, 40, 50, 60	3.2, 11.4, 15.8, 20.7, 25.2, 28.9	Locked	Powered	Off
Swept-tip blades					
5	30, 40, 50, 60, 65, 70, 74, 78, 82, 86, 89, 92, 96, 100	13.3, 18.9, 23.5, 27.4, 29.5, 31.2, 32.4, 34.3, 35.2, 37.1, 37.9, 39.0, 39.9, 40.7	Free	Freewheel	On
6	30, 40, 50, 60, 65, 70, 74, 78, 82, 86, 89, 92, 96, 100	11.9, 17.8, 22.0, 26.4 28.8, 30.8, 32.5, 33.8, 35.1, 36.3, 37.8, 38.7, 39.6, 40.6	Free	Freewheel	Off
7	30, 40, 50, 60, 65, 70, 74, 78, 82	11.1, 17.1, 22.1, 26.5, 29.1, 31.4, 32.7, 34.3, 35.1	Locked	Freewheel	Off
8	4, 20, 30, 40, 50, 60	3.4, 13.0, 16.9, 21.6, 25.9, 29.7	Locked	Powered	Off

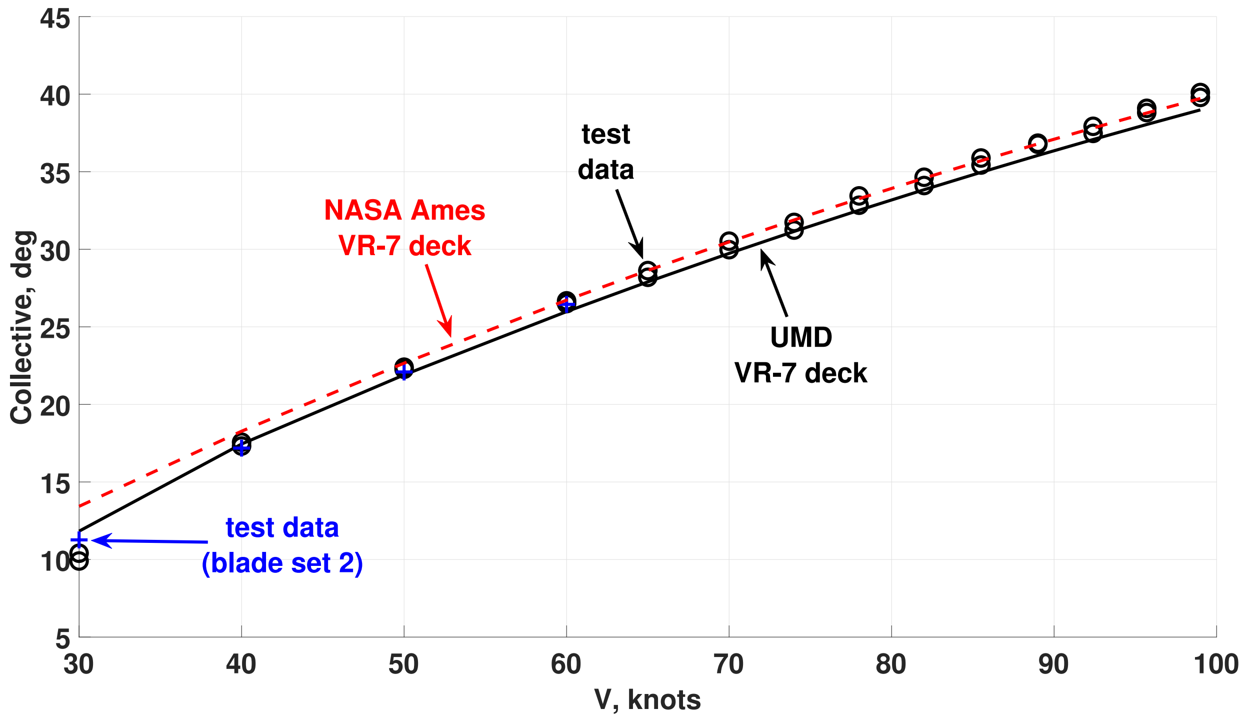

(a) Straight blades

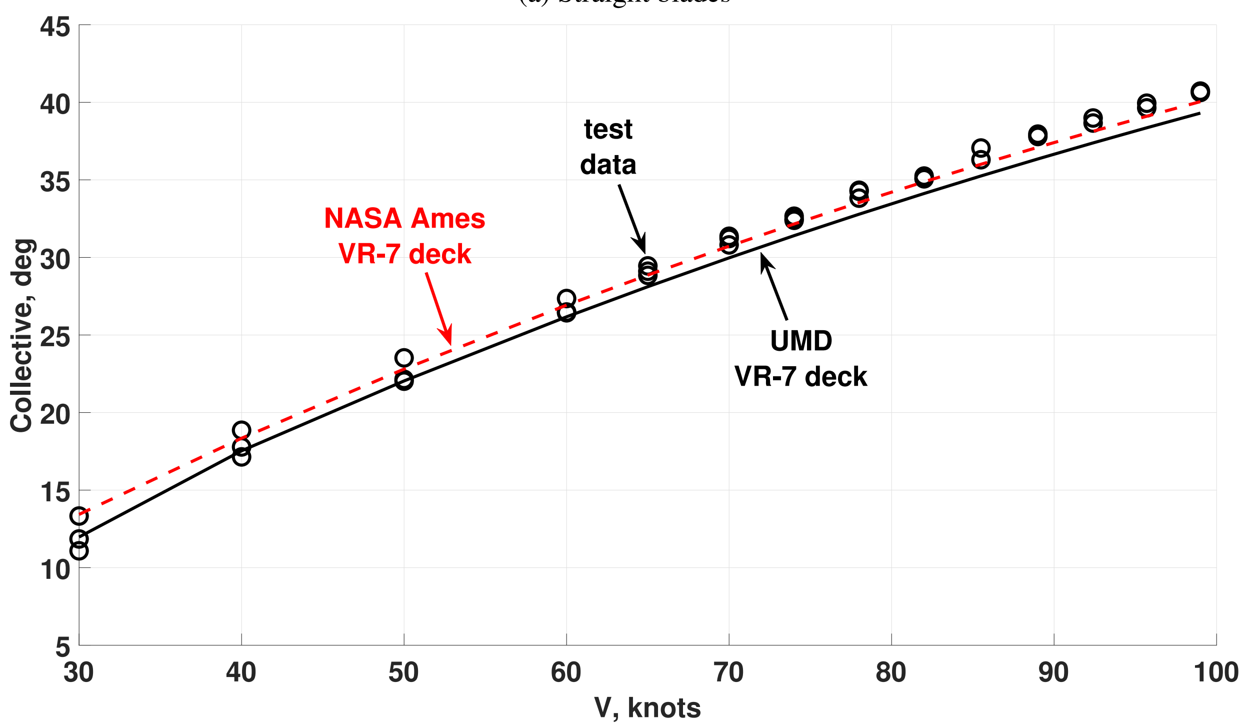

(b) Swept-tip blades

Figure 5.7: Comparison of freewheeling collective predictions with MTR test data at 1050 rpm (lines: predictions, symbols: test data)

5.4 Aeroelastic Stability

Predictions were carried out for all the configurations shown in Table 5.6 and presented in Figs. 5.8 to 5.12 for each test run. The transient response method (Chapter 2.18.2) was used for the gimbal-free results.

Figure 5.8 shows comparison of q_1 and q_2 mode frequency predictions with the test data for the gimbal-free, freewheeling, wing fairings on configuration. The predictions align with the test data. The frequencies do not change with airspeed, and no interesting observation can be made. Frequency plots will therefore not be repeated for the other configurations.

Figures 5.9 and 5.10 show comparison of q_1 and q_2 mode damping predictions with the test data for gimbal-free, freewheeling, wing fairings on and off configurations. Good agreement is observed for the q_1 mode, especially for the wing fairings on configuration, but the data is scattered at high speeds. General trend of q_2 damping was captured for both of the configurations with a maximum of 0.7% difference. The peaks in the test data is also observed in the predictions, which could be due to coalescing of the modes or numerical errors due to the transient analysis.

Figure 5.11 shows comparison of q_1 and q_2 mode damping predictions with the test data for the gimbal-locked, freewheeling, wing fairings off configuration. The agreement for q_1 damping is satisfactory, but the data is again scattered. Damping for q_2 mode for the straight blades was predicted well at high speeds but the trend at low speeds was not captured. For the swept-tip blades, q_2 mode damping trend was predicted with an offset of around 0.9%.

Figure 5.12 shows q_1 and q_2 mode damping predictions with the test data for the gimbal-locked, powered, wing fairings off configuration. Damping for the q_1 mode was predicted accurately. For the straight blades, the q_2 trend at low speeds was not captured. The trend was only predicted after 30 knots. For the swept-tip blades, the q_2 trend was predicted better.

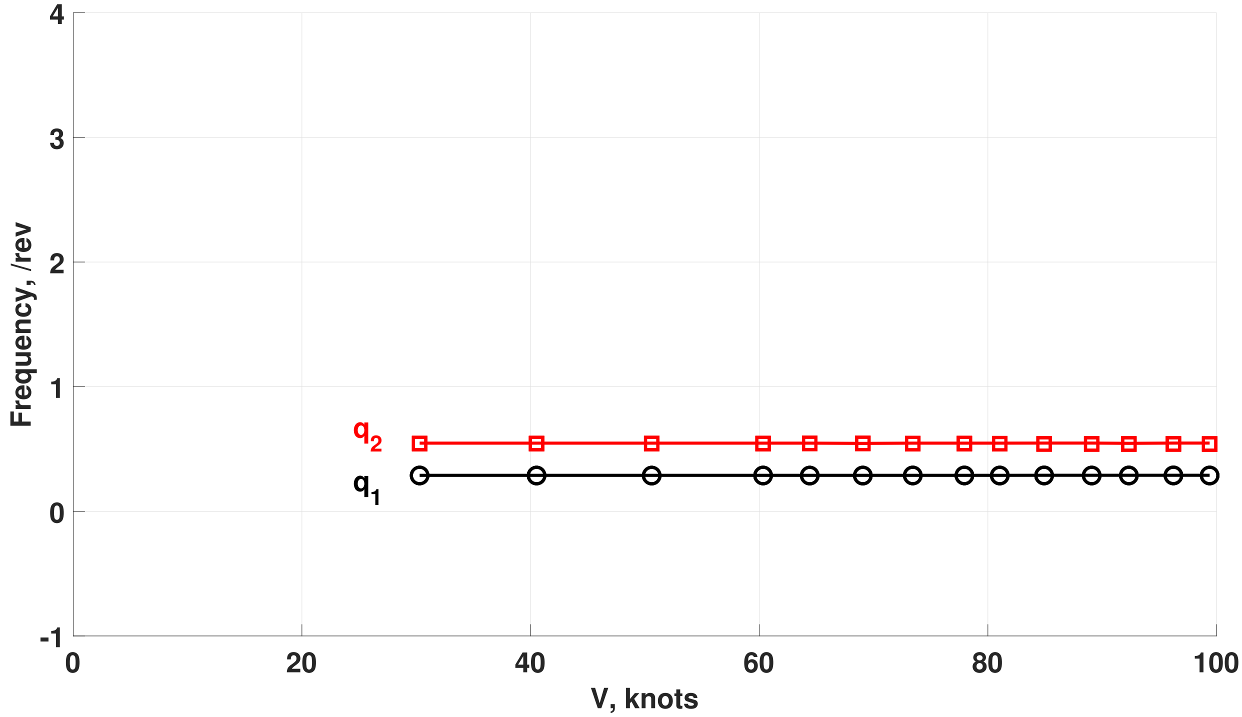

(a) Straight

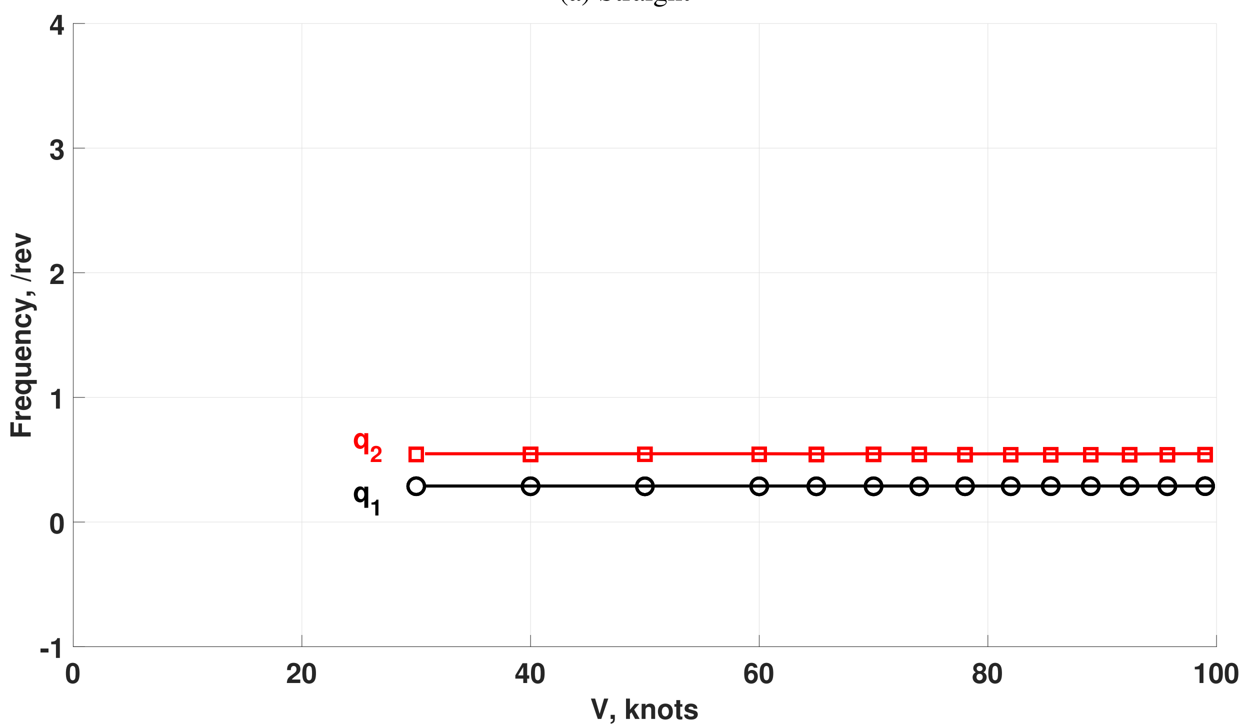

(b) Swept-tip

Figure 5.8: Comparison of frequency predictions with wind tunnel test data for gimbal-free, freewheeling, wing fairings on configuration (lines: predictions, symbols: test data)

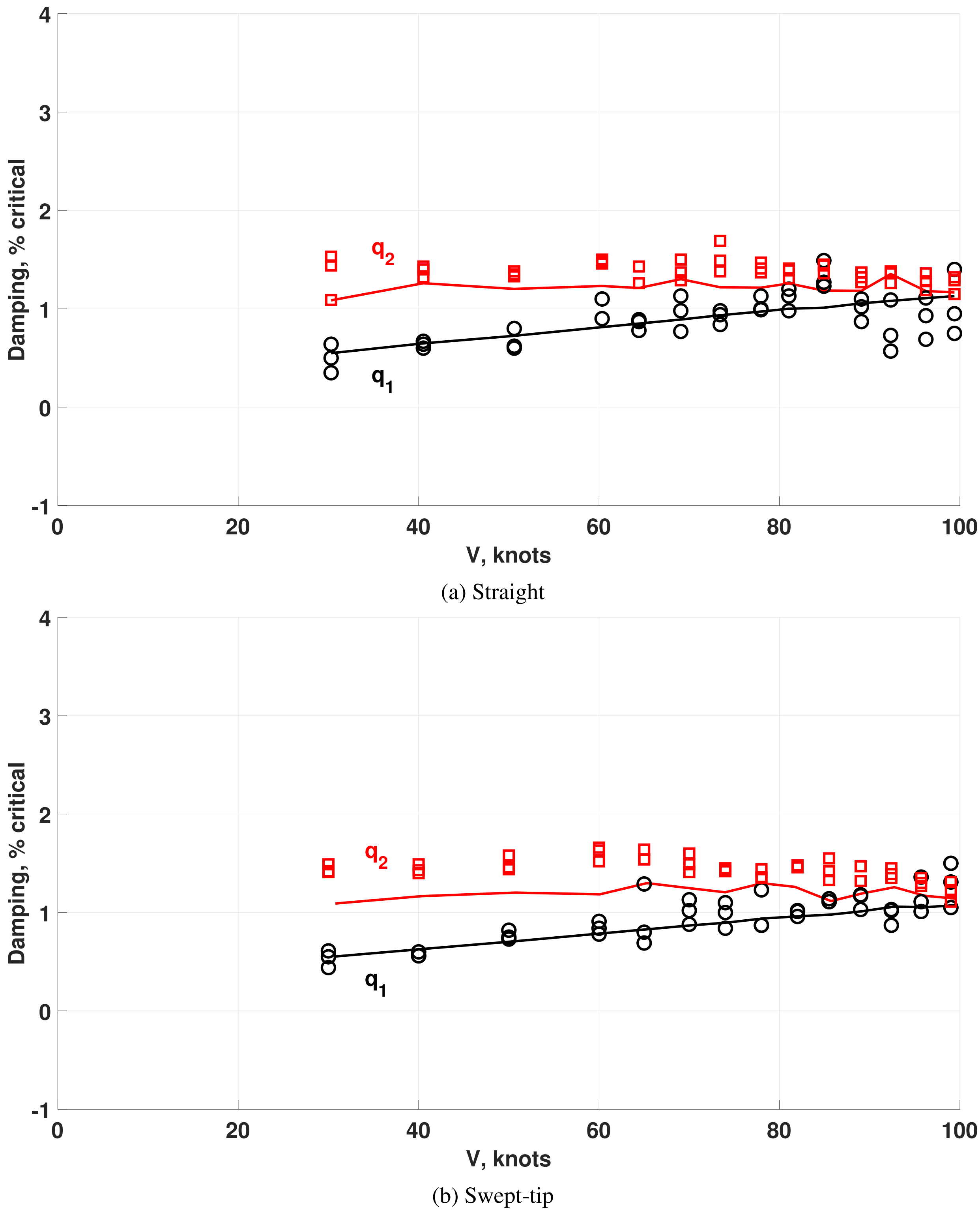

Figure 5.9: Comparison of damping predictions with wind tunnel test data for
gimbal-free, freewheeling, wing fairings on configuration
(lines: predictions, symbols: test data)

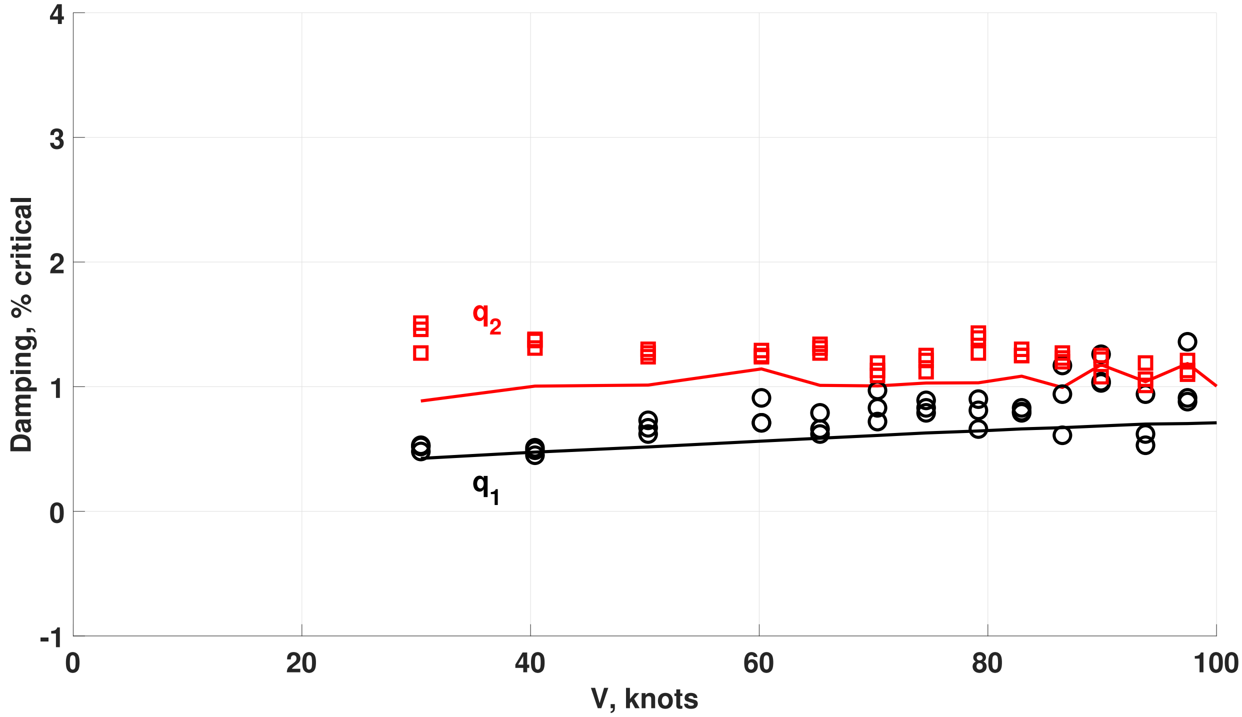

(a) Straight

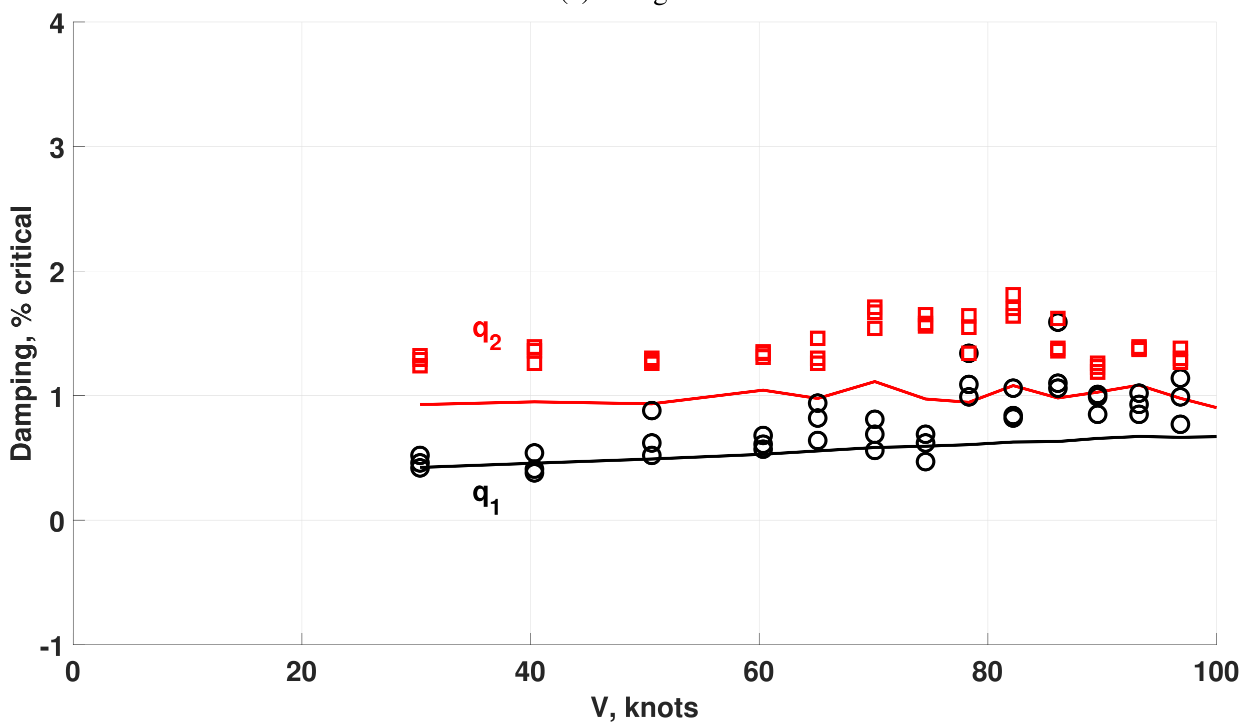

(b) Swept-tip

Figure 5.10: Comparison of damping predictions with wind tunnel test data for gimbal-free, freewheeling, wing fairings off configuration (lines: predictions, symbols: test data)

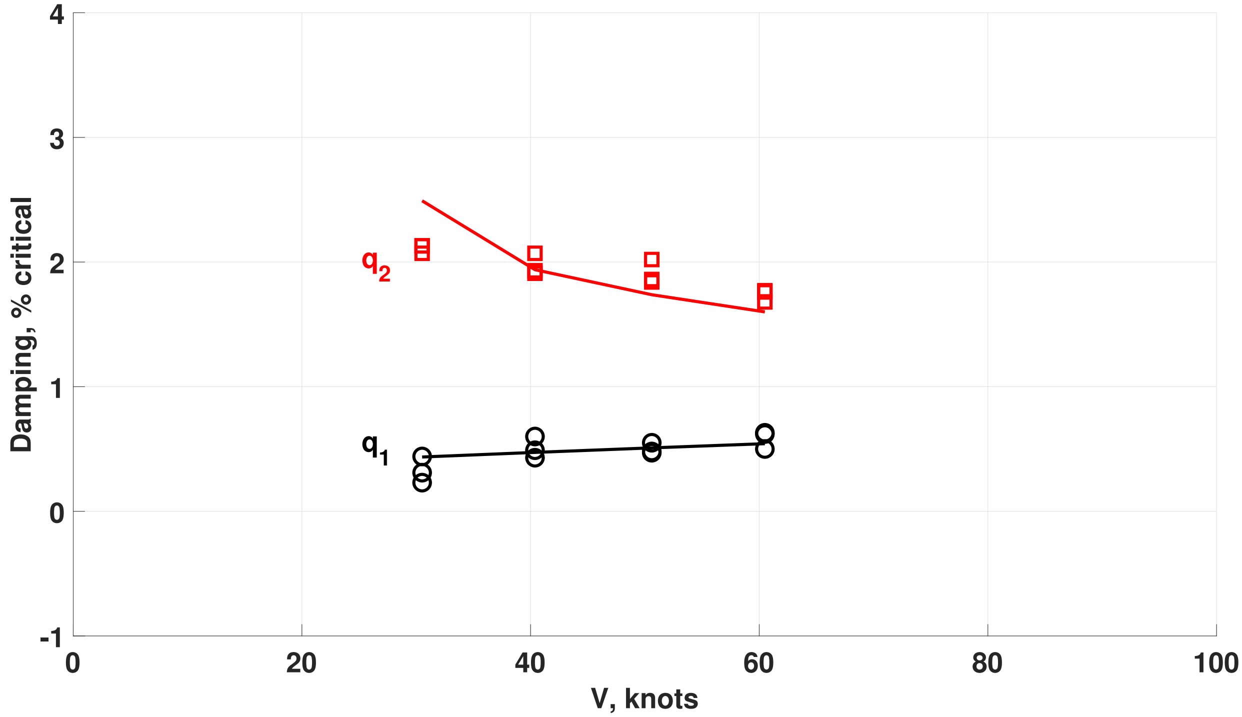

(a) Straight

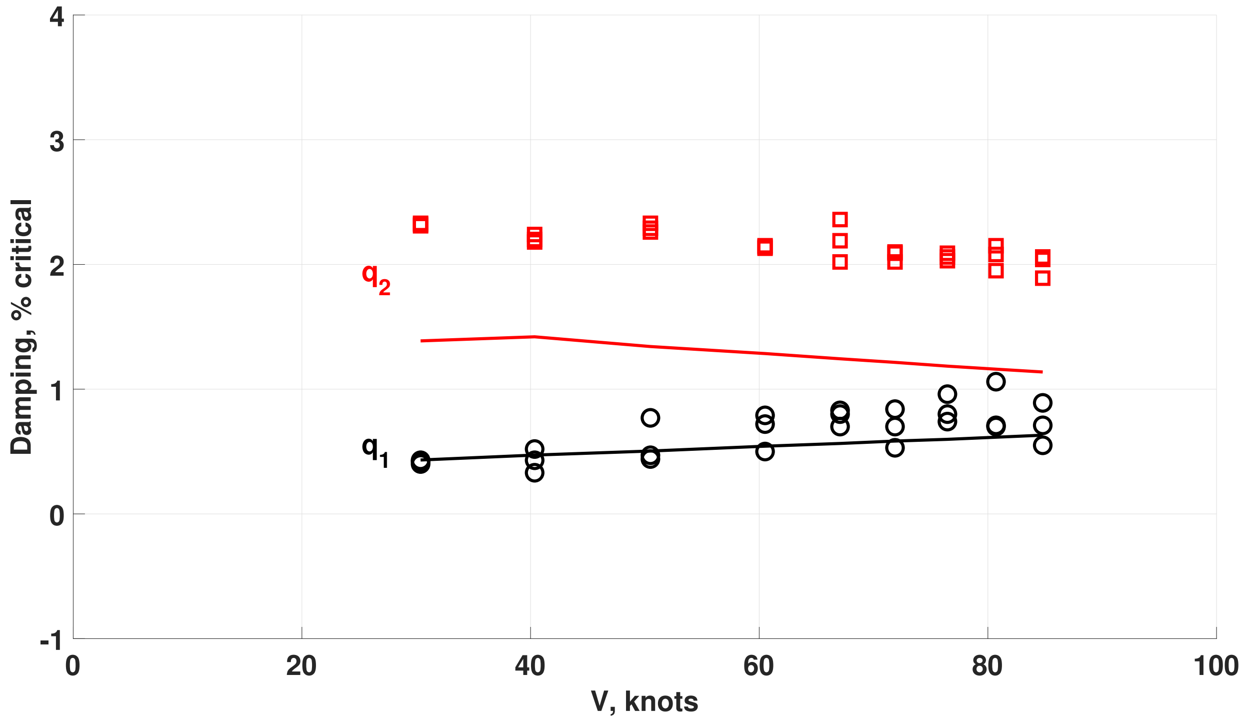

(b) Swept-tip

Figure 5.11: Comparison of damping predictions with wind tunnel test data for gimbal-locked, freewheeling, wing fairings off configuration (lines: predictions, symbols: test data)

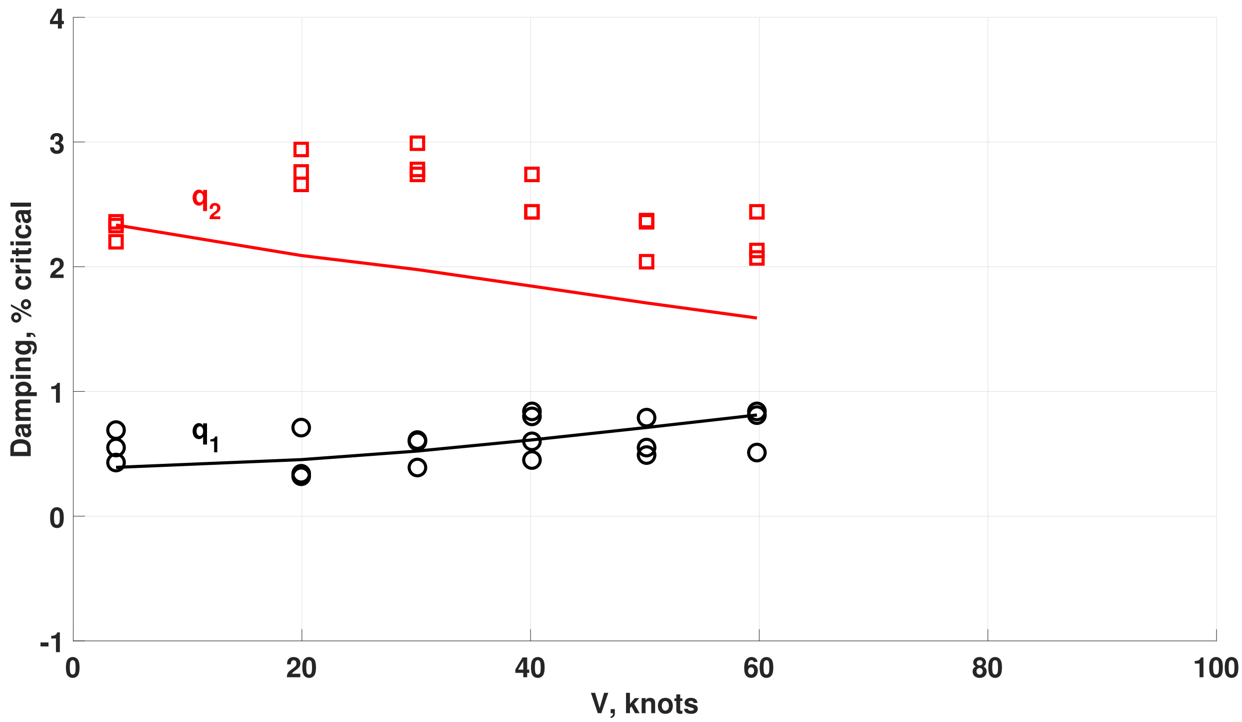

(a) Straight

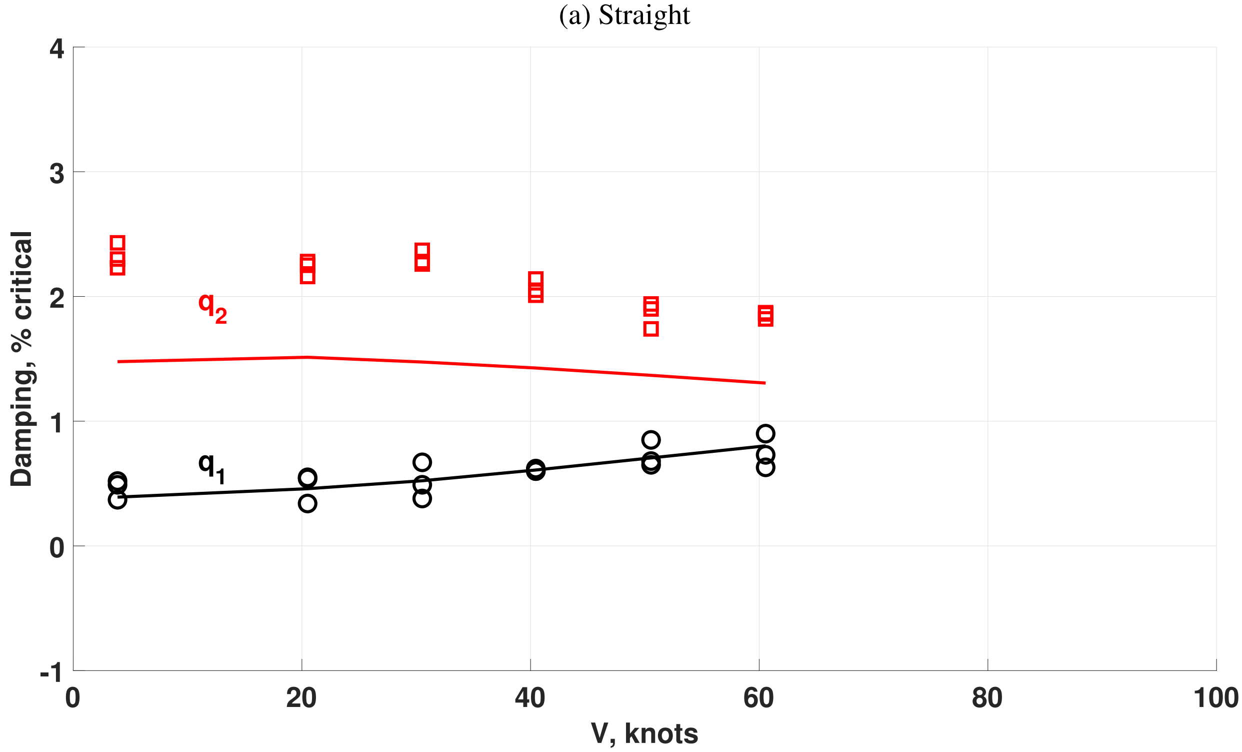

(b) Swept-tip

Figure 5.12: Comparison of damping predictions with wind tunnel test data for gimbal-locked, powered, wing fairings off configuration
(lines: predictions, symbols: test data)

5.5 Comparison of Test Configurations

Figures 5.13 to 5.16 show comparison of the various test configurations together with the predictions for a better assessment of impact of each parameter. Figure 5.13 compares the damping for straight and swept-tip blades for the gimbal-free, freewheeling, wing fairings on configuration. Damping test data of the q_1 and q_2 modes at high speeds is slightly higher with swept-tip blades, but the scatter does not allow for a clear conclusion. Figure 5.14 makes the same comparison for the gimbal-locked, freewheeling, wing fairings off configuration. A clear increase in the q_2 mode damping test data is observed, which was not predicted by the analysis.

Figure 5.15 compares gimbal-free and gimbal-locked damping for the freewheeling, wing fairings off, straight blades configuration. Gimbal-locked shows higher damping for both modes. Increase in the q_2 mode damping was picked up by the analysis.

Figure 5.16 compares freewheeling and powered mode damping for the gimbal-locked, wing fairings off, straight blades configuration. Powered mode results in slightly higher damping for q_1 mode. The scatter in the data prevents a definitive conclusion. The difference in q_2 mode is more apparent; powered mode shows a peak at around 30 knots and higher damping than freewheeling at higher speeds. Analysis did not predict this behavior.

Figure 5.17 compares wing fairings on and off damping for the gimbal-free, freewheeling, straight blades configuration. Analysis shows a distinct increase in q_1 damping at high speeds when the wing fairings are on. Although not as clear due to the scatter, the test data also shows a similar behavior. The increase in the q_2 damping test data is due to the higher structural damping when the wing fairings are installed (Table 5.4). This shows that wing aerodynamics is modeled correctly, and clears out the confusion with the Boeing M222 test data explained in Chapter 4.4.

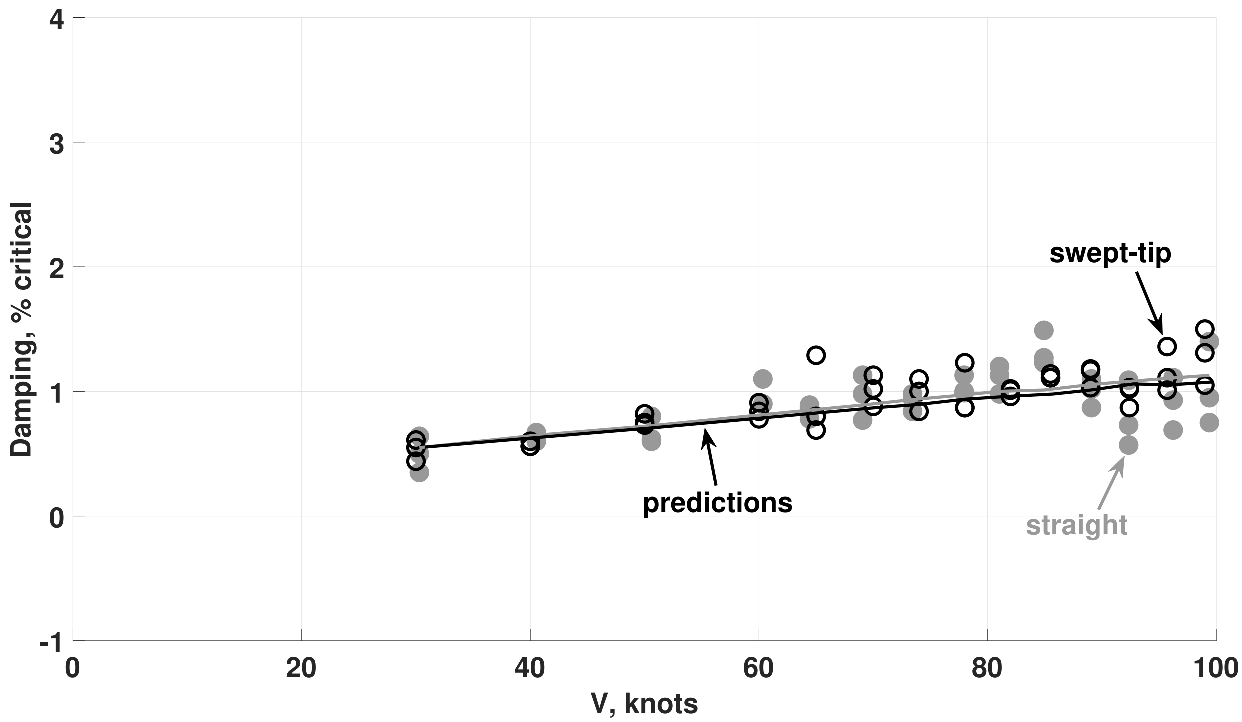

(a) Wing beam mode

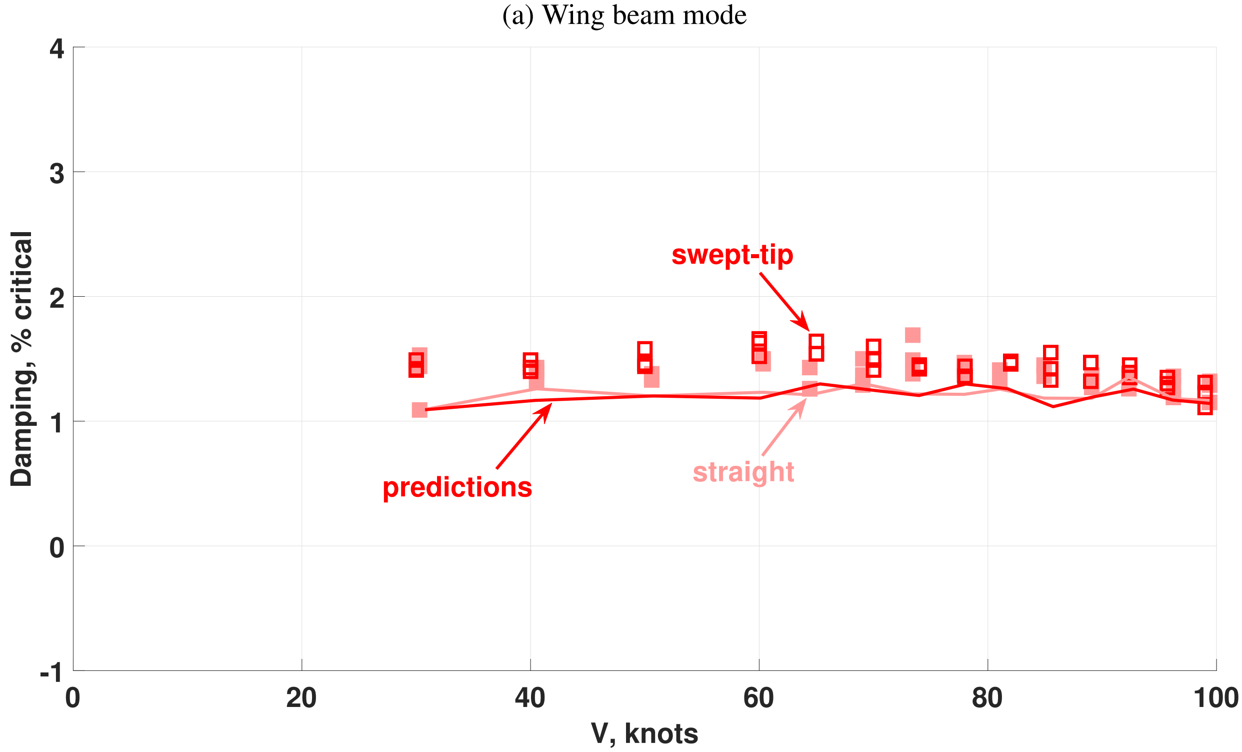

(b) Wing chord mode

Figure 5.13: Comparison of straight and swept-tip blade damping test data for gimbal-free, freewheeling, wing fairings on configuration
(lines: predictions, symbols: test data)

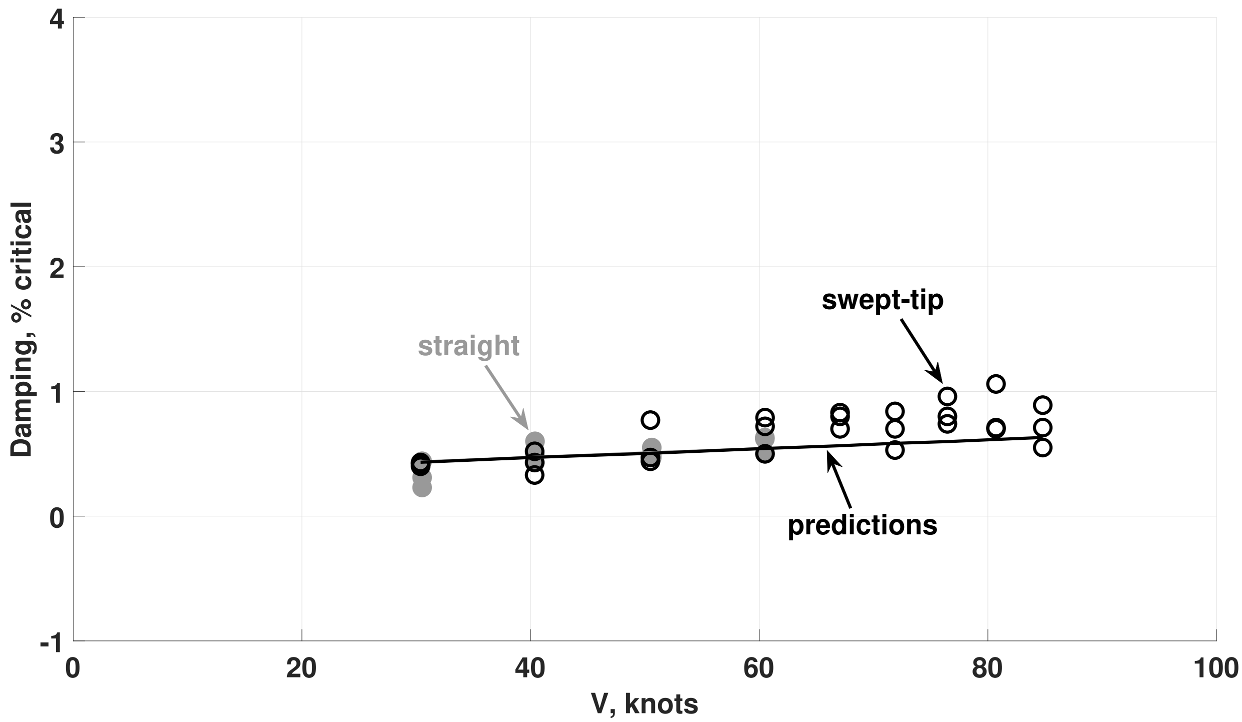

(a) Wing beam mode

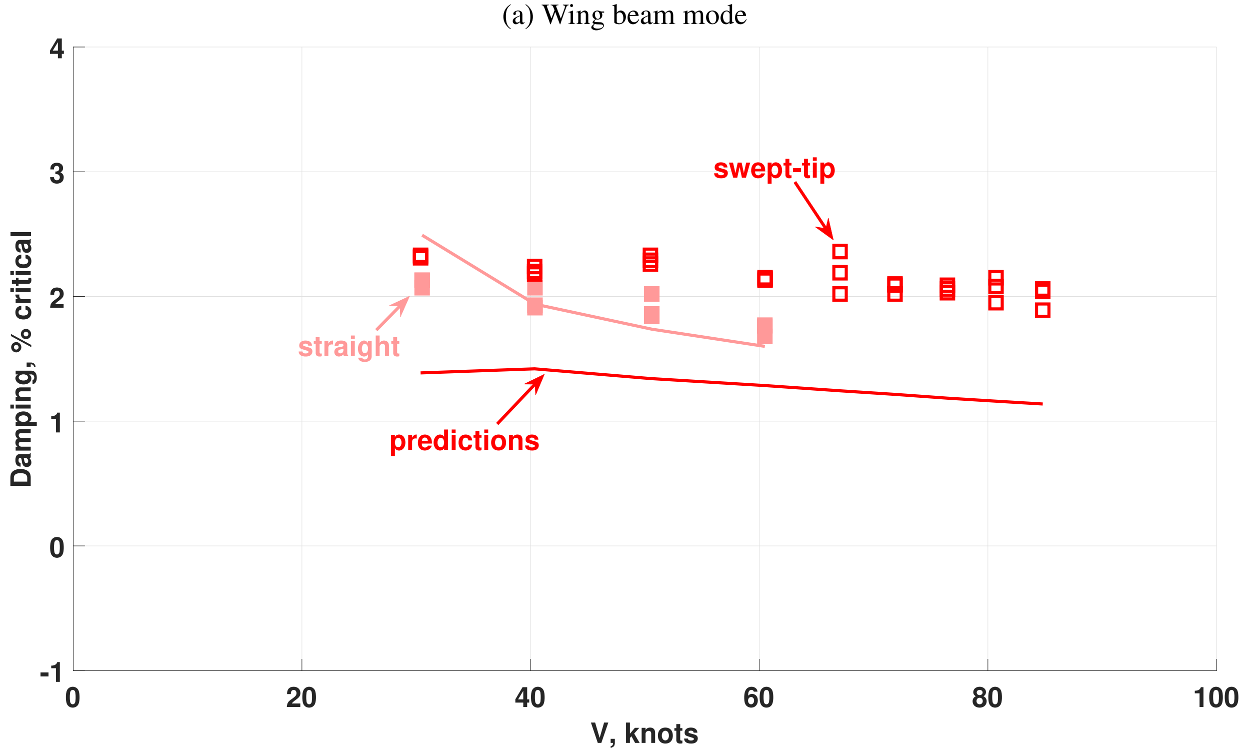

(b) Wing chord mode

Figure 5.14: Comparison of straight and swept-tip blade damping test data for gimbal-locked, freewheeling, wing fairings off configuration (lines: predictions, symbols: test data)

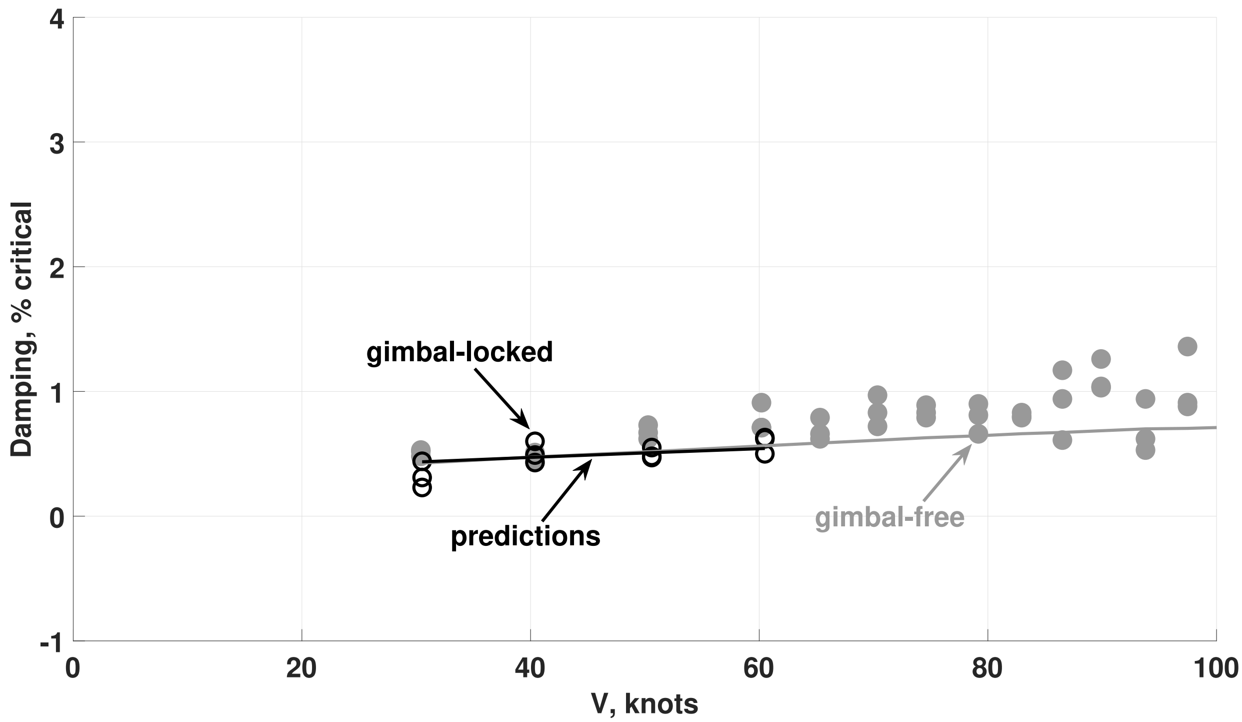

(a) Wing beam mode

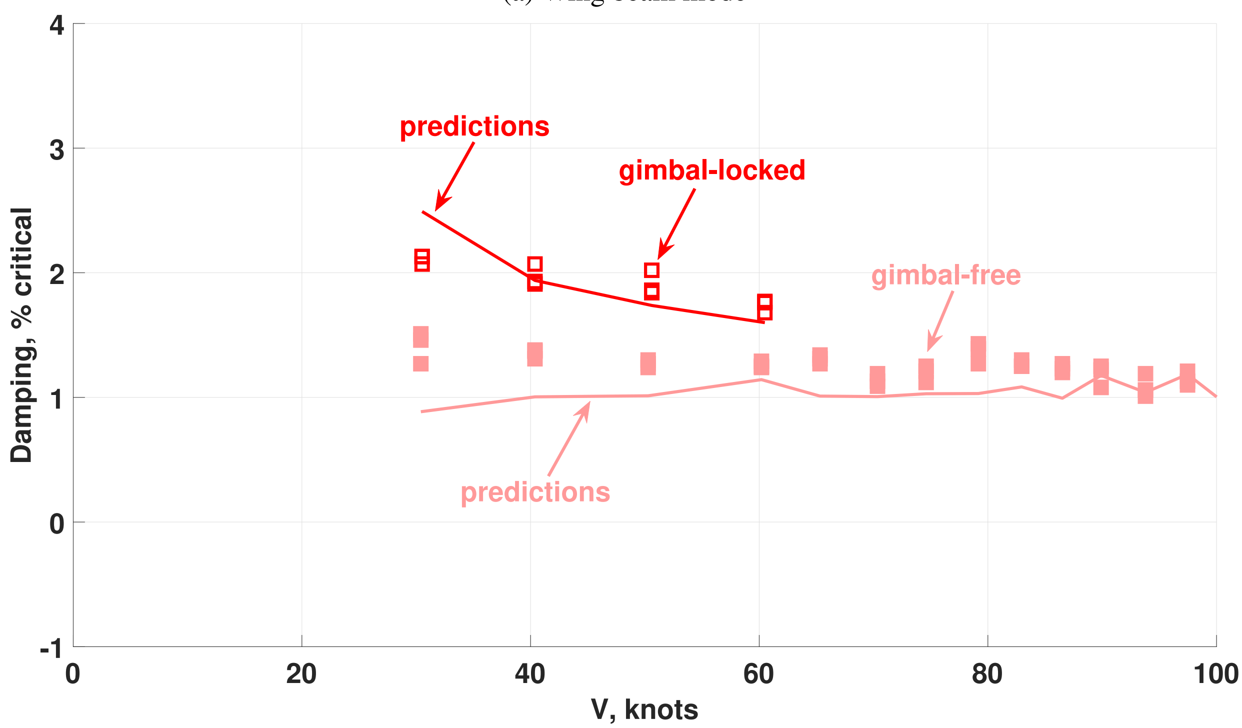

(b) Wing chord mode

Figure 5.15: Comparison of gimbal-free and gimbal-locked damping test data for freewheeling, wing fairings off, straight blades configuration (lines: predictions, symbols: test data)

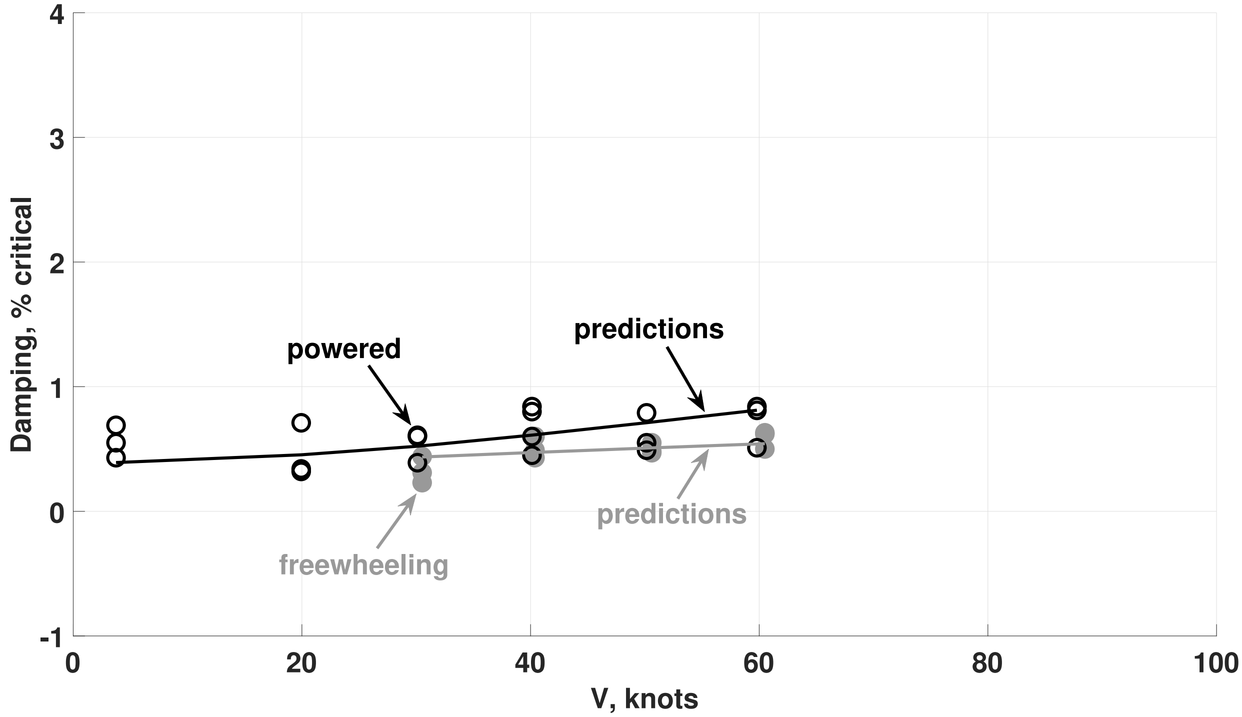

(a) Wing beam mode

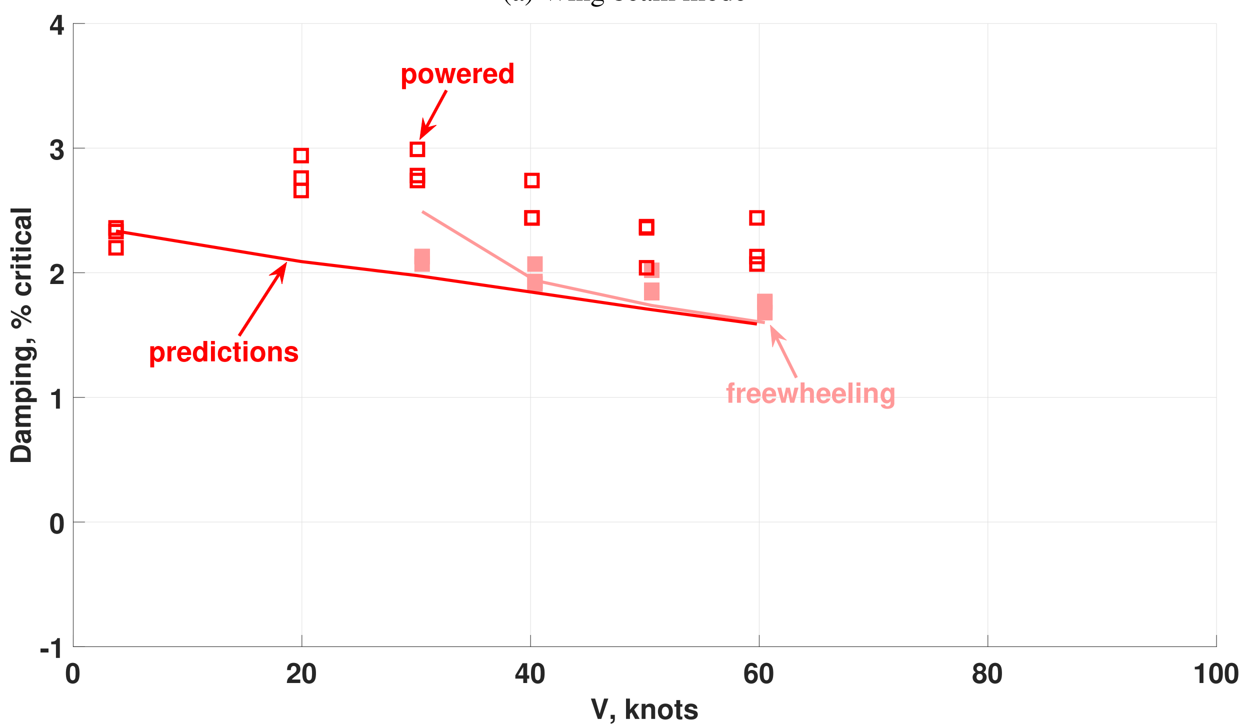

(b) Wing chord mode

Figure 5.16: Comparison of freewheeling and powered mode damping test data for gimbal-locked, wing fairings off, straight blades configuration (lines: predictions, symbols: test data)

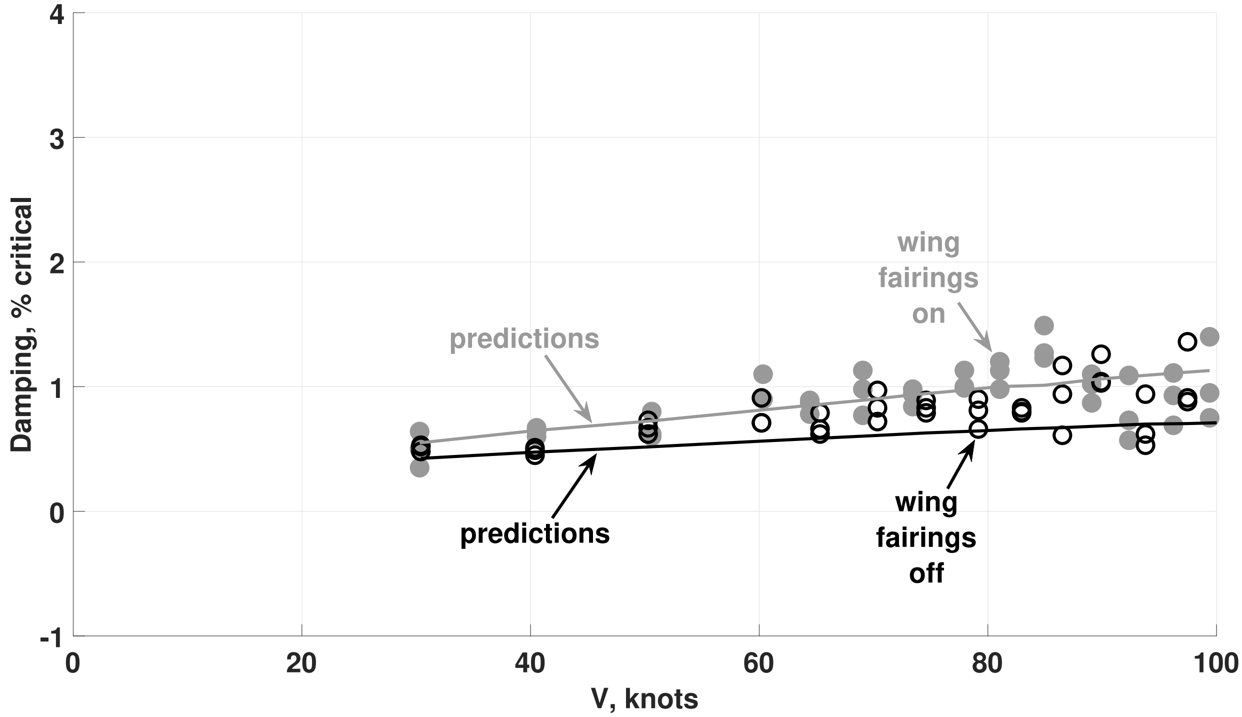

(a) Wing beam mode

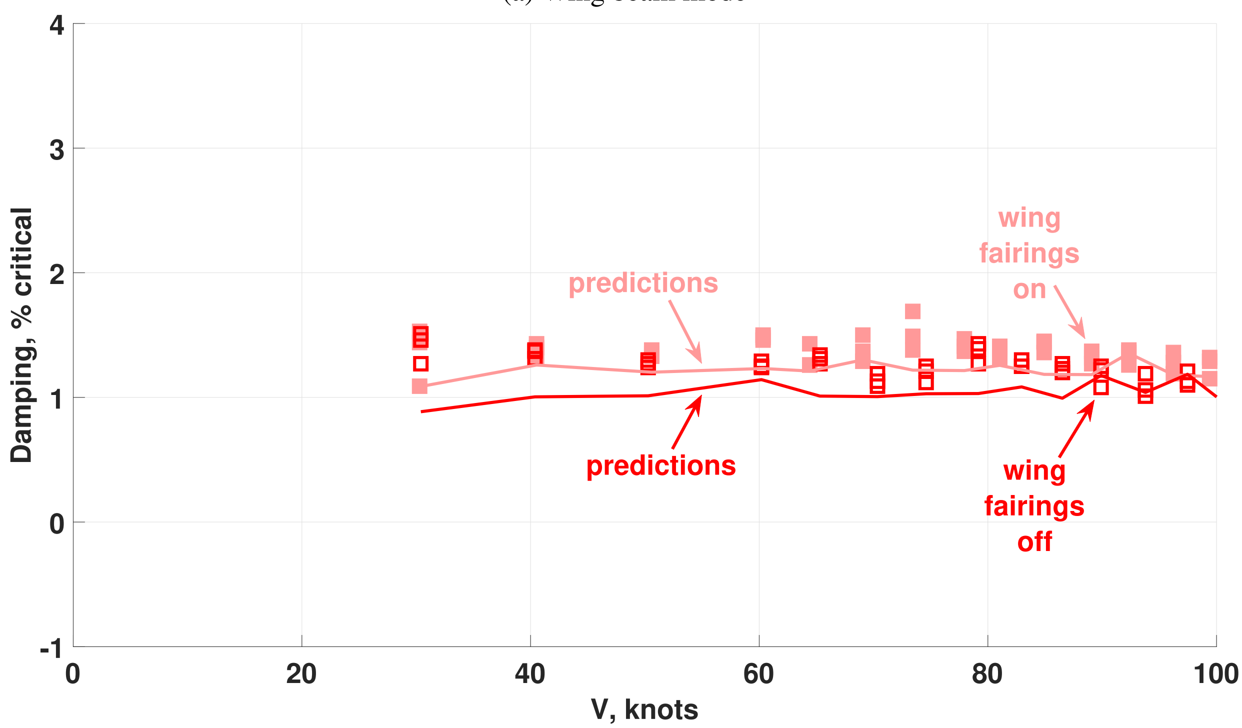

(b) Wing chord mode

Figure 5.17: Comparison of wing fairings on and off damping test data for gimbal-free, freewheeling, straight blades configuration (lines: predictions, symbols: test data)

5.6 Summary and Conclusions

UMD's Maryland Tiltrotor Rig was tested in the Naval Surface Warfare Center Carderock Division $8\text{-ft} \times 10\text{-ft}$ subsonic wind tunnel on October 26 – November 2, 2021. Frequency and damping data for wing beam and chord modes was collected up to $100\ \text{knots}$. Baseline data is gimbal-free, freewheeling, wing fairings on with straight and swept-tip blades. Gimbal-locked, powered mode, and wing fairings off data was also collected, all with straight and swept-tip blades. The test data for different configurations provided a rich source for fundamental understanding and analysis validation. Freewheeling and stability predictions were validated. The key conclusions are as follows:

1. Wing beam mode damping trends and magnitudes were predicted accurately for all configurations.
2. Wing chord mode damping was under-predicted for all configurations. The trends for the gimbal-locked, straight blade configurations (freewheeling and powered) were not captured.
3. No significant impact of swept-tip blades was observed for the gimbal-free configuration up to $100\ \text{knots}$. Blade sweep increased wing chord mode damping for the gimbal-locked, freewheeling, wing fairings off configuration. Analysis could not predict this increase.
4. Locking the gimbal provided higher damping for the wing beam and chord modes. The change in the chord mode was captured by the analysis.
5. Powered mode also resulted in higher wing chord mode damping compared to freewheeling. Analysis could not predict this behavior.
6. Wing aerodynamics increased wing beam mode damping at high speeds, although not as clearly as predictions due to the scatter in the data.

Chapter 6: Advanced Geometry Blades

There has been no previous work on advanced geometry blades for hingeless hub tiltrotors where proprotor air resonance can be the limiting phenomenon. A few analytical studies (Refs. [22, 23, 38]) undertaken were focused on gimballed hub proprotors. The objective is to determine whether tip sweep can influence the stability boundary and how. The Boeing M222 rotor/pylon/wing was used as the baseline case. This is because the wing thickness of that model was 13.5% chord (much thinner than the 23% thickness of the current technology tiltrotor wings); hence consistent with the vision of turboprop-like low-drag flight.

6.1 Stability

Figure 6.2 compares the stability roots obtained with straight and swept-tip blades (model shown in Fig. 6.1). Sweep-back angles of $10°$ and $20°$ were introduced from $80\%R$ while keeping everything else (mass, twist, chord, etc.) the same. As sweep increases, damping of q_1 mode improves at high speeds but q_2 mode stays relatively unaffected. Coupling of $\zeta - 1$ and p modes is delayed. The peak damping value for p mode decreases but the air resonance speed increases with sweep. The improvement is more than 10 knots with $10°$ sweep and more than 25 knots with $20°$ sweep bringing it to near 355 knots.

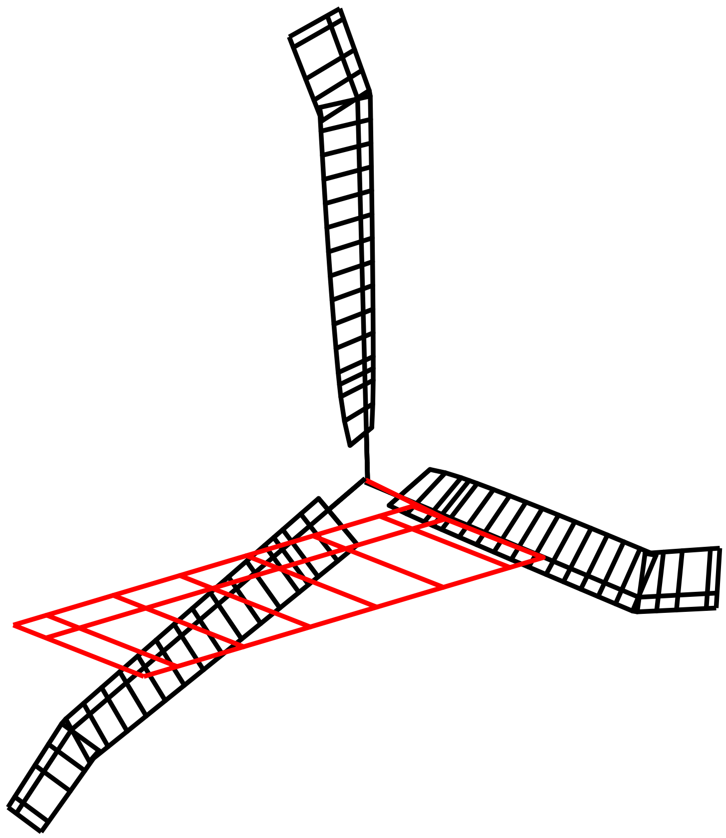

Figure 6.1: UMARC-II model of the Boeing M222 tiltrotor with swept-tip blades (rotor, pylon, and wing are beams, panels show aerodynamic segments)

Sweep introduces three changes: elastic axis, the section center of gravity (c.g.), and aerodynamic center shift back. In order to examine the cause of the improvement, section c.g. was returned back to its original unswept position in order to isolate the effect of aerodynamics alone. Figure 6.3 shows a comparison with the original 20° sweep case. Stability of the p mode at high speeds is significantly higher with the unswept c.g. The instability has virtually vanished up to more than $475\ \mathrm{knots}$.

An additional check was performed by assuming no aerodynamic loads between $90\%R$ and $100\%R$ of the blade, which accounts for half of the swept area. Both baseline and 20° sweep cases were repeated and compared in Fig. 6.4. This time sweep decreased the air resonance speed. This is because the stabilizing effect of the aerodynamics due to sweep is not present

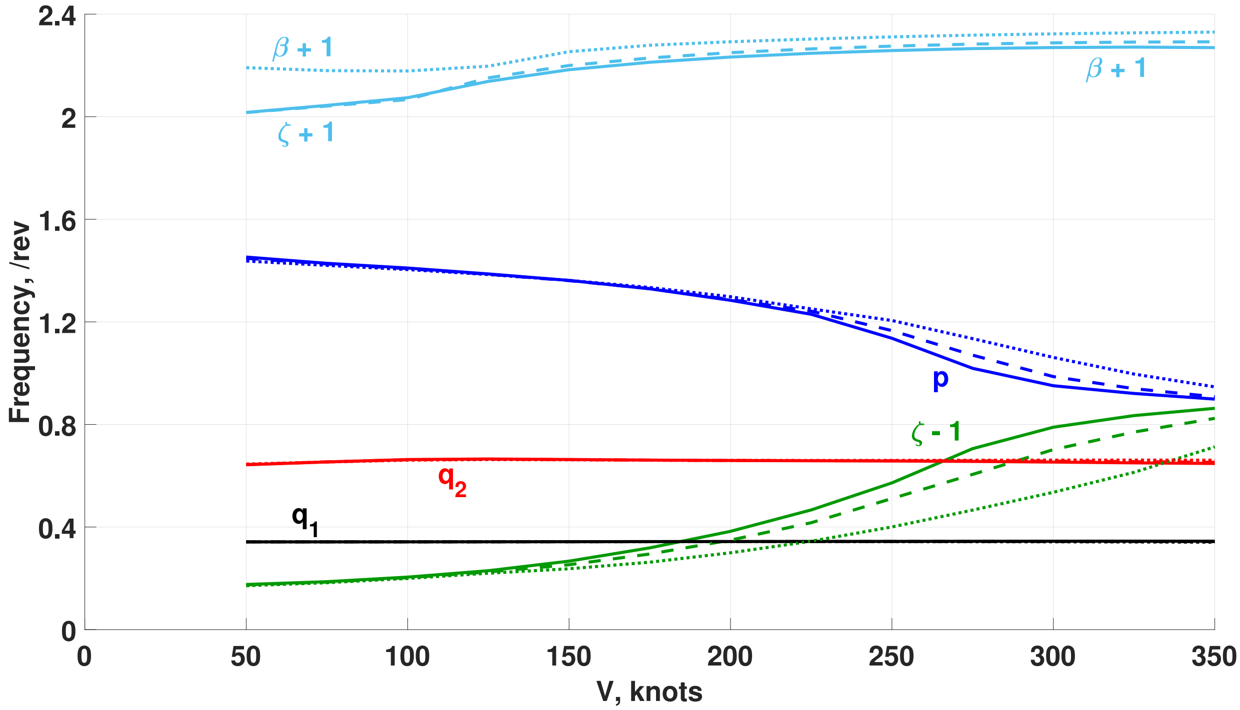

(a) Frequency

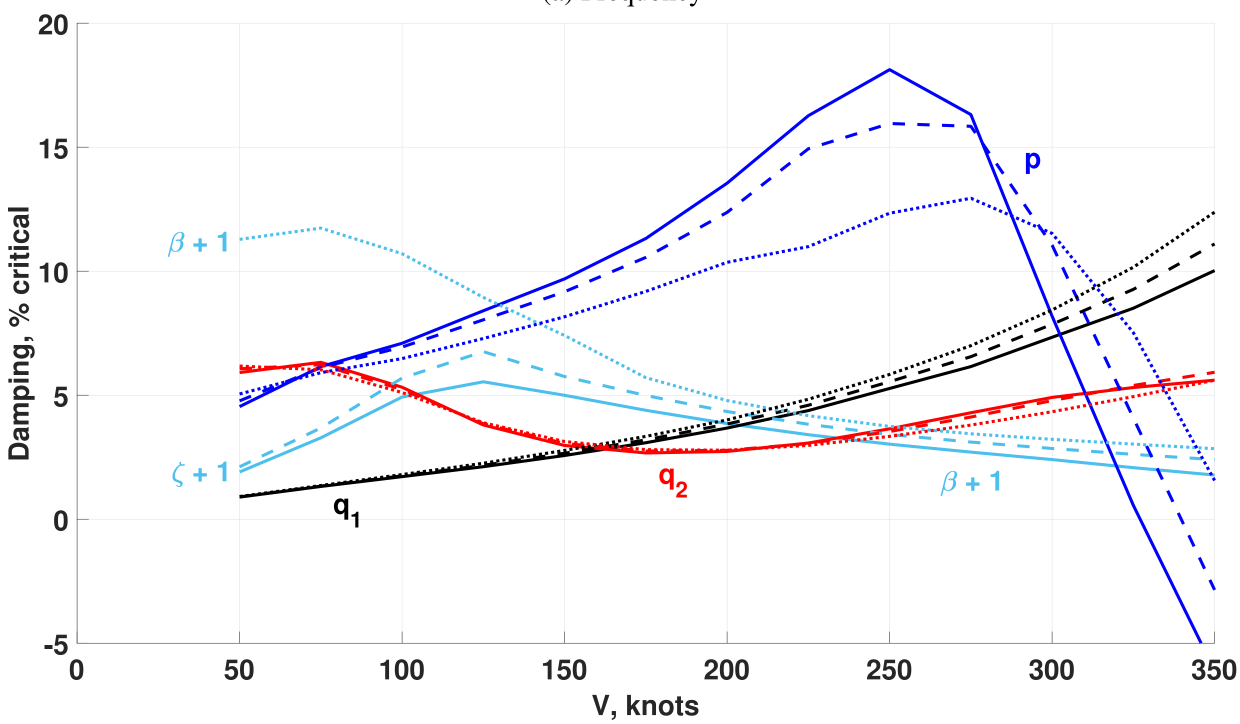

(b) Damping

Figure 6.2: Effect of tip sweep
(solid: straight blades – baseline, dash: 10° sweep, dot: 20° sweep)

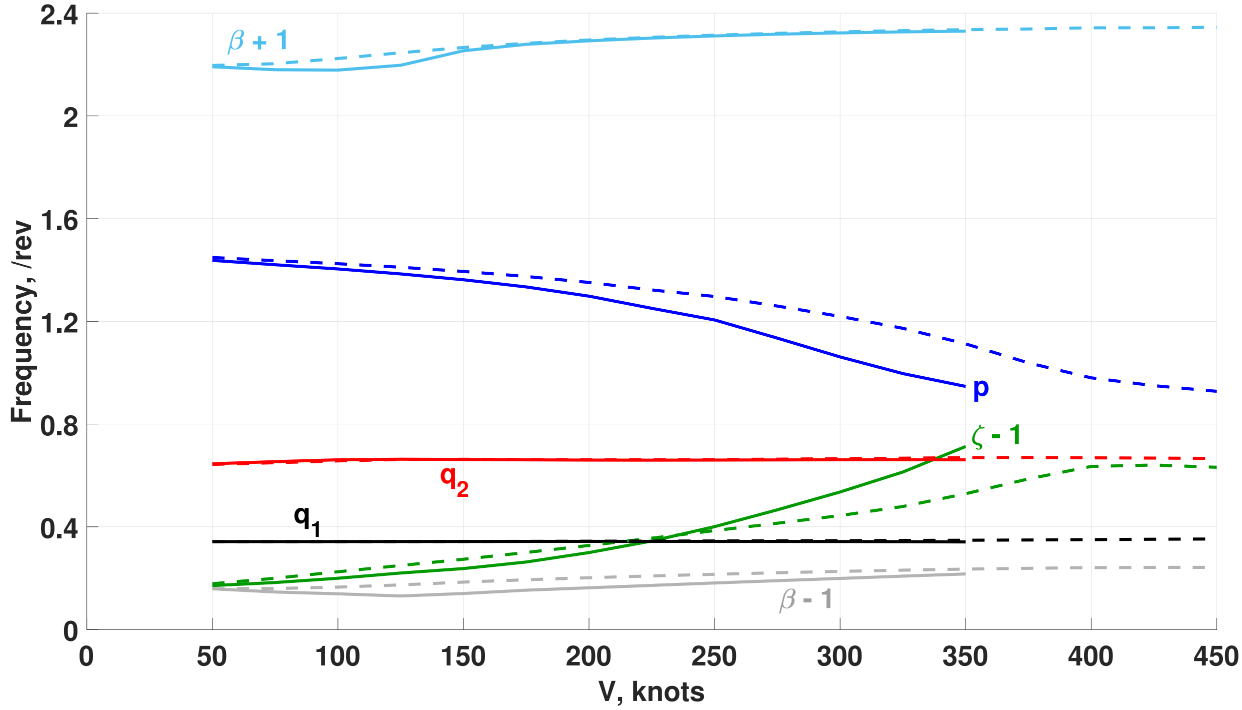

(a) Frequency

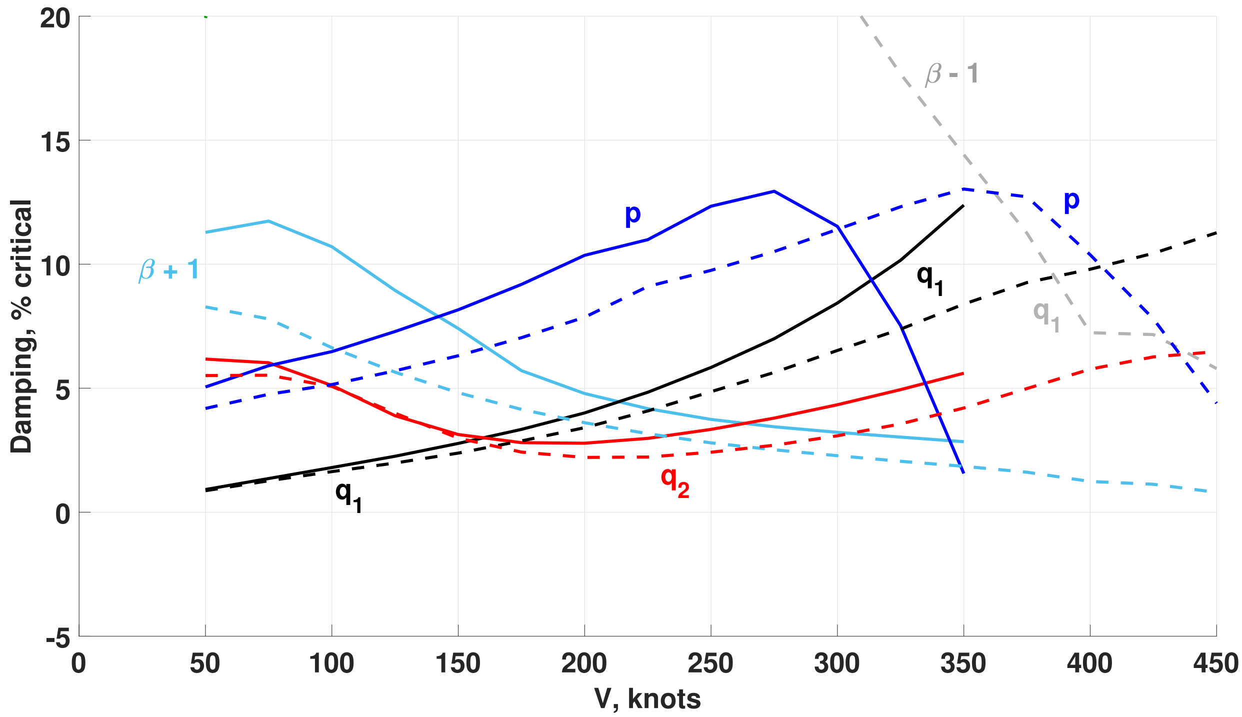

(b) Damping

Figure 6.3: Effect of c.g. sweep (solid: 20° sweep, dash: 20° sweep – c.g. unswept)

anymore. This and the previous comparison show that the main effect is from the aerodynamic center shift and its impact is greater than the detrimental c.g. shift back due to sweep. Figure 6.5 illustrates the stabilizing effect. A perturbation lift (ΔL) at the swept-tip introduces a pitch down motion with respect to the pitch axis of the blade. This, in turn, decreases the angle of attack of the blade sections and stabilizes the perturbation. Because of the high pitch angle, this stabilizes both flap and lag motions. The same way, a c.g. shift back is detrimental because any upward motion of the blade will create an inertial force (ΔF) at the c.g., which will pitch the blade up and destabilize the system.

This raises the question whether the stability would further improve if the swept region did not have a spar at all: this can be seen in many modern rotors. In order to mimic that, two cases were considered: (1) the section mass was reduced by 50% (except the tip weight shown in Fig. 4.2d) and the section c.g. was moved to 15% chord for the swept part, (2) the section mass was reduced by 50%, the tip weight was removed, and the section c.g. was moved to 35% chord for the swept part. The properties for the rest of the blade were kept the same as before. Figure 6.6 shows a comparison of the first case with the original $20°$ sweep results. Stability of the p mode improves and the air resonance speed is pushed about another 50 knots to near 405 knots. This, of course, does not mean the aircraft can fly at 405 knots; the instability speed should be sufficiently beyond the maximum design speed for safe flight. However, because the instability is sudden, even 25 knots lower flight speed brings more than 3.5% damping. Compared to the straight blades, the total speed increase is more than 75 knots. Also note the rapid decrease in q_1 damping at high speed in Fig. 6.6. This mode starts as a $\beta-1$ mode but mostly assumes a q_1 mode shape at high speeds. This is the whirl flutter mode and further improvements in air resonance can cause this mode to now appear as the critical one. Figure 6.7 shows a comparison for the

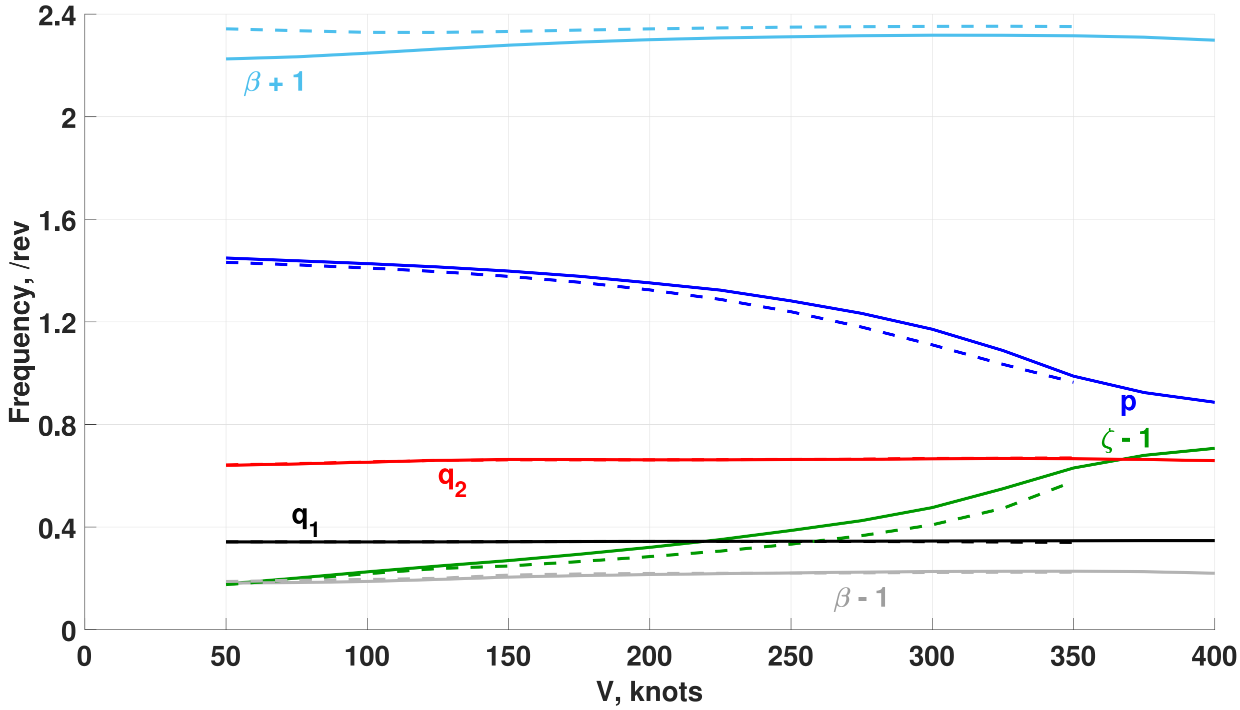

(a) Frequency

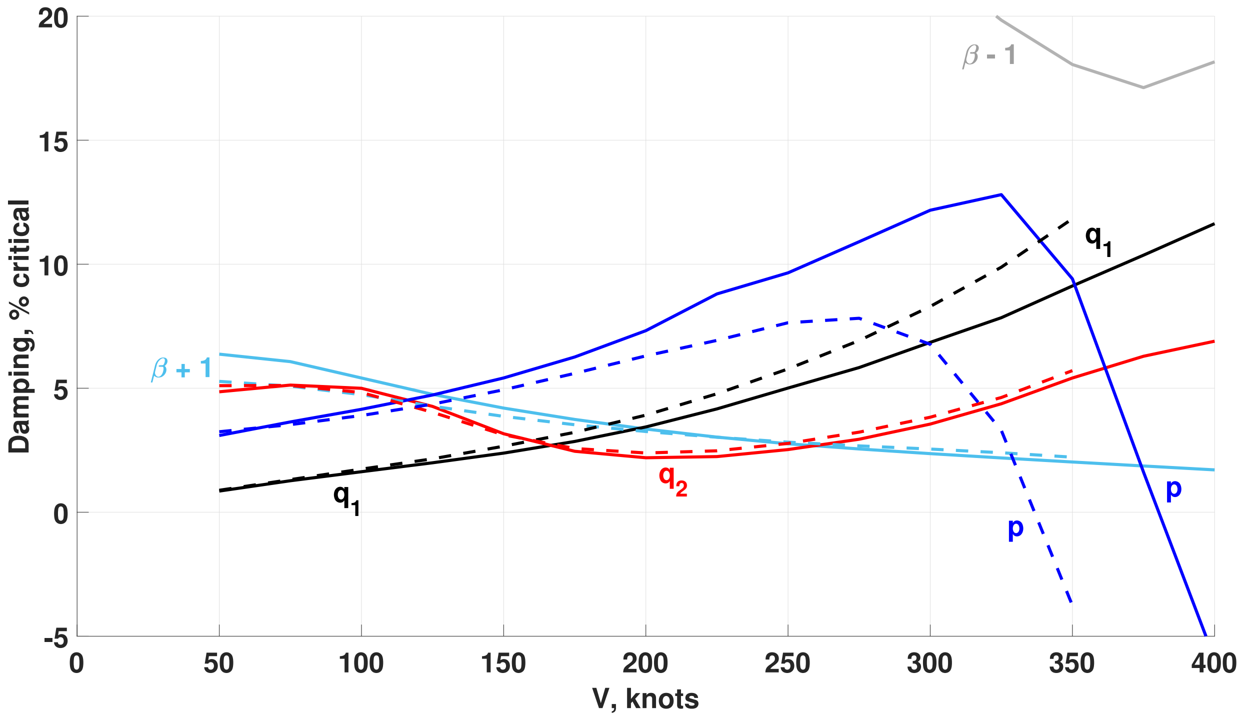

(b) Damping

Figure 6.4: Effect of sweep with no tip aerodynamics
(solid: straight blades – baseline, dash: 20° sweep)

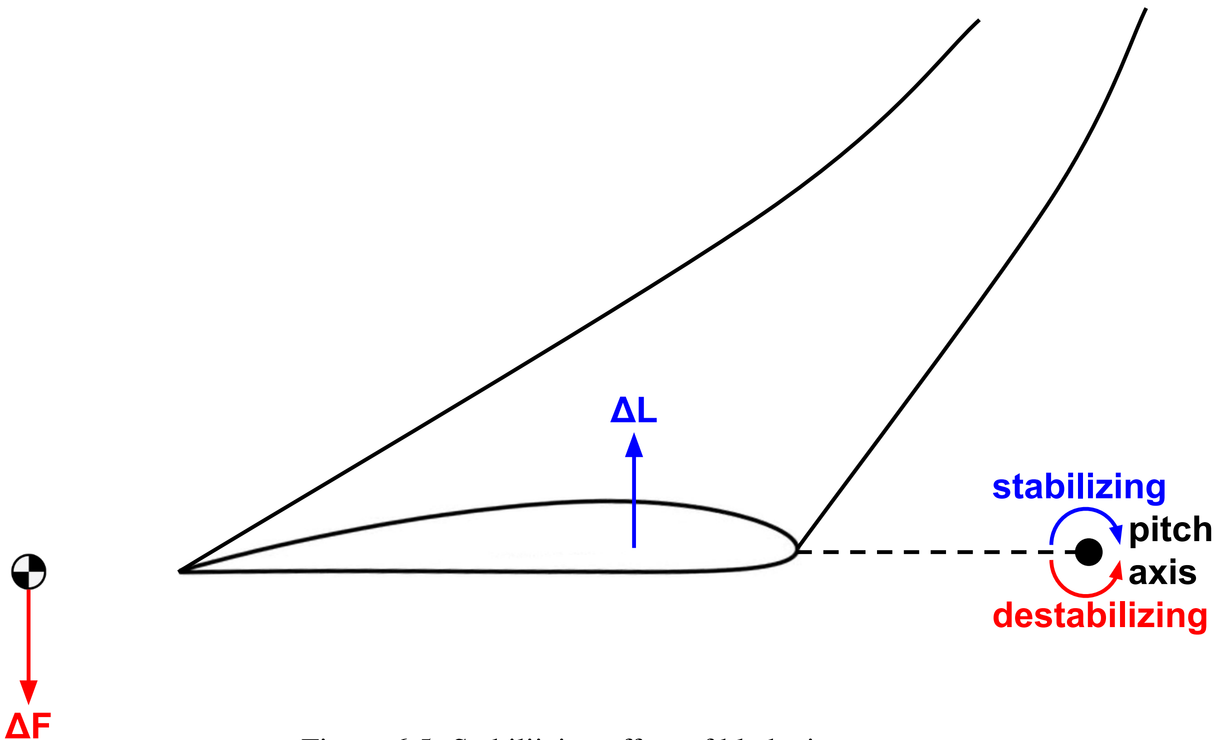

Figure 6.5: Stabiliizing effect of blade tip sweep

second case. Maximum damping of the p mode increases dramatically. Air resonance speed is pushed to near $383\ \mathrm{knots}$. Similar to the first case, note the change in the damping behavior of the q_1 mode at high speeds. This mode may become unstable at high speeds.

A double-sweep configuration was also analyzed. A $20°$ sweep forward was introduced at $80\%R$ followed by a $20°$ sweep back at $90\%R$. The objective was to investigate whether double-sweep can improve the stability comparable to the $20°$ sweep-back case. This configuration was of interest for its potential to alleviate the additional blade loads tip sweep may bring. Figure 6.8 shows a comparison with straight and $20°$ sweep-back cases. Due to the tip mass in the sweep-back region and forward offset of the aerodynamic center, the double-sweep configuration did not result in any improvement in the stability.

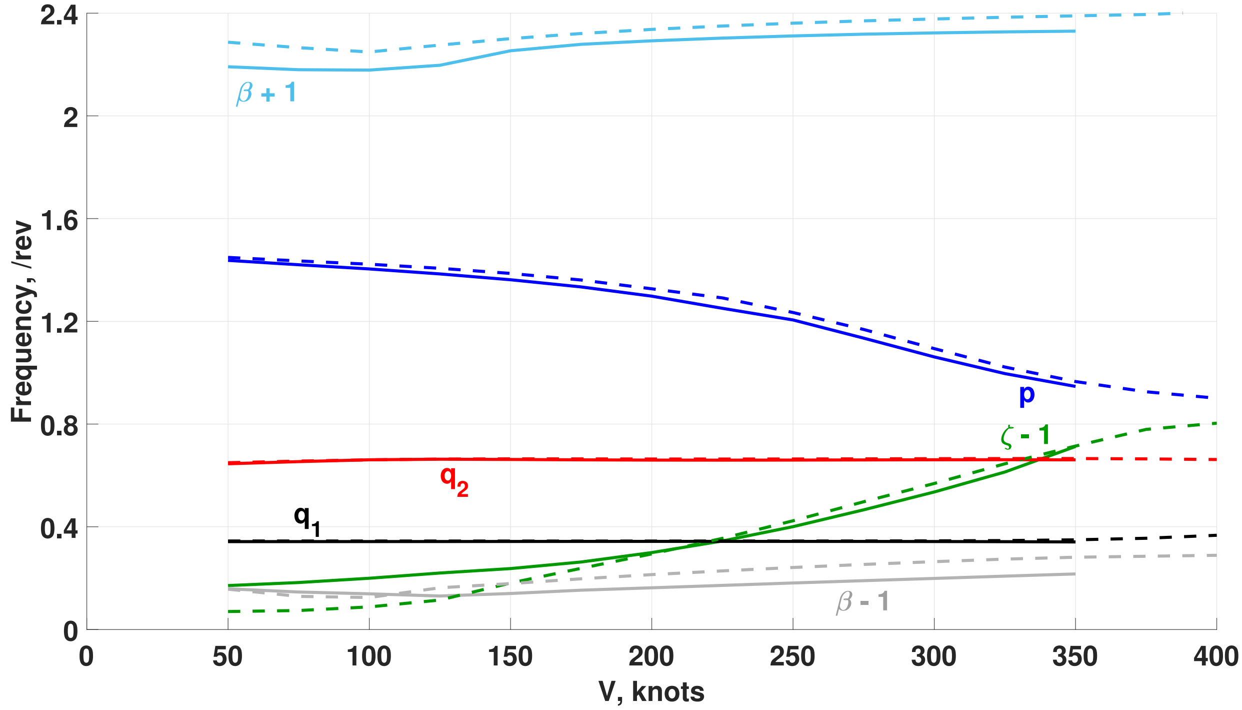

(a) Frequency

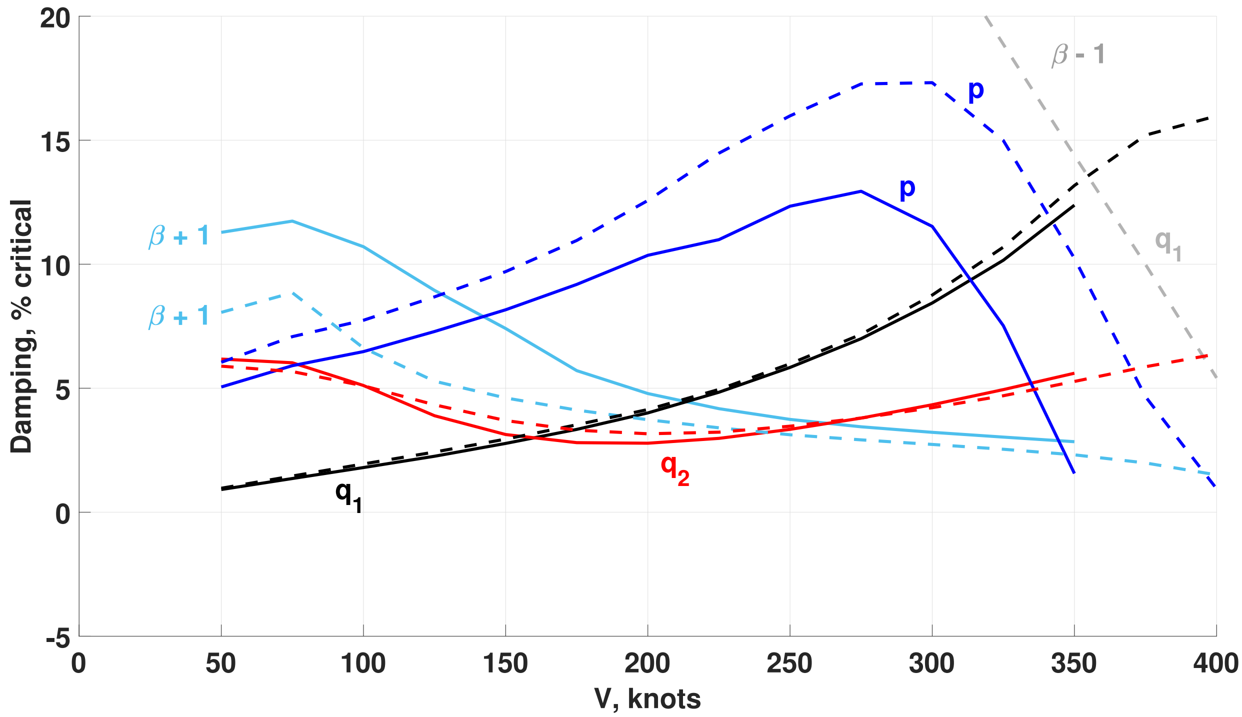

(b) Damping

Figure 6.6: Effect of spar in the swept region
(solid: 20° sweep, dash: 20° sweep without spar – case 1)

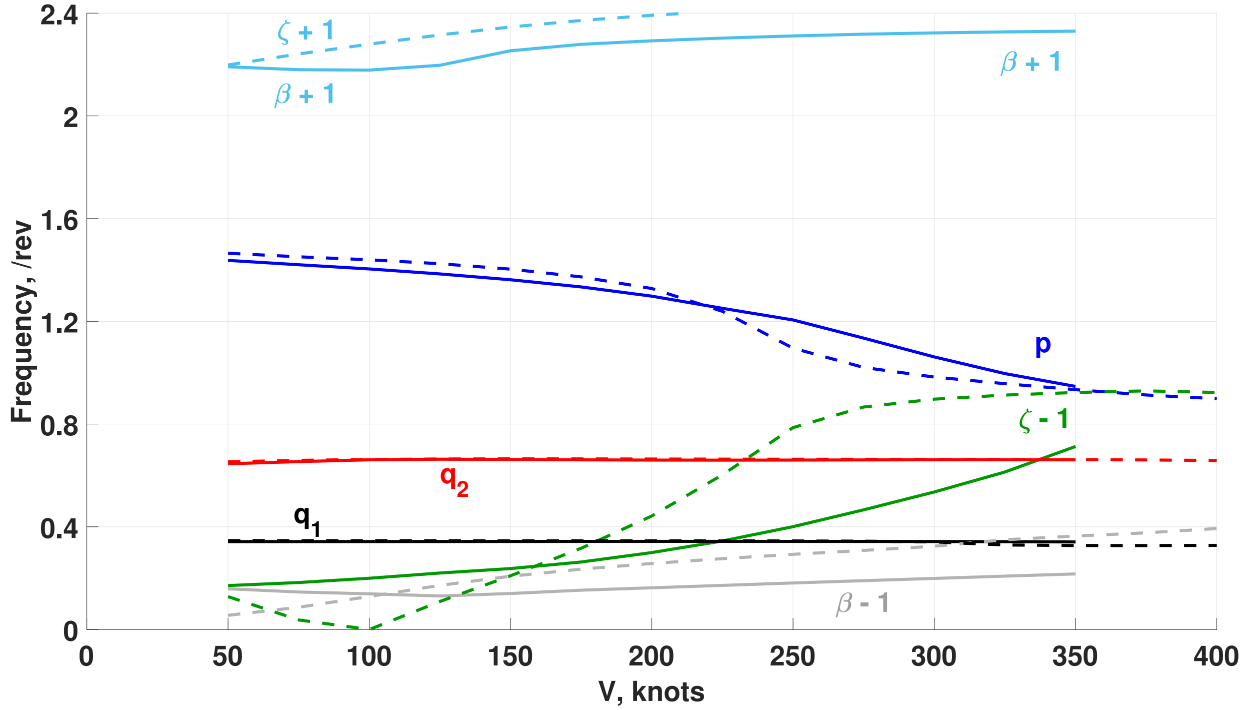

(a) Frequency

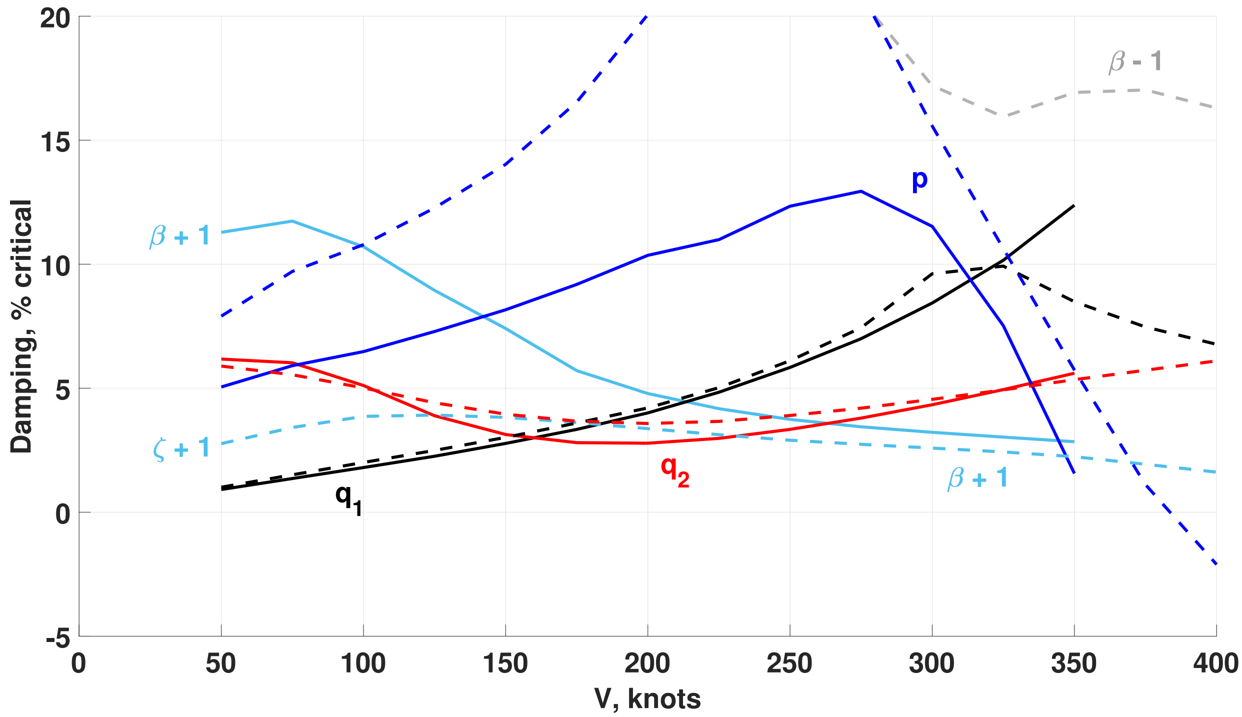

(b) Damping

Figure 6.7: Effect of spar in the swept region
(solid: 20° sweep, dash: 20° sweep without spar – case 2)

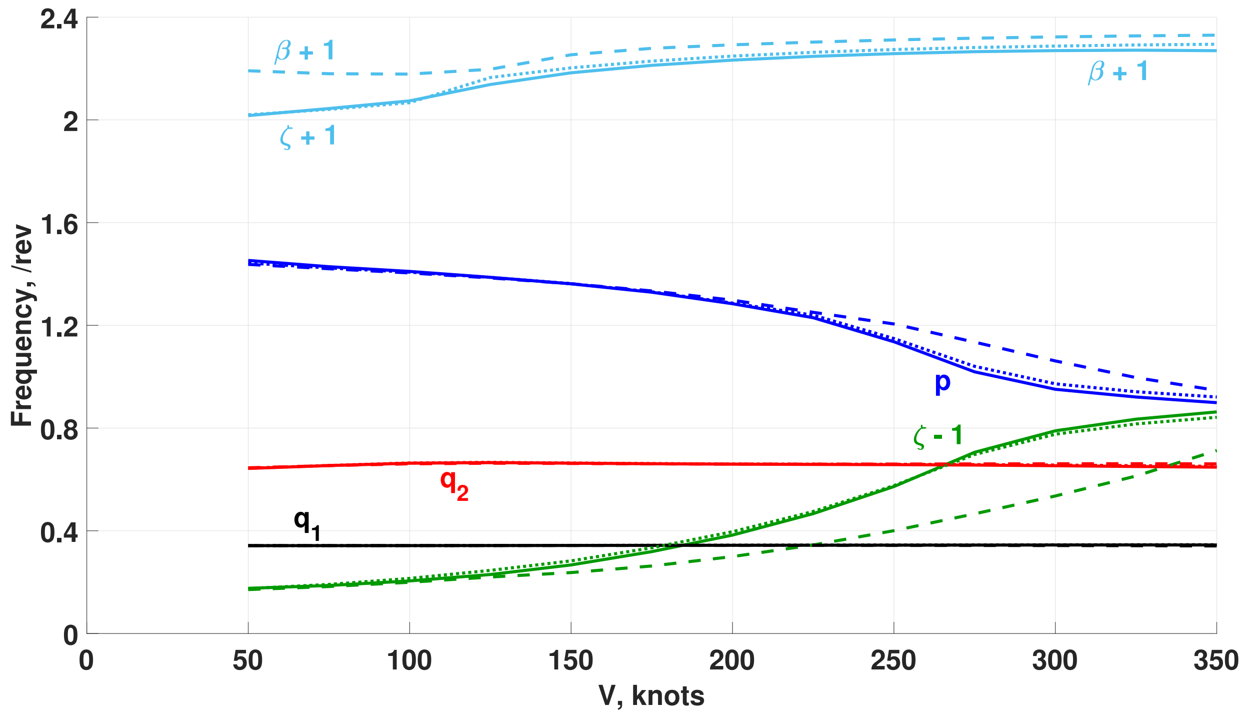

(a) Frequency

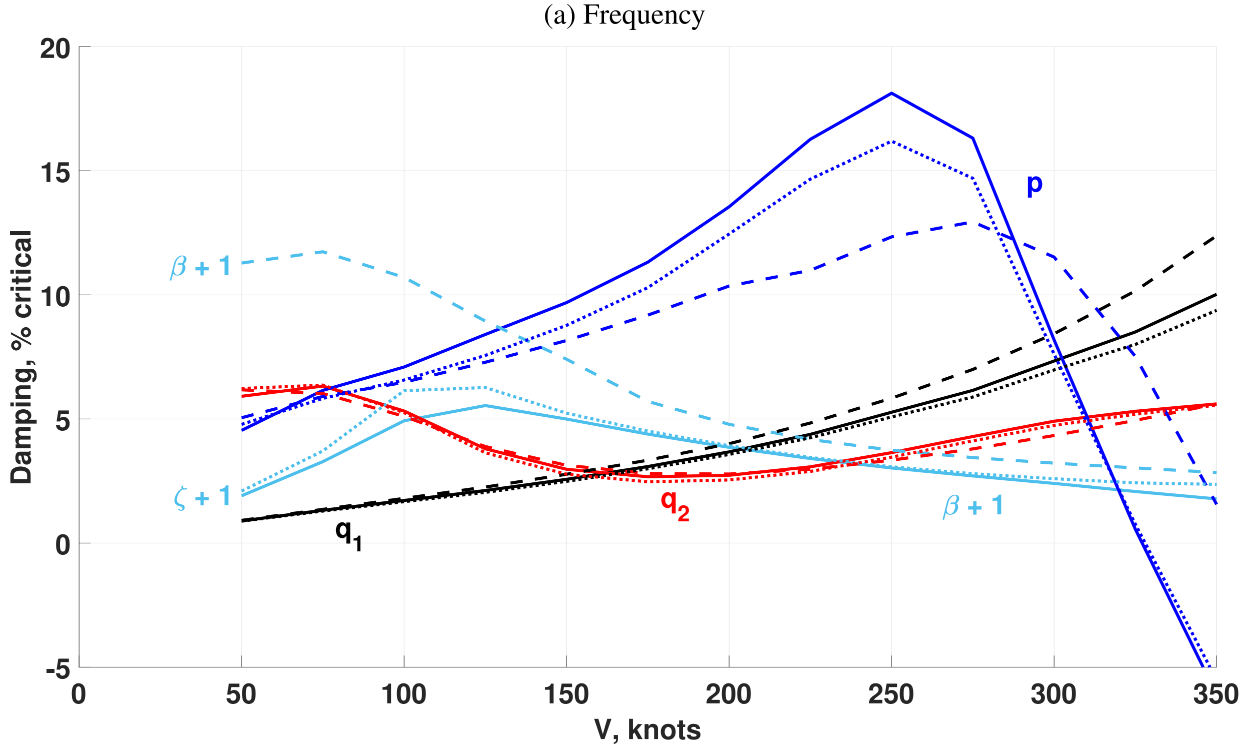

(b) Damping

Figure 6.8: Effect of double-sweep
(solid: straight blades – baseline, dash: 20° sweep, dot: 20° double-sweep)

6.2 Loads

Loads should be monitored with the introduction of sweep as it should not introduce unacceptable blade or control loads. Figures 6.9 to 6.11 show the sectional steady and oscillatory flapwise, chordwise, and torsional moments in the deformed frame for straight and swept-tip blades (without spar – case 1). The rotor was trimmed to zero hub moments and $C_T/\sigma = 0.12$ for a pure edgewise flight condition with $\mu = 0.15$ and $i_N = 90°$ from the flow. The Maryland Freewake was used with a single tip vortex and a nearwake extending $30°$ behind. Steady, $1/\mathrm{rev}$, and $2/\mathrm{rev}$ flap bending moments increase near the root with the introduction of sweep (Fig. 6.9). Significant change is observed in chordwise and torsional moments. Steady, $1/\mathrm{rev}$, and $2/\mathrm{rev}$ chordwise moments increase along the blade and at the hub (Fig. 6.10). Oscillatory torsional moments also increase (Fig. 6.11). This would have implications for the design of the blade and the control system (pitch links, swashplate, actuators) but redesign is outside the scope of this work.

Note that the jumps in the loads are merely due to the axis system definition; each span station has a different deformed axis system (due to pitch control, sweep, twist, and deformations).

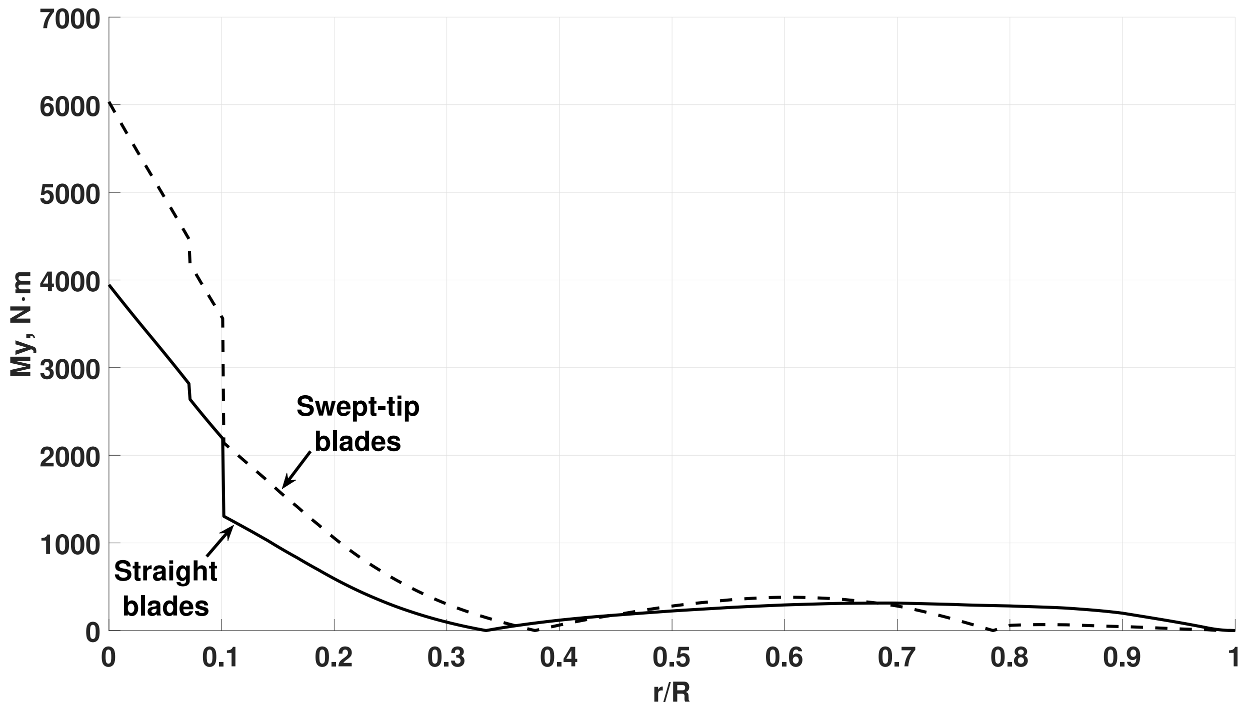

(a) Steady

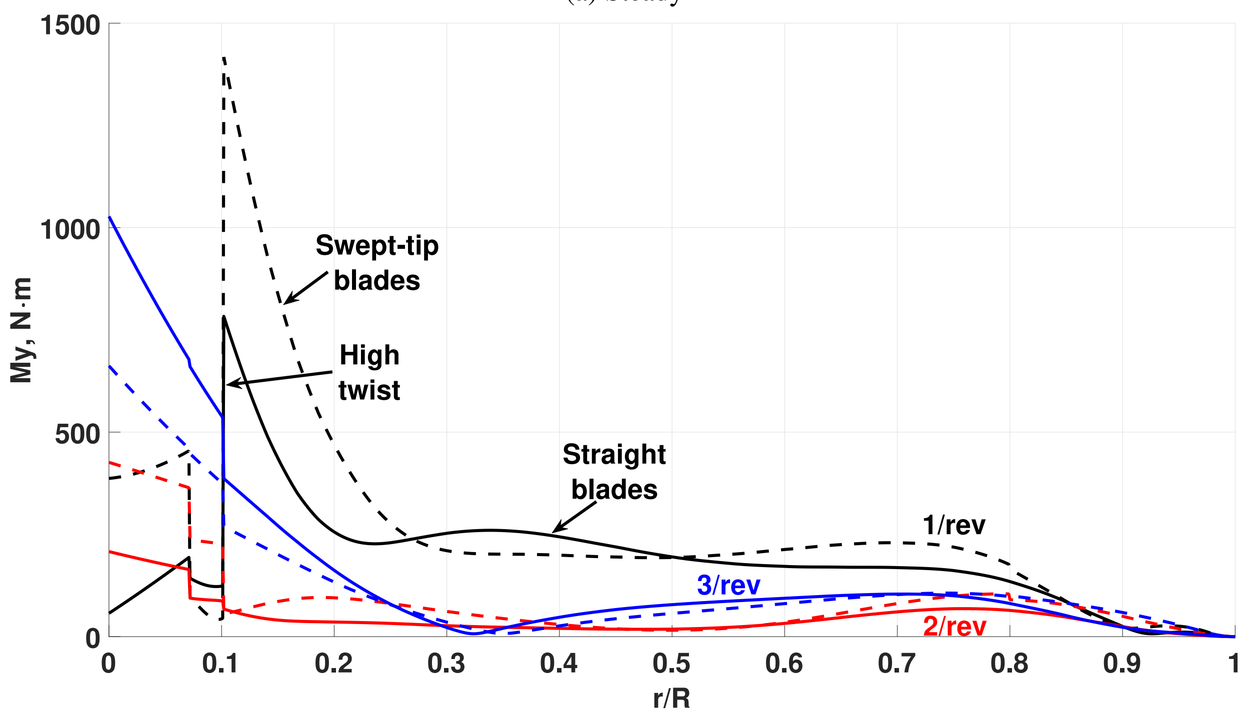

(b) Oscillatory

Figure 6.9: Flapwise bending moment
(solid: straight blades – baseline, dash: 20° sweep without spar)

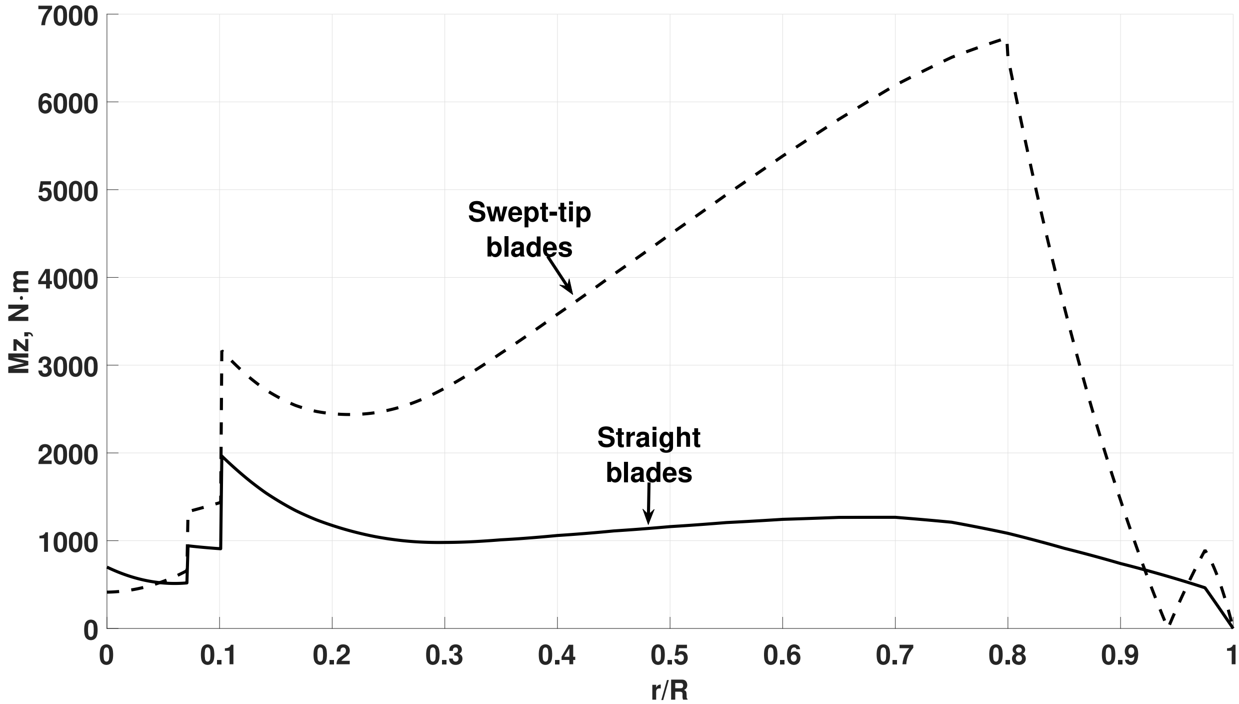

(a) Steady

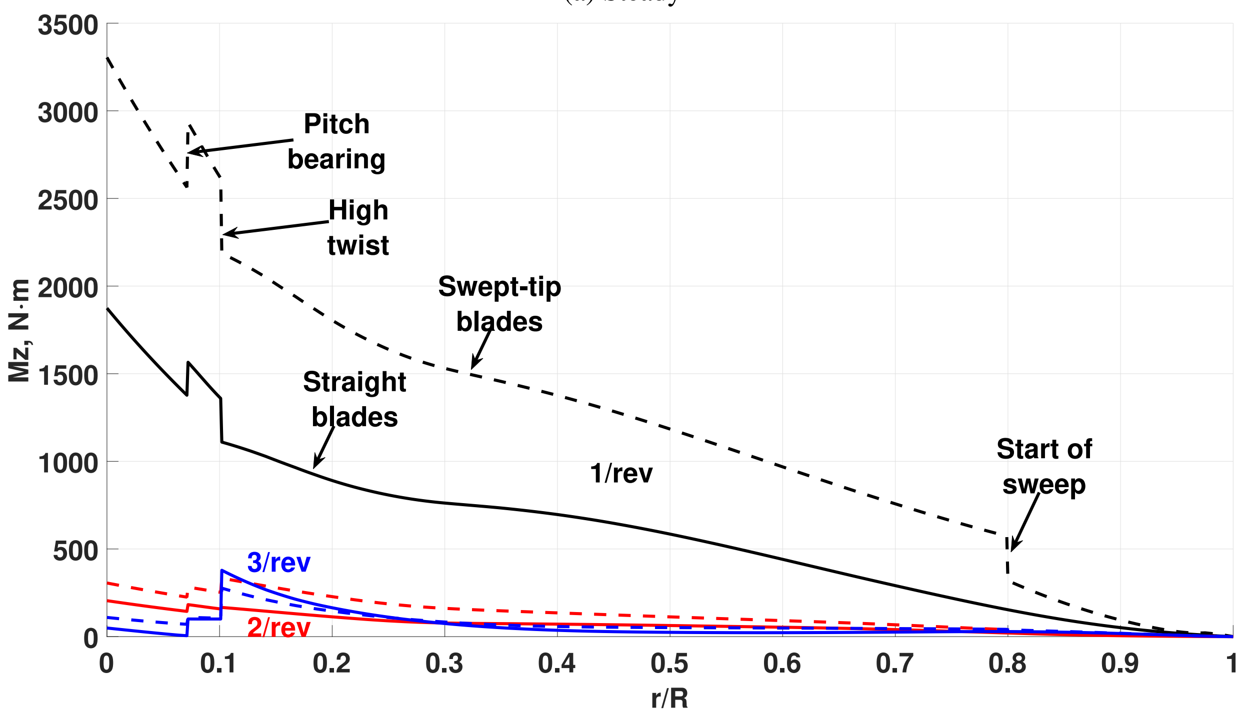

(b) Oscillatory

Figure 6.10: Chordwise bending moment
(solid: straight blades – baseline, dash: $20°$ sweep without spar)

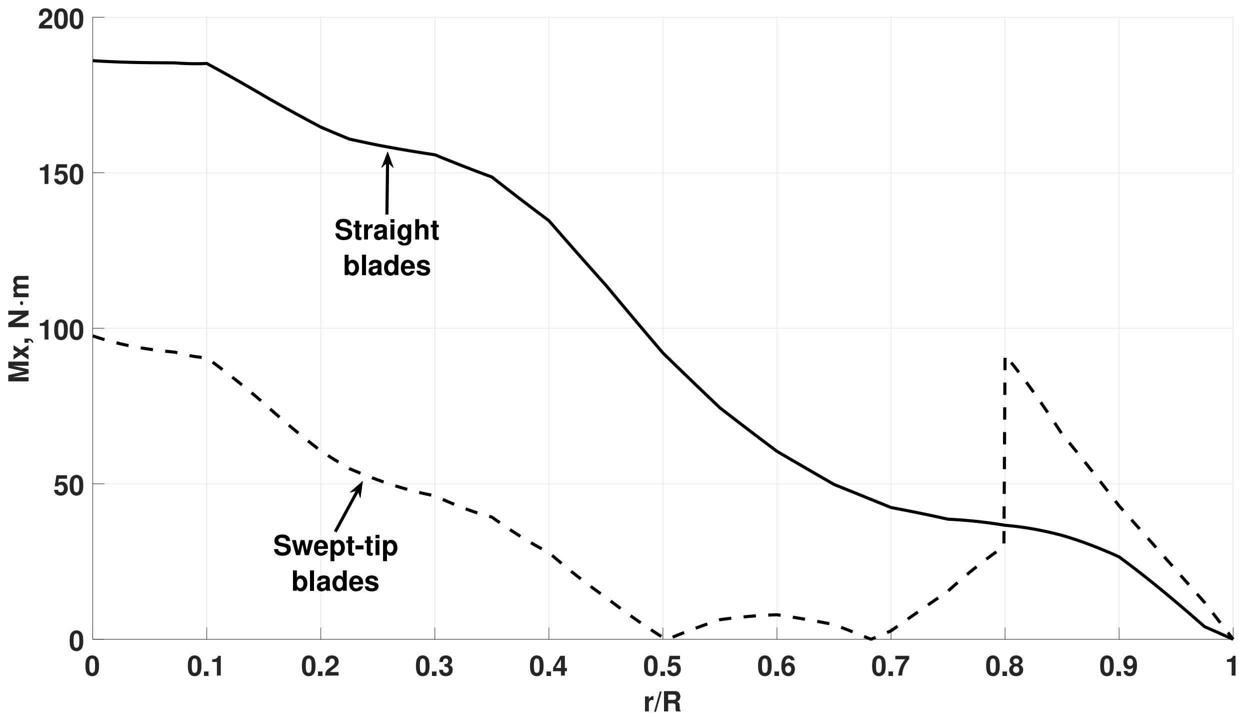

(a) Steady

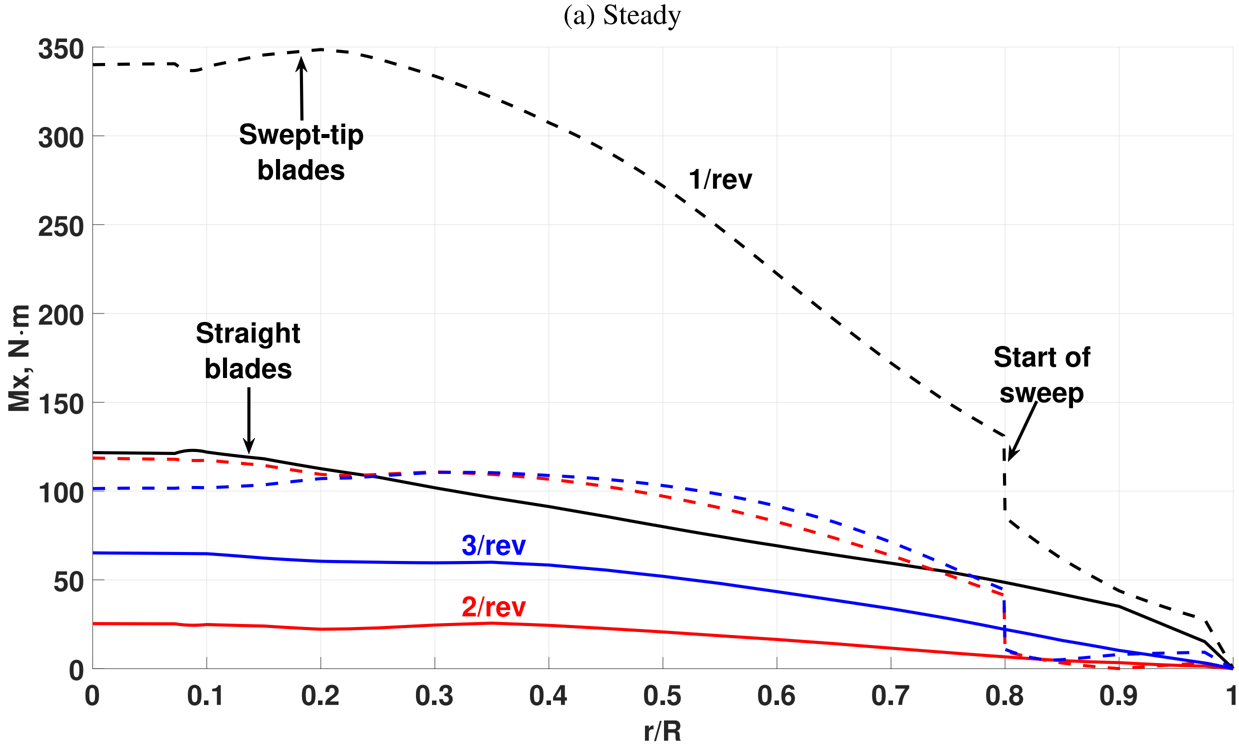

(b) Oscillatory

Figure 6.11: Torsional moment (positive pitch up)
(solid: straight blades – baseline, dash: 20° sweep without spar)

6.3 Summary and Conclusions

Effect of swept-tip blades on hingeless hub proprotor air resonance was studied in a comprehensive manner. The key conclusions are as follows:

1. A 20° sweep back from $80\%R$ pushed the instability speed by more than 25 knots.

2. Aerodynamic center shift is the key mechanism; c.g. offset due to sweep is detrimental. Implication is to sweep the blade without an internal spar.

3. A no spar swept-tip configuration was analyzed. The instability speed improved by more than 75 knots, reaching near 405 knots. The wing thickness is 13.5% chord, which is much thinner than the 23% thickness of the current technology tiltrotor wings.

4. Whirl flutter can appear as the critical phenomenon with further improvements in the air resonance speed.

5. Steady and oscillatory chordwise moments and oscillatory torsional moments increased significantly due to sweep. Blades and control system may need to be redesigned with higher loads.

6. A 20° sweep forward at $80\%R$ followed by a 20° sweep back at $90\%R$ (double-sweep) was analyzed to potentially alleviate the increase in the loads. This configuration did not show an improvement in stability due to the tip mass in the sweep-back region and forward offset of the aerodynamic center.

Chapter 7: Summary and Conclusions

7.1 Key Conclusions

A new aeromechanics solver was developed, verified, and validated. High-speed stability of hingeless hub tiltrotors was studied. The impact of blade tip sweep on the stability was analyzed. A parametric study was reported using the new MTR test results and predictions. The key conclusions are listed as follows:

1. Proprotor air resonance is the critical instability for the Boeing M222 rotor due to the soft in-plane hingeless hub, not whirl flutter. Air resonance is observed with the coupling of wing torsion and low-frequency lag modes at high speeds. The mode shape is mostly lag near instability.

2. A $20°$ sweep back from $80\%R$ pushed the instability speed by more than 25 knots.

3. Aerodynamic center shift is the key mechanism; c.g. offset due to sweep is detrimental. Implication is to sweep the blade without an internal spar.

4. A no spar swept-tip configuration was analyzed. The instability speed improved by more than 75 knots, reaching near 405 knots. The wing thickness is 13.5% chord, which is much thinner than the 23% thickness of the current technology tiltrotor wings.

5. Whirl flutter can appear as the critical phenomenon with further improvements in the air resonance speed.

6. Steady and oscillatory chordwise moments and oscillatory torsional moments increased significantly due to sweep. Blades and control system may need to be redesigned with higher loads.

7. A fundamental understanding of proprotor air resonance was provided.

8. Induced flow model bears no significance for high-speed stability predictions. Freewake is not required; a simple uniform inflow model is sufficient. Not using an inflow model is also acceptable at high speeds.

9. Predictions should be performed for both freewheeling with rotor speed perturbation and powered mode in actual flight with an ideal engine (no rotor speed perturbation) as air resonance can be more critical for the powered mode.

10. At least the first rotor flap, lag, and torsion modes must be included in the analysis.

11. Airfoil decks should be used for both the rotor and the wing. The wing aerodynamic model is only important if the wing beam mode is critical.

12. Periodic solution for freewheeling mode can be skipped before stability analysis to save computation time, provided the correct collective angle is used. However, periodic solution should be carried out for powered mode where deflections are larger.

13. Structural loads for the Boeing M222 were predicted within reasonable errors; trends were predicted but some difference in the magnitudes is present. A minimum loads point was

observed in transition; there exists a set of cyclics that alleviates the oscillatory loads because of the edgewise flow.

14. Aeroelastic stability predictions were verified with U.S. Army's predictions with CAMRAD II and RCAS for hypothetical wing/pylon and rotor models (a total of nine cases). Soft in-plane, stiff in-plane, hyper-stiff in-plane, and rigid rotors were studied. The predictions captured the general trends.

15. Air resonance predictions agreed well with U.S. Army's RCAS predictions for the Boeing M222 rotor. The agreement with the test data was good for low speeds, but some offset in the damping levels was observed for 140 and $192\ \mathrm{knots}$. The sources remain unknown.

16. University of Maryland's new Maryland Tiltrotor Rig test results provided valuable data for further validation and parametric study. Baseline data is gimbal-free, freewheeling, wing fairings on with straight and swept-tip blades. Gimbal-locked, powered mode, and wing fairings off data was also collected, all with straight and swept-tip blades.

17. Wing beam mode damping trends and magnitudes were predicted accurately for all configurations.

18. Wing chord mode damping was under-predicted. The trends for the gimbal-locked, straight blade configurations (freewheeling and powered) were not captured.

19. No significant impact of swept-tip blades was observed for the gimbal-free configuration up to $100\ \mathrm{knots}$.

20. A sweep back of $20°$ from $80\%R$ increased wing chord mode damping for the gimbal-locked, freewheeling, wing fairings off configuration. Analysis could not predict this increase.

21. Locking the gimbal provided higher damping for the wing chord mode, which was captured by the analysis.

22. Powered mode also resulted in higher wing chord mode damping compared to freewheeling. Analysis could not predict this behavior.

23. Wing aerodynamics increased wing beam mode damping at high speeds, although not as clearly as predictions due to scatter in the data.

7.2 Future Work

This work can be extended in both analysis and testing. The recommendations are outlined below in the order of importance.

7.2.1 Analysis

1. The underlying causes behind the differences in the stability predictions and the test data need to be explored. The differences between UMARC-II and RCAS/CAMRAD II should also be investigated.

2. A more detailed study for the blade tip geometry needs to be carried out. Different tip designs, including a combination of anhedral and sweep with more realistic geometries, such as a smooth transition region instead of a sudden, can be explored. The impact of higher loads on the design of blade, control system, and wing should be studied.

3. Coupling of comprehensive analysis with CFD can be significant for high-speed stability and transition blade and hub vibratory loads. The rotor – wing interactional aerodynamics can also be studied.

4. Active control can be an effective way to extend the stability boundary of a tiltrotor aircraft. Suitable control algorithms need to be investigated and the effect of such algorithms on performance, loads, and stability should be studied.

7.2.2 Testing

1. Modern test data at high speeds is needed to further validate the predictions and to eventually find elegant solutions for instability-free, high-speed, efficient flight of tiltrotor aircraft. The Maryland Tiltrotor Rig test data currently stops at $100\ \mathrm{knots}$, just when the data starts becoming interesting. This was an artificial restriction from the wind tunnel. Future tests are needed to break through this boundary to up to $175\ \mathrm{knots}$, which represents 400-knots full-scale flight. Interesting parametric validation data is expected from these tests.

2. There is no soft in-plane hingeless test data collected with modern equipment. The existing Boeing M222 data is limited in tunnel speed and provides no parametric data. As a part of the research in this dissertation, a hingeless hub, shown in Fig. 7.1, was designed for the Maryland Tiltrotor Rig to bridge this gap. This hub is currently being fabricated. A comprehensive test will be carried out with this new hub to provide experimental test data for proprotor air resonance and whirl flutter.

3. The Maryland Tiltrotor Rig can accommodate different wing spars to control the fixed system frequencies. Wings with different spars can be tested in order to understand the impact of fixed system frequencies on the high-speed stability.

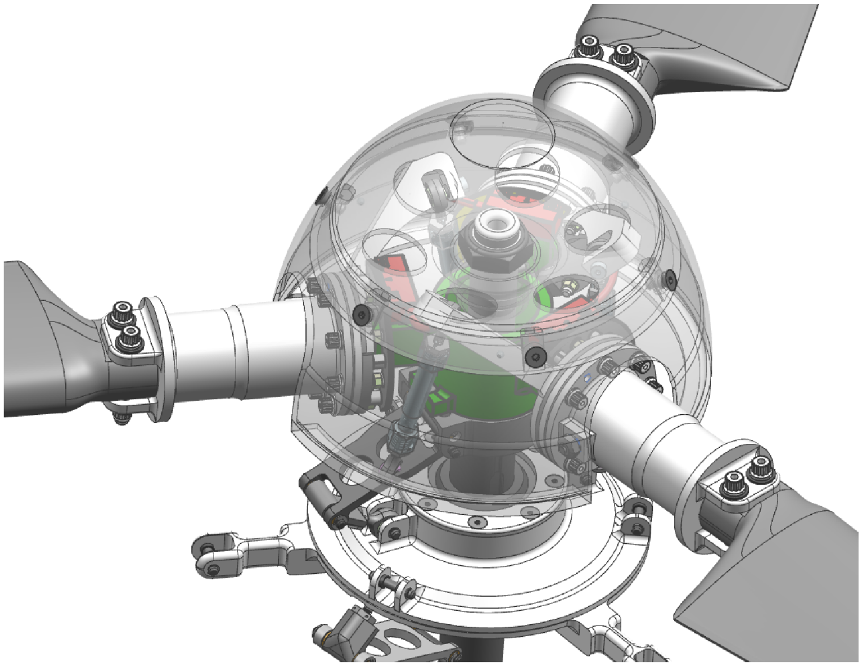

(a) Spinner and blades on

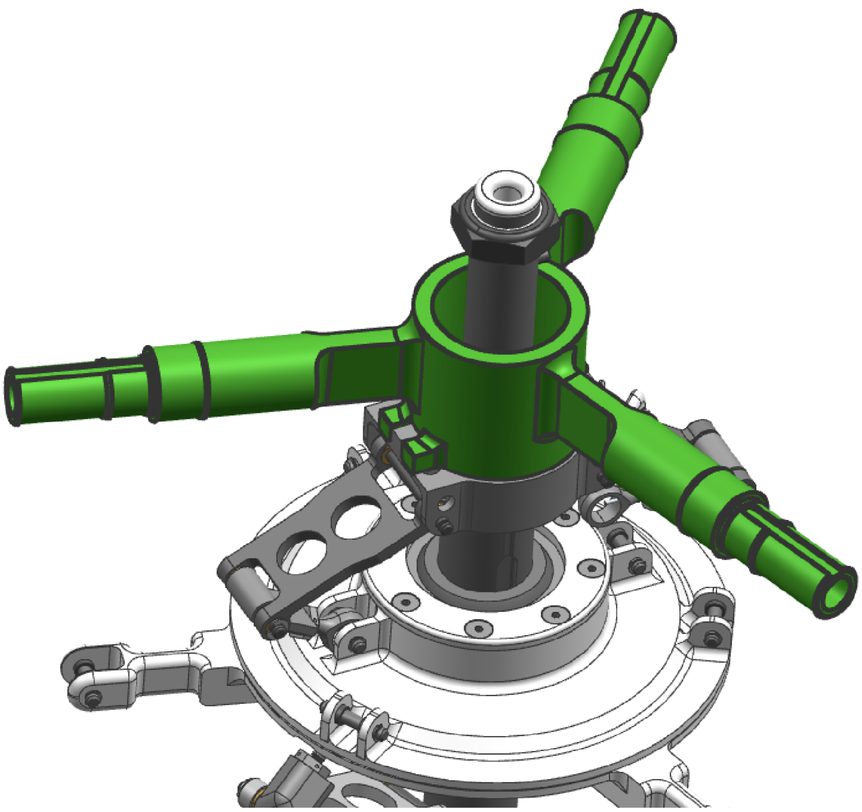

(b) Hub only

Figure 7.1: CAD Model of the Maryland Tiltrotor Rig hingeless hub

Bibliography

[1] Johnson, W., Yamauchi, G. K., and Watts, M. E., "NASA Heavy Lift Rotorcraft Systems Investigation," NASA-TP-2005-213467, December 2005.

[2] Whittle, R., "Karem Aircraft Building New Tiltrotor Ideas," *Vertiflite*, Vol. 62, (1), January-February 2016, pp. 36–38.

[3] Warwick, G., "Full-Scale Single Rotor Test Advances Maturity of Karem's OSTR," *Aviation Week & Space Technology*, Vol. 182, (45), November 2020.

[4] Johnson, W., "Dynamics of Tilting Proprotor Aircraft in Cruise Flight," NASA-TN-D-7677, NASA Ames Research Center and U.S. Army Air Mobility R&D Laboratory, May 1974.

[5] Taylor, E. S., and Browne, K. A., "Vibration Isolation of Aircraft Power Plants," *Journal of the Aeronautical Sciences*, Vol. 6, (2), December 1938, pp. 43–49. DOI: https://doi.org/10.2514/8.760

[6] Johnson, W., "A History of Rotorcraft Comprehensive Analyses," American Helicopter Society 44th Annual Forum, Phoenix, Arizona, May 2013.

[7] Blankenship, B. L., and Harvey, K. W., "A Digital Analysis for Helicopter Performance and Rotor Blade Bending Moments," *Journal of the American Helicopter Society*, Vol. 7, (4), October 1962, pp. 55–68. DOI: https://doi.org/10.4050/JAHS.7.55

[8] Blankenship, B. L., and Bird, B. J., "Program C81-11 Rotorcraft Flight Simulation," BHC Report 599-068-900, Bell Helicopter Company, January 1967.

[9] Van Gaasbeck, J. R., and Hsieh, P. Y., "Rotorcraft Flight Simulation Computer Program C81 with Datamap Interface, Volumes I and II," USAAVRADCOM-TR-80-D-38, U.S. Army Research and Technology Laboratories, October 1981.

[10] Corrigan, J. J., Bennett, R. L., and Hsieh, P. Y., "Copter 2000: The QTR and Beyond," American Helicopter Society 57th Annual Forum, Washington, D.C., May 2001.

[11] Bennett, R. L., "Rotor System Design and Evaluation Using a General Purpose Helicopter Flight Simulation Program," AGARD-CP-122, Specialists Meeting on Helicopter Rotor Loads Prediction Methods, Milan, Italy, March 1973.

[12] Yin, S. K., and Yen, J. G., "Aeromechanical Stability Analysis of COPTER," ITR Methodology Assessment Workshop, NASA Ames, June 1983.

[13] Wasikowski, M. E., Corrigan, J. J., and Bothwell, C. M., "Rotor Vibratory Hub and Blade Loads Prediction and Correlation," American Helicopter Society 55th Annual Forum, Montreal, Quebec, Canada, May 1999.

[14] Johnson, W., "A Comprehensive Analytical Model of Rotorcraft Aerodynamics and Dynamics, Parts I-III," NASA-TM-81182-81184, NASA Ames Research Center, June 1980.

[15] Johnson, W., "Development of a Comprehensive Analysis for Rotorcraft," *Vertica*, Vol. 5, (2, 3), January 1981, pp. 99–129, 185–216.

[16] Johnson, W., "CAMRAD/JA. Comprehensive Analytical Model of Rotorcraft Aerodynamics and Dynamics, Johnson Aeronautics Version," Johnson Aeronautics, Palo Alto, California, 1988.

[17] Johnson, W., "Rotorcraft Aeromechanics Applications of a Comprehensive Analysis," HeliJapan 1998: AHS International Meeting on Rotorcraft Technology and Disaster Relief, Gifu, Japan, April 1998.

[18] Johnson, W., "Technology Drivers in the Development of CAMRAD II," American Helicopter Society Aeromechanics Specialists' Conference, San Francisco, California, January 1994.

[19] Yeo, H., and Kreshock, A. R., "Whirl Flutter Investigation of Hingeless Proprotors," *Journal of Aircraft*, Vol. 57, (4), July-August 2020, pp. 586–596. DOI: https://doi.org/10.2514/1.C035609

[20] Kreshock, A. R., Thornburgh, R. P., and Yeo, H., "Comparison of Comprehensive Analyses Predicting Whirl Flutter Stability of the Wing and Rotor Aeroelastic Test System," *Journal of the American Helicopter Society*, Vol. 64, (4), October 2019, pp. 1–12. DOI: https://doi.org/10.4050/JAHS.64.042010

[21] Yeo, H., Bosworth, J., Acree, C. W., Jr., and Kreshock, A. R., "Comparison of CAMRAD II and RCAS Predictions of Tiltrotor Aeroelastic Stability," *Journal of the American Helicopter Society*, Vol. 63, (2), April 2018, pp. 1–13. DOI: https://doi.org/10.4050/JAHS.63.022001

[22] Acree, C. W., Jr., "Effects of V-22 Blade Modifications on Whirl Flutter and Loads," *Journal of the American Helicopter Society*, Vol. 50, (3), July 2005, pp. 269–278. DOI: https://doi.org/10.4050/1.3092863

[23] Acree, C. W., Jr., Peyran, R. J., and Johnson, W., "Rotor Design Options for Improving XV-15 Whirl-Flutter Stability Margins," NASA-TP-2004-212262, NASA Ames Research Center, March 2004.

[24] Acree, C. W., Jr., "An Improved CAMRAD Model for Aeroelastic Stability Analysis of the XV-15 with Advanced Technology Blades," NASA-TM-4448, NASA Ames Research Center, March 1993.

[25] Popelka, D., Sheffler, M., and Bilger, J., "Correlation of Test and Analysis for the 1/5-Scale V-22 Aeroelastic Model," *Journal of the American Helicopter Society*, Vol. 32, (2), April 1987, pp. 21–33. DOI: https://doi.org/10.4050/JAHS.32.21

[26] Johnson, W., Lau, B. H., and Bowles, J. V., "Calculated Performance, Stability, and Maneuverability of High-Speed Tilting-Prop-Rotor Aircraft," NASA-TM-88349, NASA Ames Research Center, September 1986.

[27] Anon., "RCAS Theory Manual, Version 2.0," USAAMCOM/AFDD-TR-02-A-005, US Army Aviation and Missile Command, Moffett Field, CA, June 2003.

[28] Anon., "RCAS User's Manual, Version 2.0," USAAMCOM/AFDD-TR-02-A-006, US Army Aviation and Missile Command, Moffett Field, CA, June 2003.

[29] Anon., "RCAS Applications Manual, Version 2.0," USAAMCOM/AFDD-TR-02-A-007, US Army Aviation and Missile Command, Moffett Field, CA, June 2003.

[30] Anon., "RCAS Programmers Manual, Version 2.0," USAAMCOM/AFDD-TR-02-A-008, US Army Aviation and Missile Command, Moffett Field, CA, June 2003.

[31] Saberi, H., Hasbun, M., Hong, J., Yeo, H., and Ormiston, R. A., "Overview of RCAS Capabilities, Validations, and Rotorcraft Applications," American Helicopter Society 71st Annual Forum, Virginia Beach, Virginia, May 2015.

[32] Saberi, H., Khoshlahjeh, M., Ormiston, R. A., and Rutkowski, M. J., "Overview of RCAS and Application to Advanced Rotorcraft Problems," American Helicopter Society 4th Decennial Specialists' Conference on Aeromechanics, San Francisco, California, January 2004.

[33] Bowen-Davies, G., "RCAS Aeromechanics Computations of the Boeing 222 Proprotor," AHS International Technical Meeting: Aeromechanics Design for Transformative Vertical Flight, San Francisco, California, January 2018.

[34] Bowen-Davies, G., "Comparison of Vortex Wake, VVPM and CFD Aeromechanics Computations of the Boeing 222 Proprotor," American Helicopter Society 74th Annual Forum, Phoenix, Arizona, May 2018.

[35] Bir, G., Chopra, I., and Nguyen, K., "Development of UMARC (University of Maryland Advanced Rotorcraft Code)," American Helicopter Society 46th Annual Forum, Washington, D.C., May 1990.

[36] Abhishek, A., Datta, A., and Chopra, I., "Prediction of UH-60A Structural Loads Using Multibody Analysis and Swashplate Dynamics," *Journal of Aircraft*, Vol. 46, (2), March-April 2009, pp. 474–490. DOI: https://doi.org/10.2514/1.35076

[37] Srinivas, V., and Chopra, I., "Validation of a Comprehensive Aeroelastic Analysis for Tiltrotor Aircraft," *Journal of the American Helicopter Society*, Vol. 43, (4), October 1998, pp. 333–341. DOI: https://doi.org/10.4050/JAHS.43.333

[38] Srinivas, V., Chopra, I., and Nixon, M. W., "Aeroelastic Analysis of Advanced Geometry Tiltrotor Aircraft," *Journal of the American Helicopter Society*, Vol. 43, (3), July 1998, pp. 212–221. DOI: https://doi.org/10.4050/JAHS.43.212

[39] Nixon, M. W., *Aeroelastic Response and Stability of Tiltrotors with Elastically-Coupled Composite Rotor Blades*, Ph.D. thesis, University of Maryland, 1993.

[40] Quaranta, G., Bindolino, G., Masarati, P., and Mantegazza, P., "Toward a Computational Framework for Rotorcraft Multi-Physics Analysis: Adding Computational Aerodynamics to Multibody Rotor Models," 30th European Rotorcraft Forum, Marseilles, France, September 2004.

[41] Ghiringhelli, G. L., Masarati, P., Mantegazza, P., and Nixon, M. W., "Multi-Body Analysis of the 1/5 Scale Wind Tunnel Model of the V-22 Tiltrotor," American Helicopter Society 55th Annual Forum, Montreal, Quebec, Canada, May 1999.

[42] Masarati, P., Piatak, D. J., Singleton, J. D., and Mantegazza, P., "An Investigation of Soft-Inplane Tiltrotor Aeromechanics Using Two Multibody Analyses," American Helicopter Society 4th Decennial Specialists' Conference on Aeromechanics, San Francisco, California, January 2004.

[43] Masarati, P., Piatak, D. J., Quaranta, G., and Singleton, J. D., "Further Results of Soft-Inplane Tiltrotor Aeromechanics Investigation Using Two Multibody Analyses," American Helicopter Society 60th Annual Forum, Baltimore, Maryland, June 2004.

[44] Bauchau, O. A., Damilano, G., and Theron, N. J., "Numerical Integration of Non-Linear Elastic Multi-Body Systems," *International Journal for Numerical Methods in Engineering*, Vol. 38, (16), August 1995, pp. 2727–2751. DOI: https://doi.org/10.1002/nme.1620381605

[45] Barkai, S. M., and Rand, O., "The Influence of Composite Induced Couplings on Tiltrotor Whirl Flutter Stability," *Journal of the American Helicopter Society*, Vol. 43, (2), April 1998, pp. 133–145. DOI: https://doi.org/10.4050/JAHS.43.133

[46] Gaffey, T. M., "The Effect of Positive Pitch-flap Coupling (Negative δ_3) on Rotor Blade Motion Stability and Flapping," *Journal of the American Helicopter Society*, Vol. 14, (2), April 1969, pp. 49–67. DOI: https://doi.org/10.4050/JAHS.14.2.49

[47] Hall, W. E., Jr., "Prop-Rotor Stability at High Advance Ratios," *Journal of the American Helicopter Society*, Vol. 11, (2), April 1966, pp. 11–26. DOI: https://doi.org/10.4050/JAHS.11.2.11

[48] Maisel, M. D., Giulianetti, D. J., and Dugan, D. C., “The History of the XV-15 Tilt Rotor Research Aircraft: From Concept to Flight,” NASA-SP-2000-4517, NASA, 2000.

[49] Anon., “Advancement of Proprotor Technology. Task I: Design Study Summary,” NASA-CR-114682, Bell Helicopter Company, September 1969.

[50] Anon., “Advancement of Proprotor Technology. Task II: Wind-Tunnel Test Results,” NASA-CR-114363, Bell Helicopter Company, September 1971.

[51] Maisel, M. D., “NASA/Army XV-15 Tilt Rotor Research Aircraft Familiarization Document,” NASA-TM-X-62, 407, NASA Ames Research Center, January 1975.

[52] Weiberg, J. A., and Maisel, M. D., “Wind-Tunnel Tests of the XV-15 Tilt Rotor Aircraft,” NASA-TM-81177, NASA Ames Research Center, April 1980.

[53] Settle, T. B., and Kidd, D. L., “Evolution and Test History of the V-22 0.2-Scale Aeroelastic Model,” American Helicopter Society National Specialists’ Meeting on Rotorcraft Dynamics, Arlington, Texas, November 1989.

[54] Piatak, D. J., Kvaternik, R. G., Nixon, M. W., Langston, C. W., Singleton, J. D., Bennett, R. L., and Brown, R. K., “A Parametric Investigation of Whirl-Flutter Stability on the WRATS Tiltrotor Model,” *Journal of the American Helicopter Society*, Vol. 47, (2), April 2002, pp. 134–144. DOI: https://doi.org/10.4050/JAHS.47.134

[55] Corso, L. M., Popelka, D. A., and Nixon, M. W., “Design, Analysis, and Test of a Composite Tailored Tiltrotor Wing,” *Journal of the American Helicopter Society*, Vol. 45, (3), July 2000, pp. 207–215. DOI: https://doi.org/10.4050/JAHS.45.207

[56] Nixon, M. W., Piatak, D. J., Corso, L. M., and Popelka, D. A., “Aeroelastic Tailoring for Stability Augmentation and Performance Enhancements of Tiltrotor Aircraft,” *Journal of the American Helicopter Society*, Vol. 45, (4), October 2000, pp. 270–279. DOI: https://doi.org/10.4050/JAHS.45.270

[57] Nixon, M. W., Langston, C. W., Singleton, J. D., Piatak, D. J., Kvaternik, R. G., Corso, L. M., and Brown, R. K., “Aeroelastic Stability of a Four-Bladed Semi-Articulated Soft-Inplane Tiltrotor Model,” International Forum on Aeroelasticity and Structural Dynamics, Amsterdam, The Netherlands, June 2003.

[58] Kvaternik, R. G., Piatak, D. J., Nixon, M. W., Langston, C. W., Singleton, J. D., Bennett, R. L., and Brown, R. K., “An Experimental Evaluation of Generalized Predictive Control for Tiltrotor Aeroelastic Stability Augmentation in Airplane Mode of Flight,” *Journal of the American Helicopter Society*, Vol. 47, (3), July 2002, pp. 198–208. DOI: https://doi.org/10.4050/JAHS.47.198

[59] Studebaker, K., and Matuska, D. G., “Variable Diameter Tiltrotor Wind Tunnel Test Results,” American Helicopter Society 49th Annual Forum, St. Louis, Missouri, May 1993.

[60] Matuska, D., Dale, A., and Lorber, P., “Wind Tunnel Test of a Variable-Diameter Tiltrotor (VDTR) Model,” NASA-CR-177629, NASA Ames Research Center, January 1994.

[61] Young, L. A., "Tilt Rotor Aeroacoustic Model (TRAM): A New Rotorcraft Research Facility," AHS International Meeting on Advanced Rotorcraft Technology and Disaster Relief, Gifu, Japan, April 1998.

[62] Johnson, W., "Calculation of Tilt Rotor Aeroacoustic Model (TRAM DNW) Performance, Airloads, and Structural Loads," American Helicopter Society Aeromechanics Specialists' Meeting, Atlanta, Georgia, November 2000.

[63] McCluer, M. S., and Johnson, J. L., "Full-Span Tiltrotor Aeroacoustic Model (FS TRAM) Overview and Initial Testing," American Helicopter Society Aerodynamics, Acoustics, and Test and Evaluation Technical Specialists' Meeting, San Francisco, California, January 2002.

[64] Acree, C. W., Jr., and Sheikman, A. L., "Development and Initial Testing of the Tiltrotor Test Rig," American Helicopter Society 74th Annual Forum, Phoenix, Arizona, May 2018.

[65] Kottapalli, S., and Acree, C. W., Jr., "Correlation of Full-Scale Isolated Proprotor Performance and Loads," Vertical Flight Society 75th Annual Forum, Philadelphia, Pennsylvania, May 2019.

[66] Datta, A., Tsai, F., and Sutherland-Foggio, J., "Design of a New Tilt Rotor Test Facility at the University of Maryland," AIAA SciTech Forum, San Diego, California, January 2019.

[67] Tsai, F., Sutherland, J., Akinwale, A., Morin, A., Gul, S., and Datta, A., "Whirl Flutter Test of the Maryland Tiltrotor Rig: Overview," AIAA SciTech Forum, San Diego, California, January 2022.

[68] Sutherland, J., Tsai, F., and Datta, A., "Whirl Flutter Test of the Maryland Tiltrotor Rig: Swept-tip Blades," AIAA SciTech Forum, San Diego, California, January 2022.

[69] Kreshock, A. R., Thornburgh, R. P., and Wilbur, M. L., "Overview of the TiltRotor Aeroelastic Stability Testbed," AIAA SciTech Forum, San Diego, California, January 2022.

[70] Kreshock, A. R., Thornburgh, R. P., Kang, H., and Yeo, H., "Pretest Flutter Predictions of the Upcoming Aeroelastic Tiltrotor Wind Tunnel Test," Vertical Flight Society 76th Annual Forum, Virtual, October 2020.

[71] Magee, J. P., and Alexander, H. R., "Wind Tunnel Tests of a Full Scale Hingeless Prop/Rotor Designed for the Boeing Model 222 Tilt Rotor Aircraft," NASA-CR-114664, Boeing Vertol Company, October 1973.

[72] Ham, N. D., Bauer, P. H., Lawrence, T. H., and Yasue, M., "A Study of Gust and Control Response of Model Rotor-Propellers in a Wind Tunnel Airstream," NASA-CR-137756, August 1975.

[73] Nicely, J., and Walsh, G., "Technology Data, Operations and Maintenance Manual for a Wind Tunnel Model of a Prop Rotor and Cantilever Wing," D210-10961-1, Boeing Vertol Company, June 1975.

[74] Magee, J. P., and Alexander, H. R., "Wind Tunnel Test on a 1/4.622 Froude Scale, Hingeless Rotor, Tilt Rotor Model, Volumes I-IV," NASA-CR-151936-151939, The Boeing Company - Vertol Division, September 1976.

[75] Hodges, D. H., and Dowell, E. H., "Nonlinear Equations of Motion for the Elastic Bending and Torsion of Twisted Nonuniform Rotor Blades," NASA-TN-D-7818, December 1974.

[76] Hodges, D. H., Ormiston, R. A., and Peters, D. A., "On the Nonlinear Deformation Geometry of Euler-Bernoulli Beams," NASA-TP-1566, April 1980.

[77] Johnson, W., *Helicopter Theory*, Dover Publications, New York, 1980.

[78] Tasker, F. A., and Chopra, I., "Assessment of Transient Analysis Techniques for Rotor Stability Testing," *Journal of the American Helicopter Society*, Vol. 35, (1), January 1990, pp. 39–50. DOI: https://doi.org/10.4050/JAHS.35.39

[79] Lanczos, C., *The Variational Principles of Mechanics*, University of Toronto Press, Canada, 1970.

[80] Bhagwat, M. J., and Leishman, J. G., "Stability, Consistency and Convergence of Time-Marching Free-Vortex Rotor Wake Algorithms," *Journal of the American Helicopter Society*, Vol. 46, (1), January 2001, pp. 59–71. DOI: https://doi.org/10.4050/JAHS.46.59

[81] Leishman, J. G., Bhagwat, M. J., and Bagai, A., "Free-Vortex Filament Methods for the Analysis of Helicopter Rotor Wakes," *Journal of Aircraft*, Vol. 39, (5), September-October 2002, pp. 759–775. DOI: https://doi.org/10.2514/2.3022

[82] Squire, H. B., "The Growth of a Vortex in Turbulent Flow," *Aeronautical Quarterly*, Vol. 16, (3), August 1965, pp. 302–306. DOI: https://doi.org/10.1017/S0001925900003516

[83] Vatistas, G. H., Kozel, V., and Mih, W. C., "A simpler model for concentrated vortices," *Experiments in Fluids*, Vol. 11, (1), January 1991, pp. 73–76. DOI: https://doi.org/10.1007/BF00198434

[84] Argyris, J. H., and Scharpf, D. W., "Finite Elements in Time and Space," *Nuclear Engineering and Design*, Vol. 10, (4), December 1969, pp. 456–464. DOI: https://doi.org/10.1016/0029-5493(69)90081-8

[85] Borri, M., "Helicopter Rotor Dynamics by Finite Element Time Approximation," *Computers & Mathematics with Applications*, Vol. 12A, (1), January 1986, pp. 149–160. DOI: https://doi.org/10.1016/0898-1221(86)90092-1

[86] Srinivasan, G. R., and Baeder, J. D., "TURNS: A Free-Wake Euler/Navier-Stokes Numerical Method for Helicopter Rotors," *AIAA Journal*, Vol. 31, (5), May 1993, pp. 959–962. DOI: https://doi.org/10.2514/3.49036

[87] He, C., and Zhao, J., "Modeling Rotor Wake Dynamics with Viscous Vortex Particle Method," *AIAA Journal*, Vol. 47, (4), April 2009, pp. 902–915. DOI: https://doi.org/10.2514/1.36466

[88] Zhao, J., and He, C., "A Viscous Vortex Particle Model for Rotor Wake and Interference Analysis," *Journal of the American Helicopter Society*, Vol. 55, (1), January 2010, 12007. DOI: https://doi.org/10.4050/JAHS.55.012007

[89] Sitaraman, J., Potsdam, M., Wissink, A., Jayaraman, B., Datta, A., Mavriplis, D., and Saberi, H., "Rotor Loads Prediction Using Helios: A Multisolver Framework for Rotorcraft Aeromechanics Analysis," *Journal of Aircraft*, Vol. 50, (2), March 2013, pp. 478–492. DOI: https://doi.org/10.2514/1.C031897

[90] Anon., "V/STOL Tilt Rotor Aircraft Study - Volume II: Preliminary Design of Research Aircraft," NASA-CR-114438, The Boeing Company - Vertol Division, March 1972.

[91] Tsai, F., Sutherland-Foggio, J., and Datta, A., "The Maryland Tiltrotor Rig (MTR): The Baseline Gimballed Hub," Vertical Fight Society 75th Annual Forum, Philadelphia, Pennsylvania, May 2019.

[92] Gul, S., and Datta, A., "Design Analysis for a Mach-Scaled Hingeless Hub for the Maryland Tiltrotor Rig," 8th Asian/Australian Rotorcraft Forum, Ankara, Turkey, October-November 2019.

[93] Morin, A., *Fabrication, Wind Tunnel Testing, and Freewheeling Analysis of 4.75-ft Diameter Composite Tiltrotor Blades*, Master's thesis, University of Maryland, 2021. DOI: https://doi.org/10.13016/xniw-jyuc

[94] Sutherland, J., and Datta, A., "Fabrication, Testing, and 3-D Comprehensive Analysis of Swept Tip Tiltrotor Blades," Vertical Flight Society 77th Annual Forum, Virtual, May 2021.